

*ÉCOLE DOCTORALE ED 269 Mathématiques, Sciences de l'Information et
de l'Ingénieur*

ICube – UMR 7357, L'équipe AVR – Automatique, Vision, Robotique

L'équipe IPP - Instrumentation et Procédés Photoniques

THÈSE présentée par :

Oscar Mauricio Caravaca Mora

Soutenue le : **21/02/2020**

Pour obtenir le grade de : **Docteur de l'université de Strasbourg**
Discipline/ Spécialité : Signal, image, automatique, robotique - Génie biomédical.

**Development of a novel method using optical
coherence tomography (OCT) for guidance of
robotized interventional endoscopy**

THÈSE dirigée par :

Paul Montgomery

Directeur de Recherche, CNRS, ICube

Michel De Mathelin

Professeur des Universités, ICube

Michalina Gora

Chargée de Recherche, CNRS, ICube

RAPPORTEURS :

Maciej Szkulmowski

Associated Professor, Institute of Physics, Nicolaus
Copernicus University, Torun, Poland

Nicolas Andreff

Professeur des Universités, FEMTO-ST, Besançon

EXAMINATEURS :

Hans Zappe

Professor, Institute of Microsystems Technology
IMTEK

Claude Boccara

Professeur des Universités, Institut Langevin

Acknowledgements

I thank the financial support for the doctoral project from the ATIP-Avenir grant, the ARC Foundation and the IdEx Strasbourg University. I would like to thank as well IRCAD for the access to the in vivo swine experiments, the collaborators from the AVR team and IRIS Platform: in particular Lucile Zorn, Philippe Zanne and Florent Nageotte, the collaborators from the IPB team: Natalia Zulina, Sara Gravelyn, the director and co-director of the thesis: Dr. Paul Montgomery and Pr. Michel De Mathelin, Dr. Bernard Dallemagne for his collaboration with the in vivo test and Michalina J. Gora for her important role in supervising the progress of the work. I also want to thank David Gavarrete Carballo for his collaboration in the graphics illustrations of the final system, my family and my wife Fanny for their support during the three years of thesis.

Contents

Acknowledgements	ii
Contents	iii
List of Tables	vi
List of Figures	7
List of equations.....	xvii
List of acronyms.....	xx
Introduction.....	1
Chapter 1 State of the art.....	8
1.1 Medical Context.....	9
1.1.1 Colorectal Cancer	11
1.1.2 Colorectal cancer diagnosis	13
1.1.3 Treatment of colorectal cancer	21
1.2 Robot-assisted minimally invasive surgery	23
1.2.1 Robotized flexible interventional endoscope for intraluminal surgery	28
1.3 Optical Coherence Tomography	30
1.3.1 Basics of Optical Coherence Tomography.....	32
1.3.2 Endoscopic OCT.....	34
1.3.3 Applications of endoscopic OCT	36
1.4 Advanced imaging and robotics.....	38
1.5 Motivation and objective	44
1.6 French summary of the chapter.....	45
Chapter 2 Optical Coherence Tomography Imaging console with dual imaging modes	47
2.1 OCT imaging system for pre-clinical examination.....	48
2.1.1 OCT engine	50
2.1.2 Interferometer design.....	53

2.1.3 Sample arm design	55
2.2 Linear Scanning Synchronization.....	56
2.3 Human machine interface	59
2.4 Characterization and optimization.....	61
2.4.1 Signal to noise ratio modelling.....	61
2.4.2 Signal to noise measurements and optimization	63
2.5 Experimental validation	65
2.6 Conclusions of the chapter.....	67
2.7 French summary of the chapter.....	67
Chapter 3 Novel steerable OCT instrument for flexible endoscopy	70
3.1 Optical probe.....	71
3.2 OCT 3D scanning actuation.....	74
3.2.1 Helical scanning concept	74
3.2.2 Proximal rotation and translation.....	76
3.2.3 Rotational Synchronization	77
3.2.4 Probe connection.....	79
3.3 Bending actuation	82
3.4 Characterization and optimization.....	85
3.4.1 Experimental setup and analysis.....	89
3.4.2 Two-dimensional rotational artifacts.....	92
3.4.3 Three-dimensional pullback artefacts.....	99
3.5 Experimental validation	103
3.6 Conclusions of the chapter.....	104
3.7 French summary of the chapter.....	105
Chapter 4 OCT enhanced robotized flexible endoscopy.....	109
4.1 Electro-mechanical integration of the system	110
4.2 Software compatibility and control of the system.....	113
4.3 Characterization and optimization.....	115
4.3.1 Extended scanning workspace model	116
4.3.2 Experimental validation of the workspace.....	125
4.3.3 Three-dimensional artefacts in tool-based pullback scanning.....	130

4.4 Experimental validation	133
4.5 Conclusions of the chapter.....	134
4.6 French summary of the chapter.....	135
Chapter 5 Development of standardization model for pre-clinical validation	139
5.1 Pre-clinical validation	140
5.2 The human colon model.....	140
5.3 Ex vivo swine intestine tissue imaging	143
5.4 Colorectal cancer phantom development.....	146
5.5 In vivo animal test.....	153
5.6 Conclusions of the chapter.....	156
5.7 French summary of the chapter.....	156
Conclusions and future work.....	160
Main conclusions.....	162
Future Work.....	162
French summary	165
Annexes	170
A. AJCC TNM System	171
B. Optics.....	173
C. Actuation controllers.....	177
D. Geometrical model of the flexible instrument.....	178
E. Phantom fabrication	183
F. Datasheets.....	184
Bibliography.....	199

List of Tables

Table 1.1 Robotic flexible endoscopy platforms for Gastrointestinal applications [99]..	28
Table 2.1 Specification of the AXSUN Integrated Engine [273].....	51
Table 3.1 Parameters lensed fibers fabricated by IDIL Fibers Optiques.	72
Table 3.2 Comparison table of different types of OCT catheters.	76
Table 3.3 Reference values of frame rate, the average of the actual value, the standard deviation and the percentage of error with respect to the reference.....	94
Table 3.4 Angle of flexion measured, the rounded value, the mean and standard deviation of the angle spacing.	97
Table 4.1 Summary of validated and estimated area.	129
Table 4.2 Summary of validated and estimated volume.	129
Table 5.1 Materials for phantoms fabrication [319].....	147
Table 5.2 Final composition of each layer and testing in the OCT system.	148
Table A.1 Definition of Primary Tumor.	171
Table A.2 Definition of Regional Lymph Node (N).	171
Table A.3 Definition of distant Metastasis.	172
Table A.4 AJCC prognostic stage groups.....	172
Table A.5 Categorization by cancer registries [334].	172
Table B.6 Loops sample arm for endoscopic mode.....	175
Table B.7 Loops reference arm for dual mode.....	176
Table B.8 Loops sample arm for the benchtop mode.....	176

List of Figures

Figure 1.1 Digestive system and the exocrine glands. For the National Cancer Institute © 2020 Terese Winslow LLC, U.S. Govt. has certain rights [2].	9
Figure 1.2 (A) Schematic diagram of the wall anatomy of four sections of the digestive tract and (B) examples of microscopic images of histology slides with Hematoxylin and Eosin staining of thinly sliced biopsy specimens. Reprinted/adapted by permission from Springer Nature: Springer eBook, The Digestive System I: The Alimentary Canal by Anders Rehfeld, Malin Nylander, Kirstine Karnov, © 2017 [4].	10
Figure 1.3 Estimated number of new cases of cancer in 2018 for both sexes and all ages. GLOBO CAN 2018 [12].	12
Figure 1.4 Level of invasion of pedunculated and sessile malignant polyps according to the Haggitt classification. Adapted/reprinted by permission from John Wiley and Sons: Colorectal Disease. Management of the malignant colorectal polyp: ACPGBI position statement by N. Haboubi, S. G. McGee, S. Rasheed, et al. © 2013 [15].	13
Figure 1.5 Colonoscopy relies on visual inspection of the colon wall. For the National Cancer Institute © 2020 Terese Winslow LLC, U.S. Govt. has certain rights [2].	14
Figure 1.6 Gross anatomy of the large intestine. For the National Cancer Institute © 2020 Terese Winslow LLC, U.S. Govt. has certain rights [2].	15
Figure 1.7 Layer structure of the colon wall, (A) cancer in the stage 0, (B) stage I and (C) stage IV and metastasis. For the National Cancer Institute © 2020 Terese Winslow LLC, U.S. Govt. has certain rights [2].	16
Figure 1.8 Relative survival rate in US. patients with colorectal cancer for different stages based on the SEER database [26].	17
Figure 1.9 Invasive cancer visible in white light endoscopy (A) without magnification, (B) with magnification and (C) with magnification and digital chromoendoscopy [27].	17
Figure 1.10 Schematic diagram showing the benefits of narrow band imaging. Reprinted by permission from Springer Nature: International Journal of Colorectal Disease. Rationale for and clinical benefits of colonoscopy with narrow band imaging: pathological prediction and colorectal screening by Hiroyuki Aihara, Shoichi Saito, Hisao Tajiri. © 2012 [31].	18

Figure 1.11. Schematic diagram of the AFI system [35].	19
Figure 1.12 (A) Schematic drawing showing principle of confocal endomicroscopy. Reprinted by permission from Springer Nature: Indian J Gastroenterol (2019) 38: 281. Optical biopsy in gastroenterology: Focus on confocal laser endomicroscopy, Zaheer Nabi, D. Nageshwar Reddy. © 2019 [37]. (B) Miami classification for probe-based confocal laser endomicroscopy. Reprinted by permission from Georg Thieme Verlag KG: Endoscopy 2011; 43(10): 882-891. Miami classification for probe-based confocal laser endomicroscopy, M. Wallace, G. Y. Lauwers, Y. Chen, E. Dekker, P. Fockens, P. Sharma, A. Meining. © 2011 [38].	20
Figure 1.13 Endoscopic mucosal resection procedure: (A) Cap-assisted EMR, (B) Ligation-assisted EMR Adapted/reprinted by permission from Elsevier: Gastroenterology. Endoscopic Mucosal Resection: Not Your Father's Polypectomy Anymore by Vinay Chandrasekhara, Gregory G. Ginsberg. © 2011 [48].	22
Figure 1.14 Endoscopic mucosal dissection procedure. Adapted/reprinted by permission from Springer Nature: Springer. Endoscopic Submucosal Dissection (ESD). In: Sonoda T. (eds) Advanced Colonoscopy by Niimi K., Fujishiro M., Koike K. © 2014 [52].	23
Figure 1.15 Da Vinci SP from Intuitive Surgical, Inc.	27
Figure 1.16 (A) Aer-O-Scope, (B) Endotics system, (C) Flex® Robotic System and (D) ISIS/STRAS system.	27
Figure 1.17 Distal part of the endoscopic platform. © 2018, IEEE [98].	29
Figure 1.18 (A) Master interface and (B) slave interface (B) of the STRAS robot. © 2018, IEEE [98].	29
Figure 1.19 Optical Coherence Tomography. Cross-sectional images generated by performing 1D axial scan to obtain depth information (Z), transversal plus axial (ZX) scanning for 2D information (B-scan) and axial scanning plus XY scanning for three-dimensional imaging. Adapted/reprinted by permission from Springer Nature: Springer. Introduction to OCT by James G. Fujimoto, Wolfgang Drexler. © 2015 [117].	30
Figure 1.20 Generic fiber-optic OCT system. Bold lines represent fiber-optic paths, red lines represent free-space optical paths, and thin lines electronic signal paths. Adapted/reprinted by permission from Springer Nature: Springer. Theory of Optical Coherence Tomography by Joseph A. Izatt, Michael A. Choma, Al-Hafeez Dhalla. © 2015 [117].	33

Figure 1.21 OCT endoscope designs: (A) side-viewing; (B) forward-viewing endoscope; (C) proximal scanning with a fiber-optic rotary joint for pull-back/rotation 3D imaging; (D) distal-scanning endoscope with micromotor; (E) all-fiber-optic ball lens; (F) pairs-angle-rotation-scanning forward viewing endoscope . Adapted/reprinted by permission from [204].	35
Figure 1.22 NvisionVLE Imaging Console from NinePoint Medical. Adapted/reprinted by permission from Oxford University Press: Diseases of the Esophagus. Volumetric laser endomicroscopy and its application to Barrett's esophagus: results from a 1,000 patient registry by Smith, M S; Cash, B. © 2015 [41].	37
Figure 1.23 Tethered capsule endomicroscopy. Adapted/reprinted by permission from Springer Nature: Nature Medicine. Tethered capsule endomicroscopy enables less invasive imaging of gastrointestinal tract microstructure by Michalina J Gora et al. © 2013 [185].	38
Figure 1.24 Niris OCT probe in vivo during animal robotic prostate surgery [233].	39
Figure 1.25 OCT probe under MRI guidance for neurosurgery [236].	39
Figure 1.26 Robot-assisted three-dimensional registration for cochlear implant surgery using a common-path swept-source optical coherence tomography probe (CP-SSOCT). (A) Picture of the robotic platform. (B) Close-up of the robotic arm with the mounted rotary motor (M), casing (C), 21G tubes for restricting lateral motion (T), and CP-SSOCT needle probe (P) [239].	40
Figure 1.27 (A) SMART micro-forceps, microsurgery system [260], (B) Intraocular robotic interventional surgical system (IRISS) [261], (C-D) Robotic system for OCT imaging of stationary and moving eyes [262], (E) robotic tele-manipulator for OCT guided retinal surgery [263].	41
Figure 1.28 (A) Experimental setup, (B) Multimodal imaging system architecture, and (C) the kinematic scheme of the 6 DoF robotic system, © 2016, IEEE [249].	41
Figure 1.29 (A) The CTR prototype and the OCT system, (B) Distal end of the CTR and the eye-to-hand configuration OCT probe, © 2017, IEEE [259].	42
Figure 1.30 (A) Deformed model of the sclera, (B) Force classification based on simulation-trained neural networks from OCT images. Adapted/reprinted by permission from Springer Nature: Int J CARS. Force classification during robotic interventions	

through simulation-trained neural networks by Mendizabal, A., Sznitman, R. & Cotin, S. © 2019 [269].	42
Figure 1.31 The 7-DoF robotic articulated endoscope. It has two operating channels: the camera and interchangeable instruments such as a pCLE. Adapted/reprinted by permission from Springer Nature: Surgical Endoscopy. Robot-assisted transvaginal peritoneoscopy using confocal endomicroscopy: a feasibility study in a porcine model by Newton RC et al. © 2012 [270].	43
Figure 1.32 Distal end of the balloon actuation minimally invasive device, © 2012, IEEE.	43
Figure 2.1 General scheme of the OCT Imaging Console (OCT-IC).	48
Figure 2.2 Exploded-view of the OCT-IC and its components.	50
Figure 2.3 AXSUN OCT Engine [272].	51
Figure 2.4 Block diagram implemented in the FPGA image processing pipeline [274].	53
Figure 2.5 Scheme of the Interferometer implemented in the OCT-IC, Data display and Recording and the two imaging modes. C – circulator, PBS – polarization beam splitter, DBD – dual balance detector, H – horizontal, V – vertical.	54
Figure 2.6 Components of the translation stage for the reference arm.	55
Figure 2.7 Translation stage of the reference arm and its connection with the motor driver and user PC.	55
Figure 2.8 Thorlabs Galvo system for linear scanning in benchtop mode.	56
Figure 2.9 Electrical connection for control and communication of the Benchtop imaging system, motor drivers, MCCDAQ, AXSUN OCT engine and the PC for user interaction.	57
Figure 2.10 Synchronization of the Frame acquisition through the <i>image_sync</i> signal for Benchtop imaging.	58
Figure 2.11 OCT software design and components.	60
Figure 2.12 SNR vs. Reference Power.	62
Figure 2.13 Experimental setup for SNR optimization.	64
Figure 2.14 Power of the reference arm vs. the sensitivity.	64
Figure 2.15 OCT imaging console OCT-IC.	65
Figure 2.16 Axial view of the index finger, with 13 mm field of view, 1.5 mm of penetration depth, 26.32 μm for the lateral resolution and 7.56 μm for the axial resolution, A-line 100 kHz and B-scan rate of 138 fps.	66

Figure 2.17 Two different views of the 3D OCT image reconstruction of the index finger of Figure 2.16.....	66
Figure 3.1 Lensed Fiber design. (A) Cross-sectional illustrated view of the lensed fiber. (B) Zemax specifications for the lensed fiber SER1800471 in Table 3.1.....	72
Figure 3.2 Assembly process of the optical probe. (A) The optical fiber core is inserted into the driveshaft. (B) The lensed is fixed just outside of the driveshaft. (C) Lateral view of the ball lensed showing reflected test light.	73
Figure 3.3 Assembly of the SC/APC fast mount proximal connector. (A) Optical fiber and torque coil placed into the SC/APC connector. (B) Hypo-tube covering the torque coil to avoid loops during rotation; green cap to protect the ferule of the connector. (C) Complete assembly of the optical probe.	73
Figure 3.4 Helical scanning implements rotational and translational motions.....	75
Figure 3.5 3D Components of the 3D scanner actuators with stroke length = 150 mm. .	77
Figure 3.6 Synchronization of the Frame acquisition through the <i>image_sync</i> signal for endoscopic imagine.....	77
Figure 3.7 Electrical connection for control and communication of the endoscopic catheter, motor drivers, AXSUN OCT engine and the PC for user interaction.....	78
Figure 3.8 Catheter connector assembly.	79
Figure 3.9 Description of the telescopic segment and its internal components.	80
Figure 3.10 Non-steerable OCT catheter with proximal connector, telescopic segment and protecting sheath.	81
Figure 3.11 Picture of the distal bending section of the steerable OCT catheter (A). Descriptive drawing of the bending section (B).	82
Figure 3.12 Instrument module to provide bending to the distal end of the catheter.	83
Figure 3.13 Description of the fully assembled steerable OCT catheter.	84
Figure 3.14 (A) Computation of the optimal number of samples for rotational scanning. (B) OCT catheter inside of a 3D printed rectangular tube. (C) Uniform rotation. (D) Non-uniform rotational distortion.	86
Figure 3.15 Non-uniform rotational distortion in OCT images, (A) image taken at the speed of 1000 rpm and (B) 5000 rpm.	87

Figure 3.16 Rectangular shape used to measure the rotational distortion. The picture A) represents the geometrical model, B) the 3D printed target and the actual angles, C) the target in place with the OCT catheter, D) OCT image of the target at 25 fps.	89
Figure 3.17 Measuring process of the experimental values for the angles QAm , QBm , QCm and QDm . Tools provided by the ImageJ software were used on the OCT images to perform all the measurements.	91
Figure 3.18 Frame rate versus time showing the mean and standard deviation of the frame rate, the number of collected frames, the chosen frame for NURD analysis in which there is mean and the standard deviation of the speed.	93
Figure 3.19 NURD versus speed of rotation in frames per second (fps) for regular OCT catheter.	93
Figure 3.20 NURD versus speed of rotation in frames per second (fps) for regular OCT catheter.	94
Figure 3.21 OCT images of the rectangular piece taken at a) 16.67 fps (1000 rpms), b) 58.33 fps (3500 rpms), c) 83.33 fps (5000 rpms) and d) 125 fps (7500 rpms).	95
Figure 3.22 Distal end of the steerable OCT catheter showing the vertebrae with angle of flexion $\beta \approx 93^\circ$ (a) and $\beta \approx 34^\circ$ (b).	96
Figure 3.23 NURD versus speed of rotation considering the full range of angle of flexion of the steerable catheter.	98
Figure 3.24 NURD versus speed of rotation considering the full range of speed of rotation for the steerable catheter and non-steerable catheter (A).	98
Figure 3.25 NURD versus angle of bending for the frame rates 17 fps, 33 fps, 83 fps and 125 fps.	99
Figure 3.26 NURD versus pullback scanning distance (mm).	100
Figure 3.27 Angular rotation versus the pullback scanning distance (mm).	100
Figure 3.28 Superposed OCT images of the frames corresponding to the pullback scanning distances of 2 mm, and 11 mm where there are the maximum rotations of the images with respect to the initial point in 0 mm.	101
Figure 3.29 Rotational distortion versus pullback scanning distance for regular pullback and with steerable catheter.	102
Figure 3.30 Rotation of the images along the pullback scanning distance.	102

Figure 3.31 3D reconstruction of the rectangular tube by performing regular pullback scanning (A) at 125 fps, and the sum of the frames corresponding to the scanning (B).	103
Figure 3.32 Endoscopic OCT image of a thumb and index fingers surrounding the transparent sheath (A). Only one finger under imaging (B).	103
Figure 4.1 (A) Manual Anubiscope™ [308]. (B) Manipulation of the manual Anubiscope™ and the surgical instruments by two operators [115].....	110
Figure 4.2 Instrument module to perform actuation of the deflection in one plane of the surgical instrument, © 2018, IEEE [98]......	111
Figure 4.3 Schematic drawing of the integration of the steerable OCT catheter and the robotized endoscope. The blue arrows describe the degrees of freedom performed in the endoscope.	112
Figure 4.4 OCT enhanced robotized flexible endoscope.....	113
Figure 4.5 Close-up view of one of the master interfaces, © 2018, IEEE [98].	114
Figure 4.6 Relation of the degrees of freedom in the instrument and the master controller. The system works in Master-Slave configuration.....	114
Figure 4.7 Active catheter of piecewise constant curvature, consisting of 11 vertebrae, L is the length of the vertebrae systems.	116
Figure 4.8 Three-dimensional illustration of the workspace in Figure 4.9.....	118
Figure 4.9 Lateral view of the scanning workspace.	118
Figure 4.10 Trajectory of the distal end of the OCT catheter from 0° to 90° of bending with respect to beginning of the flexible section.	120
Figure 4.11 Back view of the workspace (A) and the lateral view of the back border of the workspace (B), all dimensions in mm.....	121
Figure 4.12 Trajectory of the OCT ball lens when the tool enters the channel in retraction maximum bending angle with respect to beginning of the flexible section, $l = 9.67 \text{ mm}$, $\beta [0^\circ, 90^\circ]$, $\Delta T \geq \Delta T_{\max}$ and $\phi = 0^\circ$	122
Figure 4.13 Lateral view of the volume of the workspace.	123
Figure 4.14 Lateral view of the volume of the unreachable workspace.....	124
Figure 4.15 (A) Position of the two sensors of the electromagnetic tracker in the steerable OCT catheter. (B) Maximum bending to the right direction viewed from EMT sensor 1. (C)	

Maximum bending to the left direction viewed from EMT sensor 1 for $\Delta T = 28$, (D)	
Maximum bending to the left direction viewed from EMT sensor 1 for $\Delta T = 0$	125
Figure 4.16 Position of the tip of the OCT catheter when performing repetitive trajectories over the range of -90° to 90° of bending angle and a translation of ≈ 30 mm (XY view).	126
Figure 4.17 Position of the tip of the OCT catheter when performing repetitive trajectories over the range of -90° to 90° with a translation of ≈ 30 mm and a rotation range from 0 to 360° (YX view).	127
Figure 4.18 Position of the tip of the OCT catheter when performing repetitive trajectories over the range of -90° to 90° with a translation of ≈ 30 mm and a rotation range from 0 to 360° (XZ view).....	127
Figure 4.19 Position of the tip of the OCT catheter when performing repetitive rotational trajectories over the range of 0 to 360°	128
Figure 4.20 Point cloud rendered in MeshLab (A) resulting in an estimated area of 209.69 cm^2 and a volume of 255.29 cm^3 by using the convex hull filter (B). Axis x, y and z in red, green and blue colors respectively.	130
Figure 4.21 Rotational distortion versus pullback scanning distance for tool pullback with steerable catheter (mm).....	131
Figure 4.22 Angular rotation versus the pullback scanning distance (mm) for regular pullback and tool pullback with steerable catheter.	132
Figure 4.23 3D reconstruction of the rectangular tube by performing regular pullback scanning (a) at 125 fps, and robotic pullback scanning (c) at 125 fps, the sum of the frames corresponding to the regular pullback scanning (b) and the sum of the frames corresponding to the robotic pullback scanning (d).....	132
Figure 4.24 Free space test of the mechanical interaction of the system.	133
Figure 4.25 Free space test: (A) initial position, (B) forward translation.	134
Figure 4.26 Free space test: c) right side flexion, d) left side flexion, e) right side rotation and flexion, f) right side rotation and left side flexion.....	134
Figure 4.27 Free space test: (E) right side rotation and flexion, (F) right side rotation and left side flexion.....	134
Figure 5.1 Ascending colon model LM107C used for test, (A) external view, (B) endoscope view and peduncular polyp.....	141

Figure 5.2 Ascending colon model LM107C used for testing, endoscope view and sessile polyp.	141
Figure 5.3 (A) Excised small swine intestine for ex vivo OCT imaging. (B) Closer view of the sample.....	143
Figure 5.4 OCT imaging of the ex vivo sample using both, the benchtop and endoscopic modes.	144
Figure 5.5 Ex vivo swine small intestine imaging, (A) OCT cross-section , (B) histology.	144
Figure 5.6 Tissue marking using a cautery tool under OCT imaging. (A) Excised ex vivo swine small intestine and cautery tool, (B) Tip of tool before cauterization, (C) during cauterization and (D) after cauterization.....	145
Figure 5.7 Methylene blue injection, needle placed in the ex vivo tissue before injection.	145
Figure 5.8 Methylene blue is visualized after injection.....	146
Figure 5.9 OCT B-scans and A-scans obtained with ImageJ of (A) normal mouse colon tissue [329] and (B) tissue-mimicking phantom.....	149
Figure 5.10 Superficial polyps schematic representation.....	150
Figure 5.11 (A) Set of phantoms, (B-C) magnet mount, (D) positioning of phantoms in the artificial colon.....	150
Figure 5.12 (A) White-light endoscopy image of artificial colon with phantoms, (B) benchtop OCT image of polyp phantom.....	150
Figure 5.13 Sessile (A) and pedunculated (B) polyp phantoms with 3D-printed VeroWhite molds, (C) Polyp phantoms attached to normal colon tissue phantom with cancerous tissue insertion.....	151
Figure 5.14 (A) image of tissue-mimicking phantom; OCT images of phantoms mimicking: (B) healthy tissue; (C) hyperplastic polyp, (D) cancer.	152
Figure 5.15 (A) Preparation of the medical room and (B) installation of the robotic system close to the surgical table.....	154
Figure 5.16 In vivo test: (A) The clinician manipulates the steerable OCT catheter by teleoperation. (B) Real time visualization of the colon wall in a living swine; Endoscopic view, (C) OCT view. The submucosa is shown as the brightest layer in the OCT image.	154

Figure 5.17 Results obtained during experiments in the swine bowel in vivo. (A, C) endoscopic views of the OCT and cautery tool manipulation, (B, D) corresponding OCT images. (E, G) endoscopic views showing the needle injection, (F, H) corresponding OCT images.....	155
Figure C.1 Speed controller, performing a swept of set speed values from 5000 rpms (8.33 fps) to 7500 rpm (125 fps) with the regular catheter. Frame rate (fps) versus time (s). The graph also shows the chosen frame for image NURD analysis, the mean and standard deviation of the mean.....	177
Figure D.2 Geometrical model of the flexible section.	178
Figure E.3 Fabrication procedure.....	183
Figure F.4 (A) Matrix board wiring of the synchronization sensor of the helical scanner. (B) Back view schematic drawing. (B) Pictures of the wired circuit, front and back views.	196

List of equations

Eq. 1.1	34
Eq. 1.2	34
Eq. 1.3	34
Eq. 2.1	52
Eq. 2.2	52
Eq. 2.3	52
Eq. 2.4	61
Eq. 2.5	61
Eq. 2.6	61
Eq. 2.7	62
Eq. 2.8	63
Eq. 3.1	90
Eq. 3.2	90
Eq. 3.3	90
Eq. 3.4	90
Eq. 4.1	117
Eq. 4.2	117
Eq. 4.3	119
Eq. 4.4	120
Eq. 4.5	120
Eq. 4.6	121
Eq. 4.7	122
Eq. 4.8	122
Eq. 4.9	123
Eq. 4.10.....	124
Eq. 4.11.....	124
Eq. 4.12.....	124
Eq. 4.13.....	125
Eq. B.1	173

Eq. B.2	173
Eq. B.3	173
Eq. B.4	173
Eq. B.5	173
Eq. B.6	173
Eq. B.7	173
Eq. D.8	178
Eq. D.9	178
Eq. D.10	179
Eq. D.11	179
Eq. D.12	179
Eq. D.13	179
Eq. D.14	179
Eq. D.15	179
Eq. D.16	179
Eq. D.17	180
Eq. D.18	180
Eq. D.19	180
Eq. D.20	180
Eq. D.21	180
Eq. D.22	180
Eq. D.23	180
Eq. D.24	180
Eq. D.25	180
Eq. D.26	180
Eq. D.27	180
Eq. D.28	180
Eq. D.29	180
Eq. D.30	180
Eq. D.31	181
Eq. D.32	181
Eq. D.33	181

Eq. D.34	181
Eq. D.35	181
Eq. D.36	181
Eq. D.37	181
Eq. D.38	181
Eq. D.39	181
Eq. D.40	181
Eq. D.41	181
Eq. D.42	181
Eq. D.43	182
Eq. D.44	182
Eq. D.45	182
Eq. D.46	182
Eq. D.47	182

List of acronyms

ADC: Analog-to-Digital Conversion
CCD: Charge-Coupled Device
CLE: Confocal Laser Endomicroscopy
CMOS: Complementary Metal Oxide Semiconductor
CRC: Colorectal cancer
CSI: Coherent scanning interferometry
DAQ: Data acquisition electronics
FD-OCT: Frequency domain Optical Coherence Tomography
FFT: Fast Fourier Transform
FICE: Flexible spectral imaging color enhancement
FOV: Field of view
GI tract: Gastrointestinal tract
GRIN: Graded-Index
HD: High definition
HMI: Human-machine interface
MIS: Minimally invasive surgeries
NBI: Narrow band imaging
OCT: Optical Coherence Tomography
OCT-IC: OCT imaging console
PZT: Piezo-electric tube
SD: standard definition
SD-OCT: Spectral domain Optical Coherence Tomography
SMF: Single mode fiber
SS-OCT: Swept-source Optical Coherence Tomography
TD-OCT: Time domain Optical Coherence Tomography
WLE: White Light Endoscopy

Introduction

Colorectal cancer is the third most common cancer in the world. The 5-year survival rate decreases from 92% at stage I down to 11% at stage IV. Colorectal cancer typically starts in the form of a polyp. Polyps are very common and can be differentiated into two types: adenomatous polyps (adenomas) that are pre-cancerous and can evolve to cancer, and hyperplastic polyps that are usually benign, but can indicate a higher risk of developing adenomatous polyps. Guidelines from medical societies recommend screening for all patients over 50 years old. However, current standard of care for diagnosing diseases in the lower GI tract relies on simple visual inspection of the intestinal mucosa through a color video-endoscope that is not sufficient for rendering diagnosis. Currently all polyps detected during endoscopy are removed and submitted for pathology, which significantly increases procedure time, associated risk and cost for histological post processing. Based on recent studies, polyps with diameters less than 1 cm have much lower neoplastic potential, thus leaving them is taken into consideration, in order to mitigate the significant costs associated with polyp removal and pathologic diagnosis. The situation is however further complicated by the recent findings that small, flat polyps, termed sessile serrated adenomas, appear by colonoscopy as hyperplastic polyps, yet have malignant potential. An additional problem is a low rate for the detection of polyps caused by the complex geometry of the organ with circumferential folds that block the view of the standard of care endoscope.

In turn, only a fraction of the lower GI tract diseases is detected early, greatly impacting the chances to provide an efficient treatment to patients and increasing mortality and morbidity. There is therefore a critical need to efficiently diagnose and treat the disease as early as possible. The diagnosis of an early stage cancer gives the possibility of treating patients through minimally invasive procedures, which provide better long-term results and quality of life. In this work, the combination of Optical Coherence Tomography (OCT) and a robotized flexible endoscope is proposed as a solution to address the aforementioned clinical need. This novel method has potential to enable a single clinician to operate the flexible endoscope and resection instruments in a confined space of the colon lumen, and at the same time provide the acquisition of OCT images from the colon to obtain real-time diagnosis of diseases. The development, characterization, and optimization of a new OCT device compatible with the interventional robotized flexible endoscope is described. A new pre-clinical experimental validation approach

is developed that includes a model of the human colon with embedded artificial polyp-like structures mimicking benign and pre-cancerous lesions designed and manufactured as a part of this thesis. The polyps have different optical properties visible in OCT allowing for preselecting pre-cancerous polyps in real time and thus demonstrating the advantages of the combination of OCT with interventional robotized flexible endoscopy for real-time assessment of lesion status. The experimental platform developed has been successfully tested in *in vivo* swine experiments. Results achieved during this work lay foundation for future work where OCT images can be used as a feedback to further optimize performance of the robotized endoscope.

Overview of the report

The present report is divided into five chapters. The first chapter presents the background, state-of-the-art and medical context of the project. It introduces general concepts of the clinical problem, such as the history of the most important developments in robot-assisted surgeries for minimally invasive procedures, advanced imaging techniques and an introduction of optical coherence tomography. In Chapter 2 details of the development of the OCT imaging console with dual imaging modes and its signal to noise ratio and sensitivity analysis for optimization and experimental validation is described. Chapter 3 provides detailed description of the novel steerable OCT catheter developed and methodology for experimental characterization of artefacts, such as non-uniform rotational distortion (NURD) and its optimization. In Chapter 4 the new OCT enhanced robotized flexible endoscope is presented together with details on integration process, new degrees of freedom added to the steerable catheter and the analysis of the extended scanning workspace. Chapter 5 presents a new pre-clinical experimental validation approach that includes the model developed of a human colon for bench-top testing with embedded artificial polyps designed using literature and *ex vivo* swine tissue imaging and results from *in vivo* animal testing. Finally, the general conclusions and future work complete the manuscript. The more involved but nonetheless relevant technical information has been placed in the annex section to make the general text lighter to read.

Keywords: Optical Coherence Tomography (OCT), interventional flexible endoscopy, robotics, robot-assisted surgical procedures, biomedical imaging, lower gastrointestinal tract (Lower GI tract), colorectal cancer, intraoperative OCT, advanced optical imaging, endoscopic OCT, clinical guidance.

Publications

Peer Reviewed International Journal

O. Caravaca Mora et al., “Steerable OCT catheter for real-time assistance during teleoperated endoscopic treatment of colorectal cancer”, *Biomed. Opt. Express*, Dec. 2019. <https://doi.org/10.1364/BOE.381357>

Peer Reviewed International Conferences, Proceedings

N. Zulina, O. Caravaca, S. Gravelyn, L. Zorn, and M. Gora, “Colorectal polyps mimicking phantoms for OCT application,” 2019, p. 52. <https://doi.org/10.1117/12.2527098>

Peer Reviewed International Conferences, without proceedings

O. Caravaca Mora et al. “Real-time differentiation of healthy tissue using an OCT device steered by a robotized flexible endoscope”, SPIE Photonics Europe, Unconventional Optical Imaging, Strasbourg, France, SPIE, April 2018.

O. Caravaca Mora et al. “Steerable OCT probe for real time assistance during treatment with robotized flexible endoscope”, SPIE Photonics West, Endoscopic Microscopy XIV, San Francisco, United States, SPIE, February 2019.

O. Caravaca Mora et al. “Extended scanning workspace using steerable OCT endomicroscopy”, SPIE Photonics West, Endoscopic Microscopy XV, San Francisco, United States, SPIE, February 2020.

Miscellaneous communications

O. Caravaca Mora, P. Montgomery, S. Perrin, “The earlier the better - Optical Imaging and Robotics for Early Cancer Screening; The smaller the better – Miniaturization for Space Saving and The more interesting the better – The everyday life of a researcher”, Collège Doctoral Européen, Université de Strasbourg, April 2017. Conference "Finding a needle in a haystack", in the frame of "Science for Dummies".

O. Caravaca Mora, L. Zorn, P. Zanne, F. Nageotte, P. Montgomery, M. de Mathelin, M. Gora. Poster presentation at Biophotonics and Imaging Graduate Summer School (BIGSS`18) AUGUST 28 - SEPTEMBER 1, 2018 at The Burren and NUI Galway. Guidance of a robotic interventional endoscope using optical coherence tomography.

O. Caravaca and M. Gora. IHU 'Grand' Fellow Meeting. “Robotized Flexible Endoscope with a Steerable OCT probe for real time assistance during minimally invasive treatment in the colon”. February 2019.

O. Caravaca Mora et al. EUCOR Cross-border: Crossing Borders for Joint Exchange and Collaboration in Biomedical Engineering. “Steerable and teleoperated optical coherence tomography catheter for robotized flexible endoscopy”. Oral presentation. April 2019.

O. Caravaca Mora, L. Zorn, F. Nageotte, N. Zulina, S. Gravelyn, P. Montgomery, M. de Mathelin, B. Dallemagne, Michalina Gora. 7emes journées scientifiques de la fédération de médecine translationnelle de Strasbourg (FMTS). “Steerable and teleoperated optical coherence tomography catheter for robotized flexible endoscopy”. Oral presentation. April 2019.

French summary

Introduction

Le cancer colorectal est le troisième cancer le plus fréquent dans le monde. Avec un taux de survie après 5 ans de 92 % au stade I et 11 % au stade IV. Le cancer colorectal commence généralement sous la forme d'un polype. Les polypes sont très courants et peuvent être différenciés en deux types : les polypes adénomateux (adénomes) qui sont précancéreux et peuvent évoluer en cancer, et les polypes hyperplasiques qui sont habituellement bénins, mais qui peuvent indiquer un risque plus élevé de développement de polypes adénomateux. Les autorités de santé recommandent un dépistage pour tous les patients de plus de 50 ans. Cependant, la norme actuelle pour le diagnostic des maladies du tractus gastro-intestinal inférieur repose sur une simple inspection visuelle de la muqueuse intestinale à l'aide d'un vidéo-endoscope couleur. Or, cette inspection ne suffit pas pour poser un diagnostic. A l'heure actuelle, tous les polypes détectés pendant l'endoscopie sont enlevés et soumis à la pathologie, ce qui augmente considérablement la durée d'une intervention, le risque associé et le coût du post-traitement histologique. Selon des études récentes, les polypes de diamètre inférieur à 1 cm ont un potentiel néoplasique beaucoup plus faible : leur abandon pourrait permettre de réduire les coûts importants liés à l'ablation des polypes et au diagnostic pathologique. La situation est cependant rendue compliquée par les récentes découvertes de petits polypes plats, appelés adénomes sessiles dentelés, qui apparaissent en coloscopie comme des polypes hyperplasiques, mais qui ont un potentiel malin. De plus, la géométrie complexe de l'organe présentant des plis circonférentiels qui bloquent la vue de l'endoscope standard de soins contribue à un faible taux de détection de polypes.

Cependant, seule une fraction des maladies du tube digestif inférieur est détectée de manière précoce. De ce fait, les chances de fournir un traitement efficace aux patients sont considérablement réduites, augmentant ainsi la mortalité et la morbidité. Il est donc essentiel de diagnostiquer et de traiter efficacement la maladie le plus tôt possible. En effet, le diagnostic d'un cancer de stade précoce permet de traiter les patients par des procédures peu invasives, et ainsi d'obtenir de meilleurs résultats à long terme et une meilleure qualité de vie. Afin de répondre à ce besoin clinique, nous proposons à travers cette étude la combinaison de la tomographie par cohérence optique (OCT) et d'un endoscope flexible robotisé. Cette nouvelle

méthode a le potentiel de permettre à un seul clinicien d'utiliser l'endoscope flexible et les instruments de résection dans l'espace confiné de la lumière du côlon, tout en permettant l'acquisition d'images OCT du côlon afin d'obtenir un diagnostic en temps réel des maladies. Dans un premier temps, nous décrivons le développement, la caractérisation et l'optimisation d'un nouveau dispositif OCT compatible avec l'endoscope flexible robotisé interventionnel. Nous présentons ensuite une nouvelle approche de validation expérimentale préclinique qui comprend un modèle du côlon humain avec des structures artificielles encastrées de type polype, imitant des lésions bénignes et précancéreuses, conçu et fabriqué dans le cadre de cette thèse. Les différentes propriétés optiques des polypes visibles en OCT permettent de présélectionner les polypes précancéreux en temps réel et ainsi de démontrer les avantages de la combinaison de l'OCT avec l'endoscopie flexible robotisée interventionnelle pour l'évaluation en temps réel de l'état de la lésion. La plate-forme expérimentale développée a été testée avec succès dans des expériences in vivo sur des porcs. Les résultats obtenus au cours de ces travaux fournissent des bases pour des travaux futurs où l'utilisation des images OCT en rétrocontrôle permettrait d'optimiser davantage le rendement de l'endoscope robotisé.

Le présent rapport est divisé en cinq chapitres. Le premier chapitre présente l'historique, l'état de l'art et le contexte médical du projet. Il introduit les concepts généraux du problème clinique, tels que l'histoire des développements les plus importants de la chirurgie assistée par robot pour les procédures mini-invasives, les techniques d'imagerie avancées et l'introduction de la tomographie à cohérence optique. Le chapitre 2 décrit le développement de la console d'imagerie OCT avec deux modes d'imagerie, ainsi que l'analyse du rapport signal sur bruit et de la sensibilité pour l'optimisation et la validation expérimentale. Le chapitre 3 fournit une description détaillée du nouveau cathéter OCT orientable développé et de la méthodologie pour la caractérisation expérimentale des artefacts, tels que la distorsion rotationnelle non uniforme (NURD) et son optimisation. Au chapitre 4, nous présentons le nouvel endoscope flexible robotisé amélioré OCT avec des détails sur le processus d'intégration, les nouveaux degrés de liberté ajoutés au cathéter orientable et l'analyse de l'espace de travail de numérisation étendu. Le chapitre 5 présente une nouvelle approche de validation expérimentale préclinique qui comprend le modèle élaboré d'un côlon humain pour les essais pilotes avec polypes artificiels encastrés, conçu à partir de l'imagerie ex vivo de tissus porcins et des résultats des essais in vivo sur animaux. Enfin, les conclusions générales et les perspectives de travaux futurs complètent le manuscrit. Les informations techniques, plus complexes mais néanmoins pertinentes sont disponibles en annexe pour alléger la lecture du texte général.

Mots-clés : Tomographie par cohérence optique (OCT), endoscopie digestive interventionnelle, robotique, chirurgie assistée par robot, tractus gastro-intestinal inférieur, cancer colorectal, Imagerie préopératoire, imagerie optique médicale, imagerie endoscopique OCT.

Chapter 1

State of the art

Content

1.1 Medical Context	9
1.1.1 Colorectal Cancer	11
1.1.2 Colorectal cancer diagnosis.....	13
1.1.3 Treatment of colorectal cancer	21
1.2 Robot-assisted minimally invasive surgery.....	23
1.2.1 Robotized flexible interventional endoscope for intraluminal surgery	28
1.3 Optical Coherence Tomography	30
1.3.1 Basics of Optical Coherence Tomography	32
1.3.2 Endoscopic OCT	34
1.3.3 Applications of endoscopic OCT	36
1.4 Advanced imaging and robotics	38
1.5 Motivation and objective.....	44
1.6 French summary of the chapter	45

1.1 Medical Context

The context of the doctoral project is focused on the development of a novel method that can improve the management of diseases in the gastrointestinal (GI) tract. The GI tract is also called the digestive system, and as such it has the functionality of ingesting, passing and digesting food for transferring the nutrients to the interior of the body and to distribute them to the cells [1]. It consists of the mouth, esophagus, stomach, small intestine and large intestine and is also connected to the exocrine glands and organs located externally to the GI tract. They are necessary for the process of digestion: the salivary glands for producing saliva to provide lubrication and to allow the food to advance along the gastrointestinal tract, the pancreas for secreting pancreatic juice needed to degrade the food so that it can be absorbed and the liver for producing bile to digest and absorb fat (Figure 1.1). Figure 1.1 shows a general schematic of the digestive system and the exocrine glands.

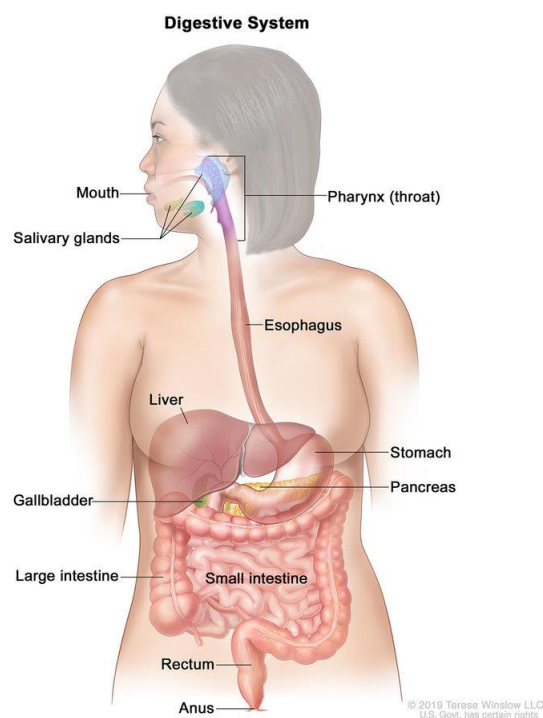


Figure 1.1 Digestive system and the exocrine glands. For the National Cancer Institute © 2020 Terese Winslow LLC, U.S. Govt. has certain rights [2].

The functioning of the digestive system is based on four physiological processes: digestion, absorption, motility and secretion [3]. The digestion is the process in which the large

molecules are decomposed into smaller molecules in the presence of the substances produced by the exocrine glands during the process of secretion. The small molecules are transported through the epithelial cell membranes using the absorption, a process that occurs in the small intestine. The motility is the motion of the food along the GI tract performed by contractions of two layers of muscle lining, and the last process is the secretion of the substances produced by the exocrine glands. The wall of the GI tract has a layered architecture, which consists of four main layers (Figure 1.2). The mucosa is the innermost layer of the GI wall and the most specialized depending on the function. It is divided into three sublayers: epithelium, lamina propria and muscularis mucosae. The mucosa layer is followed by a loose connective tissue of submucosa with blood vessels and lymphatics. The muscular layer comprises a circular muscle layer and longitudinal muscle layer that enables propulsion of the food. The outermost layer of serosa consists of strong connective tissue, which assures structural stability of the digestive system. This is illustrated in Figure 1.2(A). Figure 1.2(B) shows the histology of layer architecture for the esophagus, stomach, small intestine and large intestine, in which the main difference is in the structure of the mucosa.

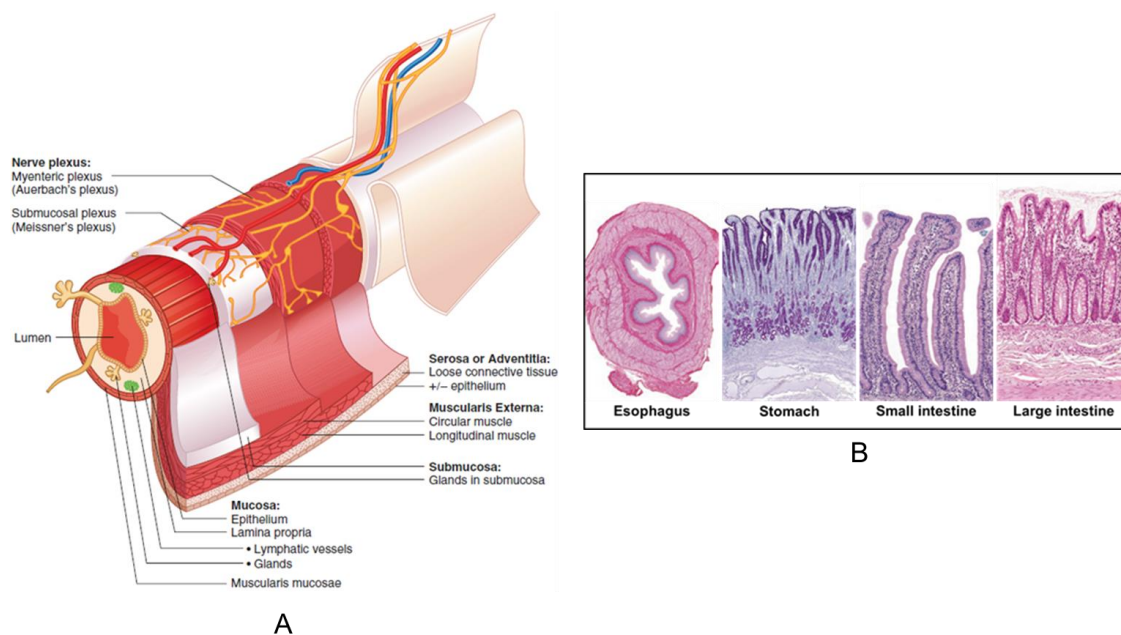


Figure 1.2 (A) Schematic diagram of the wall anatomy of four sections of the digestive tract and (B) examples of microscopic images of histology slides with Hematoxylin and Eosin staining of thinly sliced biopsy specimens. Reprinted/adapted by permission from Springer Nature: Springer eBook, *The Digestive System I: The Alimentary Canal* by Anders Rehfeld, Malin Nylander, Kirstine Karnov, © 2017 [4].

The overall length of the GI tract is about 5 meters in the average human [5] and there exists a large number of conditions that can develop throughout its length. Digestive system diseases can have symptoms that can impair proper functioning and in severe cases lead to death. Diseases of the GI tract are usually grouped based on the organ in which they are present, and a quick overview of some of them can be found in [1]. The novel developments proposed in this thesis are mostly motivated by the gastrointestinal malignancies.

Gastrointestinal malignancies can arise throughout the whole length of the digestive system, with most common presence in the colon, rectum and esophagus [1]. The carcinoma of the esophagus, also known as esophageal cancer, is a disease where malignant cells begins to develop in the squamous cells found in the layers of the tissue of the esophagus giving the name of squamous cell carcinoma [6]. There is also the case of cancer being developed in the glandular cells, from which it is known as adenocarcinoma [7]. Some of the factors that increase risk of suffering this type of malignancy are smoking, consuming alcohol and Barret's esophagus that is caused by reflux disease. Risk factors for gastric cancer, which develops in the layer of the stomach's wall are diet, age and some stomach diseases [8]. Adenocarcinoma of the pancreas is the cancer developed in the pancreatic tissue, with smoking and the general health record being related to the risk of suffering this malignancy. In the lower gastrointestinal tract, colorectal cancer tends to begin to develop in the layers of the colon wall commonly in the form of polyps. Further description of colorectal cancer, which is of the main interest of this thesis, will be given in the next sections including information about how it develops, risk factors, diagnosis and treatment, staging, optical technologies used to improve diagnosis and instrumentation to enhance treatment. In all the aforementioned types of cancer, over time the cancerous cells invade the deeper layers of the organ until they spread to other parts of the body in advanced stages of the disease. As such, early detection is crucial for efficient treatment of digestive cancers.

1.1.1 Colorectal Cancer

Colorectal cancer (CRC) is a type of cancer that develops in the colon or rectum [9]. CRC is globally the third most common cancer in the world in men (Figure 1.3) and the second most common in women. It has also fourth highest mortality among the other types of cancer in men and third in women [10]. According to the American Cancer Society [11] the 5-year relative survival rate is about 92% for people with stage I colon cancer, 87% for stage IIA, 63%

for stage IIB, 89% for stage IIIA, 69% for stage IIIB and 53% for stage IIIC colon cancer. With the stage IV having an 11% of 5-year relative survival rate, this stage is more difficult to treat, although it is still treatable in some cases.

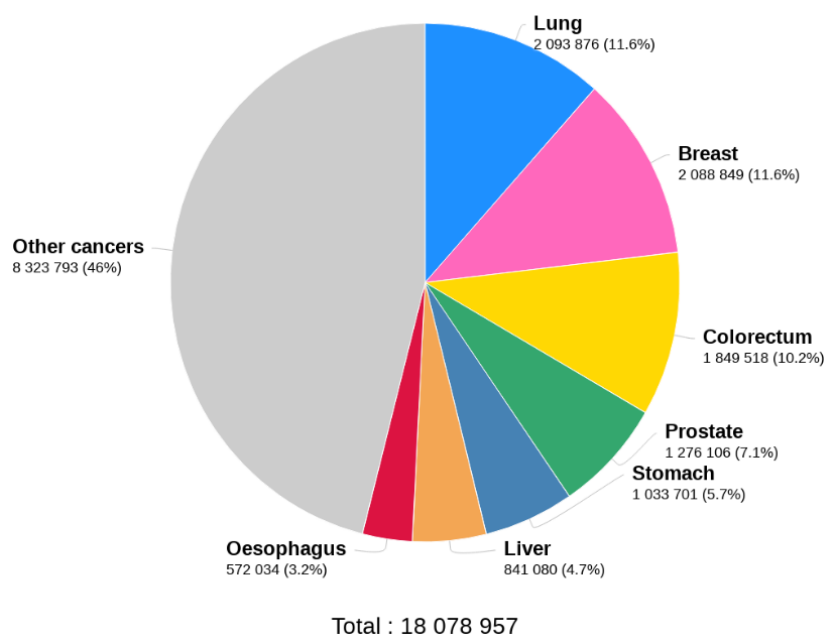


Figure 1.3 Estimated number of new cases of cancer in 2018 for both sexes and all ages. GLOBO CAN 2018 [12].

Colorectal cancer is initiated when cells begin to grow in a disorganized manner, so creating polyps (Figure 1.4). There are two main types of polyps: adenomatous polyps (adenomas) which can evolve into cancer and are considered as a pre-cancerous condition (one type) and hyperplastic polyps and inflammatory polyps, that are more common but are not considered as being pre-cancerous (second type) [9]. Among the different kinds of cancer, adenocarcinomas represents more than 90% of colorectal cancers [13]. Other types of cancer are Carcinoid tumors, Gastrointestinal stromal tumors, Lymphomas and Sarcomas [9].

Some of the factors that can affect the risk of suffering from CRC can be found listed in [14] and summarized as follows: being overweight, physical inactivity, diets based on red and processed meats, the use of frying, broiling and grilling for cooking meat, smoking, consuming alcohol, an increase in risk with age being more common after the age of fifty, previous personal or family records of colorectal polyps or cancer, inflammatory bowel disease, inherited Lynch syndrome such as hereditary non-polyposis colorectal cancer, familial adenomatous polyposis, and a certain amount of other factors for which the risks are unknown.

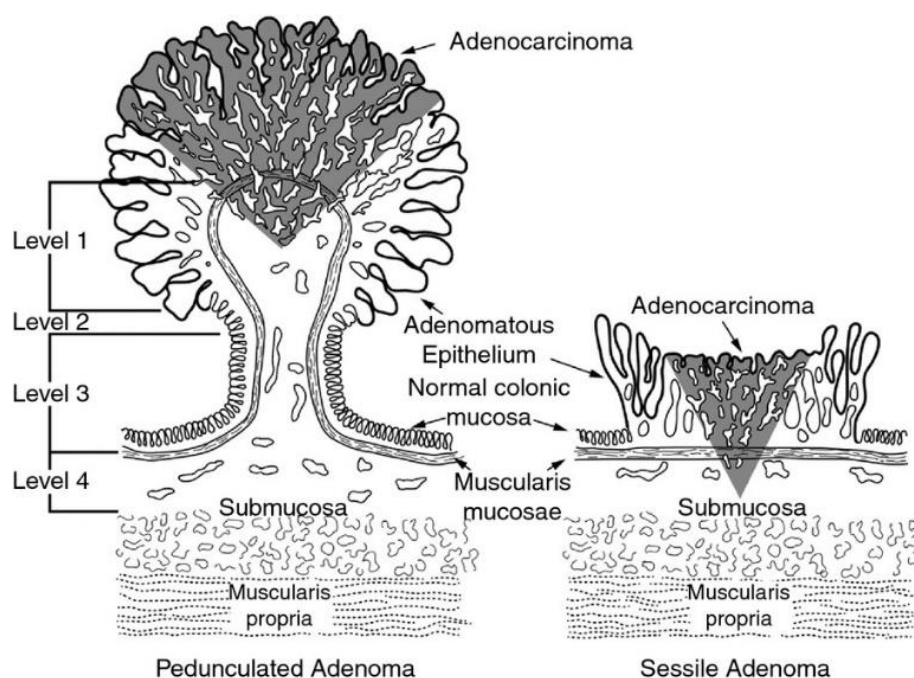


Figure 1.4 Level of invasion of pedunculated and sessile malignant polyps according to the Haggitt classification. Adapted/reprinted by permission from John Wiley and Sons: Colorectal Disease. Management of the malignant colorectal polyp: ACPGBI position statement by N. Haboubi, S. G. McGee, S. Rasheed, et al. © 2013 [15].

1.1.2 Colorectal cancer diagnosis

Currently, the standard of care of diagnosis is based on colonoscopy that relies on simple visual inspection of the intestinal mucosa by an endoscopic camera [16]–[18] (Figure 1.5). Using flexible endoscopy the clinician searches for ulcers, inflammation, bleeding, polyps and tumors [19]. Since the colorectal cancer typically starts in the form of a polyp, those that are detected during endoscopy are removed and submitted for pathology, which significantly increases procedure time. If the polyp is larger than 1 cm, it is considered as a risk factor [9], and only a small tissue sample is acquired from the polyp using biopsy forceps [20]. Two main limitations of this technology are the discomfort of the patient during the procedure and the fact that some polyps are missed, so that only a fraction of the lower gastrointestinal tract diseases are detected at an early stage. For instance, theoretically, flexible sigmoidoscopy should have a diagnose rate of 70% but in reality it is closer to 50%-60% [21].

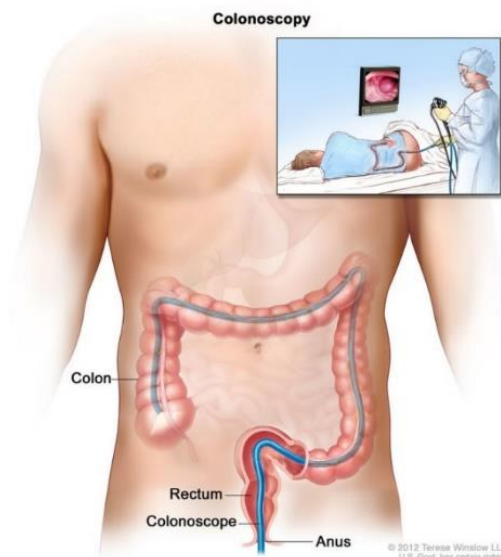


Figure 1.5 Colonoscopy relies on visual inspection of the colon wall. For the National Cancer Institute © 2020 Terese Winslow LLC, U.S. Govt. has certain rights [2].

Cancer staging

The stage of the cancer indicates the degree of invasion of the tumor and if it has reached other parts of the body beyond the original site where the cancer started to develop. The importance of knowing the stage of the cancer allows the clinician to determine the seriousness of the tumor, the survival possibilities of the patient and to plan the most appropriate treatment. The most widely used cancer staging system is the TNM system developed in collaboration between the American Joint Committee on Cancer and the Union for International Cancer Control. The description of the system was taken from [22] and summarized in the following paragraphs.

The TNM system for staging cancers is based on the size and degree of the primary tumor (T), the involvement of regional lymph nodes (N), and whether there is the presence of distant metastases (M) or not. In the TNM system, the stage is only interpreted as the combination of these three parameters and it is also related to specific time windows during the health care of the patient. The TNM parameters are called categories and the specific time windows are called the classifications. Associated to each combination of TNM there is a prognostic stage group that represent the chances of survival of the patient with the designated cancer stage. The two most important classifications are clinical and pathological. In the clinical classification (cTNM), staging is performed before performing any treatment and is

based on physical examination and imaging of the patient. Imaging techniques are important for this classification, the most used imaging technologies being computed tomography, magnetic resonance imaging, positron emission tomography, ultrasound, and X-rays [23]. Pathological classification (pTNM) is performed based on microscopic analysis of the resected specimens after surgical treatment and resection. The prognostics stage groups provide a summary of the information given by the TNM categories; they also represent a statistical survival outcome of the cancer stage. The prognostic stage groups are indicated by Roman numerals from I to IV, representing the invasion of the cancer and decadence of the prognosis outcome.

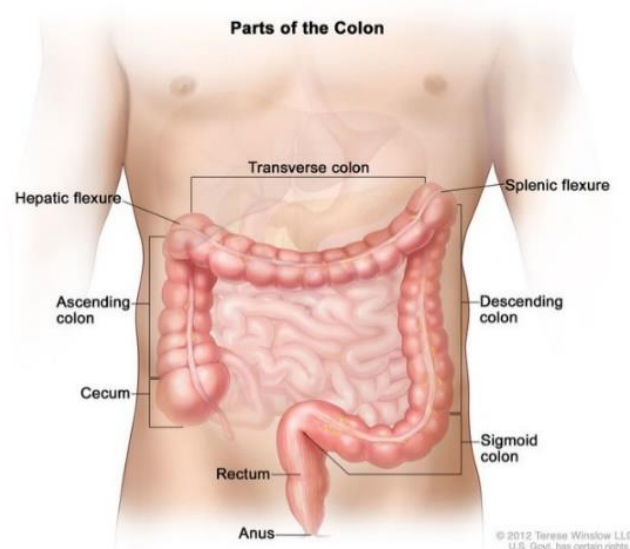


Figure 1.6 Gross anatomy of the large intestine. For the National Cancer Institute © 2020 Terese Winslow LLC, U.S. Govt. has certain rights [2].

From the perspective of cancer development, the anatomy of the colon and rectum can be divided into three sites: the primary sites, the regional lymph nodes and metastatic sites. The primary sites are illustrated in Figure 1.6 where the large intestine consist of four main parts, the cecum with the appendix, the colon (ascending colon, transverse colon, descending colon, sigmoid colon), the rectum and the anus. It is about 1,5 m long [24], and the colon wall is structured by layers starting from the inner mucosa, then the submucosa, the muscle layer and serosa as represented in Figure 1.2(B). The regional lymph nodes are located adjacent to the colon and vessels, see Figure 1.7(A-B). The metastatic sites refer to the organs reached by the cancer through the lymph nodes and vessels, as illustrated in Figure 1.7(C), a process called metastasis. More information on the definitions of TNM categories and their corresponding

prognostics groups can be found in Annex A. The same Annex A also describes another categorization used by cancer registries as specified in Table A.4, where the prognostic groups are grouped in 5 categories, this system being used for cancer statistics.

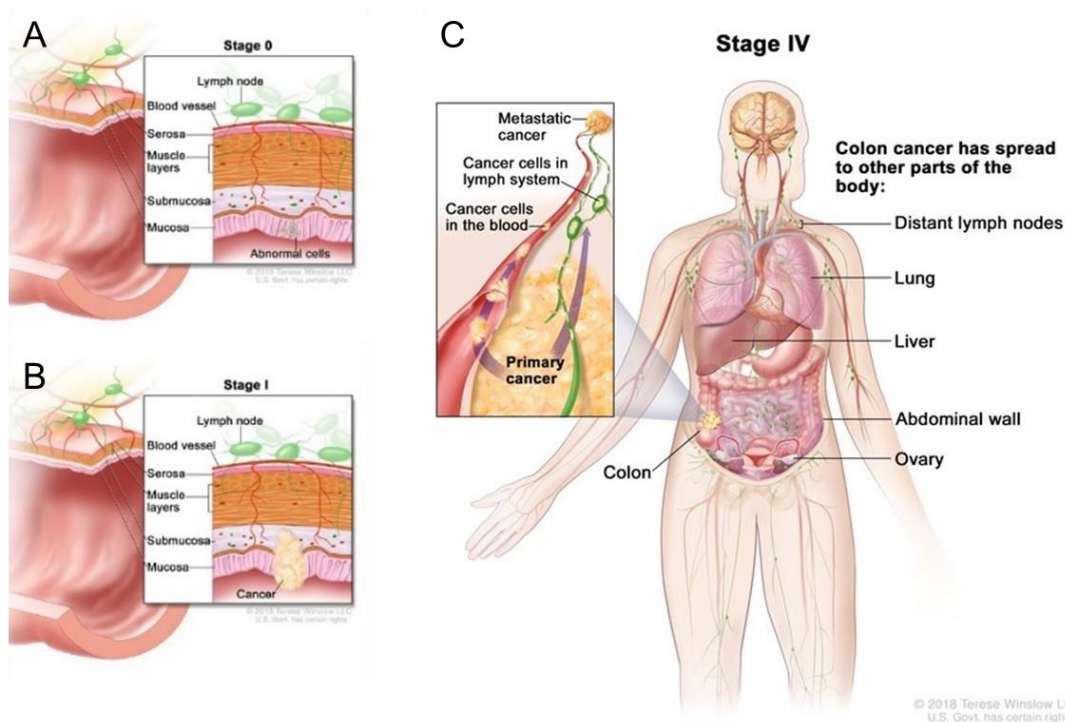


Figure 1.7 Layer structure of the colon wall, (A) cancer in the stage 0, (B) stage I and (C) stage IV and metastasis. For the National Cancer Institute © 2020 Terese Winslow LLC, U.S. Govt. has certain rights [2].

Advanced endoscopic imaging

The graph in Figure 1.8 taken from the “Surveillance, Epidemiology, and End Results database (SEER)” shows the relative survival rate for different stages of the cancer versus the number of years after the first diagnosis of the patient in the United States. Considering that Localized refers to the stages I-II, Regional to the stage III then Distant to the stage IV, it can be seen that the higher the stage and distant organs are affected the lower the relative survival rate with a rapid decay in the trend curve as the years from diagnosis increases. Because of this there is an important effort from the scientific and medical area in finding and developing new methodologies to detect cancer as early as possible and to stage the malignancy precisely. White light endoscopy (WLE) is the standard for gastrointestinal imaging, using the full

spectrum of visible light to visualize the mucosa in standard definition (SD) with a resolution of 480p and an aspect ratio of 4:3. High definition white light endoscopy (HD WLE) provides HDTV with resolutions of 1080p and 2060p (4K) [25]. More recent standard high-resolution endoscopes integrate magnification (zoom) and give a more detailed image (Figure 1.9). There are statistical studies proving that HD WLE improves the detection of adenomas, flat adenomas and dysplasia in the case of inflammatory bowel disease in comparison with SD WLE [28].

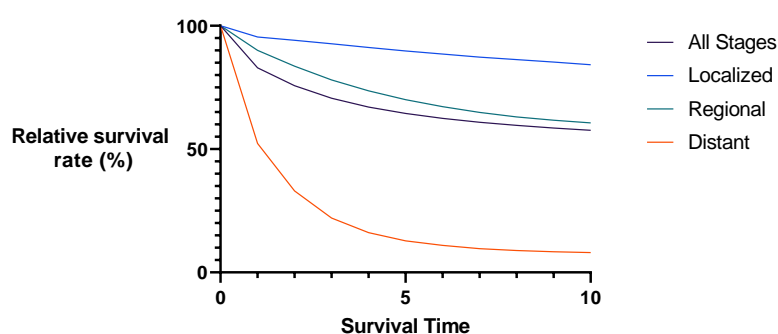


Figure 1.8 Relative survival rate in US. patients with colorectal cancer for different stages based on the SEER database [26].



Figure 1.9 Invasive cancer visible in white light endoscopy (A) without magnification, (B) with magnification and (C) with magnification and digital chromoendoscopy [27].

Digital chromoendoscopy is a set of technologies that uses light filtering or real-time post-processing algorithms to enhance visualization of tissue surface and vascular structures. One such technology is Narrow band imaging (NBI, Olympus Corporation, Tokyo, Japan), where hardware modification is added to the endoscope light source allowing filtering of the blue (415 nm) and green (540 nm) components (Figure 1.10). The spectral bandwidth of the green and blue channels is reduced from 50-70 nm to 20-30 nm. The final combination of the filtered signal and the red channel displays the micro-vessels in the mucosa and capillaries of

the submucosa layers, both appearing in a dark color due to the light absorption contrasting the reflected light coming from the rest of the mucosal tissue [29][30].

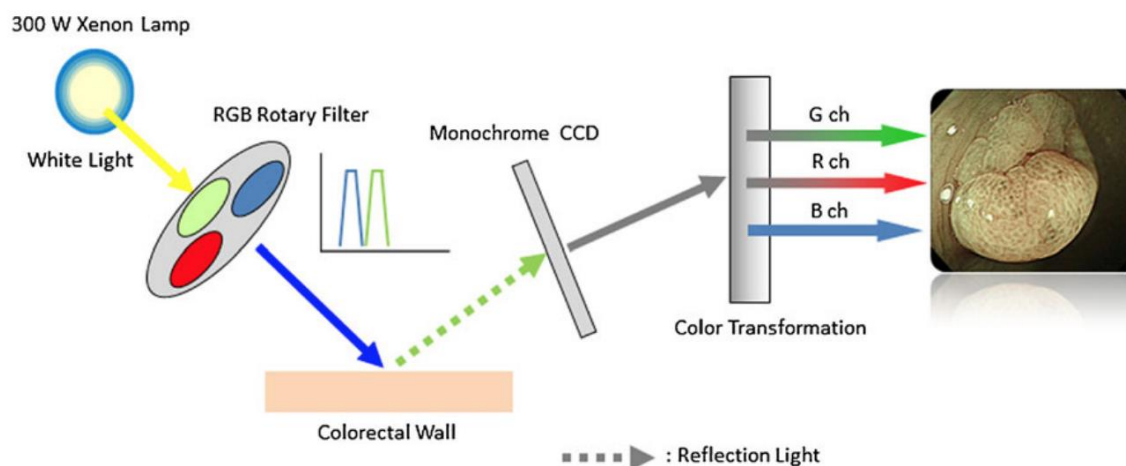


Figure 1.10 Schematic diagram showing the benefits of narrow band imaging. Reprinted by permission from Springer Nature: International Journal of Colorectal Disease. Rationale for and clinical benefits of colonoscopy with narrow band imaging: pathological prediction and colorectal screening by Hiroyuki Aihara, Shoichi Saito, Hisao Tajiri. © 2012 [31].

Other related technologies are Flexible spectral imaging color enhancement (FICE, Fujifilm, Tokyo, Japan) [32] and I-SCAN (Pentax, Tokyo, Japan) [32]. Unlike NBI they use post processing algorithms to enhance visualization of mucosal structure. FICE selects specific wavelengths, and then by a “spectral estimation” it analyses each pixel of the white light image. The images are then reconstructed using only a single selected wavelength for each red, green and blue component to finally display in real time a composite color-enhanced image [29].

I-SCAN also uses post-processing digital methods that consist of three enhancement features: SE - surface enhancement for image sharpening, CE - contrast enhancement where depressed areas look shifted to the blue, and TE - tone enhancement which is a type of digital narrowed spectrum imaging. Based on the studies reported in [33], [34] these technologies are useful in polyp characterization and are superior to standard WLE [34]. This is not the case however, for inflammatory bowel disease nor polyp detection where there is no significant improvement and its use is not recommended by the European Society of Gastrointestinal Endoscopy [29].

Autofluorescence Imaging (AFI) takes advantage of the autofluorescence emitted by natural fluorophores such as collagen, flavins, and nicotinamide adenine dinucleotide

phosphate (NADPH) following excitation with short wavelengths. Because of the variation in natural fluorophores between healthy and diseased tissues the detected autofluorescence provides additional contrast in which normal tissue is pale green, neoplastic tissue magenta, and blood vessels are dark green [36]. Figure 1.11 shows the schematic diagram of the AFI, in which a 300 W xenon lamp emits white light, a rotary filter separates this light source into an excitation light with a wavelength bandwidth of 390 nm to 470 nm and 540 nm to 560 nm for green light. The sequential radiation of these light wavelengths is applied during the observation time. The reflected excitation light is removed by placing a barrier filter in front of a monochrome charge-coupled device. Light wavelengths of 500 nm to 630 nm are detected from both autofluorescence and reflected green light. A false color image is created by assigning the detected and amplified autofluorescence signal to the green (G) channel, the reflected green light signal to the red (R) and blue (B) channels with ratios from 1 to 0.5. The clinical effectiveness of this technology, however, is still unclear, since it does not provide a significant improvement in comparison to WLE as reported in [28].

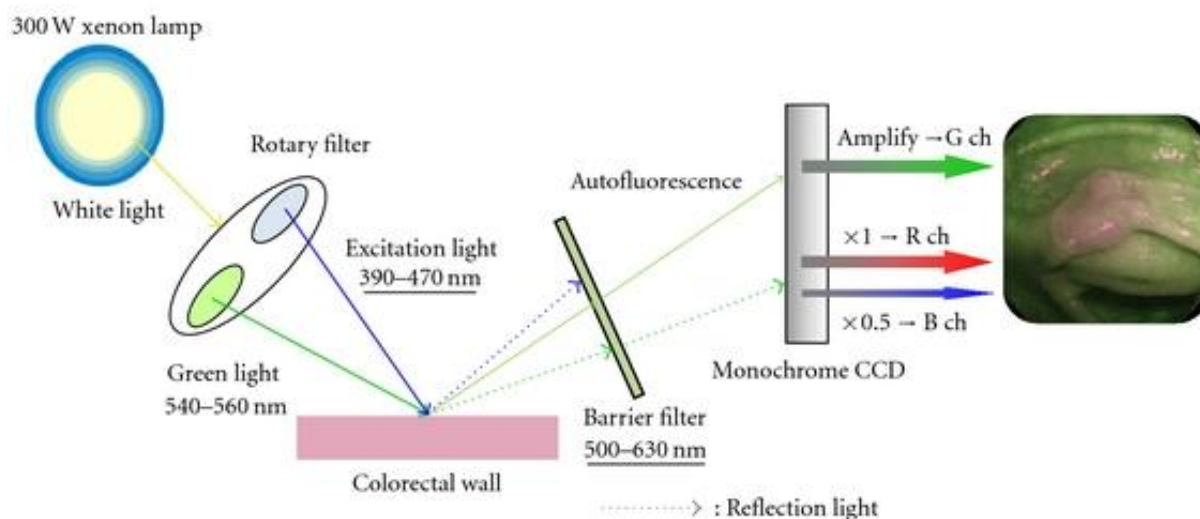


Figure 1.11. Schematic diagram of the AFI system [35].

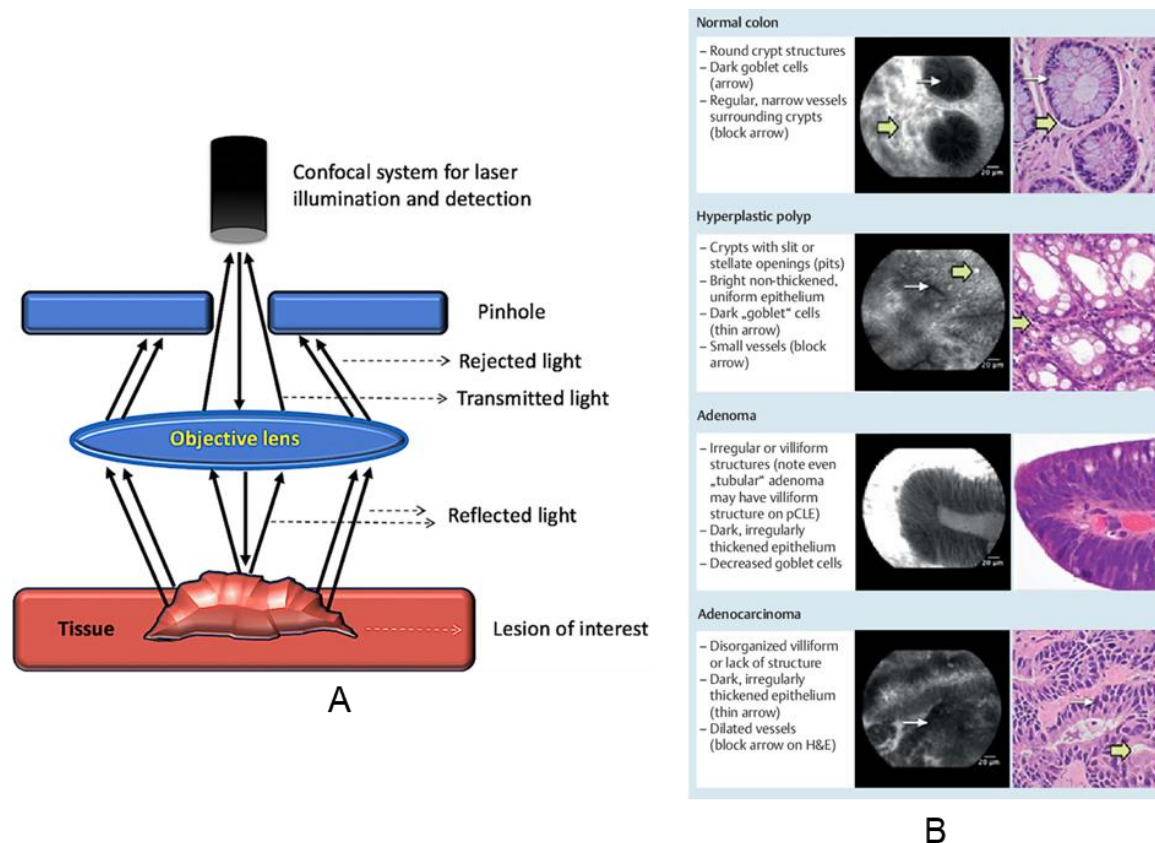


Figure 1.12 (A) Schematic drawing showing principle of confocal endomicroscopy. Reprinted by permission from Springer Nature: Indian J Gastroenterol (2019) 38: 281. Optical biopsy in gastroenterology: Focus on confocal laser endomicroscopy, Zaheer Nabi, D. Nageshwar Reddy. © 2019 [37]. (B) Miami classification for probe-based confocal laser endomicroscopy. Reprinted by permission from Georg Thieme Verlag KG: Endoscopy 2011; 43(10): 882-891. Miami classification for probe-based confocal laser endomicroscopy, M. Wallace, G. Y. Lauwers, Y. Chen, E. Dekker, P. Fockens, P. Sharma, A. Meining. © 2011 [38].

Confocal laser endomicroscopy (CLE) is an endoscopic version of confocal microscopy. Similarly, to a standard confocal microscope, the out of focus light is rejected using the laser light that is focused through a pinhole onto a selected depth in the tissue. The image obtained is the representation of the intensity of the reflected light, resulting in a high-resolution image. The addition of an intravenous fluorescent contrast agent is necessary to distinguish the subsurface architecture. The image detail is comparable to that of histology [39]. Regarding polyp detection, there is no evidence of improvement by using CLE with respect to WLE, although it is comparable to histology in the case of polyp characterization and inflammatory bowel disease. Figure 1.12 shows the schematic of confocal laser

endomicroscopy (A) and the Miami classification used for CLE image correlation with histology (B).

Optical Coherence Tomography (OCT) is an emerging technology that intends to add value in terms of tissue characterization in gastroenterology. It is similar to ultrasound providing depth information of 2-3 mm in most scattering tissue, with typical depth resolutions of 1 to 10 μm and lateral resolution of 30 to 50 μm [40], [41]. The endoscopic version of OCT has shown great potential in the early detection of cancer in the colon [42], diagnosis of inflammatory bowel diseases [43], and Barrett's esophagus [44], [45] among other applications. Further details about this technology will be presented in the next sections since it is the main subject of this work.

1.1.3 Treatment of colorectal cancer

Minimally invasive treatment of the colorectal cancer

The selection of the treatment option depends on the stage of the cancer. When the invasion of the cancerous tissues reaches the submucosa they are known as superficial neoplastic lesions and classified as pT1sm, where "p" is due to the pathologist staging report, "T1" is based on the invasion of the cancer into the submucosa according to Table A.4 in the annexes and "sm" stands for submucosa [46]. If the cancerous invasion is only into the mucosa then it is called high-grade intraepithelial neoplasia. Endoscopic treatment is recommended in the case of superficial neoplastic lesions. Two types of minimally invasive endoscopic treatment exist: endoscopic mucosal resection (EMR) or endoscopic submucosal dissection (ESD) [19], [47]. Performing one or the other depends on the size and shape of the polyps found. The ESD procedure is the most complicated of the procedures and as such has some associated challenges: it relies on visual inspection, often requires more than one clinician to manipulate the endoscope and the surgical tools, requires the localization of lesions in a follow up procedure based on the previous screening process and pathology result, requires assessment of the lesion type and its margins and has the absence of confirmation of complete elimination of the disease.

Endoscopic mucosal resection (EMR)

Endoscopic mucosal resection is a procedure initially developed in Japan to treat gastric gut cancer and was later extended to other areas such as the esophagus and colon [49].

This procedure is indicated to remove polyps with a maximum diameter of 20 mm [50], and where the tumor invasion into the submucosa is not beyond 1 mm. The procedure consists of a snare removal: directly in case of lesions that have a stalk (pedunculated polyp), or following injection of a saline solution to lift the lesion without a stalk (sessile polyp) (Figure 1.13).

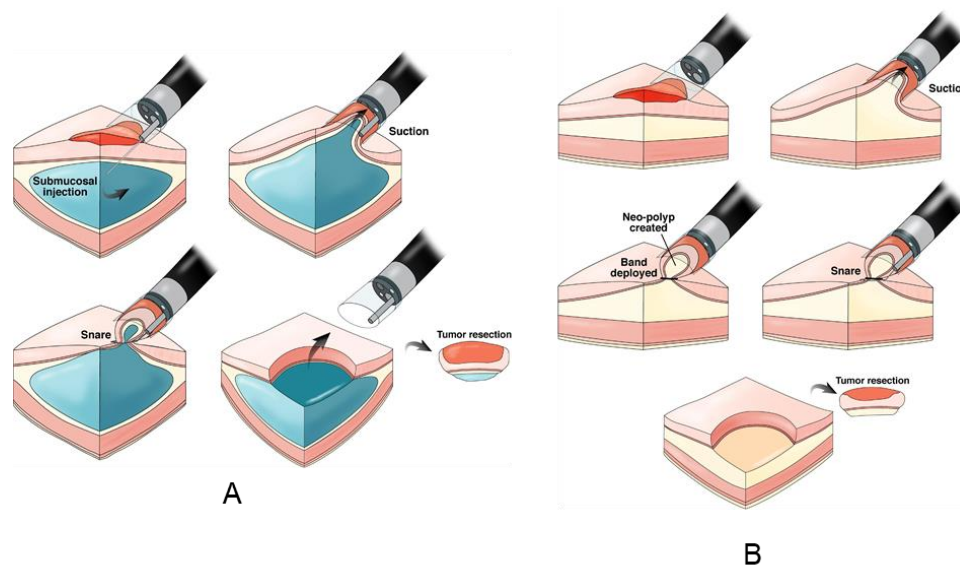


Figure 1.13 Endoscopic mucosal resection procedure: (A) Cap-assisted EMR, (B) Ligation-assisted EMR Adapted/reprinted by permission from Elsevier: Gastroenterology. Endoscopic Mucosal Resection: Not Your Father's Polypectomy Anymore by Vinay Chandrasekhara, Gregory G. Ginsberg. © 2011 [48].

Endoscopic Submucosal Dissection (ESD)

Endoscopic submucosal dissection is performed in the case of larger and/or flat lesions where normal resection by snare is not possible and is also indicated when there is a high risk of invasion. The outcome depends highly on the skills of the gastroenterologist, since it is difficult to perform [51]. The procedure involves several steps as illustrated in Figure 1.14. The first two steps are to identify the lesion using WLE in combination with chromoendoscopy and to mark the margin of the lesion using a cautery tool [52]. The next step is to lift the lesion by injecting saline to create a cushion in the submucosal layer. Then an incision is performed in the tissue surrounding the area with a knife (e.g. electro-surgical tool), and finally the tissue is dissected and collected for pathological analysis.

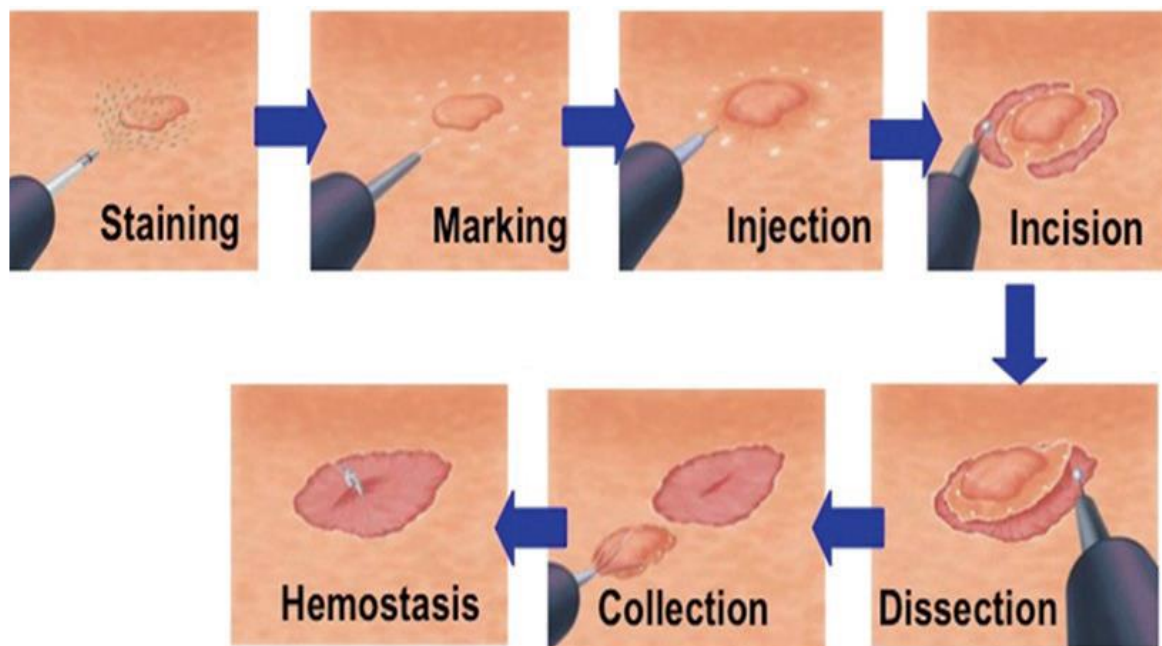


Figure 1.14 Endoscopic mucosal dissection procedure. Adapted/reprinted by permission from Springer Nature: Springer. Endoscopic Submucosal Dissection (ESD). In: Sonoda T. (eds) *Advanced Colonoscopy* by Niimi K., Fujishiro M., Koike K. © 2014 [52].

It is important to highlight that ESD is a complex procedure that can result in complications such as bleeding or perforation. Because of this, a high level of technical skills is needed, and it is time consuming since it takes longer than that for EMR and has more potential complications. The complexity of the task has led to the developments of new technologies to reduce the learning curve and the level of skills while keeping or improving the efficiency of the procedures. It is in this area where robotic endoscopy has emerged in order to provide tools that make it easier to perform the endoscopic procedures.

1.2 Robot-assisted minimally invasive surgery

Minimally invasive surgeries (MIS) aim to reduce the trauma to the patient by performing incisions less than 1 cm in size or using only the natural openings of the human body [53], [54]. The benefits of MIS include: small incisions, less pain, low risk of infection, short hospital stay, quick recovery time, and also less scarring for the patient [55]. On the other hand, MIS are more difficult to perform in terms of ergonomics in comparison to open surgeries, due to the use of rigid or flexible instruments into a limited space, diminished

sensorial feedback and the need for higher dexterity [56]. Robotics and computer assistance intend to overcome the limitations of MIS by enhancing dexterity, sensing, image guidance, stability and motion accuracy [57]. The timeline of some of the key milestones achieved in medical robotics is compiled in [56] and listed below. This timeline only includes commercial surgical platforms and does not include robots assisting patients, lifting of loads, pharmacy and biological sample analysis.

Timeline of some of the key milestones achieved in medical robotics

Year	Medical Field	System
1980s	Neurosurgery	Puma 200: First robotic system in surgery. Stereotactic brain surgery. Performed at the CT Research, Department of Radiology, Memorial Medical Center (Long Beach, CA, 1985) [58]. Neuromate: First neurosurgical robot approved by the Food and Drug Administration (FDA) in the United States (1989). Developed by Renishaw [59], [60].
1992	Orthopedics	ROBODOC: First commercially available robotics system having fist in-human case in 1992. Developed by IBM and commercialized in 1994 by Integrated Surgical Systems (Sacramento, CA) [61], [62].
1998	Laparoscopy	ZEUS/AESOP: a new concept of arranging several robotic arms for laparoscopic procedures developed by Computer Motion [63]–[65].
2001	Telesurgery	Transcontinental robotic surgery: robotic cholecystectomy in a porcine model using the ZEUS robotic platform, the teleoperation was performed between New York (US) and Strasbourg (France) [66].
	Radiation therapy	CyberKnife robotic radiosurgery: automatic detection and motion compensation. Commercialized by Accuracy Inc. [67].
	Orthopedics	

		ACROBOT: new concept in which surgeon actively cooperates with the robot to perform the surgery. Developed at Imperial College, London [68].
2003	Laparoscopy	Merger of the companies Computer Motion and Intuitive Surgical. da Vinci system introduces the fourth arms, 3D vision, and Endo-Wrist. The Da Vinci system did first human trials in 1998 and received FDA clearance in 2003 [69].
2007	Laparoscopy	Viky: voice-controlled robotic endoscope developed by Endocontrol [70].
	Vascular	Niobe developed by Stereotaxis [71].
	Vascular	Sensei for Cardiac applications developed by Hansen Medical (Currently Auris health) [72].
2009	Vascular	Endoluminal approach: steerable catheters to access/operate restricted regions not reachable with rigid laparoscopy. Magellan system for endovascular procedures developed by Hansen Medical (Currently Auris health) [73]. Concentric tube robot first developments (2006-2009) [74], [75].
2011	Spine surgery	Robot that can be mounted directly on patient Renaissance developed by Mazor Robotics [76].
2013	Orthopedics	Smaller, lightweight, safer robots for easier integration into the clinical workflow. Navio: handheld Surgical system for knee arthroplasty. Physical mapping of the anatomy developed by Smith & Nephew [77].
2015	Orthopedics	Mako system: Image-guided knee replacement developed by Stryker [78].
	Endoluminal, NOTES	Flex robotic steerable scope: Endoluminal approach developed by Medrobotics. [79].

2018	Single port Laparoscopy	da Vinci SP: Single port surgical procedures. 25-mm incision, three flexible arms, 3D vision. Developed by Intuitive Surgical [80].
	Bronchoscopy	Monarch: Robotic platform for bronchoscopy procedures, flexible robot, 3D navigation. Developed by Auris Health [81].

Many of the medical procedures for MIS make use of endoscopy to provide access and visibility to the procedures, such as diagnosis and treatment of gastro-intestinal diseases, lung tumors, gynecology, urology, vascular, heart, head and neck [82]. Endoscopy consists in inserting a rigid or flexible tube depending on the application through a small incision or natural port. This tube has a video camera and some channels for insertion of surgical instruments. The surgeon uses these instruments to perform the surgical task while viewing the interior of the patient on a monitor. The first robotic system intended for manipulation of a camera endoscope was the Automated Endoscopic System for Optical Positioning (AESOP) developed by Computer Motion in 1994 [63], [64]. This system was a voice-controlled robotic arm for holding and moving the camera endoscope in different positions [64], [83]. Some examples of other work related to telerobotic systems holding a camera endoscope are the TISKA system [84], the FIPS Endoarm [85], the telerobotic assistance for laparoscopic surgeries [86], EndoAssist [87] and the ViKY robotic scope holder [70], [88]–[90]. One of the first surgical robots used in minimally invasive surgeries in soft tissue was the PROBOT in 1991 for transurethral resection of the prostate [91]. The concept of arranging several robotics arms was introduced by Computer Motion with the AESOP/ZEUS system [65] being the predecessor of the DaVinci system [92] (Figure 1.15). Miniaturization of flexible robots represents an important advance for MIS in transluminal/endoluminal procedures, defining the concept of natural orifice transluminal endoscopic surgery (NOTES). In NOTES, laparoscopic-style external manipulation is not required, instead, flexible-robotized endoscopic procedures have been proposed to enhance access and manipulation through natural or transluminal ports. An example of robotized flexible endoscopic solution are the Aer-O-Scope colonoscope [93], the Endotics system [94], [95], the Flex® Robotic System [96], and the STRAS robotic system developed at the University of Strasbourg [97], [98] (see Figure 1.16). Other robotic platforms for gastrointestinal applications are summarized in Table 1.1, including those commercially available and under development.



Figure 1.15 Da Vinci SP from Intuitive Surgical, Inc.



Figure 1.16 (A) Aer-O-Scope, (B) Endotics system, (C) Flex® Robotic System and (D) ISIS/STRAS system.

Table 1.1 Robotic flexible endoscopy platforms for Gastrointestinal applications [99].

System	Company	Description	Commercialized	Reference
Robotic steering and automated lumen centralization (RS-ALC)	Meander Medical Center, Netherlands	Consisting of a drive unit allowing docking of the angulation wheels of a conventional endoscope.	N	[100]
Endoscopic operating robot (EOR)	University of Occupational and Environmental Health, Japan	Master-slave robotized system for manipulation of a conventional endoscope by two joysticks.	N	[101]
Invendoscope	Invendo Medical GmbH, Germany. Currently Ambu A/S, Denmark	Single use colonoscope concept	N	[102]
NeoGuide	Intuitive Surgical, United States	Computer-aid colonoscope with 16-segment insertion tube controlled independently. It also incorporates a position sensor at the tip.	N	[103]
Aer-O-scope	GI View Ltd, Israel	Self-propelled disposable colonoscope	Yes	[104], [105]
Endotics	ERA Endoscopy SRL, Italy	Flexible, steerable and disposable LED camera probe with special tank with electro-pneumatic connector.	Yes	[94], [95] [106], [107]
CUHK double -balloon endoscope	Chinese University of Hong Kong, China	Double balloon endoscope with a capsule camera at the tip.	N	[108]
MASTER	EndoMASTER Pte, Singapore	Multitasking platform using electromechanically controlled cable actuation.	N	[109]
ISIS-Scope/STRAS system	Karl Storz/IRCAD, Europe	Robotized interventional flexible endoscope with multiples modules based on the Anubis platform.	N	[98]
Endomina	Endo Tools Therapeutics, Belgium	System that can attached to a conventional endoscope to add triangulation capabilities	N	[110]
Scorpion shaped endoscopic robot	Kyushu University, Japan	It consists of two cable-driven robotic arms, haptic feedback and position sensor.	N	[111]
Viacath	Hansen Medical, United States. Currently Auris Health, Inc.	Robotic endoluminal surgical system incorporates an articulated overtube to insert a flexible endoscope and articulated instruments into the GI tract.	N	[112]
CUHK robotic gripper	Chinese University of Hong Kong, China	Bio-inspired flexible robot with shape memory alloy wire actuation.	N	[113]
Imperial College robotic flexible endoscope	Imperial College, United Kingdom	Snake like robot for endoluminal surgery	N	[114]
Flex® Robotic System	Medrobotics	Snake-like multi-articulated endoscopic system	Yes	[96]

1.2.1 Robotized flexible interventional endoscope for intraluminal surgery

The STRAS robot also known as the ISIS-scope is based on the manual ANUBIS platform [115] which is called the ANUBISCOPE™ for gastrointestinal procedures. The manual ANUBISCOPE™ platform requires more than one operator to perform the surgical procedure, one clinician to operate the endoscope and another operator to manipulate the surgical instruments. Figure 1.17 shows the distal part of the Anubis platform. It has three channels for surgical instruments, the fluid channel, bending instruments, camera, lighting,

rotation, translation and deflection motion for the main endoscope. The STRAS robot adds robotization to provide telemanipulation and single user operation to control the motions of the main endoscope and the surgical instruments. The modular design of the STRAS robot makes it easy to set up and to change the surgical instruments if needed.

Figure 1.18(A) shows the master interface of the robot that provides teleoperation through two control handles and the slave system (Figure 1.18(B)) consisting of the Endoscope, the instruments modules, the rotation-translation module, the cradle, the cart, the rotation-translation drive and the remote controller. This technology is focused on enabling one operator to perform complicated procedures with minimal training, although high-level expertise is still required to detect lesions and to make sure that the margins are correctly marked.

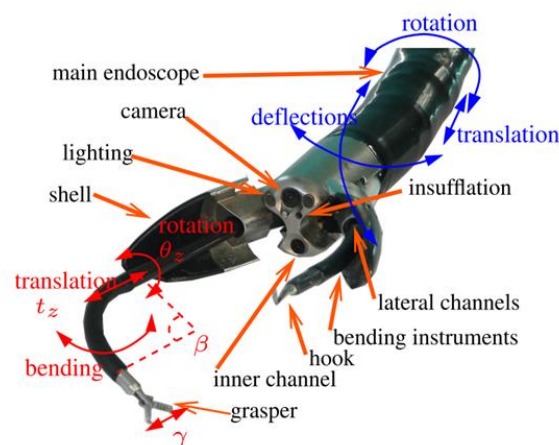
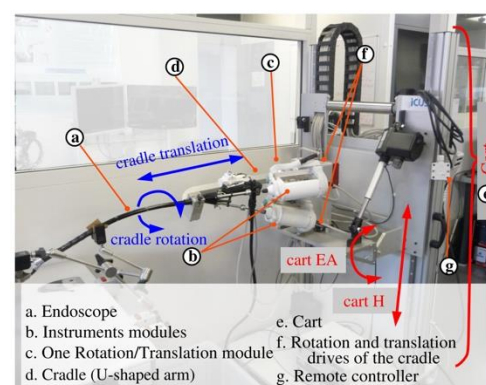


Figure 1.17 Distal part of the endoscopic platform. © 2018, IEEE [98].



(A)



(B)

Figure 1.18 (A) Master interface and (B) slave interface (B) of the STRAS robot. © 2018, IEEE [98].

1.3 Optical Coherence Tomography

Optical Coherence Tomography (OCT), is an imaging technique of great importance in the field of biomedical optical applications. In this technology the backscattered light from the internal structure of biological tissues is measured to provide high resolution and three-dimensional images of the internal architecture of the sample [116]. The tissue can be imaged in situ and in real time with resolutions of one or two orders of magnitude higher than ultrasound [117].

The operating principle of OCT is analogous to the ultrasound imaging system and it is based on measuring the “echo” time delay of the reflected light. The difference is that in OCT the time delay is not measured directly. Instead, the measurement is based on the phase difference between the backscattered light from the sample and that from a reference beam. It is implemented as a scanning methodology in which each sample represents the depth information, called the A-line, which refers to the axial scanning in the Z direction. To obtain 2D information, transversal scanning and axial scanning are combined, so that XZ information is acquired, known as the B-scan mode. The three-dimensional information is measured by adding longitudinal scanning in the Y direction to the B-scan mode. Figure 1.19 shows an illustrative description of the different types of scanning used in OCT.

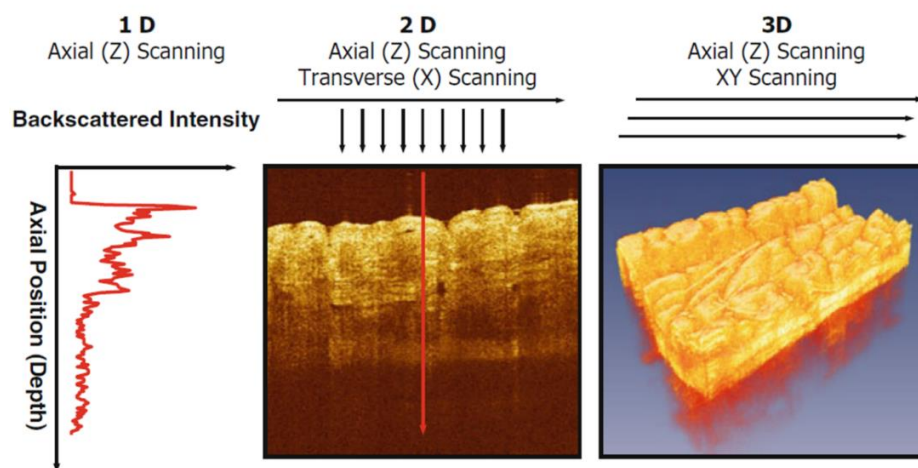


Figure 1.19 Optical Coherence Tomography. Cross-sectional images generated by performing 1D axial scan to obtain depth information (Z), transversal plus axial (ZX) scanning for 2D information (B-scan) and axial scanning plus XY scanning for three-dimensional imaging. Adapted/reprinted by permission from Springer Nature: Springer. Introduction to OCT by James G. Fujimoto, Wolfgang Drexler. © 2015 [117].

OCT has its origin in 1971 with the work of Michel Duguay at AT&T Bell Laboratories, in which he proposed the idea of using backscattered light to see inside biological tissue by demonstrating the concept of “gated picture ranging”. With this technique it was possible to recover an image by gating out undesired scattered light and collecting the desired echo light at the expected time delay related to the image target. Duguay suggested the possible usefulness of this concept in medical applications [118], [119]. J.G. Fujimoto et al. applied this concept in biological tissue in 1985 by performing femtosecond optical ranging with non-linear cross-correlation of the reflected signal with a reference pulse [120]. These results led to the use of low-coherence interferometry, a technique that was being developed at the time for fault location in optical waveguide devices in optical communications [121]. The first application of low-coherence interferometry in biological tissue was performed by Fercher et al. at the Medical University of Vienna in 1988 for eye-length measurement [122]. Huang et al. demonstrated A-scan measurements of the anterior chamber in an ex vivo bovine eye by using low coherence interferometry. Huang et al. demonstrated the first B-scans optical coherence tomography (OCT) images of ex vivo retina and coronary artery, and the work was published in *Science* in 1991 [116]. OCT resulted in the single point scanning version of low-coherence interferometry for medical imaging [123], while Coherence Scanning Interferometry (CSI) is the full field camera based version used for materials analysis [124]–[126]. Both techniques are now mature technologies in their respective domains. CSI has become a standard tool for surface roughness measurement [127] and new imaging modes have been developed, such as real time capability developed by Paul Montgomery et al. [128] from the photonics team (IPP) at the ICube laboratory in Strasbourg, France. A full-field camera based system also exists for imaging tissue samples of which Claude Boccara has been leading the development of the technique in Paris [129]. The first OCT implementations were based on time-domain detection with a scanning reference arm, low-coherence light source and interferometer. Later, frequency domain versions were developed increasing imaging speeds [130], [131], [140], [132]–[139]. The resulting two frequency domain techniques in OCT were spectral domain OCT (SD-OCT) and swept-source OCT (SS-OCT). SD-OCT was first demonstrated in retinal images in 2002 by Wojtkowski et al. [141], a collaboration between the University of Nicolas Copernicus (Poland) and the University of Vienna (Austria). SS-OCT was demonstrated in first experimental results between 1996 and 1997 at the Massachusetts Institute of Technology (MIT) [131], [132]. OCT quickly became the standard for retinal imaging [142]–[145], modern

commercial instruments being commonly used today in ophthalmology [119], [146]. The technique was then adapted to cardiology [147], [148], dermatology [149], and gastroenterology such as in the esophagus [150]–[153], colon [154]–[161] and pancreas [128]–[134].

The advantage of OCT in medical imaging applications is the capability of performing real time optical biopsy by in situ visualization of the internal structure of the tissue without causing any trauma to the patient's body [40], [169]–[177]. The several applications of OCT for clinical situations are listed in [117] and mentioned below:

1. Where the standard excisional biopsy is risky or impossible to perform such as in the eye, arteries or nervous tissue [178], [179].
2. Where the standard excisional biopsy has an unacceptable sampling error. This is the case where the biopsy misses the lesion. In this case OCT can help to reduce this type of sampling error [180].
3. For guidance of interventional procedures. The possibility to see under the tissue surface allows guidance of surgical and micro-surgical procedures [181].
4. For functional measurement and imaging such as measurement of the blood flow with Doppler OCT [182]–[184].

Optical coherence tomography can also be integrated in medical devices such as catheters [185] and endoscopes to access internal organs such as in the GI tract [44], [186]–[190] and external parts of the body such as the skin and the eye, among others.

1.3.1 Basics of Optical Coherence Tomography

Optical Coherence Tomography implements an interferometer to first split the light exiting the source into two optical paths, one called the reference arm and the other the sample arm (Figure 1.20). The reference arm is used to set up a delay path where the light is redirected with a mirror back through the same optical path. The light back scattered in the sample arm also returns through the same optical path and interferes with the light from the reference arm and is detected by the detector and digitized. A computational system processes the information to reconstruct the OCT A-line axial information. A-lines represent the depth information at a given point. Lateral scanning allows a B-scan to be built up to generate a single two-dimensional cross-sectional image and by adding another lateral axis orthogonal to the B-scan, it is possible to then build up three-dimensional information.

The OCT technology is divided into two different techniques [117]: Time Domain OCT (TD-OCT) and Frequency Domain OCT (FD-OCT). In the case of TD-OCT the light source is broadband and continuous wave. The reconstruction of the signal information consists of scanning the reference mirror along its length, to acquire the signal by using a single detector and detecting the envelope of the interference signal, where the amplitude of the successive interference signals corresponds to each scattering layer detected in the sample arm. For FD-OCT the depth information is encoded in the resultant components of frequency. It can be divided into Spectral Domain OCT (SD-OCT) and Swept-Source OCT (SS-OCT) depending on the way of accessing frequency information. In the case of SD-OCT, similarly to TD-OCT, the light source is broadband and continuous wave, the length of the reference arm is fixed to the same position of the sample, and the interference signal is dispersed by a spectrometer to separate frequency components and acquired by a Charge-Coupled Device (CCD) or Complementary Metal Oxide Semiconductor (CMOS) camera. In the case of SS-OCT, the reference arm length is also fixed to the length of the sample arm. The source performs a sweep in wavelength to separate frequency components, and the interference pattern is detected on a single detector.

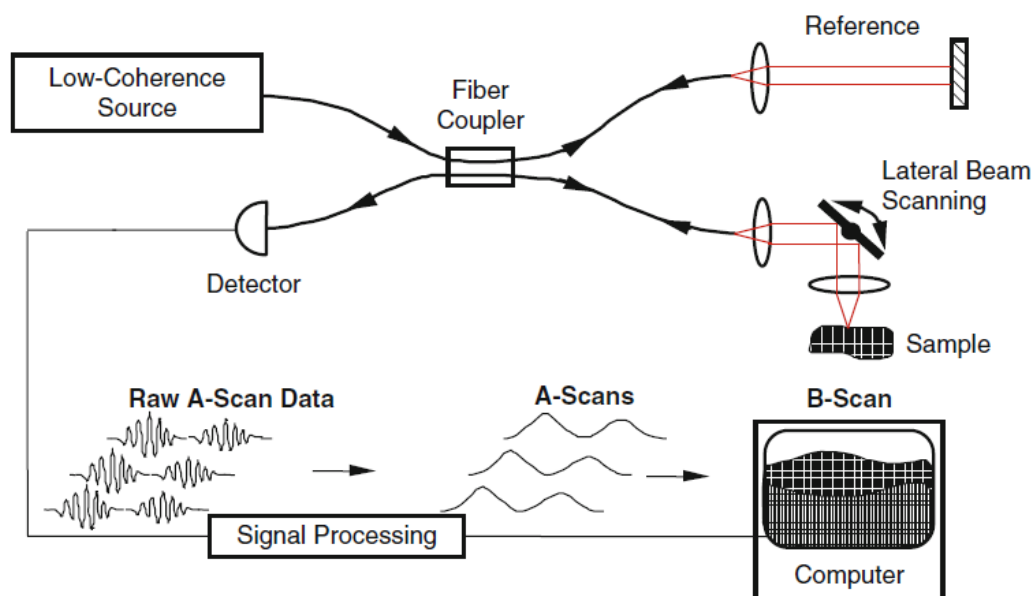


Figure 1.20 Generic fiber-optic OCT system. Bold lines represent fiber-optic paths, red lines represent free-space optical paths, and thin lines electronic signal paths. Adapted/reprinted by permission from Springer Nature: Springer. Theory of Optical Coherence Tomography by Joseph A. Izatt, Michael A. Choma, Al-Hafeez Dhalla. © 2015 [117].

The most important parameters in OCT are the axial resolution, lateral resolution and the depth of field [117], the equations being summarized below:

Axial resolution

$$\Delta z = \frac{2 \ln 2}{n \cdot \pi} \cdot \frac{\lambda}{\Delta \lambda} \quad \text{Eq. 1.1}$$

Lateral resolution

$$\Delta x = \frac{4 \lambda}{\pi} \cdot \frac{f}{d} \quad \text{Eq. 1.2}$$

Depth of Field

$$DOF = n \frac{\pi \Delta x^2}{\lambda} \quad \text{Eq. 1.3}$$

Where λ is the central wavelength, $\Delta \lambda$ the bandwidth of the source, n is the refractive index of the sample, f the focal length of the lens, and d the size of the incident beam on the lens.

1.3.2 Endoscopic OCT

OCT is a technology that provides advantages in many applications [191]–[194], [194]–[196], but has experienced most developments in the medical area, since it can be used to image the human tissue such as in the case of the eye in ophthalmology [197] or the skin in dermatology [198]. These applications are examples of imaging of external organs of the body with easy access. Endoscopic OCT refers to those applications that aim at obtaining OCT images from internal organs of the body in which access is more difficult, such as in the case of the gastro-intestinal tract [185], [186], [189], [190], [199], the circulatory system [200]–[202] and the pulmonary system [203]. OCT endoscopy aims at obtaining images by placing the focusing micro optics at the tip of an optical fiber-based catheter, and then implementing a scanning methodology to allow imaging of the sample.

There are several designs of OCT endoscopes, that can be divided into side-viewing probes and forward-viewing probes. The Figure 1.21 from Gora, M. J. et al. [204] summarizes different designs of OCT distal-end endoscopes, optics and scanning mechanisms. Figure 1.21(A) shows a side-viewing and proximal scanning configuration in which a single mode fiber (SMF) is sheathed by a torque coil (driveshaft) to provide maximum torque transmission

to the tip from the proximal rotary actuator. The fiber delivers the light to a combination of a glass rod and a micro Graded-Index lens (GRIN lens), and then a beam reflector which is used to deflect the light. The lateral resolution and the working distance are related to the length of the glass rod and the length of the GRIN lens. The image of Figure 1.21(C) represents the proximal scanning mechanism used to provide rotation/translation to the configuration of the optical probe in Figure 1.21(A) [189], in this case an optical rotary joint that couples the light between a stationary optical fiber coming from the OCT system with a rotating optical-fiber. The driveshaft provides maximum torque transmission between the rotary joint and the tip of the optical probe. The rotary joint is driven by a motor, and by adding translation (by using a linear stage) to the optical probe it is possible to perform 3D imaging. The distal-end optics is sheathed by a metal guard. A plastic sheath encloses the torque coil and the distal-end optics. Figure 1.21(E) represents an all-optical-fiber ball lens [205], where a ball lens is fabricated at

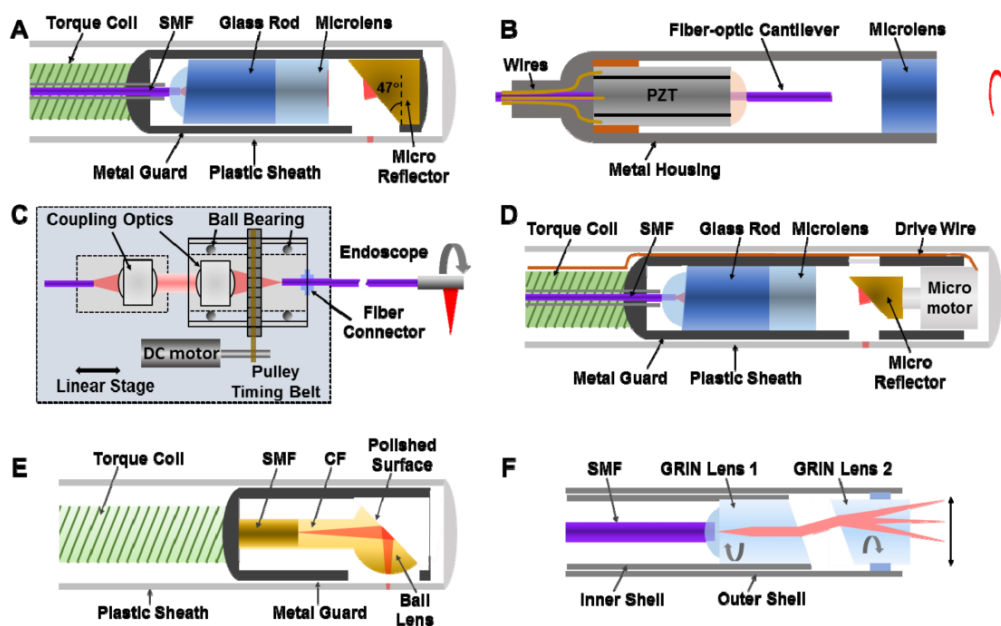


Figure 1.21 OCT endoscope designs: (A) side-viewing; (B) forward-viewing endoscope; (C) proximal scanning with a fiber-optic rotary joint for pull-back/rotation 3D imaging; (D) distal-scanning endoscope with micromotor; (E) all-fiber-optic ball lens; (F) pairs-angle-rotation-scanning forward viewing endoscope . Adapted/reprinted by permission from [204].

the end of the glass rod by using a fusion splicer. The spot size and the working distance are determined by the length of the glass rod and the diameter of the ball lens. Then a polished surface with an angle of about 47 degrees provides the required deflection. The image in Figure

1.21(D) represents the case of using a micromotor [206] at the distal-end of the probe to provide rotation to the beam reflector. The advantage of using a micromotor is to have a higher scanning speed and a more stable interference signal, although it has a high cost and is fragile. Figure 1.21(B) and Figure 1.21(F) represent designs for forward-viewing probes; the first showing a fiber-optic cantilever which is swept by a piezo-electric tube actuator (PZT). Spiral scanning can also be achieved in this configuration[207]. In the case of Figure 1.21(F) [208] the forward-viewing scanning is performed by rotating two angled GRIN lenses in the opposite direction, this method requiring good concentricity and stable spacing.

1.3.3 Applications of endoscopic OCT

Earliest applications of catheter-based OCT probes were in the intravascular field such as imaging the ex vivo human coronary artery [209], [210]. First in vivo human imaging was performed by Jang, Ik Kyung et al. to image tissue prolapse in a stent [211]. In the next developments, the OCT catheter, similar to the cardiovascular catheter was tested in other areas such the GI and respiratory tract. The first in vivo animal imaging of the gastrointestinal tract and respiratory system were performed by Guillermo J. Tearney et al. [212]. First in human studies on imaging of mucosa in respiratory, gastrointestinal, urinary and genital tracts were performed by A. Sergeev et al. in 1997 [213] and F. I. Feldchtein et al. in 1998 [214]. The endoscopic OCT probe was inserted in the digestive system using the working channel of an endoscope and investigation of various locations was achieved by placing the probe using flexion of the endoscope. OCT has been used for visualization of the pancreaticobiliary tract strictures, by quantification analysis on the thickness of the layers of the bile duct to differentiate benign, inflammatory, and malignant tissue types, an example of these studies being reported in [41]. Some studies have also demonstrated the potential of using OCT for gastric lesions evaluation [215], where submucosal tumor can be detected by OCT imaging. The small intestine is the most challenging organ due to its length and complex disposition, so that it is the least investigated organ. However, some studies have shown results using OCT for differentiating celiac disease and tumors in the small intestine [216]. The large intestine (colon) has also been investigated using OCT, studies demonstrating the feasibility of differentiating cancerous from benign tissue [42], and also inflammatory bowel diseases [43].

The main challenge was the much larger diameter of the digestive system in comparison to the cardiovascular system. Thus, the majority of the technical development of endoscopic

OCT for gastroenterology has been focused on the comprehensive visualization of the tubular organs with large diameter. These efforts were mostly focused on imaging of the esophagus.

The esophagus has been an important area of research in endoscopic OCT, due to the great benefit that this technology has brought in being able to differentiate normal tissue from Barrett's dysplasia and esophageal cancer, as well as the easier access for the OCT catheters. The originally used cardiovascular catheters were designed to work in contact, meaning that the working distance and focusing plane were just outside of the sheath and the probe had to be placed in contact with the tissue to provide high quality images. Given the diameter of around 1 mm it was not possible to comprehensively image the whole esophagus, which has a diameter of 2 cm. The most promising solution was developed at Massachusetts General Hospital, where the working distance of the catheter was extended to 1 cm and the distal part of the catheter was enclosed in an inflatable non-compliant balloon with a 2 cm diameter to assure that the esophagus was located within the working distance of the probe [217]. This technology has been successfully commercialized by NinePoint Medical in 2013 under the name NvisionVLE Imaging Console (Figure 1.22).



Figure 1.22 NvisionVLE Imaging Console from NinePoint Medical. Adapted/reprinted by permission from Oxford University Press: Diseases of the Esophagus. Volumetric laser endomicroscopy and its application to Barrett's esophagus: results from a 1,000 patient registry by Smith, M S; Cash, B. © 2015 [41].

Another design of the OCT catheter was focused on both allowing for imaging of the full circumference of the esophagus, but without the need for endoscopy. The clinical motivation was to enable population-based screening for Barrett's esophagus by developing a device that is swallowable. Tethered capsule endomicroscopy is based on OCT in which an optomechanical tethered pill is swallowed to acquire axial microscopic images of the esophageal wall as it traverses the esophagus with natural peristalsis. The lateral resolution is $30\ \mu\text{m}$ and the axial resolution is $7\ \mu\text{m}$ (Figure 1.23) [185].

OCT can also be used for endoscopic therapy guidance, to help in evaluating the treatment in patients with Barret esophagus undergoing radio frequency therapies, so as to predict efficacy and to monitor thermal injury and tissue recovery after treatment [218]–[220]. Other related examples in which OCT has been proposed are radiofrequency ablation monitoring [221], guidance of epicardial cardiac radio frequency ablation therapy, and multimodal OCT and Radio frequency ablation for real time cardiac applications [222], [223].

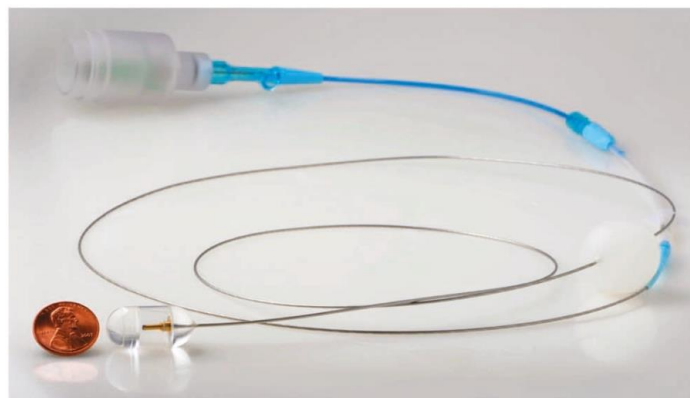


Figure 1.23 Tethered capsule endomicroscopy. Adapted/reprinted by permission from Springer Nature: Nature Medicine. Tethered capsule endomicroscopy enables less invasive imaging of gastrointestinal tract microstructure by Michalina J Gora et al. © 2013 [185].

1.4 Advanced imaging and robotics

OCT has been proposed as a promising optical imaging technique to be integrated in the workflow of medical procedures involving surgical robotic platforms [224]. In urology, for instance, OCT has been used to obtain images during and after robotic-assisted laparoscopic procedures to evaluate prostatectomy specimens, margin detection after radical prostatectomy,

identification of neural bundles, and other applications in this area referred to in [225]–[232]. See Figure 1.24.

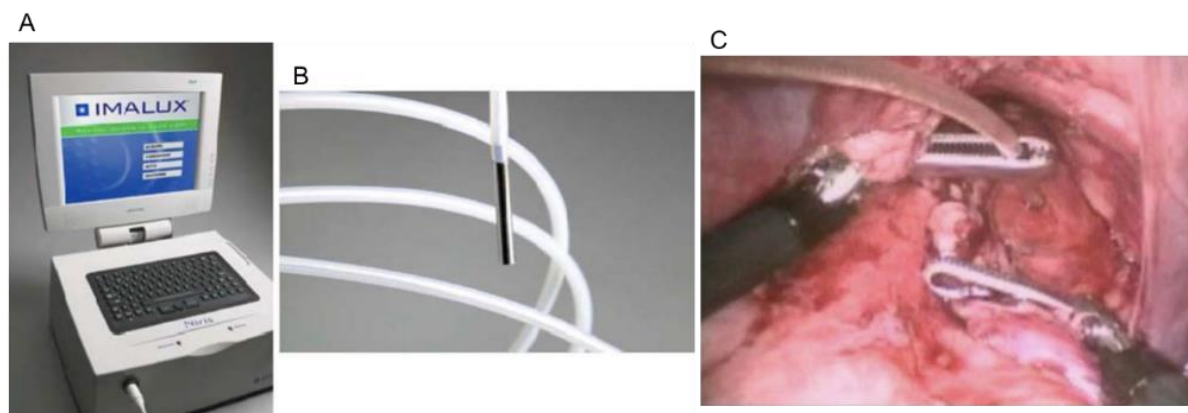


Figure 1.24 Niris OCT probe in vivo during animal robotic prostate surgery [233].

Robotized surgical microscopy has been combined with OCT for neurosurgical procedures and performing automatic OCT scanning as in [234], [235]. Concurrent multi-scale imaging has been achieved by integrating OCT with a MRI teleoperated robotic platform to manipulate a needle and co-registering both type of information for neurosurgical applications [236], see Figure 1.25.

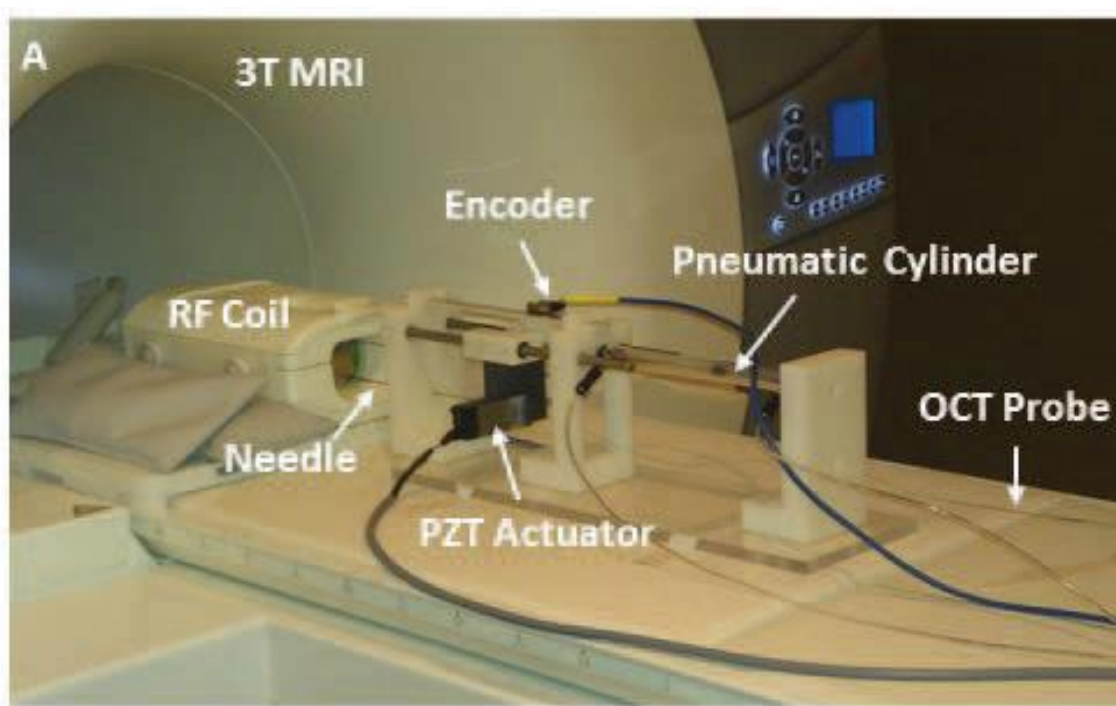


Figure 1.25 OCT probe under MRI guidance for neurosurgery [236].

OCT image-guidance for automatic laser cutting in head surgery in cochlear implants has been demonstrated in [237], [238]. An OCT probe has also been placed in a flexible robotic arm for imaging of the cochlea and surrounding temporal bone area for robotically assisted microsurgery [239], [240], see Figure 1.26.

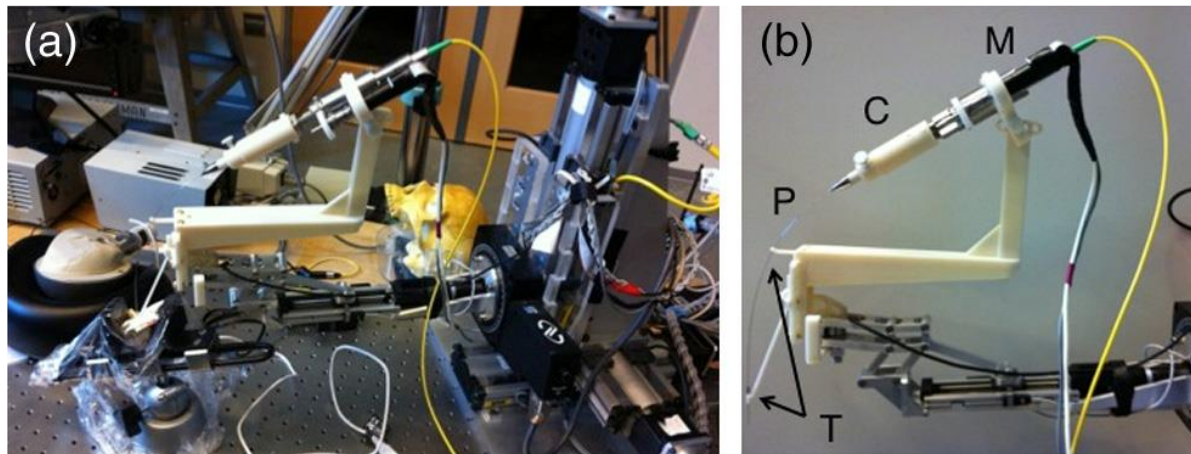


Figure 1.26 Robot-assisted three-dimensional registration for cochlear implant surgery using a common-path swept-source optical coherence tomography probe (CP-SSOCT). (A) Picture of the robotic platform. (B) Close-up of the robotic arm with the mounted rotary motor (M), casing (C), 21G tubes for restricting lateral motion (T), and CP-SSOCT needle probe (P) [239].

A majority of the effort has been carried out in microsurgical procedures in areas such as ophthalmology with handheld robotic instruments in which OCT is used for image guidance [241]–[244]. The use of OCT for needle insertion force measurement into the eye [245], suturing evaluation in ophthalmic robot-assisted microsurgeries [246], 3D imaging feedback in teleoperated robots in ophthalmic surgeries [247], tip positioning based on OCT images in an intraocular robotic interventional surgical system (IRISS) [199]–[200], real time OCT image guidance in a cooperative robotic assist device for deep anterior lamellar keratoplasty [250], and OCT for robotic intraocular needle navigation [251] among others. Figure 1.27 shows examples of a few robotic systems using OCT.

Combination of OCT and white light images has been proposed for visual servoing of a 6 DoFs robot to automatically reposition the benchtop OCT probe in the exact location of a previous biopsy for diagnostic monitoring [252], [253], [254], [255], see Figure 1.28. A steerable OCT cannula has been proposed in [256], [257], such as a continuum robot for multi-

scale motion tested with an OCT probe in [258], OCT-based position control of a concentric tube robot (CTR) has also been proposed in [259], see Figure 1.29.

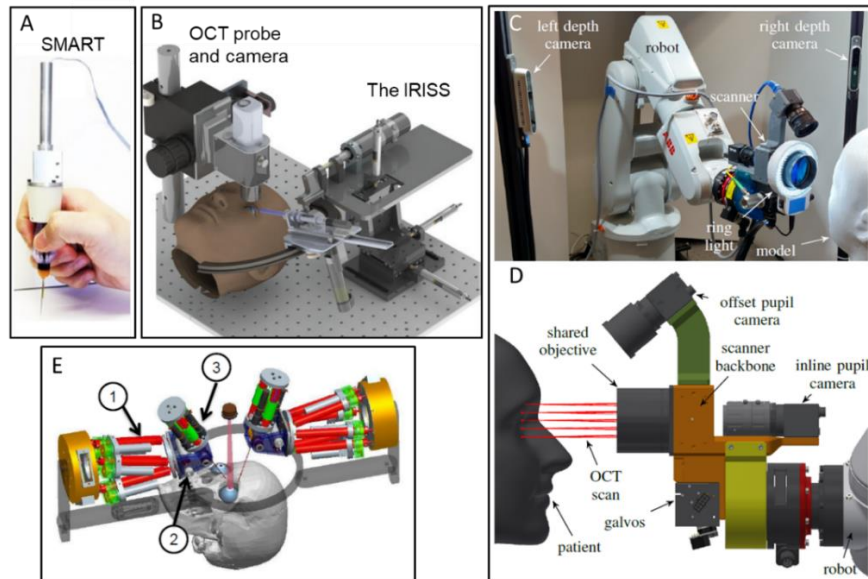


Figure 1.27 (A) SMART micro-forceps, microsurgery system [260], (B) Intraocular robotic interventional surgical system (IRISS) [261], (C-D) Robotic system for OCT imaging of stationary and moving eyes [262], (E) robotic tele-manipulator for OCT guided retinal surgery [263].

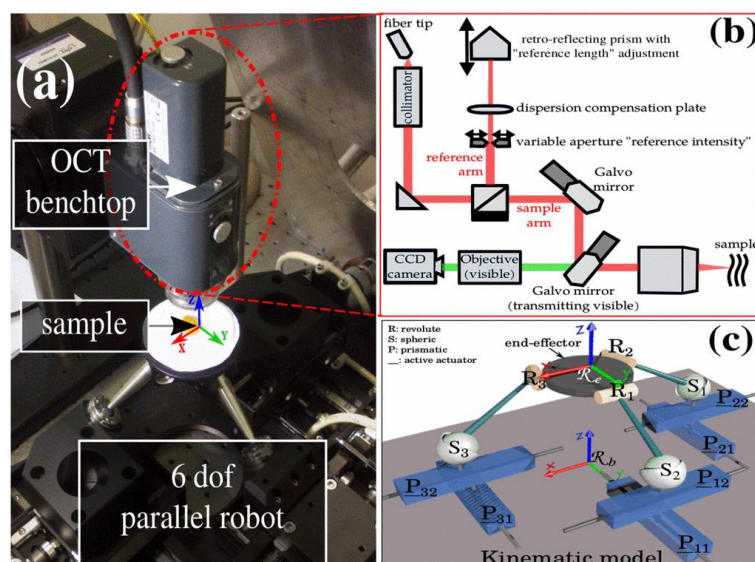


Figure 1.28 (A) Experimental setup, (B) Multimodal imaging system architecture, and (C) the kinematic scheme of the 6 DoF robotic system, © 2016, IEEE [249].

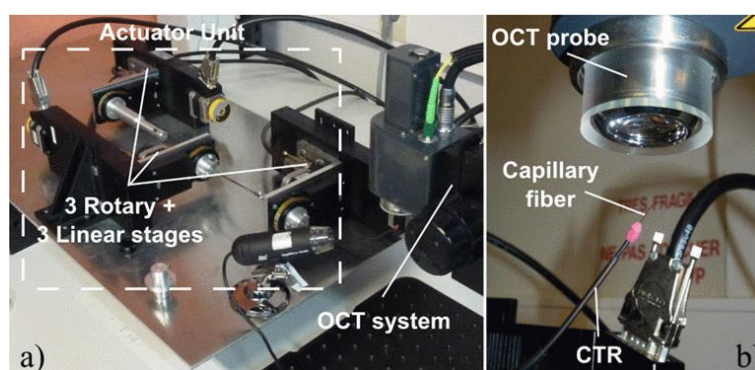


Figure 1.29 (A) The CTR prototype and the OCT system, (B) Distal end of the CTR and the eye-to-hand configuration OCT probe, © 2017, IEEE [259].

It is important to mention as well the use of deep and machine learning techniques using OCT, such as for instance, needle pose estimation and localization as in [251], [264], [265]. Figure 1.30 shows an OCT-based simulation-trained neural networks for force classification to improve safety characteristics in intravitreal injection [266], [267] and OCT for motion compensation is demonstrated in [268].

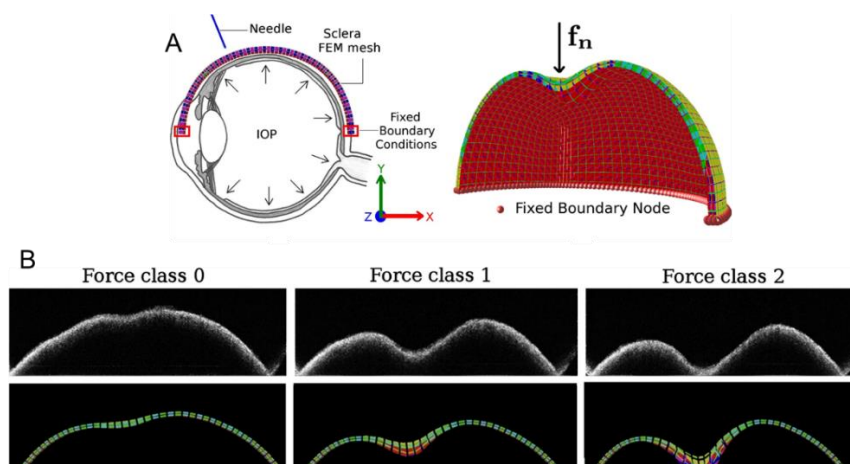


Figure 1.30 (A) Deformed model of the sclera, (B) Force classification based on simulation-trained neural networks from OCT images. Adapted/reprinted by permission from Springer Nature: Int J CARS. Force classification during robotic interventions through simulation-trained neural networks by Mendizabal, A., Sznitman, R. & Cotin, S. © 2019 [269].

Probe-based Confocal laser endomicroscopy (pCLE) being a technology that shares similarities with OCT has also been implemented in combination with robotic systems as in

the case of the work of R.C. Newton et al. [270] in robot-assisted transvaginal peritoneoscopy using confocal endomicroscopy in a porcine model. Figure 1.31 shows the robotic articulated endoscopy with two channels, one for the CCD camera and the other for the pCLE probe.

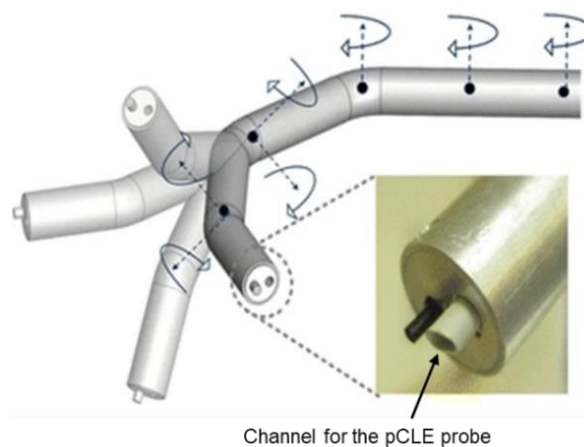


Figure 1.31 The 7-DoF robotic articulated endoscope. It has two operating channels: the camera and interchangeable instruments such as a pCLE. Adapted/reprinted by permission from Springer Nature: Surgical Endoscopy. Robot-assisted transvaginal peritoneoscopy using confocal endomicroscopy: a feasibility study in a porcine model by Newton RC et al. © 2012 [270].

Benoit Rosa et al. have proposed visual servoing using confocal endomicroscopic images for large image stitching during scan trajectories; the concept was demonstrated in a balloon actuation minimally invasive device (Figure 1.32) [271].

These references are a sample of the work being carried out to demonstrate the usefulness of advanced optical imaging techniques such as OCT in the medical robotic field, in which, the OCT technology is used to perform tasks beyond image and tissue analysis according to the needs in robotic-assisted medical systems.

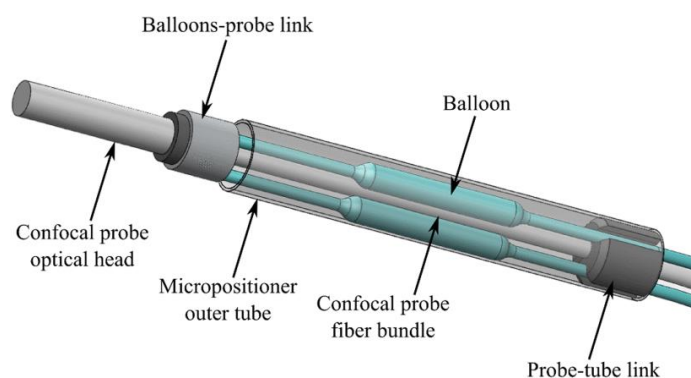


Figure 1.32 Distal end of the balloon actuation minimally invasive device, © 2012, IEEE.

1.5 Motivation and objective

There exists an unmet clinical need to provide doctors with a new method that streamlines minimally invasive treatment to single operator procedures assisted by in-situ and real-time accurate tissue characterization for informed treatment decisions in management of colorectal cancer. A promising solution to this problem has been developed by the AVR team at the ICube laboratory, in which the flexible interventional endoscope (Karl Storz) was completely robotized, so allowing a single operator to independently telemanipulate the endoscope and two insertable therapeutic instruments with a joint control unit. However, the robotic-assisted flexible endoscope is subject to the same diagnostic accuracy limitations as standard endoscopy systems. It has been demonstrated that endoscopic OCT has a good potential for imaging disorders in the gastrointestinal track and differentiating healthy tissue from diseased. Currently, OCT is limited to imaging of the human esophagus, which has a simple geometry and easy access. Neither OCT, nor the robotized endoscope can solve the limitations of current standard of care for colon cancer management alone. Combining these two technologies and developing a new platform for early detection and treatment of cancer is the main interest of this thesis, with the aim of developing a state-of-the-art OCT imaging console and probe integrated with the robotized endoscope. The main hypothesis behind this doctoral project is that a fusion of real-time microscopic endoscopic OCT with a robotized interventional flexible endoscope can allow imaging of the interior of the large intestine for tissue characterization and treatment assistance allowing a single operator to perform minimally invasive treatment in the telemanipulation mode. To test this hypothesis a novel endoscopic OCT device has been developed that comprises a steerable OCT catheter and an external OCT imaging console built around an Axsun OCT engine with 1300 nm swept source laser. This OCT imaging console (OCT-IC) provides the laser light source, the photodetectors, data acquisition and processing, the interferometer and the computational system to display the graphical interface for user interaction. The novel steerable OCT instrument comprises an internal optical fiber probe rotated by a rotary joint inside an outer shaft. The shaft has 3.5 mm outer diameter and has 3 degrees of freedom (DoFs): flexion, translation and rotation. To enable OCT imaging a plastic tube is attached to the distal end of the shaft. For local inspection of tissues, the OCT probe optics side-focuses the near infrared light just outside the plastic sheath to a spot of 30 μm in size. The OCT instrument is inserted in one of the two side-channels of

the flexible endoscope designated for the treatment instruments. The addition of OCT to the robotized flexible interventional endoscope allows real-time assistance in exploration of the colon lumen and in the steps of treatment. This new approach for minimally invasive diagnosis and treatment is validated in bench-top and in vivo animal experiments.

1.6 French summary of the chapter

Il manque actuellement aux médecins une nouvelle méthode qui rationalise le traitement peu invasif pour en faire des procédures à opérateur unique, assistées par une caractérisation précise des tissus in situ et en temps réel, en situation de prise de décisions dans la gestion du cancer colorectal. Une solution prometteuse à ce problème a été développée par l'équipe AVR (Automatique, Vision et Robotique) du laboratoire ICube, au sein de laquelle l'endoscope interventionnel flexible (fabriqué par Karl Storz) a été entièrement robotisé, permettant ainsi à un seul opérateur de télémanipuler indépendamment l'endoscope et deux instruments thérapeutiques insérables avec une unité de contrôle commune. Cependant, l'endoscope flexible assisté par robot est soumis aux mêmes limites de précision diagnostique que les systèmes d'endoscopie standards. En effet, il a été démontré que l'OCT endoscopique présente un potentiel pour l'imagerie des troubles de la voie gastro-intestinale et pour la différenciation de tissus sains des tissus malades. Actuellement, l'OCT se limite à l'imagerie de l'œsophage humain, qui présente une géométrie simple et un accès facile. Ni l'OCT, ni l'endoscope robotisé ne peuvent résoudre à eux seuls les limites de la norme actuelle de soins pour la prise en charge d'un cancer du côlon. La combinaison de ces deux technologies et le développement d'une nouvelle plate-forme pour la détection et le traitement précoce du cancer constituent l'objet principal de cette thèse, avec la vision de développer une console d'imagerie OCT et une sonde de haute technologie intégrée à l'endoscope robotisé. L'hypothèse principale derrière ce projet de doctorat suppose qu'une fusion de l'OCT microscopique endoscopique en temps réel avec un endoscope flexible interventionnel robotisé peut produire l'imagerie de l'intérieur du gros intestin pour la caractérisation des tissus et l'aide au traitement, permettant ainsi à un seul opérateur d'effectuer une intervention peu invasive en mode télémanipulation. Pour tester cette hypothèse, un nouveau dispositif d'OCT endoscopique a été mis au point. Il est constitué d'un cathéter d'OCT orientable et d'une console d'imagerie OCT externe construite autour d'un moteur d'OCT Axsun avec un laser à source balayée de 1 300 nm. Cette

console d'imagerie OCT (OCT-IC) fournit la source de lumière laser, les photodétecteurs, l'acquisition et le traitement des données, l'interféromètre et le système de calcul pour afficher l'interface graphique qui servira d'interaction avec l'utilisateur. Le nouvel instrument OCT orientable comprend une sonde à fibre optique interne mise en rotation par un joint rotatif installé dans un arbre extérieur. L'arbre a un diamètre extérieur de 3,5 mm et possède 3 degrés de liberté (DoFs) : flexion, translation et rotation. Pour permettre l'acquisition de l'imagerie OCT, un tube en plastique est fixé à l'extrémité distale de la tige. Pour l'inspection locale des tissus, la sonde OCT focalise la lumière proche infrarouge à l'extérieur immédiat de la gaine plastique sur un point de 30 μm . L'instrument OCT est inséré dans l'un des deux canaux latéraux de l'endoscope flexible prévu pour les instruments de traitement. L'ajout de l'OCT à l'endoscope interventionnel flexible robotisé permet une assistance en temps réel dans l'exploration de la lumière du côlon et dans les différentes étapes du traitement. Cette nouvelle approche pour le diagnostic et le traitement minimalement invasifs est vérifiée dans des expériences sur animaux de laboratoire et in vivo.

Chapter 2

Optical Coherence Tomography Imaging console with dual imaging modes

Content

2.1 OCT imaging system for pre-clinical examination	48
2.1.1 OCT engine	50
2.1.2 Interferometer design	53
2.1.3 Sample arm design.....	55
2.2 Linear Scanning Synchronization	56
2.3 Human machine interface.....	59
2.4 Characterization and optimization	61
2.4.1 Signal to noise ratio modelling	61
2.4.2 Signal to noise measurements and optimization.....	63
2.5 Experimental validation	65
2.6 Conclusions of the chapter	67
2.7 French summary of the chapter	67

Having presented the state of the art of OCT imaging and robotics in medical imaging, the next section presents the OCT imaging console that has been developed, together with its characterization.

2.1 OCT imaging system for pre-clinical examination

The OCT Imaging Console referred to from now on as OCT-IC is a state-of-the-art swept source OCT system. In addition to optical components in charge of light generation and the interferometer it is also the main processing unit in charge of acquiring the signal collected from the optical probe for interpretation, construction of the image frame, providing control to the two scanning modes implemented, and transmitting and displaying the information to the user. The main challenges associated with this system are:

1. Supporting microscopic and endoscopic modes in a plug-and-play style.
2. Compatibility with the use in the clinic.
3. Portability.
4. Software and hardware design allowing implementation in a robotized and teleoperated system.

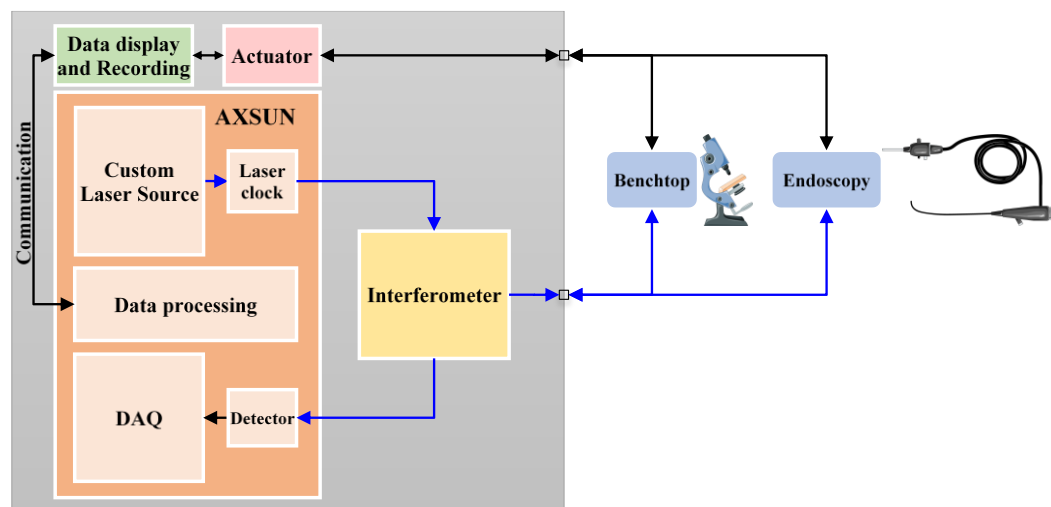


Figure 2.1 General scheme of the OCT Imaging Console (OCT-IC).

The OCT-IC is composed of several other components such as the data display and recording system, the actuators, the commercial OCT engine from AXSUN Technologies and the interferometer. It provides: 1) the Benchtop imaging mode for laboratory experiments, optimization and ex vivo analysis for correlation between histology and OCT images, and 2) the Endoscopic mode aimed to acquire OCT images from the lower gastro intestinal tract, to

enable real time, faster and accurate disease diagnosing. The general scheme of the OCT-IC system is shown in Figure 2.1.

The OCT-IC is enclosed in a case designed to be compact and portable. It has external ON-OFF switches to allow power to the internal components. Other important design requirements are related to the standards of safety for use in the clinical room, such as electromagnetic compatibility, laser-on indication, heating, dust, water leaks, noise, etc. Below there is a list of the requirements considered as design inputs:

1. Visualization of 1 to 2 mm of the epithelial tissue.
2. Transportable by one person with common means such as in a car.
3. Easy to put on a table of the clinical room.
4. Compatible with the electrical installation of a French hospital.
5. Electrically safe when it is closed or opened.
6. Protected against high internal temperatures.
7. Protected against dust.
8. Liquid proof.
9. Vibration proof.
10. Silent.
11. Laser safety: there must be a light indicator to know if the laser is ON or OFF.
12. Laser safety: interlock to switch off the laser when the case is being opened.
13. Easy to access the switch for the main power supply.
14. Easy to connect a screen display, keyboard and mouse to interact with the integrated computer.
15. Accessible to extract data from the integrated computer.
16. Easy to change any internal component if needed.
17. Easy to connect both imaging systems: Benchtop and Endoscopic modes.

Figure 2.2 shows an exploded-view of the internal design in CREO (3D CAD software) of the OCT-IC system. The level 1 comprises the AXSUN Engine, the power supply TDK Lambda and the mirror of the reference arm mounted on a motorized translation stage. On the Level 2 the Computer for Human Machine Interaction (HMI) and the 3 motor drivers iPOS3604/02 on the iPOS360x-ST-CAT motherboard from Technosoft and part of the interferometer that splits the light into the sample and reference arm are installed. The rest of the components related to the receiver section of the interferometer are placed on the Level 3,

corresponding to the polarization splitter and controllers connected to the photodetectors of the AXSUN Engine.

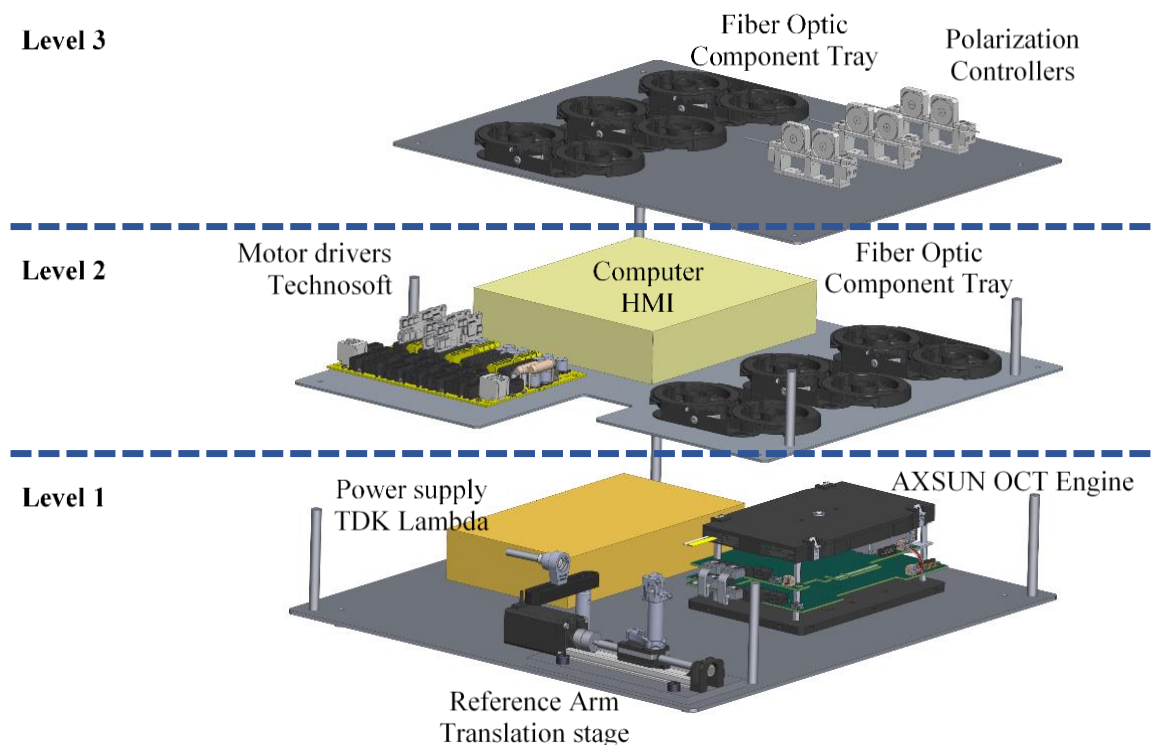


Figure 2.2 Exploded-view of the OCT-IC and its components.

2.1.1 OCT engine

Thanks to the fast development of the OCT in the last 25 years, there are multiple companies providing either subcomponents or fully functional OCT systems. The most important choice for the successful use of the OCT system in a defined clinical application is the right choice of the central wavelength. Due to the trade-off between the axial resolution and penetration depth it is important to correctly choose the wavelength from three available options: 800 nm, 1060 nm or 1310 nm. In the vast majority of previously published literature in the field of imaging epithelial tissues in the digestive system, light sources centered at 1310 nm are used to allow for penetration of 1-2 mm of the digestive wall [202]. An interesting solution in this wavelength region has been developed by AXSUN Technologies, that incorporates the swept-source laser source, dual balanced photodetectors and high-speed data acquisition electronics. The system has been specifically designed for medical applications and thus has a very small form factor. AXSUN OCT Swept Source Engine will be referred to from now on as the OCT Engine in this document.



Figure 2.3 AXSUN OCT Engine [272].

Table 2.1 Specification of the AXSUN Integrated Engine [273].

Parameter	Value	Min	Max
Sweep Rate (kHz)	100.16	99.90	100.20
Center Wavelength (nm)	1301.23	1290.00	1315.00
Wavelength Tuning Range (nm)	133.84	125.00	
Average power (mW)	27.80	25.00	
Duty cycle (%)	76.80		
Sample Duty cycle (%)	46.40	42.00	55.00
MZI path length diff. (μm)	-22.20	-308.00	308.00
External Clock Min Frequency (MHz)	209.50	40.00	500.00
External Clock Max Frequency (MHz)	410.20	40.00	500.00
Sampling Clocks (count)	1700.00	1700.00	

Table 2.1 contains the specifications of the OCT Engine used for the project described in this report. The light source is a swept source laser with a sweep rate of 100.16 kHz, 1700 samples per A-line, a central wavelength of 1301.34 nm and a tuning range of 133.84 nm, a coherence length of 12 mm, and an average optical power provided by the laser of 27.8 mW. The system used was an OEM version as shown in Figure 2.3 with an FC/APC pigtail fiber optic output, a sweep trigger provided via SATA connector and an SMA connector output for external scanner systems, an image synchronization input and one Ethernet port for communication with the user computer. The high-speed data acquisition electronics (DAQ) is based on field-programmable gate array (FPGA) technology, two interfaces between the DAQ hardware and the host PC software being provided, one of them referred to as the “Control” interface and the another one as the “Capture” interface [274]. The Control interface is bidirectional, of limited bandwidth, and aimed at diagnostics, configuration, firmware update on either the DAQ or laser boards and status monitoring by message exchange between the data acquisition hardware and the host software. The Capture interface receives information only from the DAQ to the host, is high-bandwidth and aimed at OCT image data stream from the DAQ to the host

software for image display, storing, and analysis. The Control and Capture interfaces are built from two dynamic libraries: AxsunOCTControl.dll and AxsunOCTCapture.dll, these libraries allowing the creation of a personalized Graphical User Interface to add customized functionalities not included in the Control and Capture interfaces. Examples are capabilities such as Signal to Noise Ratio optimization, implementation of linear and rotational scanning, patient information management, specification of field of view, number of A-line samples to acquire, pixel to distance calibration in millimeters, data export to JPEG and AVI format and video recording, etc.

Figure 2.4 describes the block diagram implemented in the FPGA image processing pipeline. The OCT engine provides a two channel dual balanced detector for Analog-to-Digital Conversion (ADC) for the acquisition of horizontal (H) and vertical (V) polarization OCT signals in a polarization diverse detection configuration [275]. In this first stage 1700 samples are taken (Table 2.1), then additional zeros are concatenated to complete a total vector length of 2048 points as input for the IFFT block. In the blocks IFFT, Complex Modulus, Channel Mixer and Square Root-Background Subtraction the Fast Fourier transform (FFT) is computed and the negative frequencies are truncated. The complex modulus is calculated on 1024 samples, the polarization diverse output is also computed and the linear-scale OCT intensity signal (I) is computed using the mathematical expression in Eq. 2.1.

$$I = \sqrt{(Re(H))^2 + (Im(H))^2 + (Re(V))^2 + (Im(V))^2} \quad \text{Eq. 2.1}$$

The block Linear to Log converts the information from a linear to a logarithmic scale with 16-bit precision using Eq. 2.2. Then the logarithmic information is converted to 8-bit for grey scale pixel representation using Eq. 2.3 (Log to 8-bit Pixel) and finally JPEG Compression is performed to reduce the network bandwidth consumption through the Ethernet Interface.

$$Ps_{16} = 20 \cdot \log_{10}(I) = 3.0103 \cdot 2 \cdot \log_2(I) \quad \text{Eq. 2.2}$$

$$Ps_8 = GAIN \cdot 2 \cdot \log_2(I) + OFFSET \quad \text{Eq. 2.3}$$

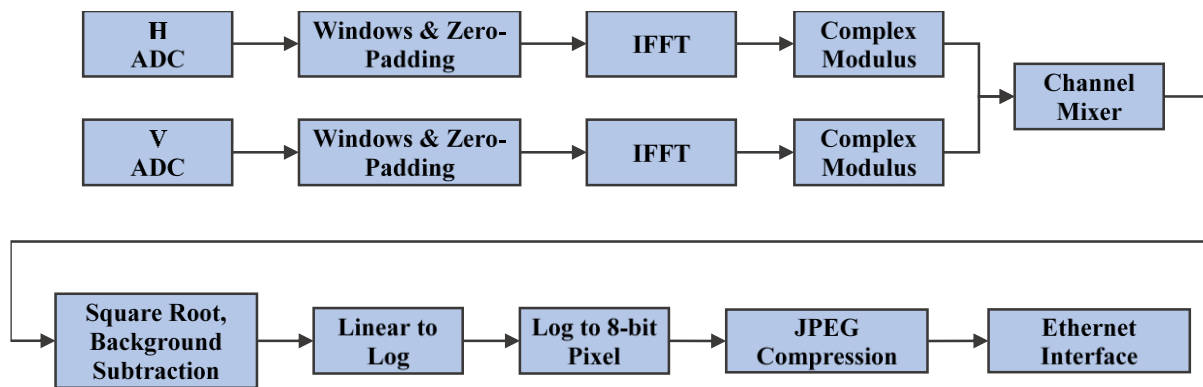


Figure 2.4 Block diagram implemented in the FPGA image processing pipeline [274].

2.1.2 Interferometer design

When choosing the interferometer design for the OCT system there are many aspects that have to be taken into account. First, it has to be chosen depending on the interference signal detection method. One of the advantages of the swept-source OCT over spectral domain OCT is the availability of the dual balance detection, which provides better noise reduction and dynamic range [276]. To enable balanced detection, the interferometric signal needs to be split into two components with equal intensity and shifted in phase by 180 degrees [277]. Secondly, the possibility of matching polarization between the sample and the reference arm has to be taken into account. If polarization mismatch between the sample and reference arms is not constant in time, which usually is the case in the endoscopic devices where optical fiber motion introduces polarization change [278], it is important to introduce polarization diverse detection to compensate for the mismatch [275]. Lastly, given the fact that biological specimens have very low reflectivity the light throughput in the interferometer is extremely important to assure that the maximum allowed power is first delivered to the tissue [279] and collected back with the detectors.

Based on the literature [280] the Mach-Zehnder interferometer with a low coherence light source was implemented as shown in Figure 2.5. The light from the swept-source laser output is divided into two optical paths, the Sample arm and the Reference arm. For this design 90% of the optical power of the laser is delivered to the sample arm, and 10% to the reference arm using a 90:10 fiber splitter (TW13002A1, Thorlabs). The circulators C1 and C2 (CIRC-3-31-P-BB-156, Gould Technology, LLC) redirects the light from the laser to the sample and reference arm, respectively, and also redirects the backscattered light from the sample and

reference arm to the fiber 50:50 splitter (TW1300R5A2, Thorlabs) where both of the backscattered light signals interfere with each other.

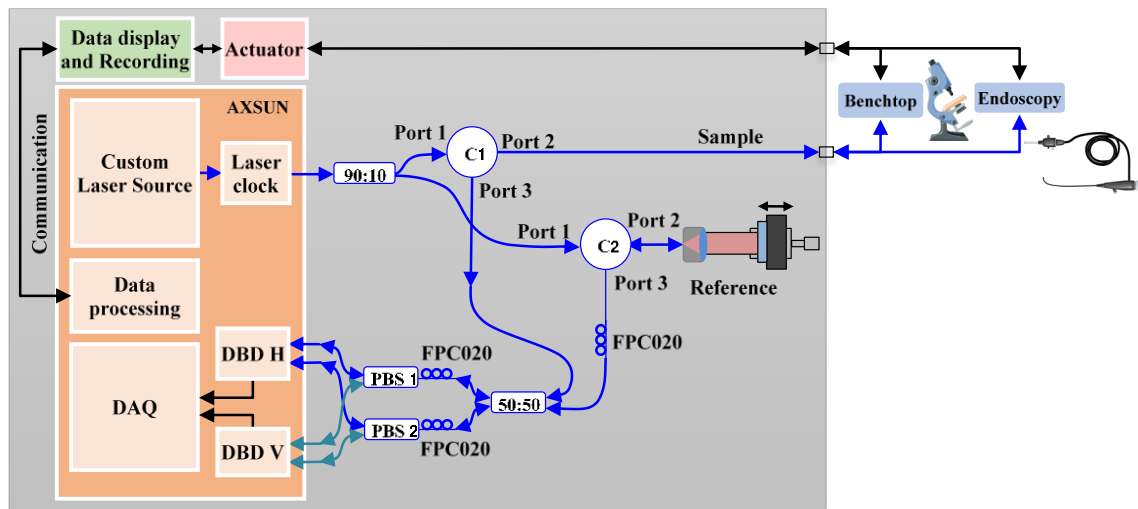


Figure 2.5 Scheme of the Interferometer implemented in the OCT-IC, Data display and Recording and the two imaging modes. C – circulator, PBS – polarization beam splitter, DBD – dual balance detector, H – horizontal, V – vertical.

To compensate for a mismatch of polarization between the reference and sample arm the system utilizes a polarization diverse detection (Figure 2.5) where the interference signal is split into two and each half is redirected to a fiber polarization beam splitter PBS 1 and PBS 2 (POBS-13-L-3-5-2-28ER, PFF Inc.). The output of each polarization beam splitter is then the input for each dual balance photodetector of the channels DBD H and DBD V, where DBD means Dual Balanced Detector, and H and V stands for the horizontal and vertical components of the polarization of the light. Miniature 2-Paddle Polarization Controllers (FPC020, Thorlabs) are placed in the input ports of the 50:50 combiner, PBS 1 and PBS 2 to optimize light intensity and polarization. The Reference arm is implemented with an optical fiber connected via connector FC/APC to the collimator in Figure 2.6 the light is then reflected back by the protected gold mirror (PF10-03-M01 - Ø1") mounted on a kinematic-post from Thorlabs. In order to assure that the length of the optical path of the reference and sample arms is the same, an additional fiber loop is added between the circulator C2 and the 50:50 beam splitter, which was calculated to match the design of the sample arm so that it is possible to switch between the two imaging modes. Table B.6 to Table B.8 in section B of annexes summarize the fiber loop computation. The mirror and the kinematic-post mount are placed on a motorized

translation stage (igus®) to allow for adjustment of optical path length between the two arms of the interferometer. The stepper motor of the translation stage is controlled by a driver from Technosoft (iPOS3604/02). The control commands for forward -backward motion of the translation stage are sent to the iPOS3604/02 driver via a serial communication from the customized software hosted in the user PC. The maximum translation distance of the stage is 60 mm. Figure 2.7 illustrates the connections of the translation stage, the motor driver and the user PC.

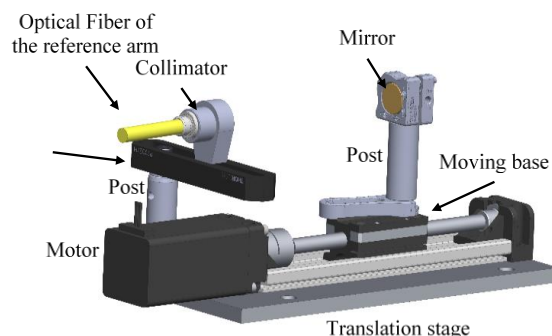


Figure 2.6 Components of the translation stage for the reference arm.

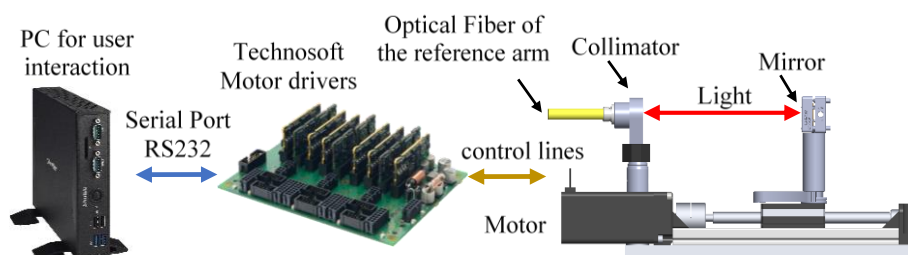


Figure 2.7 Translation stage of the reference arm and its connection with the motor driver and user PC.

2.1.3 Sample arm design

The sample arm in OCT is the portion of the light used to scan the sample that requires a specific optical design of the lens system to provide a focus length and a spot size according to the needs and imaging modalities. For this project two imaging modes are implemented, one called the Benchtop mode and the other one the Endoscopic catheter mode. The Benchtop mode is aimed for use in laboratory analysis for ex vivo correlation between histology and OCT images. It implements a linear scanning technique based on the dual axis galvo system (GVS002, Thorlabs) and the scan lens for laser scanning microscopy (LSM04, Thorlabs) as shown in Figure 2.8. More detailed description and calculation of the optical parameters are summarized in annex B.

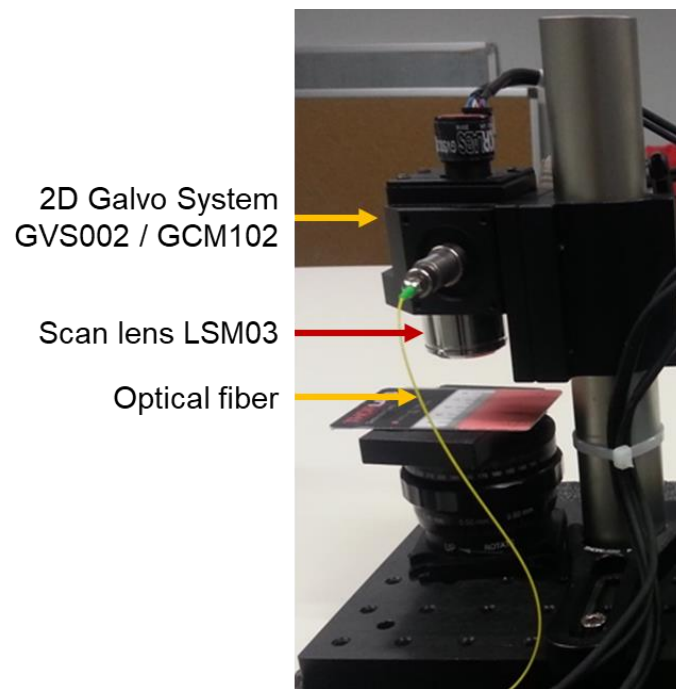


Figure 2.8 Thorlabs Galvo system for linear scanning in benchtop mode.

The Endoscopic catheter mode is aimed for use in real time imaging of the colon lumen to provide accurate diagnosis of diseases in the lower GI tract. It implements a customized ball lens attached to the tip of an optical fiber sheathed by a drive shaft to enable insertion through the surgical channel of the flexible endoscope, therefore making imaging of the internal section of the colon possible. The Endoscopic mode will be described in detail in Chapter 3.

2.2 Linear Scanning Synchronization

The OCT engine provides the light source, the photodetectors and the acquisition board and it is in charge of interpreting the collected signal from the optical probe. However, it does not know how many A-lines compose a B-scan which correspond to an image frame, and neither does it know which A-line is the first and the last one of each image frame. Therefore, synchronization is required between the scanning motions and the image acquisition to define the number of A-lines making up the image frame. The OCT engine has an input called *image_sync*, that works on rise edge detection and allows the defining of each image frame by generating two pulses to this input. When these pulses are provided, the OCT engine interprets that all the A-lines collected between these two pulses make up an image frame or B-scan. This means that each pulse indicates the end of the previous image frame and the beginning of the next one.

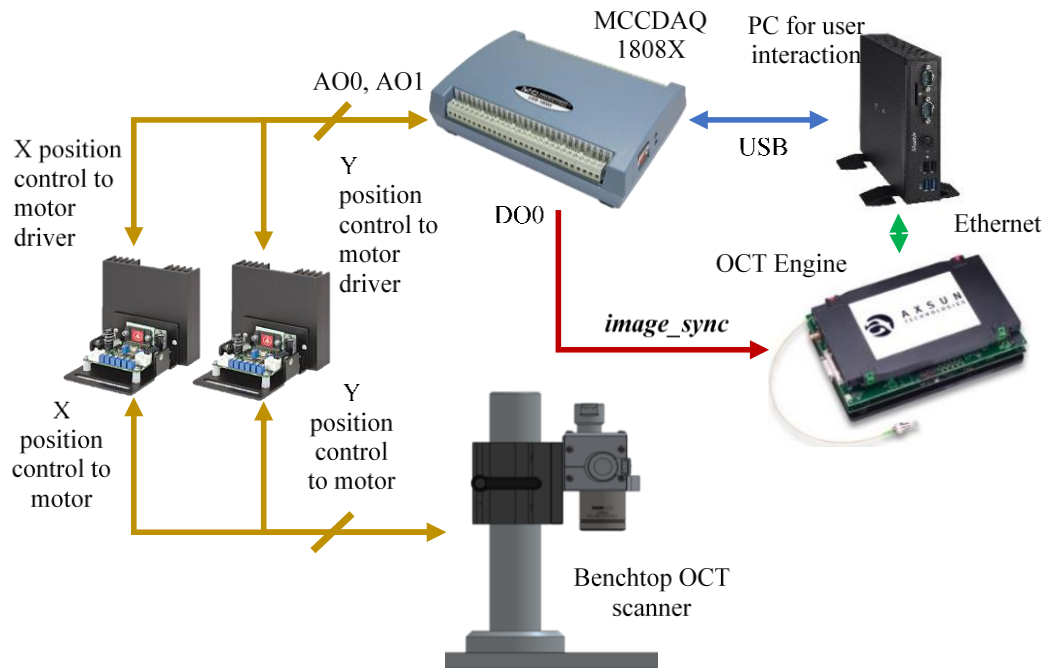


Figure 2.9 Electrical connection for control and communication of the Benchtop imaging system, motor drivers, MCCDAQ, AXSUN OCT engine and the PC for user interaction.

Figure 2.9 shows the elements involved in the linear scanning and the generation of the *image_sync* signal. In this case the galvo scanning system is used to perform the raster scanning consisting of two mirrors mounted on the shafts of two motors, the motor drivers and their power supply. The motor drivers have an analog input to generate the desired scanning pattern. The data acquisition board MCCDAQ USB-1808X is used to generate a sawtooth wave signal for each motor having the axis name of the galvo system. In this implementation the x-axis is used for the linear B-scan which has a faster sawtooth applied to it compared to that of the y-axis which is used for the 3D scanning and has a slower sawtooth applied to it. The frequency of the slow axis is a function of the number of B-scans (image frames) acquired and the frequency of the fast axis is a function of the number of A-lines acquired at the sampling rate of 100 kHz. Figure 2.10 shows a time diagram of the synchronization of the sawtooth signals for each axis and the *image_sync* signal required for the OCT engine to construct the image frames, in which it can be noticed that every image frame is defined on the zero-crossing of the signal on the fast axis. The three signals represented in Figure 2.10 are generated and synchronized by the MCCDAQ USB-1808X. They correspond to the acquisition of 600 image frames of 600 A-lines per frame, the frequency of the sawtooth signal on the fast axis being 166 Hz at 100 kHz A-line rate and a total acquisition time of 3600 ms for a 3D scan.

to protect the 2D scanner from going above this limit of frequency, the minimum of $N_s = 600$ samples for a maximum frequency of 166.67 Hz of sawtooth waveform has been set.

The frequency f_y for the y-axis is set accordingly to the frequency f_x of the x-axis and number of samples, which in the case of a round beam should be the same as in the x-axis:

$$N_Y = \frac{L_y}{\Delta y} \rightarrow \frac{14.1 \text{ mm}}{26 \mu\text{m}} \approx 542$$

The frequency f_y for the y-axis is computed as the ration between the frequency f_x of the x-axis and the B-scans N_Y to acquire; using maximum f_x and N_Y based on a spacing equal to $26 \mu\text{m}$ as computed above, then f_y is computed as below:

$$f_y = \frac{f_x}{N_Y} \rightarrow \frac{170 \text{ Hz}}{542} = 0.32 \text{ Hz}$$

Setting $f_y = 0.32 \text{ Hz}$, $f_x = 175 \text{ Hz}$ with $f_s = 100 \text{ kHz}$, the system acquires 542 frames of 600 samples per B-scan in the FOV of 14.1 mm x 14.1mm in 3 s. If a reduction in the 3D acquisition time is required while scanning the same FOV, then a larger B-scan spacing is necessary at the cost of acquiring less B-scan frames, and thus obtaining less information per acquisition. Therefore, there is a tradeoff between the number of samples and the acquisition time.

2.3 Human machine interface

The interaction between the user, the OCT engine and any external hardware (see Chapter 4 for integration with the robotized flexible endoscope) is performed by a special software developed in-house to acquire the OCT images, to provide synchronization of the electromechanical components and optical devices. The software is based on the OCT Control and Capture libraries provided by Axsun, Emgu CV .Net wrapper to the OpenCV image processing library and C# for the graphical interface. It also integrates the C# libraries provided by Measurement Computing for signal generation and synchronization of the MCCDAQ USB-1808X, and ImageJ is included with the software for offline image processing and data manipulation.

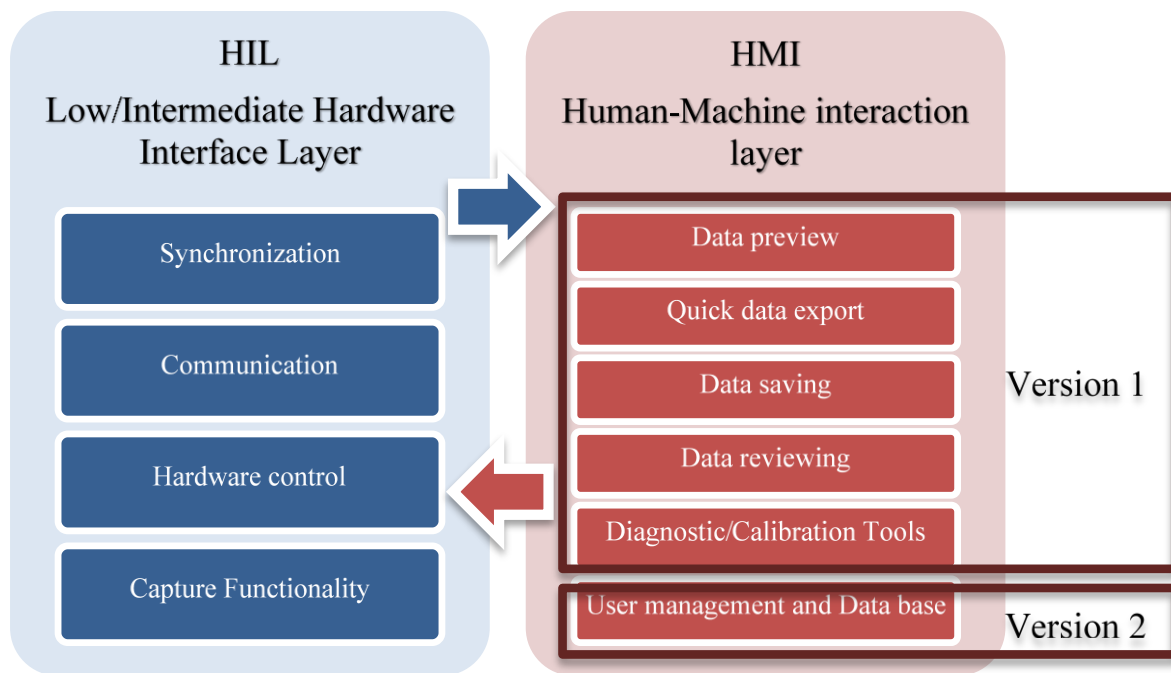


Figure 2.11 OCT software design and components.

The software has been developed and improved step by step, having begun with separate programs for the control and capturing capabilities. Afterwards, both programs were integrated to have all the control and capturing functionalities in the same application, as well as incorporating control of the motor drivers. The software was built in a bottom-top way starting from command line versions of the control and capture libraries, creating the main layers as the base of the program, then adding the graphical user interface feature for user-friendly utilization. Figure 2.11 shows the two main layers of the software. The Hardware Interface Layer oversees low level functionalities related to external hardware control, communication, synchronization, and data streaming from the OCT engine to the user PC and encloses all the driver software to interact with the external devices. On the other hand, the Human Machine Interface layer takes care of higher-level functionalities related to user interaction such as live data preview, data reports, data saving, data reviewing, diagnostic and calibration tools, user management and data base. The advantage of having this separation of layers is the possibility of modifying one layer independently without affecting the other one. For example, in the case of changing the MCCDAQ USB-1808X for another type of device, only the Hardware Interaction Layer needs to be modified to provide support for this new device without affecting the layer in charge of higher levels functionalities. It is important to

highlight that the software has been in constant modification according to the different needs that emerged as the project progressed.

2.4 Characterization and optimization

Two of the most important parameters that are used to describe an imaging system for biomedical applications are the signal to noise ratio (SNR) and the sensitivity. Both terms are used interchangeably, SNR denoting the ratio of the detected signal after photocurrent transformation to the root mean square of the noise, and sensitivity referring to the minimum detectable optical power with respect to a perfect reflector and expressed in decibel units [281]. One of the main challenges of OCT imaging in biomedical applications is the weak signal returning to the imaging system [282]. Given the fact that a medical imaging system must fulfill safety requirements describing allowed tissue exposure it is important to assure high detection efficiency by optimization of the system. As explained in this section, there are several sources of noise that affects SNR in OCT systems, so that their understanding is important for optimization of the system to achieve the best sensitivity.

2.4.1 Signal to noise ratio modelling

The Signal-to-Noise Ratio in an OCT system is defined in two principle ways in the literature [283], the first definition being given as in Eq. 2.4,

$$SNR = \left(\frac{i_g}{\sigma_i}\right)^2 \quad \text{Eq. 2.4}$$

where i_g is the electric current of the signal in the detector due to the photoelectric transformation, and σ_i is the root mean square (RMS) of the noise current [283]. The second definition is the ratio of 100% of the back-scattered light in a sample that is perfectly reflective and the minimum detectable back-scattered light, expressed in Eq. 2.5.

$$SNR = \frac{1}{R_{min}} \quad \text{Eq. 2.5}$$

From Eq. 2.4 the peak value of the interference signal is expressed as in Eq. 2.6:

$$i_g = \frac{\eta e}{h\nu_0} \sqrt{2P_R P_S} \quad \text{Eq. 2.6}$$

where η is the quantum efficiency of the detector, e is the electronic charge, h is the Planck's constant, ν_0 is the mean frequency of the incident light, and P_R , P_S are the optical powers detected from the reference and sample arm.

The RMS of the noise can be described as:

$$\sigma_i^2 = \langle \Delta i_{sh}^2 \rangle + \langle \Delta i_{ex}^2 \rangle + \langle \Delta i_{th}^2 \rangle \tag{Eq. 2.7}$$

where $\langle \Delta i_{sh}^2 \rangle$ is the shot noise, and represents the optimal operation point for OCT systems since the SNR is proportional to the signal power, $\langle \Delta i_{ex}^2 \rangle$ is the excess photon noise for the case where the power in the photodetector is too high and the SNR depends on the frequency bandwidth of the detector, and $\langle \Delta i_{th}^2 \rangle$ is the thermal noise for the case of low power from the reference arm. In references [283] and [280] are described the mathematical expressions to compute each of the noise contributions in Eq. 2.7, such as the relation of the SNR between time domain OCT (TD-OCT) and swept source OCT (SSOCT) in [284]. Following the same principle, the curve of the total SNR with respect to the power in reference arm has been plotted in Figure 2.12.

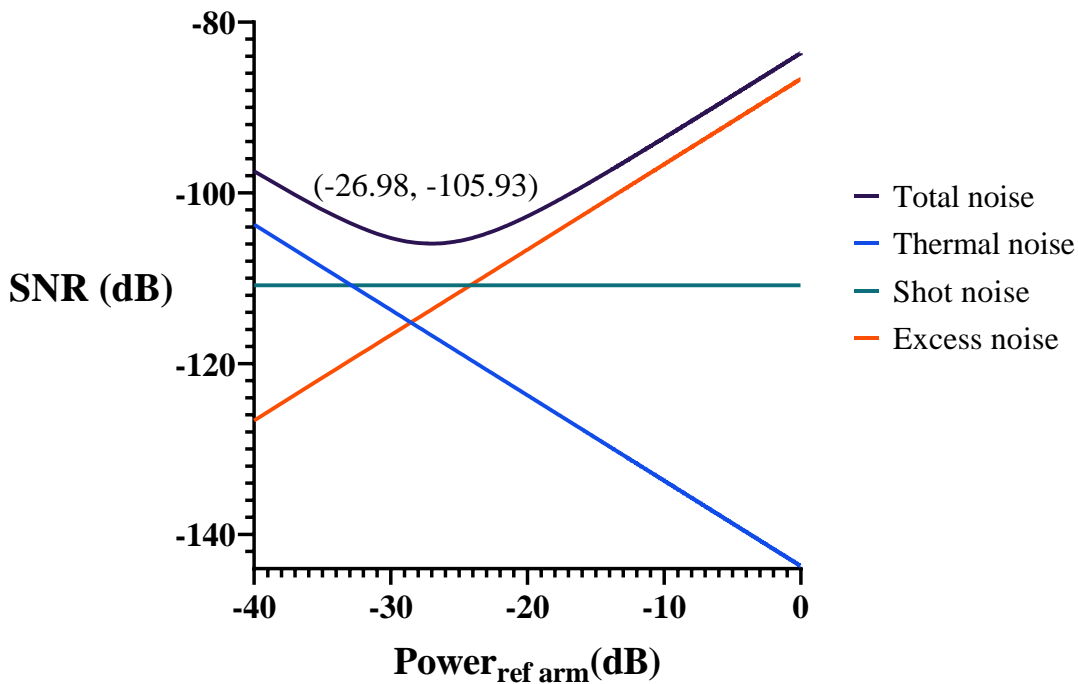


Figure 2.12 SNR vs. Reference Power.

Figure 2.12 shows the characteristic curves that describe the changes of the SNR as a function of varying the optical power in the reference arm from high to low values. It can be

noticed that for high values of power in the reference arm the excess noise dominates and the SNR decreases, whereas for lower values of reference power, the thermal noise is dominant, and the SNR also decreases. The optimal value of the reference power where the sensitivity of the OCT system is maximum (-105.93 dB) corresponds to an optical power in the reference arm where the shot noise is dominant.

2.4.2 Signal to noise measurements and optimization

The first approximation of the optimal operation point of the OCT system developed in this project was found experimentally using the following principle. First a mirror was placed as an object in the sample arm as a perfectly reflecting sample. This mirror and the mirror of the reference arm were orientated to reflect the maximum power to the detector, so that the detectors were saturated. The power in the sample arm was then reduced using a neutral density filter with OD 3 and an attenuation of 33 dB to decrease the optical power below the saturation point. By keeping the reference power at its maximum, the information of the peak of the signal and the variance of the noise are obtained to compute the SNR_{max} using Eq. 2.8 from [285]:

$$SNR_{max}(dB) = 20 \cdot \log\left(\frac{i_g}{\sigma_i}\right) - 10 \cdot \log(R_s T_{filt}^2) \quad \text{Eq. 2.8}$$

where the right term represents the attenuation in the sample arm. The reference power is then attenuated by using a neutral density filter with OD 3 and the value of the SNR is computed again for the new value of the peak of the signal and the variance of the noise. The layout of the experimental setup is shown in Figure 2.13. The process was repeated several times to reproduce the curve in Figure 2.12 so as to find the optimal operation point of the OCT system. The results of this experiment are plotted in Figure 2.14. The maximum value of the sensitivity obtained is -97 dB with an attenuation of -32 dB in the reference power.

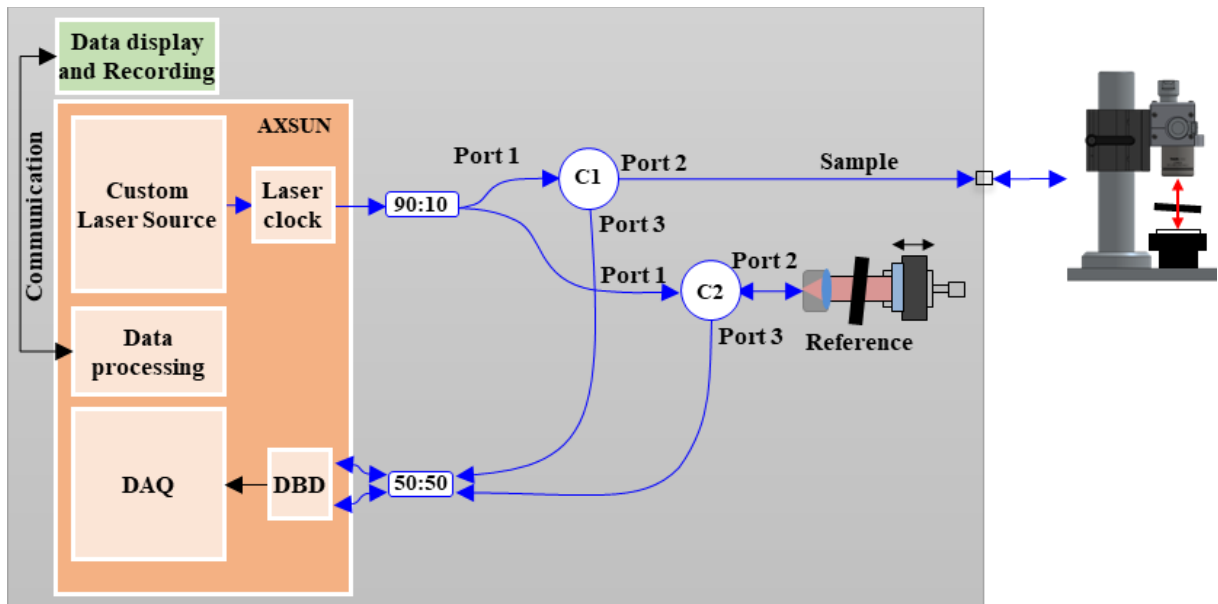


Figure 2.13 Experimental setup for SNR optimization.

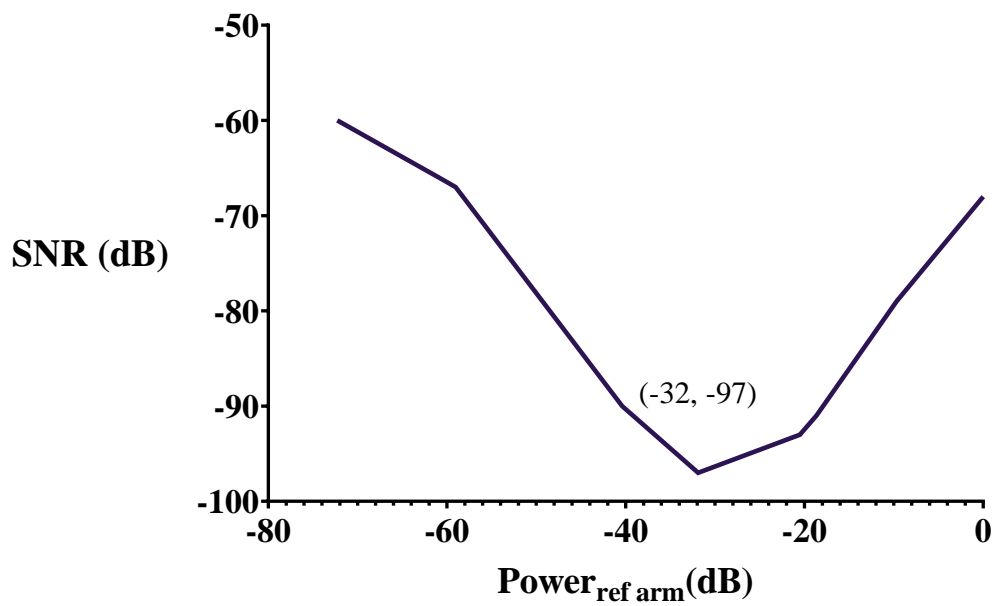
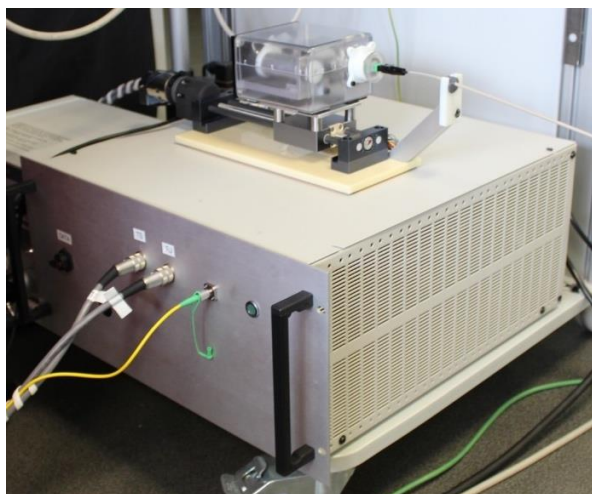


Figure 2.14 Power of the reference arm vs. the sensitivity.

2.5 Experimental validation

Figure 2.15(A) shows a picture of the developed OCT imaging console. On the front panel of the box a yellow optical fiber can be connected to either the Benchtop or Endoscopic scanning arms. A rotation-translation mechanism for the Endoscopic mode that can be seen on top of the system will be described in detail in the next Chapter. All the components described in section 2 are enclosed in this box: the OCT engine, the interferometer, the motor drivers, and the power supply. Figure 2.15(B) shows the portability of the system.

An initial evaluation of the imaging performance of the OCT-IC system was carried out by obtaining OCT images of the human skin as shown in Figure 2.16. A typical OCT cross-section of an index finger can be seen with the skin surface, the sweat ducts, the epidermis and dermis clearly distinguishable. The image scale is shown in the right corner for the x direction, and for the z direction it is represented by 1.5 mm of penetration depth from the skin surface of the finger. The field of view for this image is $13 \times 13 \text{ mm}^2$, the axial and lateral resolution are $7.56 \text{ }\mu\text{m}$ and $26.32 \text{ }\mu\text{m}$ respectively and the A-line rate is 100 kHz. Figure 2.17 shows an en-face view and a 3D reconstruction from a set of B-scans acquired over 13 mm of the finger achieved in 5.3 seconds.



(A)



(B)

Figure 2.15 OCT imaging console OCT-IC.

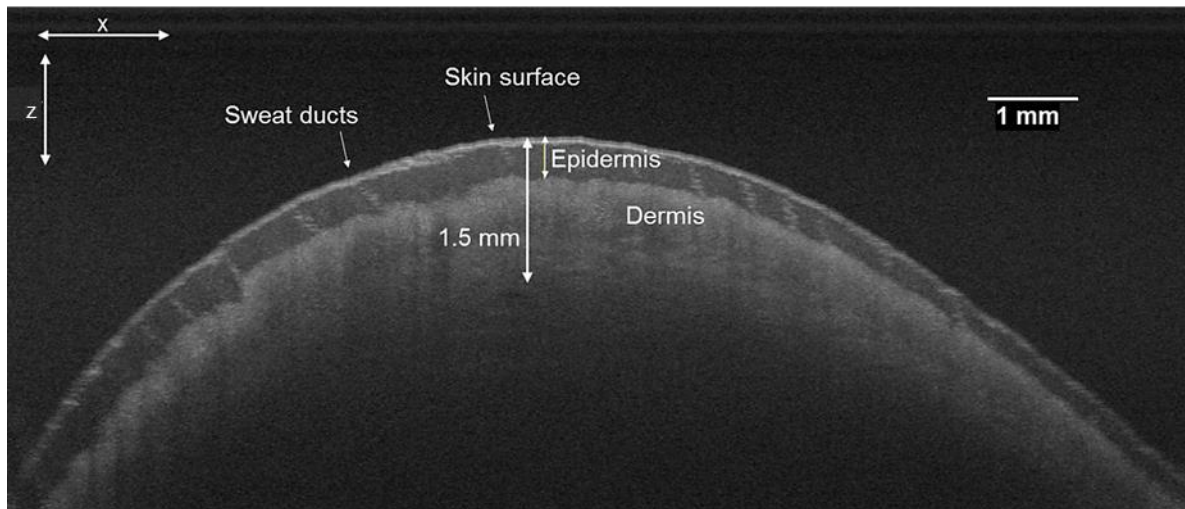


Figure 2.16 Axial view of the index finger, with 13 mm field of view, 1.5 mm of penetration depth, $26.32\ \mu\text{m}$ for the lateral resolution and $7.56\ \mu\text{m}$ for the axial resolution, A-line 100 kHz and B-scan rate of 138 fps.

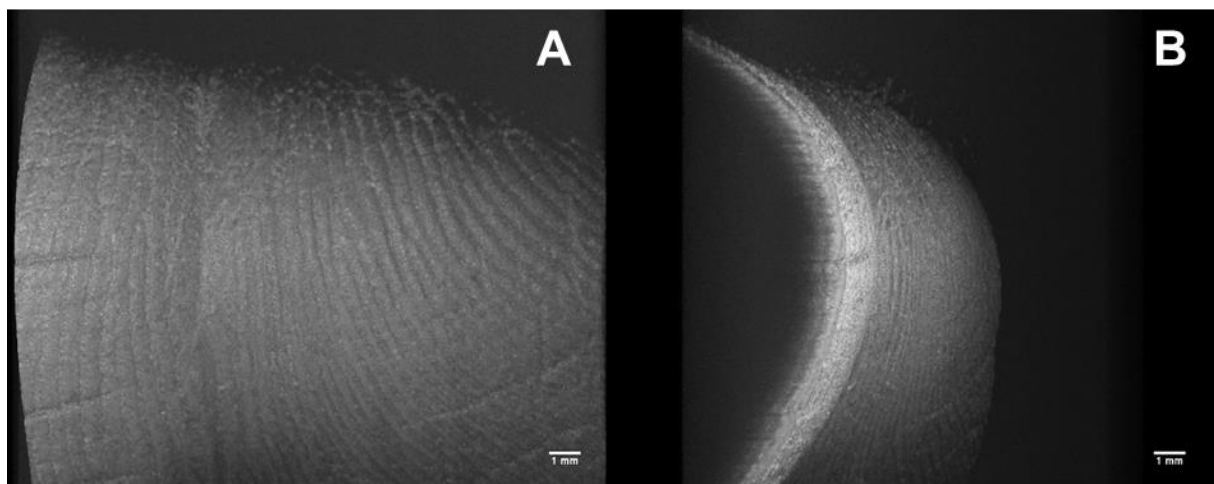


Figure 2.17 Two different views of the 3D OCT image reconstruction of the index finger of Figure 2.16.

2.6 Conclusions of the chapter

The first stage of the project was to build the OCT imaging console (OCT-IC) for acquisition and processing of the OCT data. The OCT-IC has been developed to support two imaging modes: the benchtop mode for ex vivo analysis of samples and the endoscopic mode for in vivo imaging of the lower GI tract. The design of the interferometer has been described; the sample arm compatible with the two modalities has been made by matching the length of the optical path, such as the required software-hardware to provide linear scanning and synchronization of B-scans and 3D scanning. A human-machine interface was developed, and the SNR was characterized, giving -97dB of sensitivity. The OCT imaging performance was verified by imaging the skin of an index finger.

2.7 French summary of the chapter

Système d'imagerie OCT pour l'examen préclinique

La console d'imagerie OCT(OCT-IC) est un système OCT à source balayée de haute technologie. En plus des composants optiques chargés de la génération de la lumière et de l'interféromètre, elle est également l'unité de traitement principale chargée d'acquérir le signal collecté par la sonde optique pour interprétation, de construire le cadre de l'image, d'assurer le contrôle des deux modes de numérisation mis en œuvre, et de transmettre et d'afficher les informations à l'utilisateur. Les principaux défis associés à ce système sont le support des modes microscopiques et endoscopiques dans un style *plug-and-play*, la compatibilité avec l'utilisation en clinique et la conception de logiciels et de matériel permettant l'implantation dans un système robotisé et téléopéré. L'OCT-IC se compose du moteur OCT, de l'interféromètre, du bras d'échantillonnage, du bras de référence et de l'interface homme-machine. Le moteur Axsun OCT avec une longueur d'onde de 1300 nm, une plage d'accord de 133 nm et une puissance optique de 27 mW a été choisi pour assurer une pénétration des tissus de 1 à 2 mm. L'interféromètre Mach-Zehnder avec une source de lumière à faible cohérence a été mis en œuvre en intégrant la détection de la diversité de polarisation afin de compenser les décalages de polarisation. La double modalité a été mise en œuvre en réglant la longueur du trajet du bras de référence à une valeur égale pour les deux modes de bras d'échantillonnage. L'interface homme-machine est le logiciel permettant le contrôle et la visualisation de la console d'imagerie OCT.

Caractérisation

Parmi les paramètres qui sont utilisés pour décrire un système d'imagerie pour des applications biomédicales, les plus importants sont le rapport signal/bruit (SNR) et la sensibilité. SNR désigne le rapport du signal détecté après transformation de la photo courant à la moyenne quadratique du bruit, et la sensibilité se rapporte à la puissance optique minimale détectable par rapport à un réflecteur parfait et exprimée en décibels.

$$\text{SNR} = \left(\frac{i_g}{\sigma_i}\right)^2$$

$$\text{Sensibilité} = \frac{1}{R_{min}}$$

L'approximation du point de fonctionnement optimal du système OCT développé dans ce projet a été réalisée en plaçant d'abord un miroir dans le bras d'échantillonnage en tant qu'échantillon parfaitement réfléchissant. Ce miroir et le miroir du bras de référence étaient orientés de manière à refléter la puissance maximale du détecteur, de sorte que les détecteurs étaient saturés. La puissance dans le bras d'échantillonnage a ensuite été réduite à l'aide d'un filtre à densité neutre avec une densité optique (OD) de 3 et une atténuation de 33 dB pour diminuer la puissance optique en dessous du point de saturation. En maintenant la puissance de référence à son maximum, l'information est obtenue à partir du pic du signal et de la variance du bruit pour calculer la SNR_{max} comme suit :

$$\text{SNR}_{max}(dB) = 20 \cdot \log\left(\frac{i_g}{\sigma_i}\right) - 10 \cdot \log(R_s T_{filt}^2)$$

Où le terme de droite représente l'atténuation dans le bras de l'échantillon. La puissance de référence est alors atténuée en utilisant un filtre à densité neutre de densité OD 3 et la valeur du SNR est calculée à nouveau pour la nouvelle valeur du pic du signal et la variance du bruit. Le processus a été répété plusieurs fois pour trouver le point de fonctionnement optimal du système TCO. La valeur optimale de la sensibilité obtenue est de -97 dB avec une atténuation de -32 dB dans la puissance de référence.

Évaluation expérimentale

Une première évaluation de la performance d'imagerie du système OCT-IC a été effectuée en obtenant des images OCT de la peau humaine. Une coupe transversale typique du doigt index a été imagée, où il est possible d'observer la surface de la peau, les canaux

sudoripares, l'épiderme et le derme. Une profondeur de pénétration d'environ 1,5 mm a été obtenue à partir de la surface de la peau du doigt. Le champ de vision pour cette image est de 13x13 mm², les résolutions axiale et latérale sont 7,56 µm et 26,32 µm respectivement et la fréquence de la ligne A est de 100 kHz. Nous présentons une vue en face et une reconstruction 3D d'un ensemble de scans B acquis sur 13 mm du doigt réalisée en 5,3 secondes.

Conclusions du chapitre

La première étape du projet consistait à construire la console d'imagerie OCT (OCT-IC) pour l'acquisition et le traitement des données OCT. L'OCT-IC a été développé pour supporter deux modes d'imagerie : le mode *benchtop* pour l'analyse ex vivo des échantillons et le mode endoscopique pour l'imagerie in vivo du tractus gastro-intestinal inférieur. Nous avons décrit la conception de l'interféromètre ; le bras d'échantillonnage compatible avec les deux modalités a été réalisé en faisant correspondre la longueur du trajet optique, par exemple dans le matériel-logiciel nécessaire pour assurer la numérisation linéaire et la synchronisation des numérisations B et 3D. Une interface homme-machine a été développée, et le SNR a été caractérisé, donnant une sensibilité de -97 dB. La performance d'imagerie de l'OCT a été vérifiée par l'imagerie de la peau d'un index.

Chapter 3

Novel steerable OCT instrument for flexible endoscopy

Content

3.1 Optical probe	71
3.2 OCT 3D scanning actuation	74
3.2.1 Helical scanning concept	74
3.2.2 Proximal rotation and translation	76
3.2.3 Rotational Synchronization	77
3.2.4 Probe connection	79
3.3 Bending actuation	82
3.4 Characterization and optimization	85
3.4.1 Experimental setup and analysis	89
3.4.2 Two-dimensional rotational artifacts	92
3.4.3 Three-dimensional pullback artefacts	99
3.5 Experimental validation	103
3.6 Conclusions of the chapter	104
3.7 French summary of the chapter	105

Having detailed the imaging console in the previous chapter, now the robotized endoscopic OCT catheter is described. The first sections 3.1 to 3.2 explain how OCT is implemented as a conventional OCT catheter that can be introduced inside the human body using the working channel of a flexible endoscope intended for colonoscopy. In this way, OCT images can be taken from the interior of the colon by performing helical scanning. A conventional OCT catheter is a passive device, which means that it is manipulated by manually moving the entire endoscope, which is not an easy task due to the complex shape of the large intestine. Manual manipulation requires extensive training and experience of the clinician in colonoscopy procedures. Adding steerability to the OCT catheter and teleoperation capabilities facilitate its manipulation and reduces the learning curve for performing such procedures. These two steps take the conventional OCT catheter from being a passive device to an active OCT catheter that can be teleoperated. To achieve steerability, mechanical modification is added to the design in section 3.3 to provide bending capabilities to the distal end of the OCT catheter. Teleoperation is achieved by adding compatibility between the novel steerable OCT catheter and the robotized flexible endoscope described in 1.2.1. This compatibility is achieved by making the OCT catheter function as a teleoperated surgical instrument of the robotized flexible endoscope. Characterization and experimental validations are described in sections 3.4 to 3.5.

3.1 Optical probe

The optical probe consists of an optical fiber core with micro-optics, a protecting driveshaft and a proximal connector. The optical core consists of an angled polished ball lens welded onto a distal end of an optical SMF 28 fiber. The fiber has 125 μm of cladding diameter and a coating diameter of 250 μm . The lensed fiber was designed in Zemax and subcontracted for fabrication to IDIL [286]. The micro-lens is first manufactured at the end of the fiber and polished at an angle of 48° to side focus the light reflected by the polished side of the lens and acting as a mirror (Figure 3.1). The spherical shape of the lens focuses the light beam at a specific distance just beyond the transparent sheath. The probe has been designed to focus light to 1 mm outside of the sheath, which means that the highest quality images are obtained when the sample is in contact with the transparent sheath. Several lensed fibers with different working distances and spot sizes were made and are summarized in Table 3.1. Figure 3.1(A) shows an illustrative description of the lensed fiber with polished ball lens of radius R , length

spacer L, and the SMF 28 fiber core. Figure 3.1(B) shows the optical design with actual specifications and dimensions for the lensed fiber SER1800471 from Table 3.1.

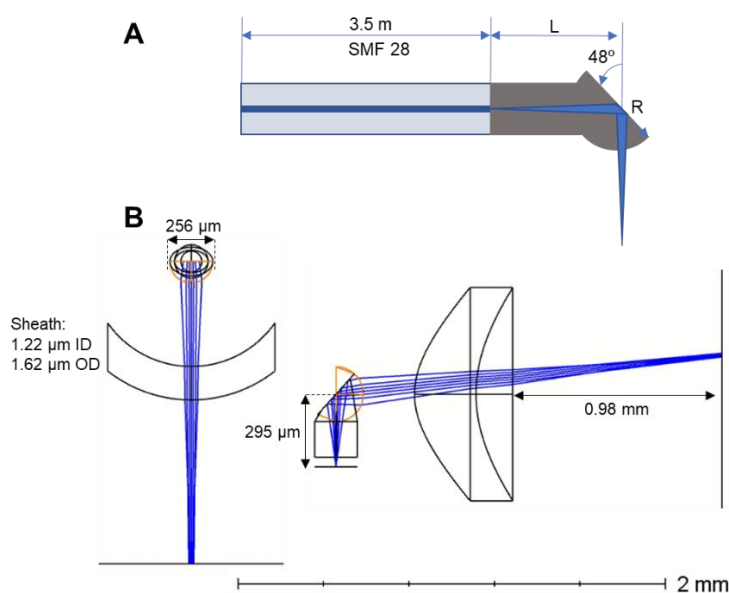


Figure 3.1 Lensed Fiber design. (A) Cross-sectional illustrated view of the lensed fiber. (B) Zemax specifications for the lensed fiber SER1800471 in Table 3.1.

Table 3.1 Parameters lensed fibers fabricated by IDIL Fibers Optiques.

Serie number	Length of the material (μm)	Measured spacer length L (μm)	Measured ball diameter (μm)	Ball radius R (μm)	Working distance from the sheath OD = 1.62 (mm)	Spot size (μm)
SER1800467	1018.00	271.00	255.00	127.50	1.28	40.00
SER1800468	1024.00	301.00	257.50	128.75	0.93	30.00
SER1800469	1020.00	286.00	259.50	129.75	1.30	40.00
SER1800470	1020.00	277.00	259.00	129.50	1.56	46.00
SER1800471	1033.00	295.00	256.50	128.25	0.98	33.00
SER1800472	1030.00	319.00	255.50	127.75	0.66	24.00
SER1800473	1030.00	319.00	259.50	129.75	0.74	26.00
SER1800474	1030.00	332.00	258.00	129.00	0.57	22.00

The optical core is inserted in the torque coil (Figure 3.2 (A)) to enable transmission of the torque for three-dimensional scanning, as explained in detail in section 3.2. The torque coil is 2500 mm long and was manufactured by Asahi Intecc. USA, Inc. [287] (further information is given in annex F). Once the ball lens was outside of the torque coil it was fixed in position with an epoxy (EPO-TEK[®] 730) as shown in Figure 3.2(B,C). Figure 3.2(C) shows the red-light beam from a test laser being reflected in the border of the ball lens. The room temperature curing EPO-TEK[®] 730 epoxy was chosen over the previously used EPO-TEK[®] 353ND-T that required higher temperature curing (see data sheets in annex F).

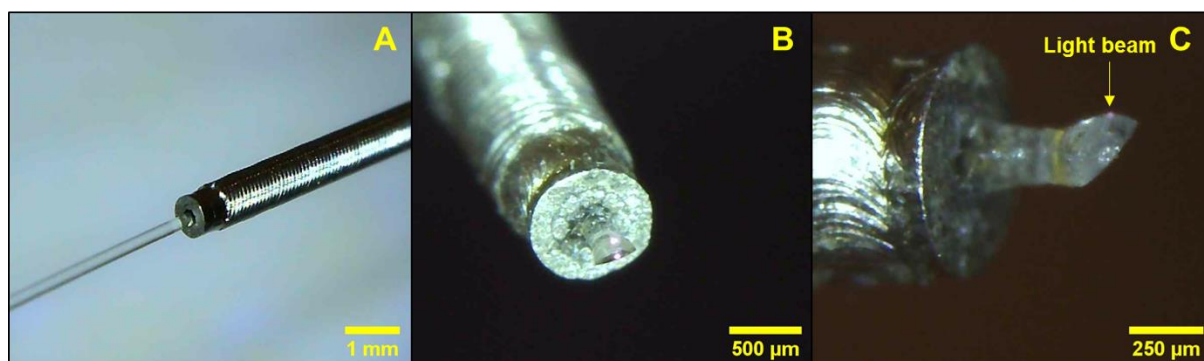


Figure 3.2 Assembly process of the optical probe. (A) The optical fiber core is inserted into the driveshaft. (B) The lensed is fixed just outside of the driveshaft. (C) Lateral view of the ball lensed showing reflected test light.

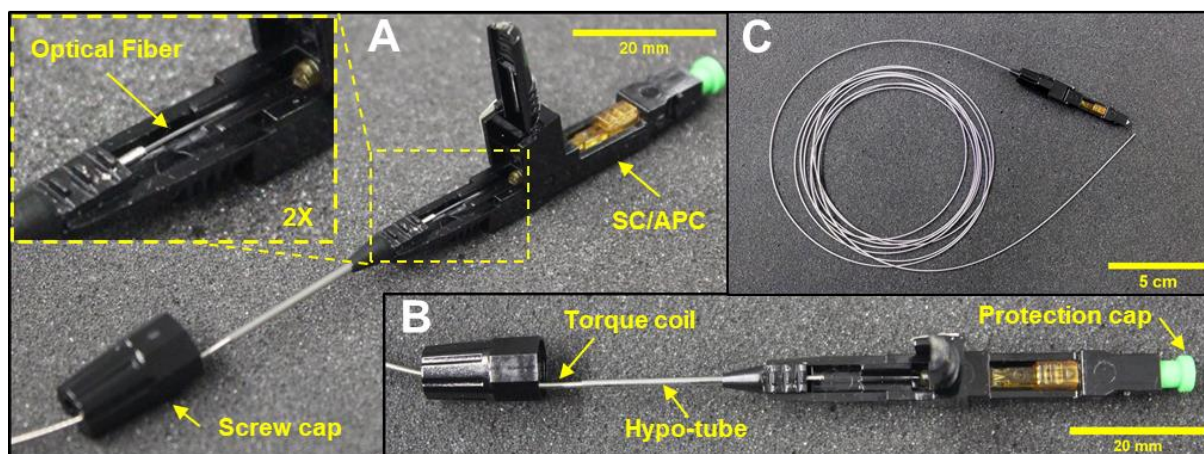


Figure 3.3 Assembly of the SC/APC fast mount proximal connector. (A) Optical fiber and torque coil placed into the SC/APC connector. (B) Hypo-tube covering the torque coil to avoid loops during rotation; green cap to protect the ferule of the connector. (C) Complete assembly of the optical probe.

In the next step the proximal end of the optical core was terminated with the SC/APC Type A single mode mechanical connector for fast and cheap assembly (FS.com) [287]. While probes are usually connected using a fiber splicer with a specialized connector and holder, in this case the use of mechanical connector enabled fast and low-cost probe termination without the need for specialized equipment. Figure 3.3(A) shows the connection of the optical fiber and torque coil with the SC/APC connector. Figure 3.3(B) shows a hypo-tube being placed between the tail of the SC/APC connector and the torque coil to add a rigid section to avoid loops being formed close to the connector. The optical fiber is attached to the torque coil with the EPO-TEK® 730 epoxy, as well as the torque coil to the hypo-tube. The green cap is a protection for

the ferule that is removed when the probe is used. The assembled optical probe is shown in Figure 3.3(C). The probe can be used in various designs of outer sheath depending on the clinical use.

The optical probe assembling process requires very high precision and 24 hours to assemble one probe given the time necessary for curing the epoxy. For the purpose of this thesis four optical cores (SER1800469, SER1800474, SER1800472, and SER1800473) were assembled into fully functioning optical probes. The probes with the first two cores were used to acquire OCT images presented in the following chapters. The rest of the optical cores from the Table 3.1 were damaged or suffered deterioration during the process of prototyping.

3.2 OCT 3D scanning actuation

The endoscopic catheter mode is designed to perform a volumetric scanning of a luminal organs (e.g. colon) by simultaneous rotational and translational motions of the optical probe and creating a helical scan. To achieve this motion, a custom electro-opto-mechanical system for proximal actuation was built to provide rotational motion at different speeds and translations at different displacements. The actuator consists of the fiber optic rotary joint (FORJ) to couple a static optical fiber that transmits the light from the OCT imaging console with the rotating OCT fiber probe. The probe is connected to the actuator with a custom connector and a telescopic segment that accommodates for the pullback of the probe. The synchronization of the mechanical system and image acquisition is achieved using an optical sensor.

3.2.1 Helical scanning concept

The scanning method used with the OCT catheter implements rotational motion of the optical probe to acquire radial B-scans, so that the frame rate is defined by the speed of rotation of the optical probe. In the case of 3D scanning, in addition to the rotation, the probe is pulled back using a translation stage, see Figure 3.4. The Axsun OCT engine implements a sampling rate of 100 kHz allowing acquisition of one axial scanning (A-line) every $10 \mu s$. The sampling rate of the OCT engine and the speed of rotation limit the number of samples acquired per B-scan. For example, if the rotation speed $v = 6000 \text{ rpm}$, then the frame rate $f_r = \frac{v}{60} \rightarrow 100 \text{ fps}$, so that the number of samples $N_s = \frac{f_s}{f_r} \rightarrow 1000$. In rotational scanning, similarly to the galvo system, N_s is defined based on the lateral resolution of the optical probe and the

required radial field of view. As described in section 2.1.3, the lateral resolution is computed as: $\Delta x_{FWHM} = \frac{0.59 \times d}{2}$, where d is the spot size. For the case of the probes SER1800469 and

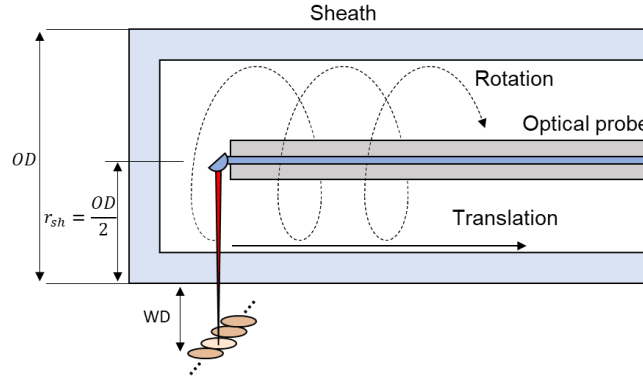


Figure 3.4 Helical scanning implements rotational and translational motions.

SER1800474 from Table 3.1 with spot sizes of $40 \mu m$ and $22 \mu m$ respectively, lateral resolutions are computed as: $11.8 \mu m$ and $6.5 \mu m$. The working distances WD for each probe are $1.3 mm$ and $0.57 mm$. The radial field of view is estimated as the circumference with a radius equal to the working distance plus the outer radius of the sheath $r_{sh} = \frac{OD}{2} \rightarrow 0.81$ (Figure 3.4). Therefore $FOV = 2\pi(r_{sh} + WD)$, which for each probe can be calculated as $13.26 mm$ and $8.67 mm$ respectively. Given the equation $N_s = \frac{FOV}{\Delta x_{FWHM}}$ the optimal number of samples per acquisition can be calculated as 1123 samples for the probe SER1800469 and 1333 samples for the probe SER1800474. To achieve the right sampling of 1123 samples per B-scan the frame rate of $f_r = \frac{f_s}{N_s} \rightarrow 89 fps$ must be set with a speed of rotation $v = f_r \cdot 60 \rightarrow 5343 rpm$; and the frame rate of 75 fps with a rotation speed of 4501 rpm for the probe SER1800474 for an acquisition of 1333 samples per B-scan.

The speed of the pullback motion v_{pb} is a function of the translation length y divided by the pullback acquisition time t_{pb} , hence $v_{pb} = \frac{y}{t_{pb}}$. The acquisition time of the pullback motion is estimated as the number of B-scans N_B divided by the frame rate f_r , therefore $t_{pb} = \frac{N_B}{f_r}$. The number of B-scans is computed as the translation length divided by the desired spacing between B-scans frames, for which the optimal spacing is equal to the lateral resolution such that $N_B = \frac{y}{\Delta x_{FWHM}}$. For example, with the pullback length of $20 mm$, $N_B = 1739$ B-scans when working with the probe SER1800469, and $N_B = 3076$ B-scans for the case of the probe

SER1800474. The pullback acquisition time t_{pb} is 19.54 and 41 ms correspondingly. Therefore, the speed of the pullback motions v_{pb} are 1 mm/s and 0.5 mm/s respectively. In gastrointestinal applications such as imaging of the esophagus, the spacing of 40 to 50 μm is typically used. Table 3.2 shows compiled parameters of the balloon [288][289], capsule [185],[290] and low-profile [291] OCT catheters found in the literature. Low-profile refers to smaller sheath diameters compatible with endoscopic working channels.

Table 3.2 Comparison table of different types of OCT catheters.

Parameters	Balloon	Capsule	Low-profile
Axial resolution Δz (μm)	7	7	7
frame rate (fps)	20	20	20
N_s	4000	2048	4000
Balloon/capsule/sheath diameter OD (mm)	14, 17, 25	12.8	2.8
Lateral resolution Δx_{FWHM} (μm)	40	35	40
Pullback speed v_{pb} (mm/s)	3	variable	3
Spacing (μm)	50	150 + 131	50
Pullback length y (cm)	6	25	6
Pullback acquisition time t_{pb} (s)	20	58	20

3.2.2 Proximal rotation and translation

The custom proximal actuator is built around a commercially available fiber optic rotary joint (FORJ, Princetel) that couples a static optical fiber from the OCT imaging console to the rotating OCT fiber probe. Figure 3.5 shows the components of the 3D scanning actuator. Figure 3.5(A) shows the pulley wheel attached to the shaft of the motor that drives the FORJ. It also shows the rotational output of the FORJ to which the optical probe is connected. The static optical fiber that transmits the light from the laser source is shown in yellow, and the electrical control cables of the actuators in gray color. The white cover shown in Figure 3.5(A) protects the motor and connections of the translation stage and also serves as the base for the support of the telescopic segment (Figure 3.5(B)). Figure 3.5(B) shows a lateral view to better visualize the configuration on the translation stage in the base supporting the motor and FORJ that is placed on the carriage of the stage. The linear guides of the stage with a stroke of 150 mm are also shown. The encoder lines of the motor and the power source cables can be observed in this figure. The optical sensor circuit board (see annex F for electrical schematic) is placed on top of the base of the rotational output as shown in Figure 3.5(A). The close-up view in Figure 3.5(C) shows the optical sensor GP1A52LRJ00F from SHARP Corporation under the circuit

board aligned with a shutter made by 3D printing attached to the rotor of the FORJ. The belt coupling both pulley wheels of the FORJ and the motor is shown in this figure.

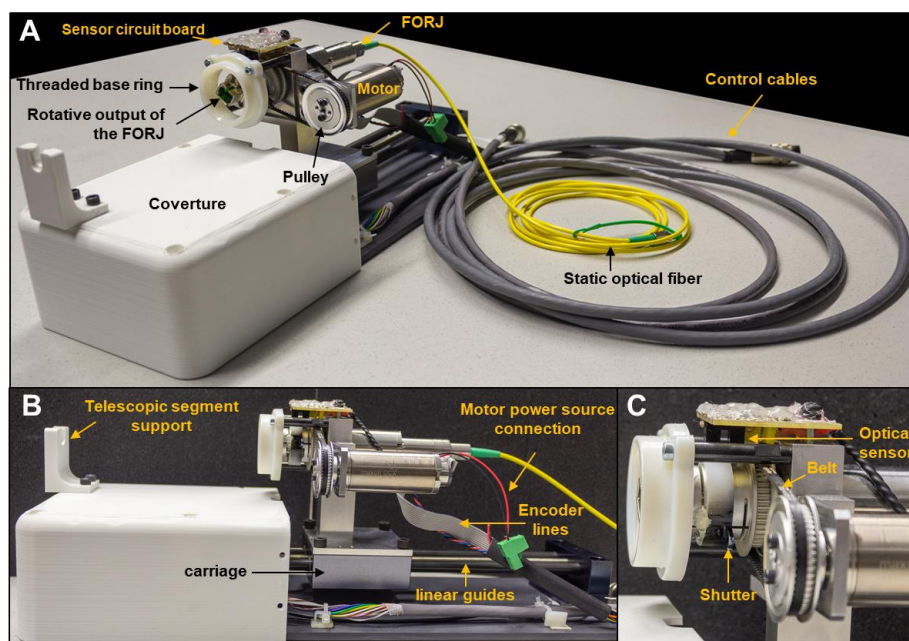


Figure 3.5 3D Components of the 3D scanner actuators with stroke length = 150 mm.

3.2.3 Rotational Synchronization

When rotation is produced with the motor to the FORJ, for every turn, the shutter interrupts the light of the LED of the optical sensor, so generating a high level pulse of 3.3 V in the output of the sensor that is used as the input image synchronization signal *image_sync* in the OCT engine. As in the case of the linear scanning in section 0, the pulse of this signal indicates the beginning of the A-lines acquisition and the end for creating the image frame.

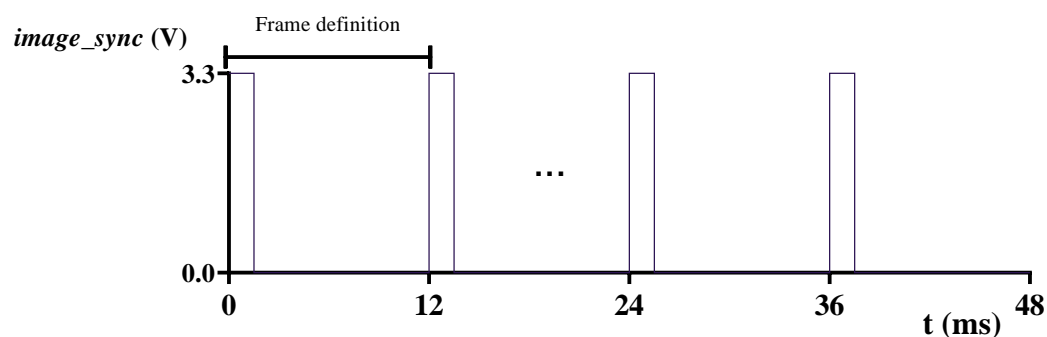


Figure 3.6 Synchronization of the Frame acquisition through the *image_sync* signal for endoscopic image.

Figure 3.6 illustrates the rotational synchronization. Since the frame is defined by every turn of the rotor of the FORJ as shown in Figure 3.5(C), therefore all the A-lines collected on each turn make up an image frame. The OCT engine has a fixed A-line rate of 100 kHz, which implies 10 μ s per A-line sample. The size of the acquired frames is related to the number of A-line samples collected for a given frame rate.

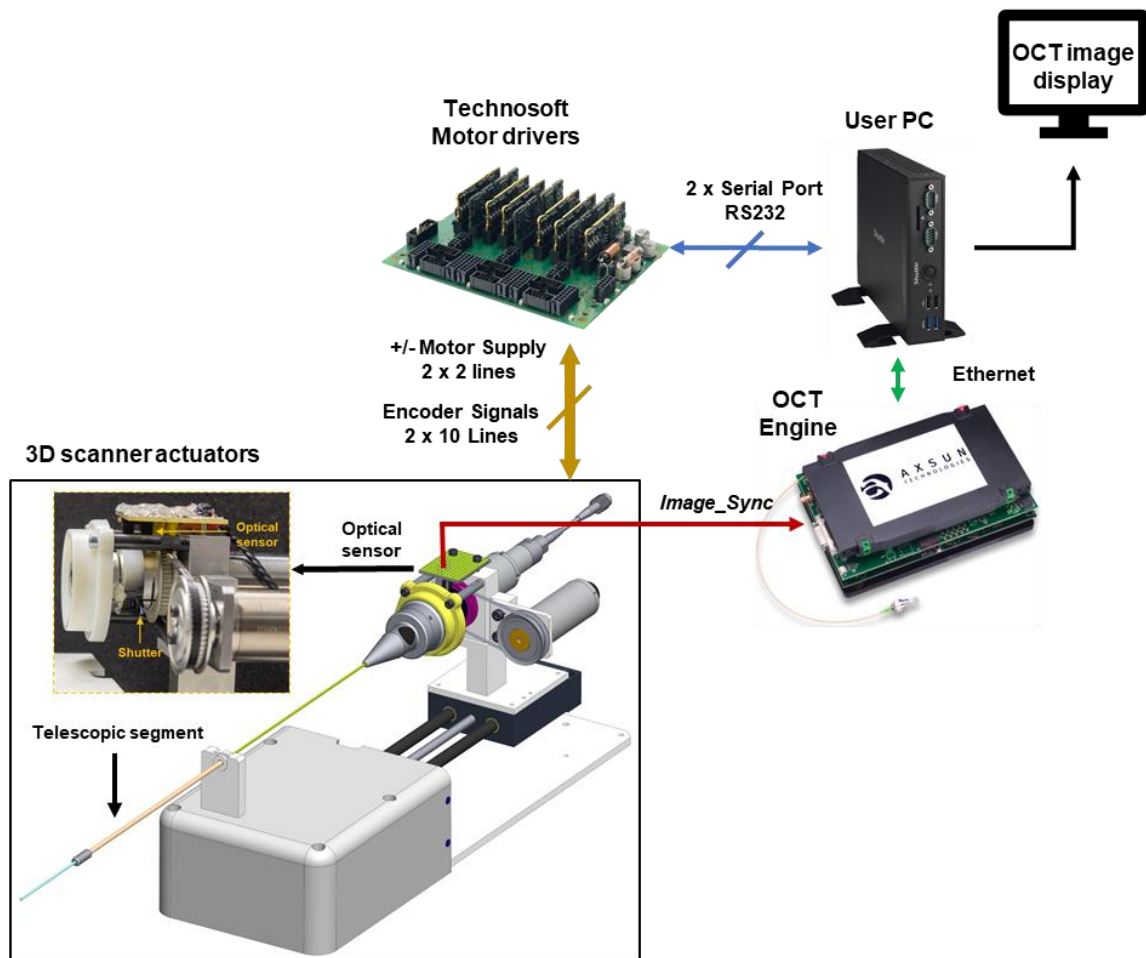


Figure 3.7 Electrical connection for control and communication of the endoscopic catheter, motor drivers, AXSUN OCT engine and the PC for user interaction.

The motors providing rotation and translation motion are driven in closed loop with a Technosoft controller driver. Figure 3.7 shows an electrical scheme of the interconnected devices related to the control and synchronization of the rotational scanning. The user PC provides access to start-stop scanning, display the information, etc. When the user PC sends the command to start scanning, the Technosoft devices drive the motors to the requested speed

and position. The OCT engine builds the image frame based on the *image_sync* synchronization signal pulses generated on the detection of each turn by the optical sensor, and then sends the image frames by streaming the information through the ethernet interface to the user PC for data displaying.

3.2.4 Probe connection

Because of the rotational scanning, the connector that plugs the optical probe to the actuator must allow free rotation of the probe. To enable connectivity of the probe with a custom catheter, a connector was created in a plug-and-play design. Figure 3.8(A) shows the parts making up the catheter connector. The C-type retaining ring is used to keep in place the ball bearing surrounding the outer SC/APC support as shown in Figure 3.8(B). The SC/APC connector of the probe is attached to the outer SC/APC support (3), and this support is attached to the ball bearing (2) which is held in place by the C-type retaining ring (Figure 3.8(B)). The green housing of the SC/APC connector is not used in the assembly of the probe, but instead is attached to the SC/APC support (3) to accommodate the SC/APC connector of the probe as in Figure 3.8(C). Finally, this assembly is inserted into the threaded outer shell (5) and the outer shell (6) to complete the catheter connector (Figure 3.8(D)).

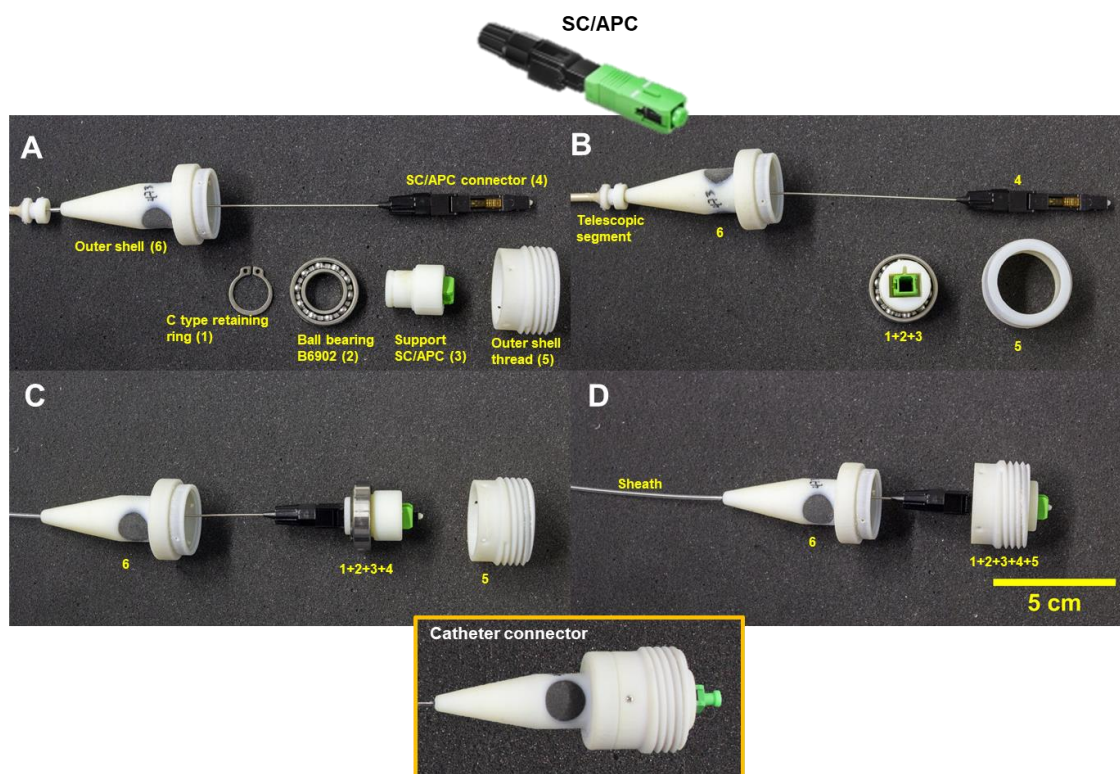
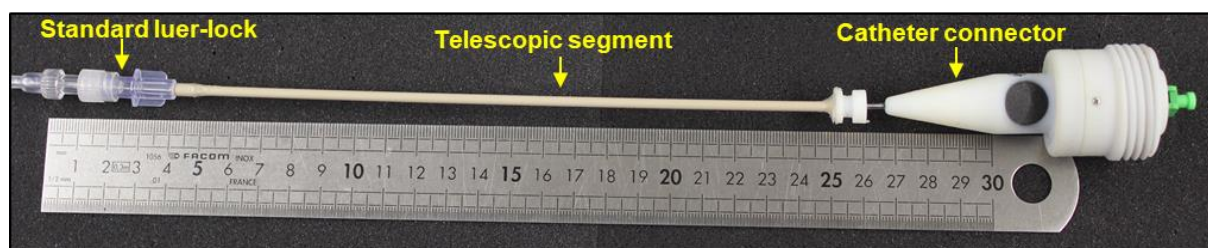
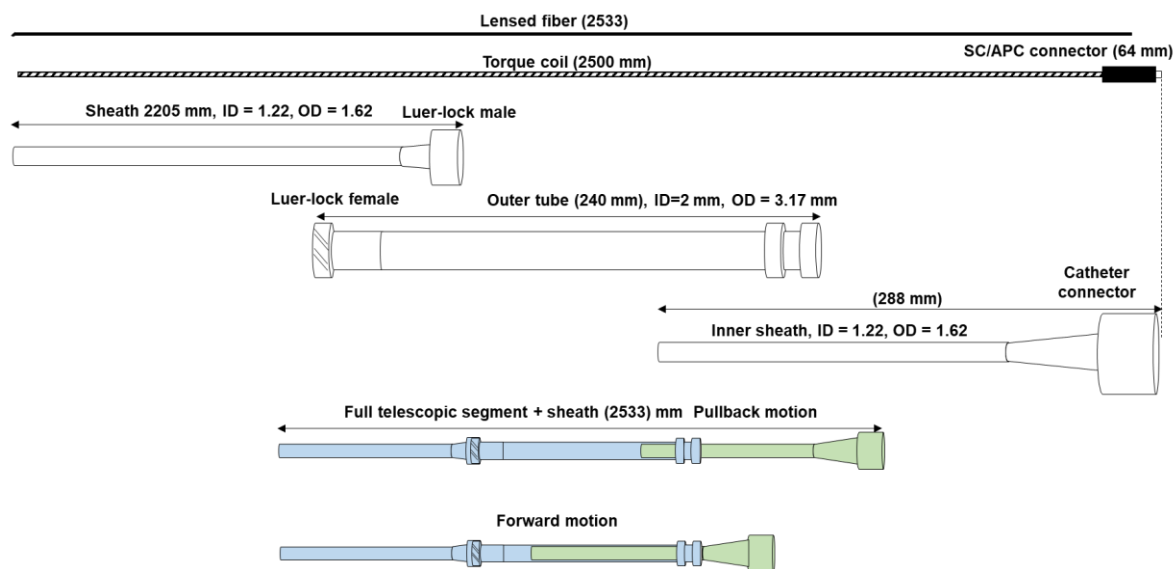


Figure 3.8 Catheter connector assembly.



(A)



(B)

Figure 3.9 Description of the telescopic segment and its internal components.

The output of the FORJ has the base ring on which the catheter connector is threaded to couple the OCT catheter with the 3D scanner actuators (Figure 3.5(A)) by threading the catheter connector from Figure 3.8(A) to the threaded base ring. In Figure 3.8(B, D) can be observed the support of the telescopic segment and the sheath attached to the catheter connector. The telescopic segment is described in detail in Figure 3.9. It allows the pullback motion of the optical probe while keeping the outer protection sheath of the OCT catheter static. Figure 3.9(A) shows a picture of the telescopic segment coupling the catheter connector (on the right) and the sheath (on the left). Figure 3.9(B) shows the description of the components making up the telescopic segment. The telescopic segment consists of two tubes: one inner sheath tube that has an inner diameter such that the optical probe can be threaded through it and the outer tube. This outer tube keeps the sheath attached with a standard luer-lock and static while allowing forward-pullback motion of the inner sheath fixed to the catheter connector

according to the motion provided by the translation stage. In Figure 3.9(B) the moving parts are represented in green color, and light blue refers to the static segments. The total length of the OCT catheter is 2533 mm. PEBAX material was used for the transparent sheath and the outer tube of the telescopic segment is made of PEEK material with an inner diameter $ID = 2\text{ mm}$ and outer diameter $OD = 3.17\text{ mm}$.

The optical probe consisting of the SC/APC connector, the optical fiber and the torque coil make up the whole length of the OCT catheter, while the sheath starts from the end of the outer tube of the telescopic segment. To test the optical performance of the optical probes they were inserted in a non-steerable plastic sheath. The outer diameter (OD) of 1.62 mm and 2.5 m length of the sheath, and thus the length of the optical core and the torque coil, were chosen to assure compatibility with the standard of care colonoscopes. The inner diameter was 1.22 mm to accommodate for the optical probe. The transparent sheath was made of Pebax 72D material for medical applications and fabricated by MS-Techniques [286]. The selection of the sheath's material is extremely important to assure high flexibility for passing the catheter through a working channel of the endoscope, while maintaining high durability to avoid kinking of the tether. The functionality of the sheath is to protect and to provide sealing to the optical probe and to connect its proximal end to the 3D scanner actuators.

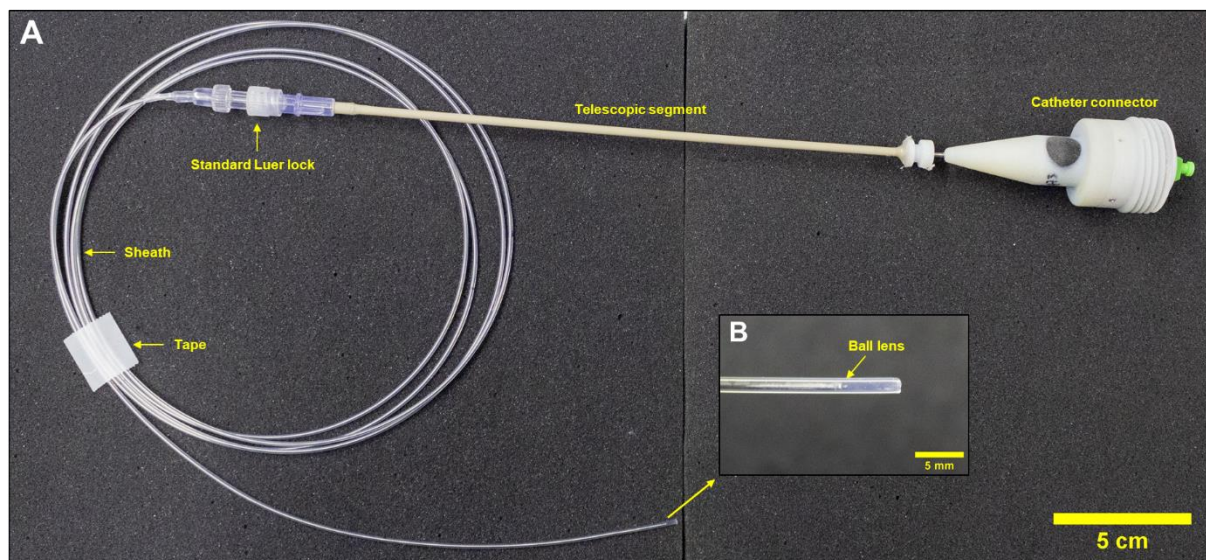


Figure 3.10 Non-steerable OCT catheter with proximal connector, telescopic segment and protecting sheath.

Figure 3.10(A) shows a picture of the non-steerable catheter which consists of the optical probe inserted into the catheter connector, the telescopic segment, the section of the sheath attached to the connector and the section of the sheath attached to the telescopic segment with a standard luer-lock. Figure 3.10(B) presents a picture of the distal end of the non-steerable catheter where the ball lens is visualized inside the sheath. The telescopic segment is used to perform translational motion of the probe while keeping the sheath static, which is important when performing 3D scanning. Further details are given in the next section that describes the 3D scanning actuator.

3.3 Bending actuation

To enable bending of the OCT catheter, an instrument designed for the Anubiscope™ interventional endoscope (Karl Storz) was used. The bending motion of the instruments is possible thanks to the 11 vertebrae at the distal end of the instrument's shaft driven by two antagonist tendons, which allows bending in both directions in one plane. The distal part is described in Figure 3.11.

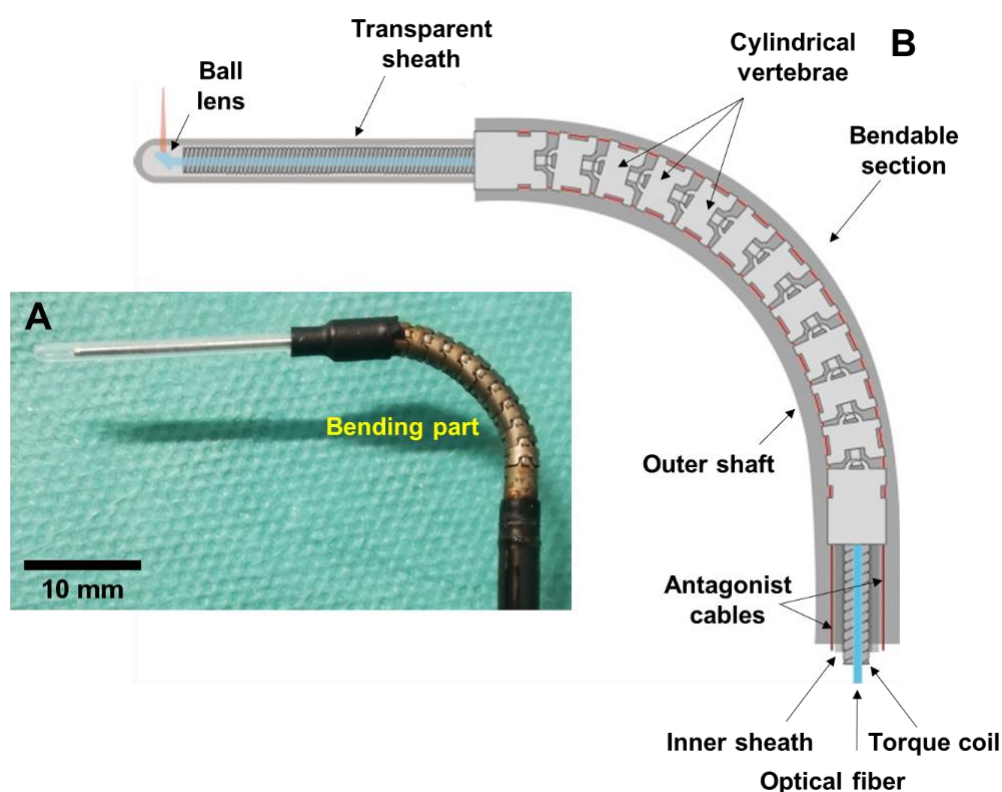


Figure 3.11 Picture of the distal bending section of the steerable OCT catheter (A). Descriptive drawing of the bending section (B).

The outer shaft in black color (Figure 3.11(A)) envelops the cylindrical vertebra mechanism with 11 links (in the picture the vertebra has been left exposed on purpose). The antagonist tendons are used to pull in both directions to provide the bending in one plane (Figure 3.11(B)). The bendable shaft is hollow to allow for insertion of different types of end-effectors, either a grasper or a hook for electrosurgery. The end-effector is inserted and attached by screwing at the distal tip. The instrument was modified to adapt for the insertion of the OCT probe and to allow the acquisition of images. The OCT probe dimensions were designed to assure compatibility with the inner diameter of the steerable shaft. Thus, in the first iteration, a transparent extension of the distal end of the bendable shaft was added to enable helical scanning of the tissue. The same transparent sheath (PEBAX) with $ID = 1.2\text{ mm}$ and $OD = 1.62\text{ mm}$ was used as for 3D actuation testing in section 3.2. A 10 cm long section of the sheath was cut off and a threaded ring was added for attaching to the bendable shaft. The length of the exposed distal sheath was then shortened to 20 mm to ensure that polyps larger than 10 mm in size could be imaged, corresponding to those with a risk of invasive carcinoma of 38.5 % [292].

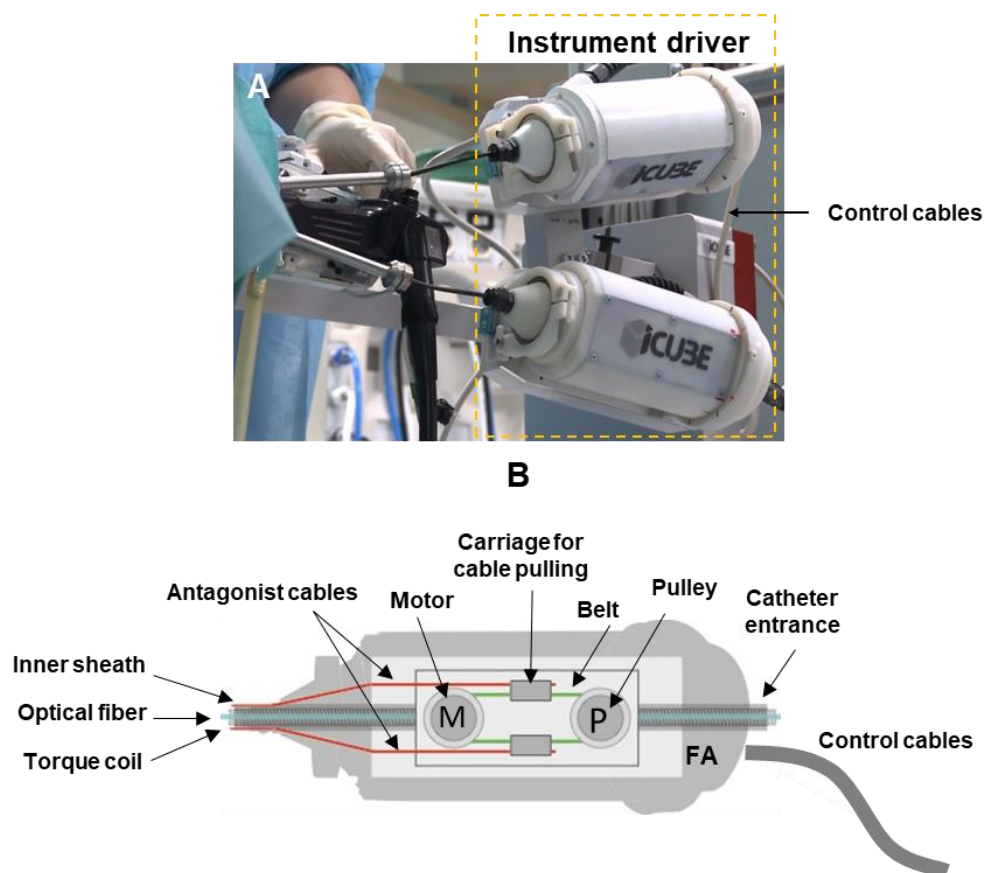


Figure 3.12 Instrument module to provide bending to the distal end of the catheter.

Bending of the steerable shaft is effectuated by an instrument module previously designed in the AVR team at the ICube Laboratory as shown in Figure 3.12(A) [98]. The instrument shaft is driven by the two tendons (Figure 3.12(B)) operated by the pulley-belt based motorized mechanism in the instrument module. This system is controlled by the master software of the robot, so that the user can steer the distal end of the instrument by actuating the flexion mechanism that pulls the tendons either to the left or to the right direction. The instrument module also includes the actuation of the grasper of the electrical components of the hook for electrosurgery. The steerable shaft tendons represented by antagonist cables in Figure 3.12(B) are directly attached to the carriage of the mechanism for cable pulling. The module is directly connected to the steerable shaft, which has a length of 850 mm. Because the designed optical probe as shown in this chapter is 2533 mm in length, which is longer than the 850 mm length of the steerable shaft, the actuator had to be modified. First components for the grasper actuation and electrosurgery hook were removed since they were not needed for the OCT probe. Then the end-effector insertion channel of the shaft originally terminated inside the module was extended by adding a transparent sheath threaded out through the back of the module to provide an access path through the instrument module to the instrument sheath (Figure 3.12(B)). The length of the proximal extension tube was chosen so that it could be directly connected using a luer-lock to the telescopic segment.

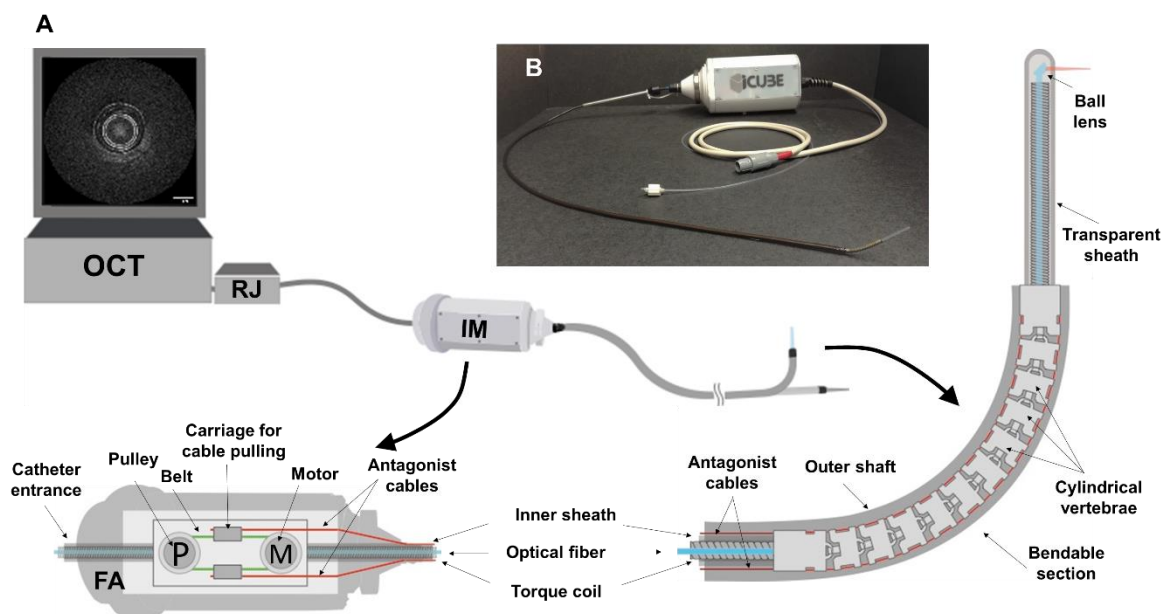


Figure 3.13 Description of the fully assembled steerable OCT catheter.

Following a number of experiments a second set of modifications was implemented. The proximal imaging cap, the inner sheath of the steerable shaft and the proximal extension sheath were eliminated and replaced by a single segment of the transparent sheath from the telescopic segment to the distal end. The sheath was extended beyond the distal end of the shaft and locked in position. The purpose was to provide uniformity of the channel to avoid extra friction added by the different junctions along the lumen of the catheter. The last modification consisted of changing the transparent sheath for one with a smaller inner diameter $ID = 1\text{ mm}$ and outer diameter $OD = 1.6\text{ mm}$. The purpose of this was to keep better centering of the probe ($OD = 0.9\text{ mm}$) with respect to the sheath.

Figure 3.13(A) shows a description of the fully assembled steerable OCT catheter capable of bending of the distal end in both directions in one plane. The OCT box in the figure represents the OCT imaging console in charge of processing the OCT data and controlling the 3D scanning actuators labeled as RJ. IM refers to the instrument module enclosing the bending actuator. The flexible and steerable shaft is connected to the output of the IM. The RJ and IM are connected by a segment of the transparent sheath. The full steerable OCT catheter is visualized in the picture shown in Figure 3.13(B). The steerable OCT catheter is an active device that incorporates a mechanism to perform bending motion, and therefore does not require moving of the endoscope to place the probe in the range of -60° to 90° , from the left to right sides. The reason for this difference in bending is due to the asymmetries in the tension of the cables acting as tendons, motor range and friction caused by the sheath of the tool.

3.4 Characterization and optimization

The endoscopic OCT catheter described in the previous sections implements proximal actuation and the torque coil to generate helical scanning by performing rotational-translational motion of the focusing optics at the distal end of the optical fiber. This system typically suffers from image artefacts that can cause deformation of the image and its rotation in time (precession). The artefact that is visualized as distortion of the image is usually due to non-uniform rotational distortion (NURD). This can be caused by: 1) mechanical friction between the torque coil and the outer sheath, 2) the variation of the motor speed and 3) transmission of the speed to the distal end of the optical probe by the torque coil [293]. The artefacts related to precession are usually visualized as random rotation of the image between frames during the three-dimensional pullback motion [294], [295]. Bending of the catheter and the pullback

motion of the fiber during scanning of the sample can contribute to an increase in the presence of both types of distortions. Figure 3.14 illustrates the problem of rotational distortion in which Figure 3.14(A) gives an example of computing the speed of rotation for optimal sampling of the field of view (FOV), this computation is based on the OCT sampling rate, the field of view and the spot size. Figure 3.14(C) describes the expected OCT image of a rectangular tube (Figure 3.14(B)) considering uniform rotation, while Figure 3.14(D) represents the deformation of the rectangular tube shape caused by non-uniform rotational distortion.

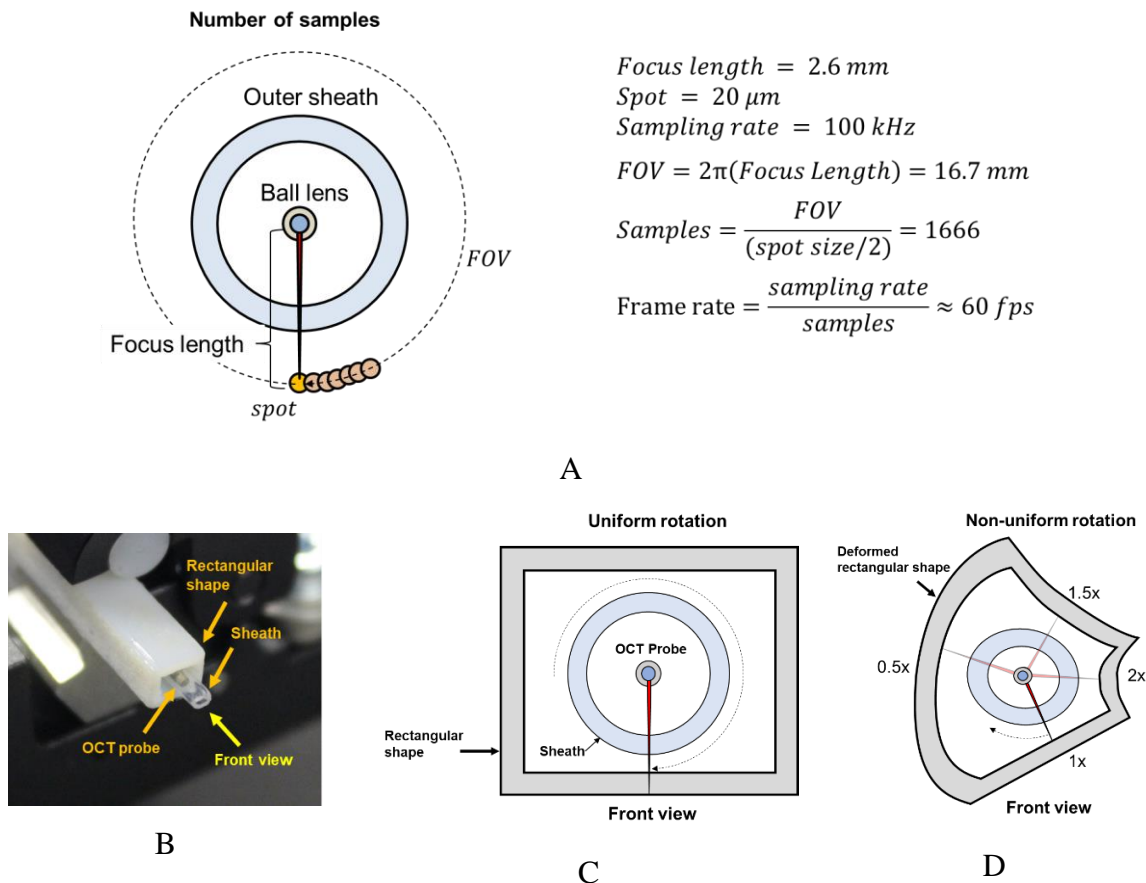


Figure 3.14 (A) Computation of the optimal number of samples for rotational scanning. (B) OCT catheter inside of a 3D printed rectangular tube. (C) Uniform rotation. (D) Non-uniform rotational distortion.

Figure 3.15(A) shows an example of two OCT images in which the speed of the rotation fluctuates during one full circle, having speed variations from 0.56 to 2.20 times the average speed of 1000 rpm (≈ 16.67 fps). Figure 3.15(B) displays an image obtained with the same catheter but with an average speed of 5000 rpm (≈ 83.33 fps) during which much lower variation between 0.95 and 1.06 times was observed that correspond to the uniform rotation

and reduced distortion. Increased or reduced variation of the distortion has been observed, as well, for other speeds of rotation. This observation was at the basis of the hypothesis that the NURD performance depends on the rotational speed and as such an optimal speed can be found depending on the design of the catheter.

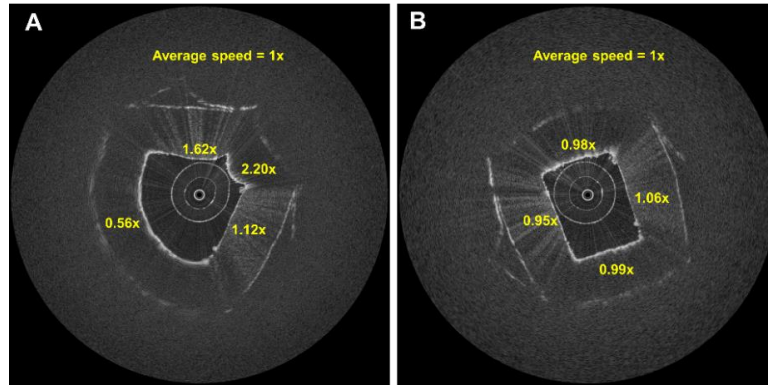


Figure 3.15 Non-uniform rotational distortion in OCT images, (A) image taken at the speed of 1000 rpm and (B) 5000 rpm.

The aforementioned hypothesis is particularly important since non-uniform rotational distortion is a known issue in endoscopic OCT catheters. However, for most of the endoscopic systems the rotational speed is chosen based on the optimal sampling rate (sections 2.2 and 3.2) and not NURD. The speed of rotation and thus the frame rate, depends on the catheter size and optical performance designed to target specific applications, such as imaging of the esophagus [185], cardiovascular [202], pulmonary tract[296], gastrointestinal [297], uterine cervix and urine bladder [298], and larynx[299] among others [204]. As an example, the non-steerable catheter used for this analysis has a spot size of $d = 22 \mu\text{m}$, and hence a lateral resolution $\Delta x_{FWHM} = \frac{0.59 \times d}{2} \approx 6.5 \mu\text{m}$ (see Optics section in annex B). The working distance is 0.57 mm, and the distance from the polished border of the ball lens to the sheath is 0.8 mm, so that the circumference to image is $FOV = 2\pi(1.37 \text{ mm}) \approx 8.6 \text{ mm}$, the minimum number of samples per acquisition is $N = \frac{6.8 \text{ mm}}{6.5 \mu\text{m}} \approx 1323$, and the optimal frame rate considering 100 kHz of sampling rate of the OCT engine is $f_r = \frac{100 \text{ kHz}}{1323} = 75.6 \text{ Hz}$. However, as has been mentioned before, if the rotational distortion depends on the speed of rotation, and a characteristic curve of the NURD can be measured, it should be possible to reduce the distortion by adjusting the rotational speed. The hypothesis is that the rotational speed selection should be made in two steps: 1) calculation of the speed based on optimal sampling and 2) speed

adjustment based on NURD characteristics. If the speed is lowered it will result in an increased number of samples and a better quality of acquired images but longer acquisition time. If the speed is increased, this will result in a lower number of samples and a lower image quality but shorter acquisition time.

The remaining artefacts can be then corrected by additional post-processing techniques. Correction of rotational distortion has been addressed in the literature, targeting the alignment of the images between frames due to variations of the speed and motion artefacts, together with the deformation caused by non-uniform rotation. Most of these are based on image processing techniques, for example dynamic programming [293] to align frames, image registration [300] to compensate for motion artefacts, the use of fiducial marks around the probe for detection and alignment [301], or the reflections from the sheath and optical components of the catheters to correct rotational variations [302], and using speckle decorrelation to correct the rotational distortion[303]. This work is focused on minimizing motion artefacts by optimization of the hardware design and operational settings. The experimental set-up and analysis was based on the method previously published in [294]. In the experiments a target sample with a known geometry was used to observe two-dimensional distortion that causes the deformation of the shape, as well as three-dimensional distortion that causes precession of the image visible such as the rotation of the image when performing pullback scanning due to the torsion added by the tortuous path of the optical fiber and the torque coil. To estimate the rotational distortion of the geometry in acquired OCT images it is compared to the expected values as reported in [294], [304]. The behaviour of NURD in the steerable OCT catheter developed was characterized as a function of the rotational speed and the bending of the distal end of the tool. The results obtained were compared to the performance of the standard non-steerable catheter. For both catheters the NURD and the angle of rotation (precession of images) was measured with respect to the scanning pullback distance. Based on these results the optimal speed of the operation of the catheter could be determined in which the NURD is reduced. The experiment did not target the artefacts caused by the motion of the sample with respect to the probe[300], or due to the variation of the speed of the motor. Even though the speed of the motor is controlled in a closed loop, there is still a small variation of the velocity around its average, which combined with the differences of the transmitted speed at the tip of the probe introduces the stretching-compressing and hovering of the images around its position [301].

3.4.1 Experimental setup and analysis

A rectangular tube with known dimensions was used to measure the four angles formed by the diagonals traced from the center of the sheath to each corner of the interior section of the sample. Figure 3.16(A) shows the geometrical model used to create the target that was then 3D printed (Figure 3.16(B)). The width of the internal section is 2.5 mm and the height 2 mm. The angles are formed when the transparent sheath of the catheter is in contact with two borders of the interior rectangle as shown in Figure 3.16(A). The angles are named as QA, QB, QC, and QD with the theoretical values of 101.31° , 109.80° , 60.40° and 88.50° correspondingly. The geometrical model was 3D printed in VEROWHITE material [305] using the 3D printer Connex OBJET350 from Stratasys [306]. Given the theoretical precision of the printer of $\pm 200 \mu\text{m}$ [306], the printed target was photographed using a microscope next to a standard millimetric ruler as shown in Figure 3.16(B). Using ImageJ actual dimensions and angles of the target were manually annotated and calibrated using the adjacent ruler. The measured width and height were $2.67 \text{ mm} \pm 0.01 \text{ mm}$ and $2.09 \text{ mm} \pm 0.01 \text{ mm}$ respectively.

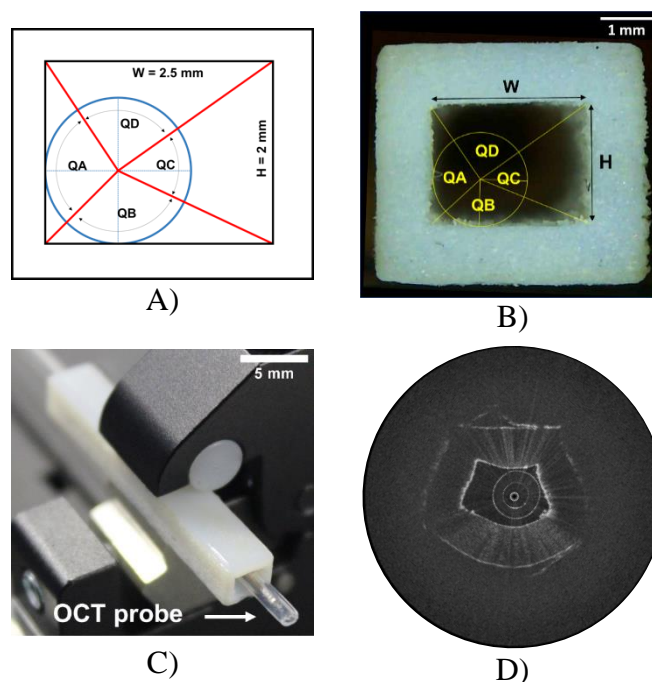


Figure 3.16 Rectangular shape used to measure the rotational distortion. The picture A) represents the geometrical model, B) the 3D printed target and the actual angles, C) the target in place with the OCT catheter, D) OCT image of the target at 25 fps.

The measured angles were $QA = 100.09^\circ \pm 0.29^\circ$, $QB = 115.89^\circ \pm 0.43^\circ$, $QC = 55.02^\circ \pm 0.25^\circ$, $QD = 89.01^\circ \pm 0.38^\circ$. Figure 3.16(C) shows the regular OCT catheter being placed inside the 3D printed piece for acquisition of images. Figure 3.16(D) shows a cross-sectional OCT image of the 3D printed piece at the rotation speed of 1500 rpm (25 fps). As can be seen, a cross-sectional OCT image is clearly a distorted representation of the expected shape of the rectangular tube, caused by the non-uniform rotational distortion. In this case, the rotational speed transmitted to the distal end of the optical probe is not constant during one full rotation of the probe. The probe is rotating with lower speed in some part of the trajectory and faster in others to compensate the motion to keep a constant overall speed.

OCT image analysis for NURD measurement

Measurement of NURD was based on the work of Kawase et al. [304] where the comparison of NURD between OCT and IVUS is performed by using the mean absolute error as the metric to measure NURD and is given with the standard deviation. The mean absolute error (MAE) refers to the mean of the absolute value of the difference between the expected and the measured values [307]. MAE is expressed as in Eq. 3.1 and the standard deviation (STD) as in Eq. 3.2.

$$MAE = \sum_{i=1}^n \frac{|e_i|}{n} \quad \text{Eq. 3.1}$$

$$STD = \sqrt{\frac{\sum_{i=1}^n (e_i - MAE)^2}{n - 1}} \quad \text{Eq. 3.2}$$

where n is the number of angles, and e_i is the difference between the expected and the measured value. Considering QA , QB , QC and QD as the expected values of angle and QA_m , QB_m , QC_m and QD_m the measured values, the NURD is expressed as:

$$MAE = \frac{|QA - QA_m| + |QB - QB_m| + |QC - QC_m| + |QD - QD_m|}{4} \quad \text{Eq. 3.3}$$

$$NURD = MAE(STD) \quad \text{Eq. 3.4}$$

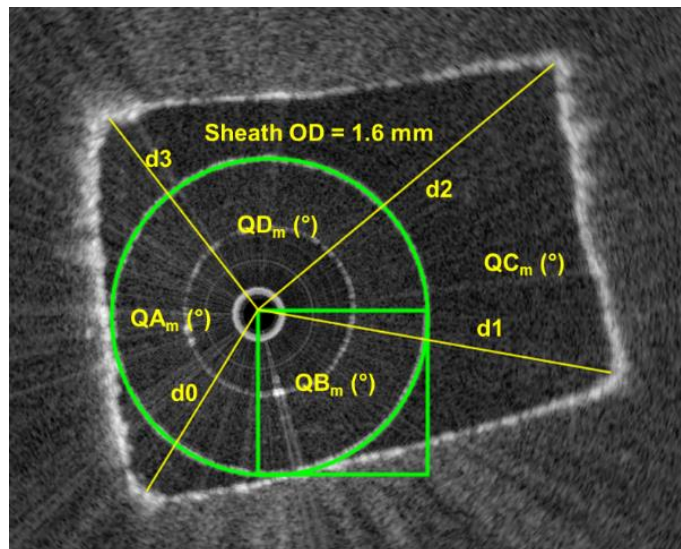


Figure 3.17 Measuring process of the experimental values for the angles QA_m , QB_m , QC_m and QD_m . Tools provided by the ImageJ software were used on the OCT images to perform all the measurements.

The procedure to measure the angles was performed using ImageJ, the calibration of the corresponding scaling from pixels to millimeters being done using known outer diameter of the circular sheath. Figure 3.17 shows the procedure for measuring the experimental values following the steps below in ImageJ:

1. Scale calibration: set up the scaling based on known diameter of the outer circumference of the sheath to 1.6 mm as in the figure.
2. Sheath center: draw a square with the dimension equal to the radius of the circle, then place in in the sheath in such a way that two opposite corners of the square intersecting the borders of the circle to mark its center. (this accommodates for situations where the probe is off to one side from the center of the sheath due to the gap between the sheath and the optical probe).
3. Diagonals: draw the diagonal lines from the center of the circle to each corner. The order for drawing the lines must begin with d0, then d1, d2 and d3, always from the center to the corners. The lines must correspond to the position relative to the circle and the rectangular shape as shown in Figure 3.16a, so that d0 is always the line from the center of the circle to the closest corner of the target, d1 from the center of the circle to the next corner in the larger side of the target, d2 from the center of the circle to the

opposite corner regarding d_0 , and d_3 towards the opposite corner with respect to d_1 .

The order must be respected for all the frames from the beginning of the measurements.

4. Angle measurement: measure the angles using ImageJ tools such that: $QA_m = \sphericalangle d_0d_3$, $QB_m = \sphericalangle d_1d_0$, $QC_m = \sphericalangle d_2d_1$, $QD_m = \sphericalangle d_3d_2$.
5. NURD computation: use Eq. 3.3 and Eq. 3.4 to compute NURD and its standard deviation.

OCT image analysis for precession measurement

The measurement of precession was performed using ImageJ to measure the initial angle of each diagonal d_0 , d_1 , d_2 and d_3 from Figure 3.17 corresponding to the first frame. Then this angle is subtracted from the angle measured on each scanning distance of each diagonal and computing the average. The progression of the precession during performing pullback scanning can be plotted as angle versus scanning distance.

3.4.2 Two-dimensional rotational artifacts

OCT frame selection for NURD calculation

For each setting of rotational speed and angle on average 160 OCT frames were collected. Thus, overall, during the distortion analysis presented in this section 39391 OCT frames were collected. Because the NURD image analysis was performed manually using the tools provided by ImageJ it was necessary to develop a frame selection criterion. During experiments, in which rotational speed was a variable, the criteria to select the frame to process was based on choosing the frame with the closest size to the average size corresponding to the set speed. For example, Figure 3.18 shows 36 frames corresponding to the set speed of 5000 rpm (83fps), and the average values of the frame rate and the standard deviation are calculated. Since the variation of the frame rate causes a variation in the frame size, it is possible to find the frame with the size corresponding to the mean frame rate, which is the frame to use for NURD analysis. Figure 3.19 shows the selected frame using this criterion for the frame rate of 42.28 fps. In this case, NURD was computed for 9 different frames from the OCT images collected when the speed was set constant. It can be observed that the selected frame is very close to the mean value of the NURD. In the case where multiple frames fulfilled the criteria the frame with visually estimated lowest distortion was used.

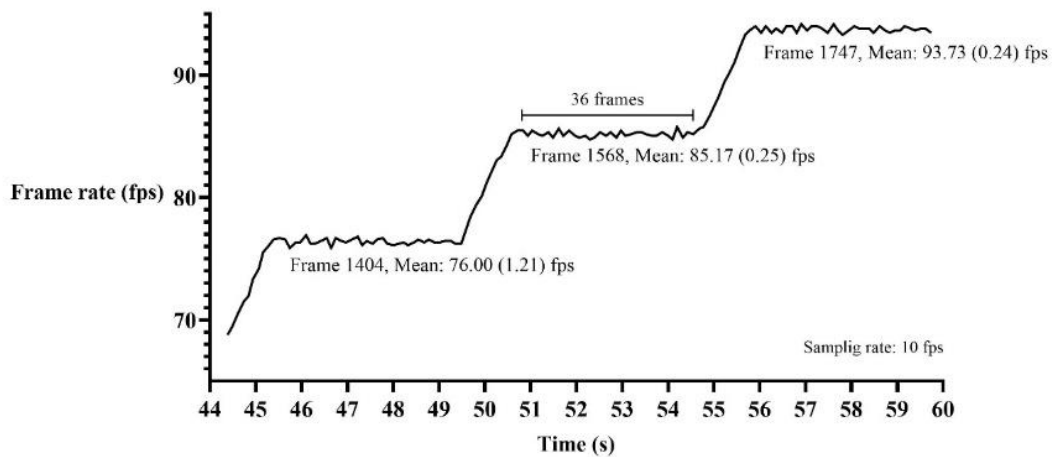


Figure 3.18 Frame rate versus time showing the mean and standard deviation of the frame rate, the number of collected frames, the chosen frame for NURD analysis in which there is mean and the standard deviation of the speed.

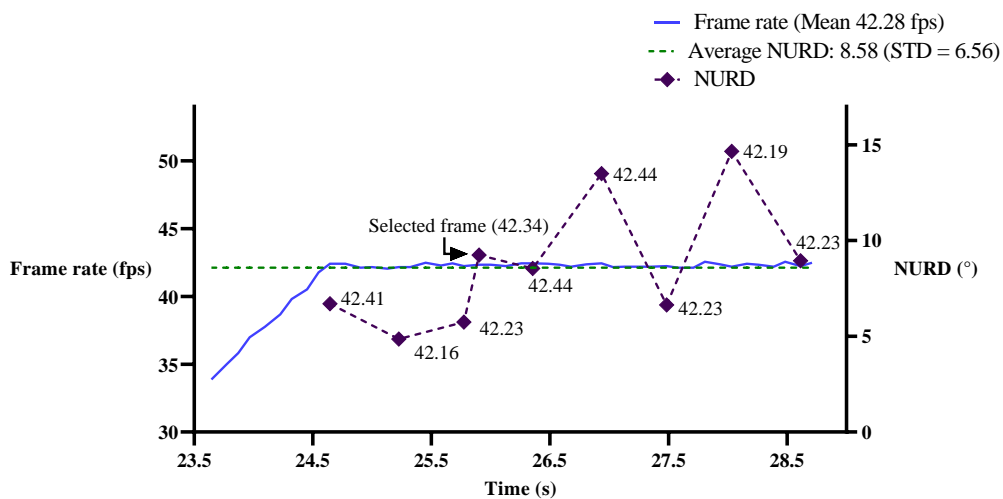


Figure 3.19 NURD versus speed of rotation in frames per second (fps) for regular OCT catheter.

Rotational distortion versus speed of rotation in non-steerable OCT catheter

Figure 3.20 shows a graph of the NURD versus the speed of rotation using the non-steerable OCT catheter as described in section 3.2. To construct this plot OCT images were acquired starting from the frame rate of 8.33 fps (500 rpm) up to 125 fps (7500 rpm). The actual values are summarized in Table 3.3, where the set values start from 8.33 fps up to 125 fps. The actual values are listed as the average of the speed in every frame, the standard deviation and

the percentage of error with respect to the reference. For the rest of the analysis of the present section the frame rate will be referred to as its set value.

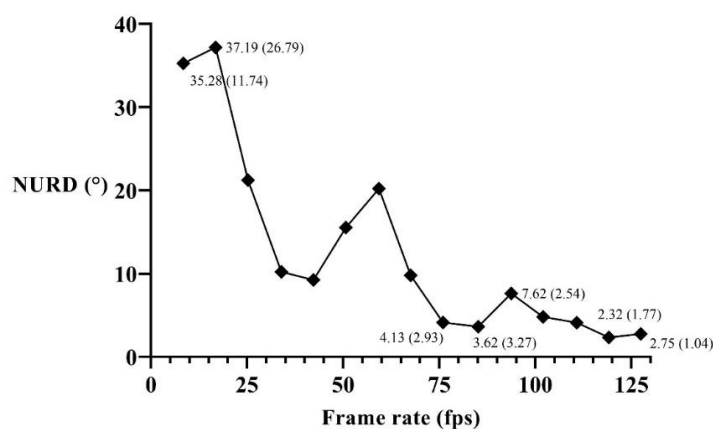


Figure 3.20 NURD versus speed of rotation in frames per second (fps) for regular OCT catheter.

Table 3.3 Reference values of frame rate, the average of the actual value, the standard deviation and the percentage of error with respect to the reference.

Set frame rate (fps)	Measured average of the actual frame rate (fps)	STD (fps)	% Error
8.33	8.44	0.0403	1.28%
16.67	16.84	0.0827	1.06%
25.00	25.25	0.1030	0.98%
33.33	33.95	0.1216	1.84%
41.67	42.28	0.1592	1.48%
50.00	50.72	0.1881	1.44%
58.33	59.32	0.8095	1.68%
66.67	67.57	1.2947	1.36%
75.00	76.00	1.2085	1.34%
83.33	85.17	0.2451	2.20%
91.67	93.73	0.2400	2.25%
100.00	102.02	0.3853	2.02%
108.33	110.77	0.3633	2.25%
116.67	119.14	0.3415	2.12%
125.00	127.43	0.6121	1.95%

It can be observed that the NURD has three maxima of mean error as it decreases with the increase of the speed. The greatest distortion of 37.19° (26.79°) was measured when acquiring images at 16.67 fps that corresponds to the rotational speed of 1000 rpm. The graph shows a strong trending of the NURD reduction as the rotation speed increases. For this case minimum distortion occurred at the frame rate of 116.67 fps (7000 rpm) with 2.32° (1.77°) of NURD. After 75 fps the distortion is reduced to about between 80% and 92%.

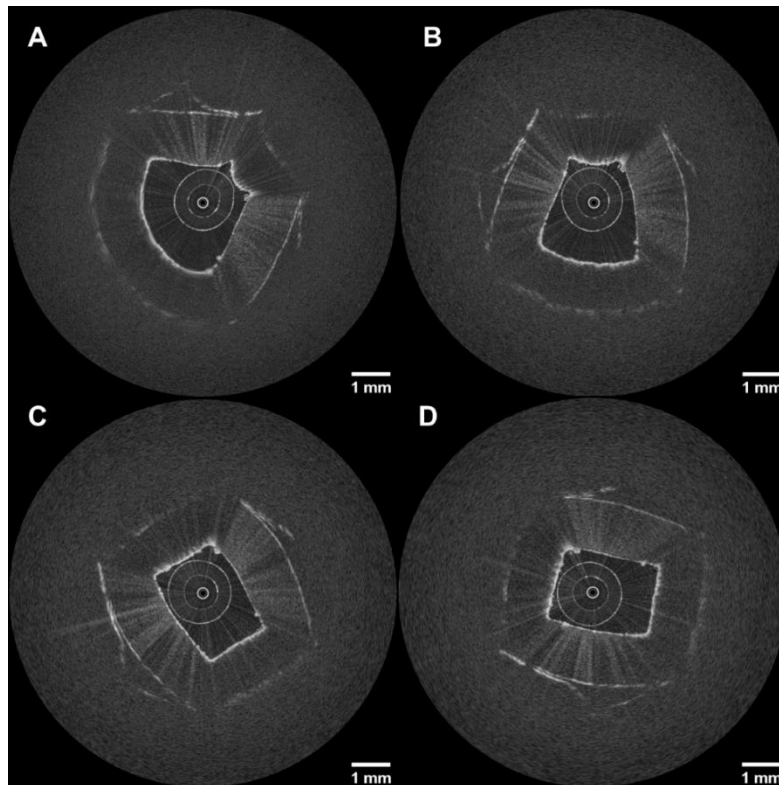


Figure 3.21 OCT images of the rectangular piece taken at a) 16.67 fps (1000 rpms), b) 58.33 fps (3500 rpms), c) 83.33 fps (5000 rpms) and d) 125 fps (7500 rpms).

Figure 3.21 shows the OCT images for each of the maxima in the graph of Figure 3.20, as well as the frame that corresponds to 125 fps. It can be observed how the shape in all four cases changes significantly depending on the speed. The largest distortion is presented in Figure 3.21a and Figure 3.21c and Figure 3.21d represents the OCT images of the rectangular 3D printed target that corresponds to what is expected with 80% and 92% of reduced rotational distortion. It is important to clarify that this experiment was performed in a non-steerable catheter in which the distal end of the probe was straight. The interest of performing the characterization of a non-steerable catheter is to: 1) obtain a gold standard, as such catheters are the most commonly used and 2) provide a means of optimizing the OCT image acquisition, by selecting only those speeds of rotation where the rotational distortion is minimum or acceptable. For example, the minimum NURD is found at 116.67 fps (7000 rpm). However, the optimal speed from the standpoint of minimizing time of the procedure while maintaining sufficient sampling is calculated as being 125 fps. In this case increasing the frame rate to 125 fps will reduce the scanning time at a cost of 18% higher rotational distortion with respect to

the NURD at 116.67 fps, but this distortion is still acceptable since visually it does not represent a significant difference as shown in Figure 3.21(C, D).

Rotational distortion in the steerable OCT catheter

The steerability of the OCT catheter enables better positioning of the probe and possibly an extension of the examination area. However, the bending of the tool adds friction to the catheter, which has a negative impact on the rotational distortion. The steerable catheter developed as a part of this work performs bending up to 93° of flexion in one direction and a maximum of 66° in the other direction, the angle of flexion being annotated as β in Figure 3.22(A). These differences in bending are caused by asymmetries related to the range of the motor actuator, tension in the pull wires and friction added by the sheath of the instrument. To characterize the NURD, measurements of rotational distortion were performed as a function of frame rate (as done previously for the regular OCT catheter in Figure 3.20) and bending angle over the full available bending range with the spacing of 15° . Figure 3.22(A) shows the maximum bending of the tool at 93° . Each angle was set up manually using a protractor as in Figure 3.22(B). The different bending angles measured for each configuration are summarized in Table 3.4, the mean of the spacing being 15.93° with a standard deviation of 4.64° .

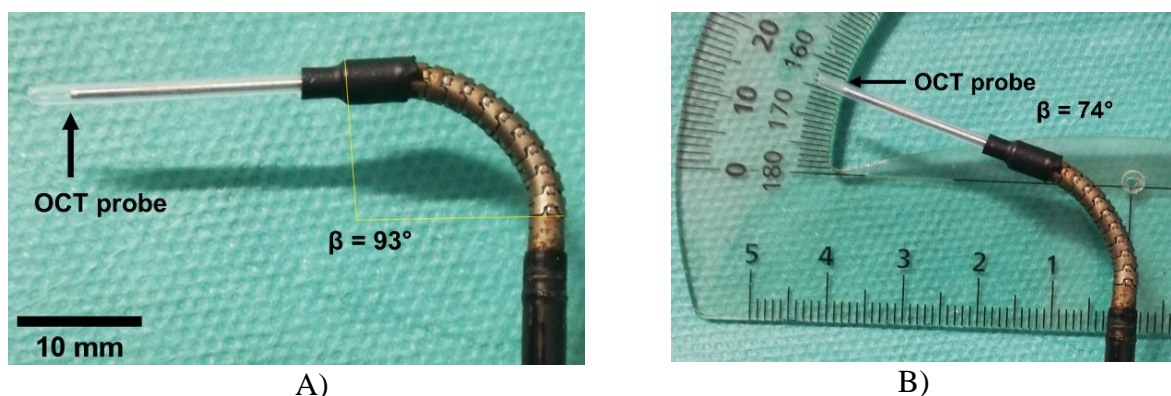


Figure 3.22 Distal end of the steerable OCT catheter showing the vertebrae with angle of flexion $\beta \approx 93^\circ$ (a) and $\beta \approx 34^\circ$ (b).

To characterize the performance of the steerable OCT catheter, the NURD analysis as a function of frame rate was performed for each of the angles listed in Table 3.4. After measuring NURD for each angle and frame rate, the graph in Figure 3.23 was built, representing the distortion through the whole range of bending angle versus the frame rate or

speed of rotation. It can be observed in the graph in Figure 3.23 that the resultant mean curve trend in blue is similar to that in Figure 3.20.

Figure 3.23 shows that in comparison with the regular catheter in Figure 3.20 and considering the angles of flexion listed above, the optimal frame rate for minimum rotational distortion based on the blue curve of mean NURD is at 125 fps (7500 rpms) with NURD of 4.99° then the set frame rates of 91.67 fps (5500 rpm) and 83.33 fps (5000 rpm) are good options since the rotational distortions are very close to the optimum.

Table 3.4 Angle of flexion measured, the rounded value, the mean and standard deviation of the angle spacing.

β ($^\circ$)	$\approx \beta$ ($^\circ$)	Spacing ($^\circ$)
92.95	93	0.00
73.64	74	19.31
53.25	53	20.39
43.24	43	10.02
32.72	33	10.52
18.49	18	14.22
2.29	2	16.20
-18.19	-18	20.48
-34.34	-34	16.15
-56.44	-56	22.10
-66.34	-66	9.90
	Mean	15.93
	Std	4.64

Figure 3.26(A) shows the comparison between the curves of NURD versus frame rate for both types of catheters. Figure 3.26(B) gives a sample of the rotational distortion versus the angle of flexion for different frame rates. Interestingly, it can be observed that the angles of flexion in which the steerable catheter experience more rotational distortion are those close to the straight position. A probable reason is because the torque coil is already placed into the sheath of the instrument, which by default adds friction to the catheter. This friction being compensated at greater angles of bending at the distal end. Less NURD compensation happens at smaller angles of bending mainly for lower frame rates. However, the optimal frame rate set at 125 fps (7500 rpm) presents a flatter curve keeping the rotational distortion under 7.08° (5.09°) for the whole range of angle of flexion, for this case NURD is not dependent on the bending angle.

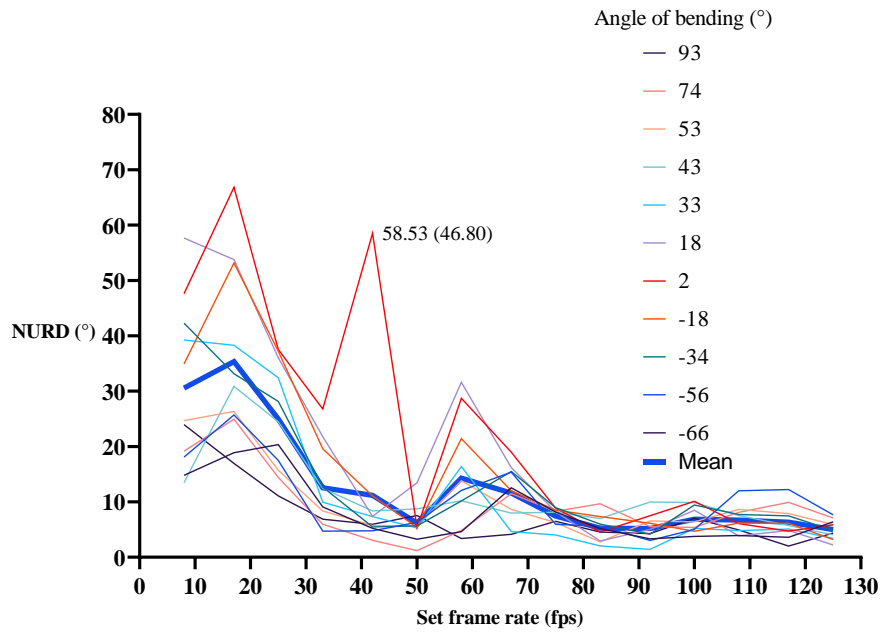


Figure 3.23 NURD versus speed of rotation considering the full range of angle of flexion of the steerable catheter.

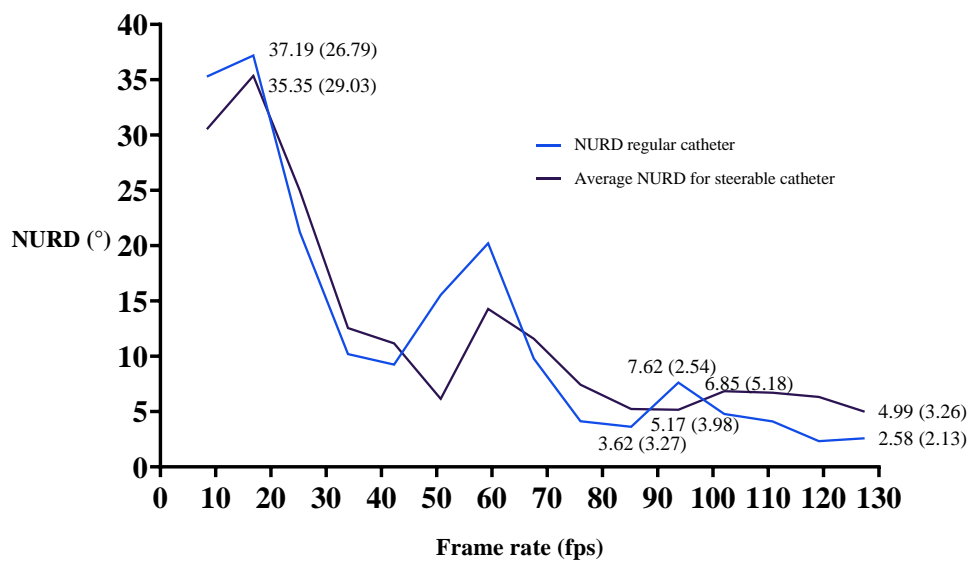


Figure 3.24 NURD versus speed of rotation considering the full range of speed of rotation for the steerable catheter and non-steerable catheter (A).

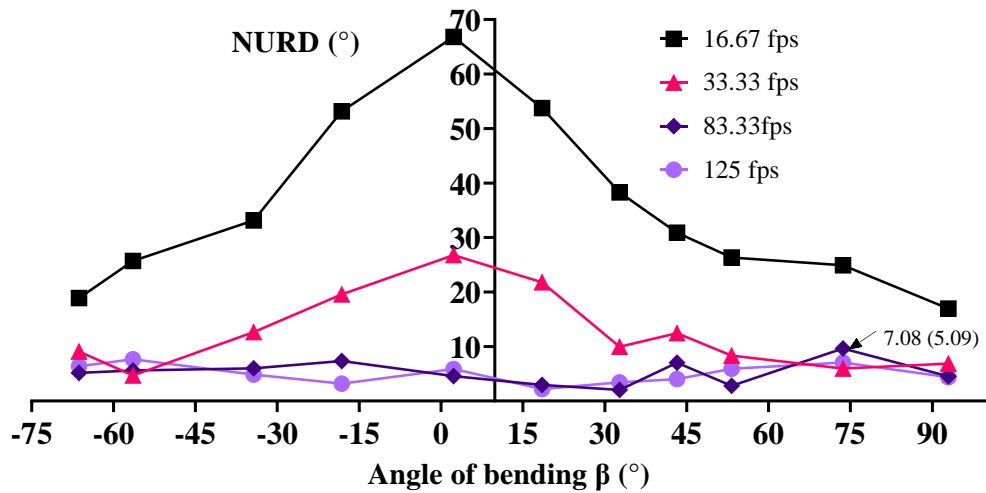


Figure 3.25 NURD versus angle of bending for the frame rates 17 fps, 33 fps, 83 fps and 125 fps.

3.4.3 Three-dimensional pullback artefacts

Non-steerable OCT catheter during 3D scanning

The characterization of the NURD based on the speed of rotation allows the optimization of OCT image acquisition at the initial position of the optical probe. In the next step it is important to measure the rotational distortion during the regular pullback scanning, for three-dimensional imaging. In this case, the torque coil that protects the optical fiber and

most importantly transmits the rotational motion from the external actuator to the distal end can experience additional friction during its translation and so cause distortion. This can be observed in the graph presented in Figure 3.26, where a pullback scanning of 20.82 mm was performed at 83.33 fps and NURD was analyzed for the frame corresponding to a spacing of 1.04 mm. The rotational distortion at the initial point equaled 2.89° (1.99°), then it decreased to the minimal value of 0.74° (0.60°) at 2.08 mm, and reached the maximum NURD value of 9.45° (5.81°) in 8.33 mm. The average NURD was 4.25° (3.38°).

In the next step the precession of the image between frames has been analyzed. This instability of the image presented in Figure 3.27 has been measured using the same pullback scanning dataset performed to collect the information in Figure 3.26.

Figure 3.27 shows the angle of rotation of the image in the frames corresponding to each position of the pullback scanning in the spacing of 1.04 mm with respect to the initial

position-frame. It can be observed that images rotate from the initial 0° position to the maximum angle of 8.07° (1.95°) at 2.08 mm, then to a minimum angle of -14.98° (5.36°) at 11.45 mm, ending in 2.67° (2.74°) at 20.9 mm (positive angles indicate counterclockwise direction and negative angles, clockwise).

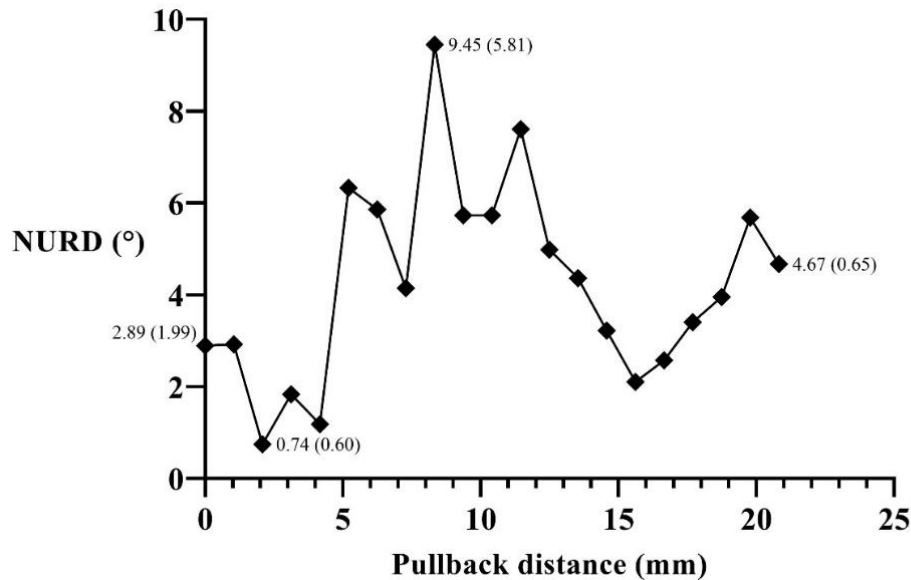


Figure 3.26 NURD versus pullback scanning distance (mm).

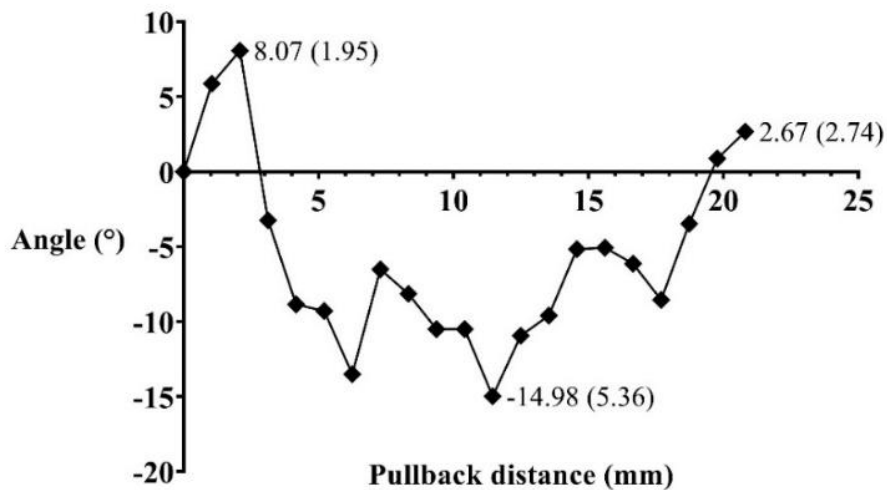


Figure 3.27 Angular rotation versus the pullback scanning distance (mm).

Figure 3.28 shows the OCT images corresponding to the position of 0 mm, 2.08 mm and 11.45 mm for maximum rotation in both directions. The rotation of the image of the target is an artifact that is problematic for volumetric reconstruction of a three-dimensional set of

images acquired after a regular pullback scanning. The origin of this precession is not clear. It could be due to an extra torsion applied during the pullback on account of how the torque coil is placed into the sheath of the instrument and can be addressed by implementing image processing techniques as mentioned in the introduction of this section.

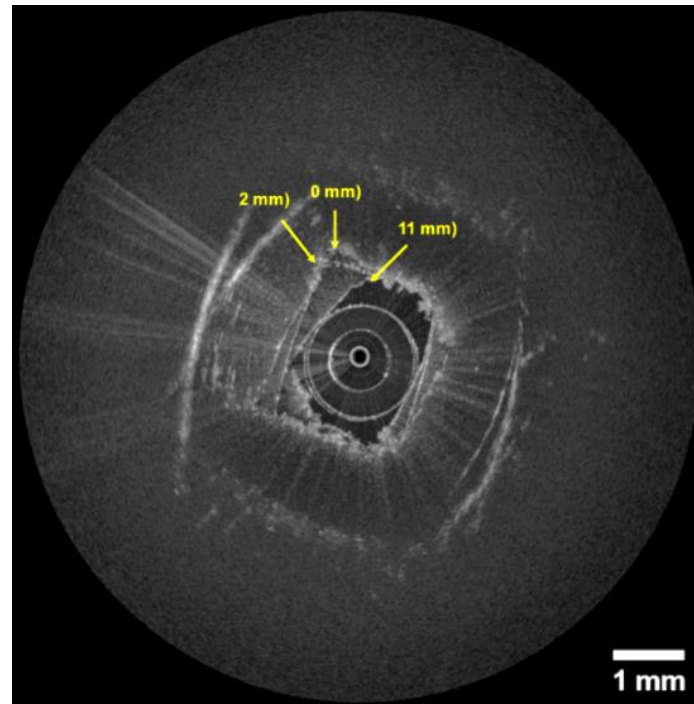


Figure 3.28 Superposed OCT images of the frames corresponding to the pullback scanning distances of 2 mm, and 11 mm where there are the maximum rotations of the images with respect to the initial point in 0 mm.

Steerable OCT catheter during 3D scanning

Based on the characterization curves in Figure 3.22 and Figure 3.23 a frame rate of 125 fps has been chosen to have a minimum distortion when performing the pullback scanning over a distance of 20 mm in order to evaluate the rotational distortion during the performing of pullback scanning.

Figure 3.29 shows the NURD distortion versus the pullback distance when performing a regular internal pullback of the optical fiber for the actual distance of 20.9 mm. The speed of the internal translation was 2.47 mm/s. The overall resultant NURD after performing the full 20.9 mm of translation is 4.59° (3.75°), having maximum and minimum NURD 7.03° (6.84°) at 4.2 mm and 1.4° (0.96°) in 7.34 mm.

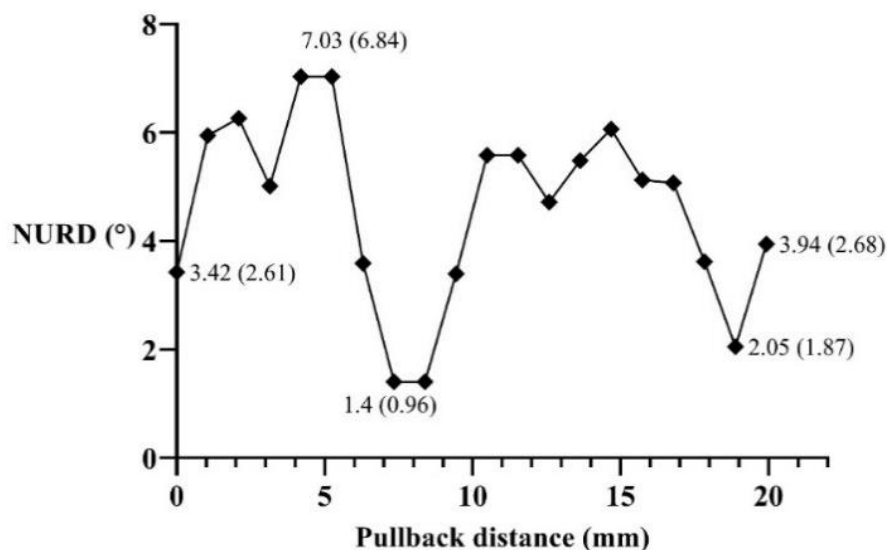


Figure 3.29 Rotational distortion versus pullback scanning distance for regular pullback and with steerable catheter.

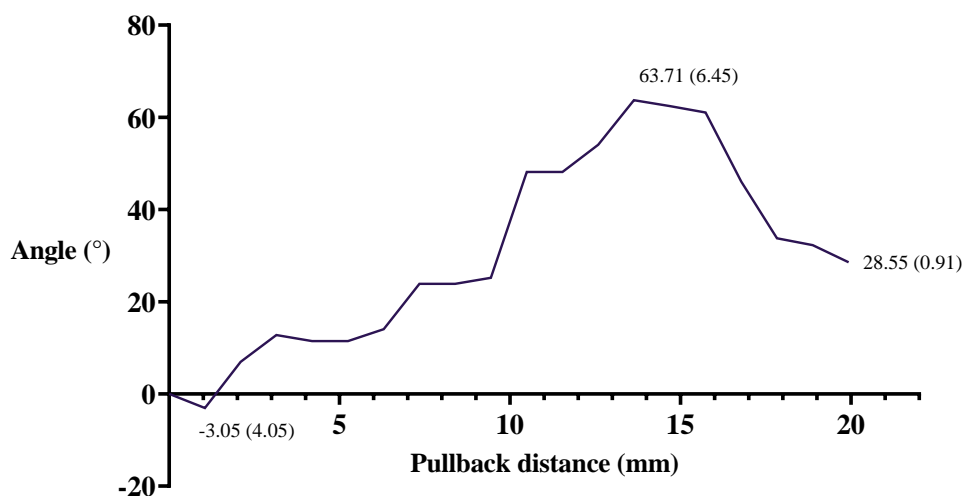


Figure 3.30 Rotation of the images along the pullback scanning distance.

The precession that occurred during the pullback motion is described in Figure 3.30. At the beginning of the pullback motion, the image rotates counterclockwise from the initial position to -3.05° (4.05°), then the rotation changes to the clockwise direction until reaching the maximum rotation angle of 63.71° (6.45°), and then changes direction again to end at 28.55° (0.91°).

Figure 3.31(A) shows the 3D reconstruction of the image at the set frame rate of 125 fps. It is expected here to be able to observe the 3D representation of the hollow rectangular

target with a length of 20.9 mm, but because of the rotational distortion the expected geometry becomes unclear, mainly due to the precession. This can also be observed in Figure 3.31(B) where all the frames have been summed to visualize the rotation of the images.

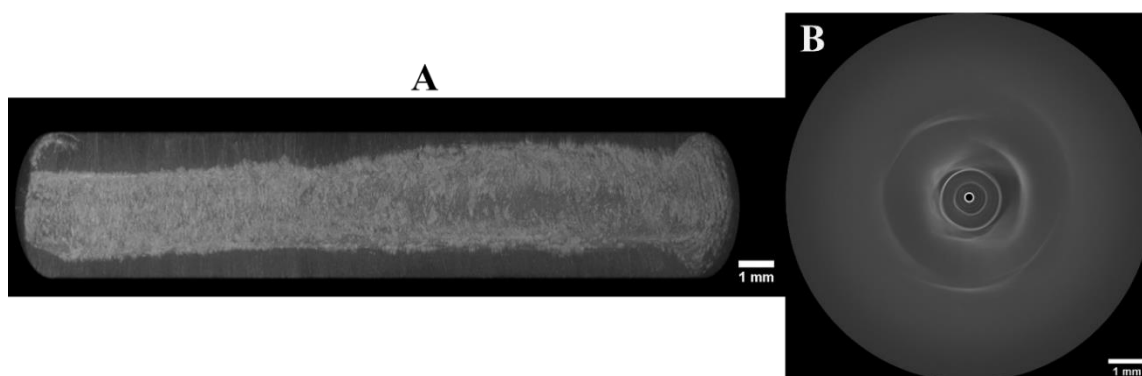


Figure 3.31 3D reconstruction of the rectangular tube by performing regular pullback scanning (A) at 125 fps, and the sum of the frames corresponding to the scanning (B).

3.5 Experimental validation

To validate the imaging capabilities of the steerable OCT instrument developed with optimized rotational speed, images of the top skin layers of two finger were made by gripping the end of the probe between thumb and index (Figure 3.32). The inner and outer borders of the transparent sheath of the catheter are clearly visible, as are the sweat ducts, the dermis and the skin surface of the fingers. Figure 3.32(A) shows the thumb and the index fingers surrounding the sheath while Figure 3.32(B) shows only one of the fingers in touch with the sheath. These first results are very encouraging.

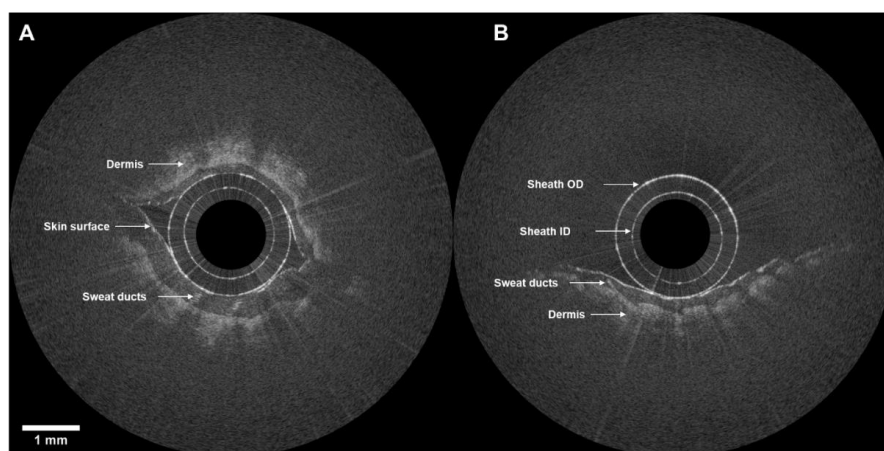


Figure 3.32 Endoscopic OCT image of a thumb and index fingers surrounding the transparent sheath (A). Only one finger under imaging (B).

3.6 Conclusions of the chapter

In Chapter 3 the novel steerable OCT catheter has been introduced, starting from the description of the optical design of the ball lensed fiber with a working distance of about 1 mm from the sheath. The assembly of the optical probe consisting of the lensed fiber sheathed in a torque coil using a low-cost SC/APC pre-polished ferrule fast connector, thus, eliminating the need of specialized splicing equipment for the assembly. The development of a custom-made catheter connector to allow protected connection of the optical probe to the 3D scanner actuators has been detailed.

The custom 3D scanner actuators to perform helical scanning has been built and described. Information about scanning speed calculation has been given, such as details about the optomechanical design. The addition of a special sensor at the rotor of the fiber optic rotary joint (FORJ) for turn detection and B-scan synchronization with the OCT engine has been introduced.

The non-steerable endoscopic OCT catheter has been assembled by using a transparent PEBAX sheath. In a first step the catheter was used for testing the OCT image acquisition, synchronization, 3D scanning pullback and the user interface. The telescopic segment has been incorporated as part of the 3D scanner actuators to allow pullback scanning while keeping the transparent sheath static and protecting the probe.

The novel steerable OCT catheter has been introduced in this chapter by adding bending capabilities to the flexible shaft. The design was based on the surgical instrument of the robotized flexible endoscope. The vertebra mechanism at the distal end of the catheter allowed bending of the probe in two directions of one plane, this is done by the pulling of the antagonist tendons attached to the pulley mechanism enclosed in the instrument module.

Non-uniform rotational distortion (NURD) has been analyzed for both, the non-steerable and the steerable catheters. The analysis of the variation of NURD according to the speed of rotation has been introduced, as well as its variation according to the angle of bending in the case of the steerable catheter. This analysis has demonstrated that the selection of the frame rate should be based on a trade-off between NURD according to the speed of rotation and the number of samples per acquisition, and not only based on the optimal number of samples. As numerical result, NURD has been demonstrated to be reduced by up to ~80 % for frame rates greater than 80 fps. As part of the NURD analysis, precession of the OCT images between frames during pullback scanning has been identified and characterized. OCT images

of an index finger and an ex vivo swine sample were made with rotational scanning. Volumetric OCT images of the rectangular tube are presented as experimental validation.

3.7 French summary of the chapter

Après avoir détaillé le système d'imagerie dans le chapitre précédent, nous décrivons maintenant le cathéter endoscopique robotisé de l'OCT. Nous expliquons comment notre système OCT est inséré dans un cathéter OCT conventionnel qui peut être introduit dans le corps humain. Pour cela, le canal de travail d'un endoscope flexible destiné à la coloscopie est utilisé. De cette façon, les images de l'OCT sont acquises depuis l'intérieur du côlon en effectuant un balayage hélicoïdal. Un cathéter OCT conventionnel est un dispositif passif, ce qui signifie qu'il est manipulé en déplaçant manuellement l'ensemble de l'endoscope. Or, ce n'est pas une tâche facile en raison de la forme complexe du gros intestin. En effet, cette manipulation manuelle exige une formation et une expérience approfondies du clinicien dans les procédures de coloscopie. L'ajout d'un système de guidage au cathéter OCT et de capacités de télé-opération facilitent sa manipulation et réduisent le temps d'apprentissage pour la réalisation de ces procédures. Ces deux étapes font passer le cathéter OCT conventionnel d'un dispositif passif à un cathéter OCT actif pouvant être téléopéré. Pour obtenir la manœuvrabilité, une modification mécanique est ajoutée à la conception détaillée dans la partie 3.3 afin de fournir des capacités de flexion à l'extrémité distale du cathéter OCT. La télé-opération est obtenue en ajoutant la compatibilité entre le nouveau cathéter OCT orientable et l'endoscope flexible robotisé, décrit au point 1.2.1. Cette compatibilité est obtenue en faisant fonctionner le cathéter OCT comme un instrument chirurgical téléopéré de l'endoscope flexible robotisé. La caractérisation et les validations expérimentales sont décrites dans les parties 3.4 à 3.5.

Sonde optique

La sonde optique se compose d'un noyau de fibre optique avec micro-optique, d'un arbre d'entraînement protecteur et d'un connecteur proximal. Une lentille sphérique polie et angulée est soudée à l'extrémité d'une fibre optique monomode SMF 28. La fibre a un diamètre de gaine de 125 μm et un diamètre de revêtement de 250 μm . La fibre lenticulaire a été conçue via le logiciel Zemax et sa fabrication a été sous-traitée à IDIL. La microlentille est d'abord fabriquée à l'extrémité de la fibre et polie à un angle de 48° pour une focalisation latérale de la lumière. La lumière est réfléchiée par la face polie de la lentille afin d'agir comme un miroir

(figure 3.1). La forme sphérique de la lentille concentre le faisceau lumineux à une distance de travail spécifique au-delà de la gaine transparente. La sonde a été conçue pour focaliser la lumière à 1 mm à l'extérieur de la gaine, offrant ainsi des images de qualité maximale lorsque l'échantillon est en contact avec la gaine transparente.

Actionnement de la numérisation 3D OCT

Le mode cathéter endoscopique est conçu pour effectuer un balayage volumétrique d'un organe luminal (par exemple le côlon) par des mouvements simultanés de rotation et de translation de la sonde optique, permettant donc un balayage hélicoïdal. Par conséquent, un système électro-opto-mécanique sur-mesure pour l'actionnement proximal a été construit dans le but de fournir un mouvement de rotation à différentes vitesses et des translations à différents déplacements. L'actionneur est constitué d'un joint rotatif à fibre optique (FORJ) pour coupler une fibre optique statique – qui transmet la lumière de la console d'imagerie OCT – à la sonde rotative à fibre OCT. La sonde est connectée à l'actionneur avec un connecteur spécifique et à un segment télescopique qui permet le retrait de la sonde. Lors de la phase de retrait, les acquisitions interférométriques sont réalisées. La synchronisation du système mécanique et de l'acquisition d'images est réalisée à l'aide d'un capteur optique.

Actionnement de flexion

Pour permettre le pliage du cathéter OCT, un instrument conçu pour l'endoscope interventionnel Anubiscope™ (Karl Storz) a été utilisé. Le mouvement de flexion des instruments est possible grâce aux 11 vertèbres situées à l'extrémité distale de la tige de l'instrument, entraînées par deux tendons antagonistes, ce qui permet de fléchir dans deux directions sur un même plan.

Caractérisation et optimisation

Le cathéter OCT endoscopique met en œuvre un actionnement proximal et une bobine de torsion. Un balayage hélicoïdal est alors généré en effectuant un mouvement de rotation-translation de l'optique de focalisation à l'extrémité de la fibre optique. Ce système est généralement impacté par des artefacts d'image qui peuvent entraîner une déformation de l'image et de sa rotation dans le temps (précession). Ils sont généralement dus à une distorsion de rotation non uniforme (NURD). Les causes de cette distorsion peuvent être le frottement

mécanique entre la bobine de torsion et la gaine extérieure, la variation de la vitesse du moteur et la transmission de la vitesse par la bobine de torsion à l'extrémité distale de la sonde optique. Les artefacts liés à la précession conduisent généralement à une rotation aléatoire de l'image entre les différents cadrages tridimensionnels générés par le mouvement de retrait du dispositif. La flexion du cathéter et le mouvement de retour de la fibre pendant le balayage de l'échantillon peuvent contribuer à augmenter ces deux types de distorsion.

Validation expérimentale

Pour valider les capacités de l'instrument OCT orientable mis au point avec une vitesse de rotation optimisée, des images des couches supérieures de la peau de deux doigts humains ont été réalisées en saisissant l'extrémité de la sonde entre le pouce et l'index (figure 3.32). Les bords intérieurs et extérieurs de la gaine transparente du cathéter sont clairement visibles, tout comme les canaux sudoripares, le derme et la surface de la peau des doigts. La figure 3.32(A) montre le pouce et l'index entourant la gaine, tandis que la figure 3.32(B) ne montre qu'un des doigts en contact avec la gaine. Ces premiers résultats sont très encourageants.

Conclusions du chapitre

Dans le chapitre 3, nous avons présenté le nouveau cathéter OCT orientable à partir de la conception optique de la fibre à lentille sphérique avec une distance de travail d'environ 1 mm de la gaine. La sonde optique est constituée d'une fibre optique gainée dans une bobine de torsion à l'aide d'un connecteur rapide à virole pré-polie SC/APC à faible coût. Cela élimine ainsi le besoin d'un équipement d'épissage spécialisé pour l'assemblage. Nous avons également décrit la phase de développement d'un connecteur de cathéter sur-mesure pour permettre une connexion protégée de la sonde optique aux actionneurs du scanner 3D.

Les actionneurs de scanner 3D sur-mesure capables d'effectuer une numérisation hélicoïdale ont été construits. Nous avons fourni des informations sur le calcul de la vitesse de balayage, comme par exemple des détails sur la conception opto-mécanique. Par ailleurs, nous avons présenté l'ajout d'un capteur spécial au rotor du joint tournant à fibre optique pour la détection des virages et la synchronisation du B-scan avec le moteur OCT.

Le cathéter endoscopique non orientable OCT a été assemblé à l'aide d'une gaine PEBAX transparente. Dans un premier temps, le cathéter a été utilisé pour tester l'acquisition d'images OCT, la synchronisation, la numérisation 3D et l'interface utilisateur. Le segment

télescopique a été incorporé dans les actionneurs du scanner 3D pour permettre une acquisition du signal interférométrique lors de la phase de retrait de la sonde tout en gardant la gaine transparente statique et en protégeant la sonde.

Dans ce chapitre, nous avons également présenté le nouveau cathéter OCT orientable, conçu par l'ajout de capacités de flexion à la tige flexible. La conception était basée pour l'instrument chirurgical de l'endoscope flexible robotisé. Le mécanisme des vertèbres à l'extrémité distale du cathéter a permis de plier la sonde dans deux directions sur un même plan ; ceci est réalisé par la traction des tendons antagonistes attachés au mécanisme de poulie inclus dans le module d'instrument.

La distorsion de rotation non uniforme (NURD) a été analysée pour les cathéters non orientables ainsi que pour les cathéters orientables. Nous avons analysé la variation de la NURD en fonction de la vitesse de rotation ainsi que sa variation en fonction de l'angle de flexion dans le cas du cathéter orientable. Cette analyse a démontré que le choix de la fréquence de rotation devrait être fondé sur un compromis entre la NURD en fonction de la vitesse de rotation et du nombre d'échantillons par acquisition, et non seulement en fonction du nombre optimal d'échantillons. Il a été démontré que la NURD est réduite jusqu'à ~80 % pour des cadences d'acquisition supérieures à 80 images/seconde. Dans le cadre de l'analyse NURD, la précession des images OCT entre les acquisitions pendant le balayage de retrait a été identifiée et caractérisée. Des images OCT d'un index et d'un échantillon de porc ex vivo ont été réalisées par balayage rotatif. Les images OCT volumétriques du tube rectangulaire ont été présentées à titre de validation expérimentale.

Chapter 4

OCT enhanced robotized flexible endoscopy

Content

4.1 Electro-mechanical integration of the system	110
4.2 Software compatibility and control of the system	113
4.3 Characterization and optimization	115
4.3.1 Extended scanning workspace model.....	116
4.3.2 Experimental validation of the workspace	125
4.3.3 Three-dimensional artefacts in tool-based pullback scanning	130
4.4 Experimental validation	133
4.5 Conclusions of the chapter	134
4.6 French summary of the chapter	135

The steerable catheter described in the previous chapter has only bending capabilities in one plane. In this section, a description is given of the integration of the steerable OCT catheter and the robotized endoscope to provide translation and rotation capabilities to the OCT device.

4.1 Electro-mechanical integration of the system

STRAS is a robotic platform aimed at robotic-assisted surgical endoscopic procedures. It is based on the manual Anubiscope™ platform developed by Karl Storz (Figure 4.1(A)) [115]. This platform has been robotized using the concept of designing a teleoperated modular system for easy set up while adding minimum modifications to the original Anubiscope™. The main advantage of the robotized platform is the suppression of the need for the cooperation of at least two clinicians to operate the manual Anubiscope™. The system works in a Master/Slave configuration as described in section 1.2.1.

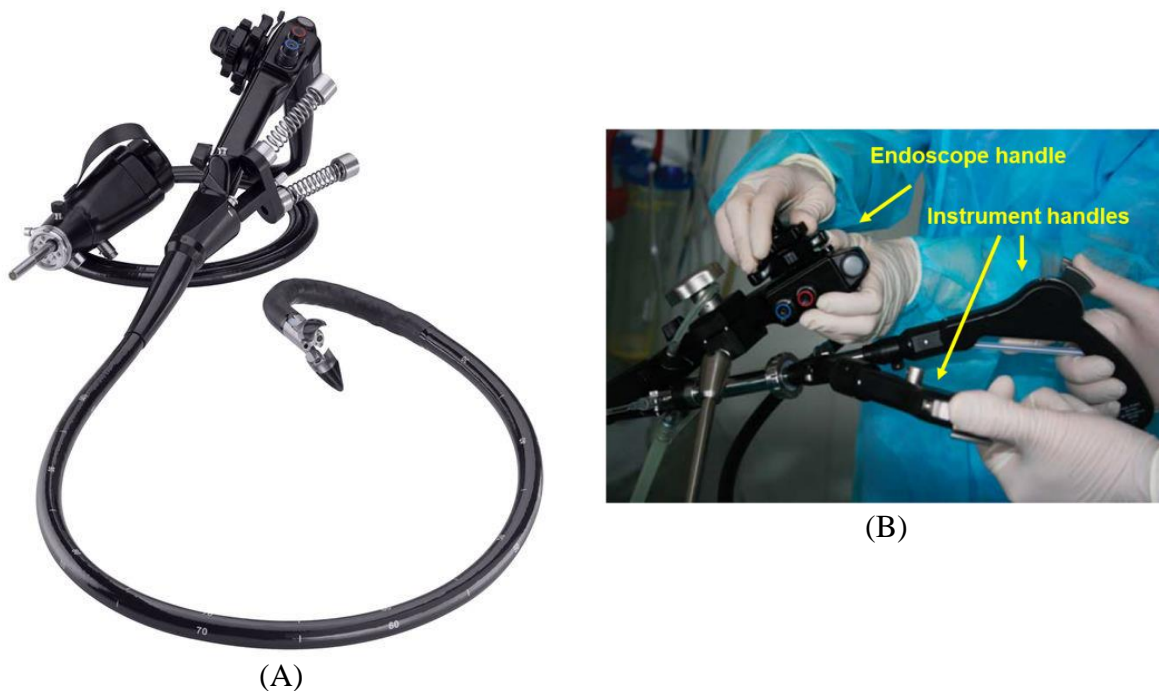


Figure 4.1 (A) Manual Anubiscope™ [308]. (B) Manipulation of the manual Anubiscope™ and the surgical instruments by two operators [115].

The robotization of the surgical instruments and main endoscope was performed by replacing the manual wheels of the endoscope handle (Figure 4.1(B)) with motors with gears to actuate the tendons of the two in-plane deflections. The instrument handle in Figure 4.1(B)

was replaced by an instrument module (IM) that incorporates the actuation mechanism to drive two tendons to perform deflection in one plane; this was done for the two instruments allowed for use through the two instrument channels available in the endoscope. The translation and rotation of the surgical instrument are performed by externally moving the instrument module with the translation-rotation module (T/RM). Figure 4.2 shows the components of the instrument and TR/M modules.

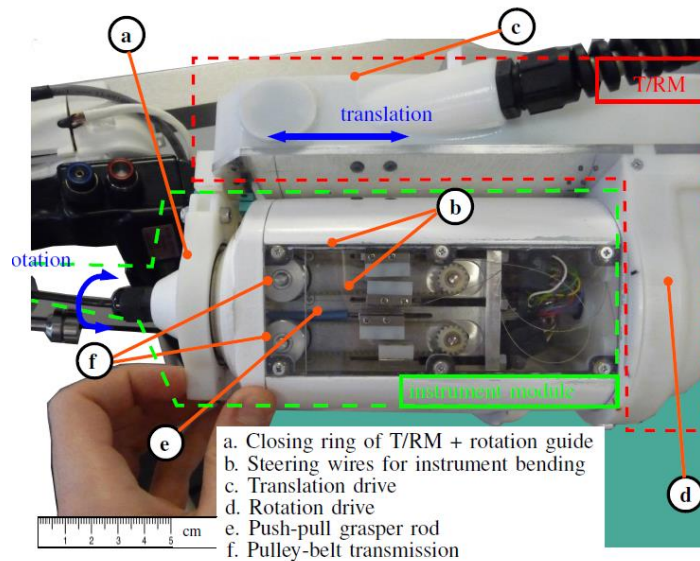


Figure 4.2 Instrument module to perform actuation of the deflection in one plane of the surgical instrument, © 2018, IEEE [98].

Figure 4.3(A) shows the schematic drawing of the full robotic platform in which the clinician manipulates the controllers named the Master interfaces. This allows control of the four degrees of freedoms of the endoscope by performing translation, rotation and bending of the two axes. The Master PC hosts the software for sending motion commands to the slave system which includes the main endoscope and the instruments. The steerable OCT catheter has been designed to be used in combination with the robotized flexible endoscope, which implies that the bending motion is performed through the user controllers of the robot, so that manual bending is not allowed. The steerable OCT catheter must be integrated with the robotic system for its use by inserting it into the instrument channel, coupling the IM to the robot in the same manner as any other surgical instrument, connecting the control cables of the IM to the control panel and the optical probe (represented in yellow color in the figure) to the RJ. The OCT imaging features are independent of the robotic system. The clinician has visual feedback from the endoscope processor and the OCT imaging console. The portable OCT imaging

console (OCT) was added next to the endoscope processor (Endo P) and light source (Endo LS). The main endoscope is mounted on a U-shaped cradle allowing translation motion of up to 100 mm; rotation in the range of -90° to 30° and bending in two orthogonal axes in the range of -90° to 90° . The instrument modules (IM1 and IM2) are placed together with the endoscope on the cradle. The slave components are all carried on the cart which is a mobile platform that incorporates the control panel for communication with the master. Figure 4.3(B) shows an illustration of the front view of the distal end of the endoscope and instruments. The two instrument channels and the working channel are indicated in the figure. One of the instruments represents the OCT catheter and the other, a surgical grasper. It also incorporates an insufflation channel, the lighting, and the camera.

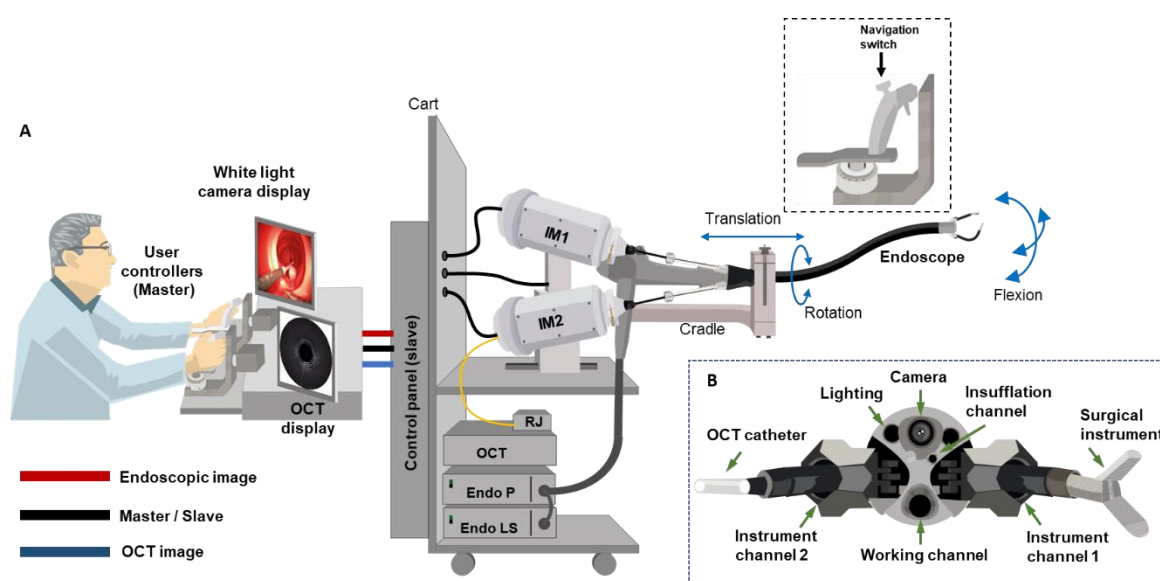


Figure 4.3 Schematic drawing of the integration of the steerable OCT catheter and the robotized endoscope. The blue arrows describe the degrees of freedom performed in the endoscope.

Figure 4.4 shows a picture of the OCT imaging console and the OCT instrument integrated into the robot during experimental testing with the phantom colon (LM107, KOKEN CO). This phantom was used to perform the first test on the mechanical interaction of the components of the new OCT system instrument and the robotized endoscope. This is explained later in Chapter 5. The OCT system shares the space with the endoscope processor. The data display and control and the user controllers are highlighted.

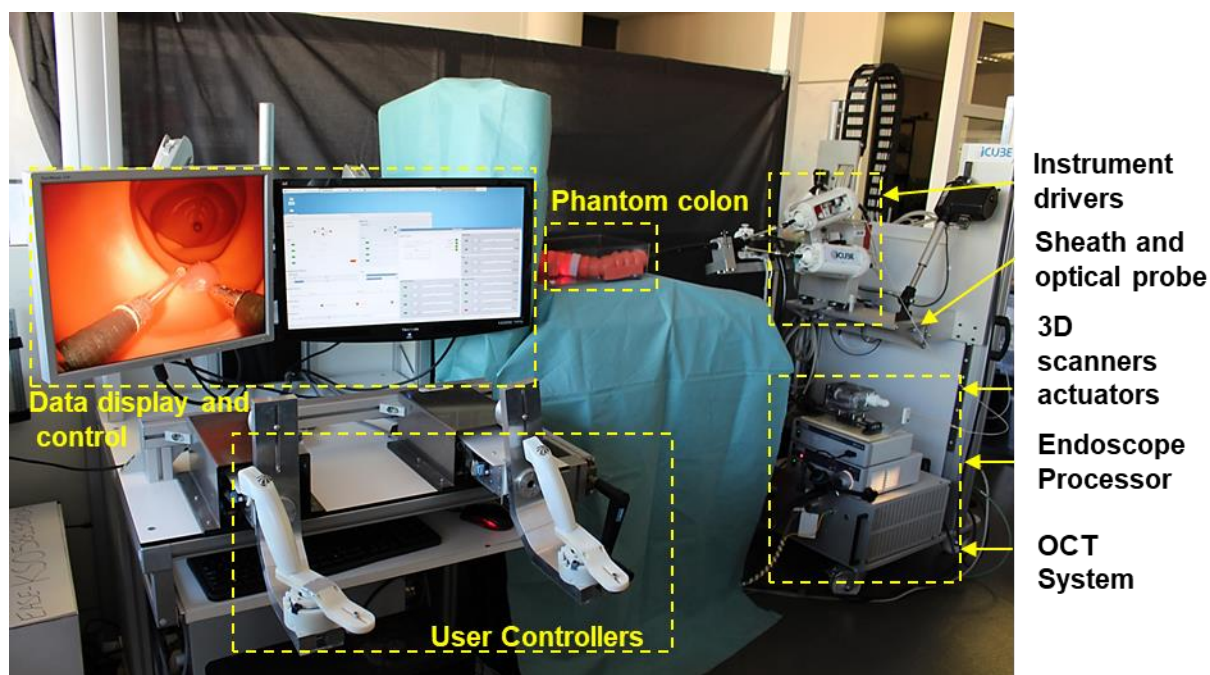


Figure 4.4 OCT enhanced robotized flexible endoscopy.

4.2 Software compatibility and control of the system

In terms of the software for the robotized endoscope, no modification was performed for the incorporation of the new OCT catheter, the design compatibility making the integration of the OCT catheter transparent to the system. The system requires the same start-up and calibration procedure for its use as described in [98] and summarized as follows: To launch the software application on the Master PC, to position the IM to the marked reference and to bring each joint of the Master interface to the limits of its range, these steps are done manually, and the calibration of the slave is automatically performed in ~3 min. After calibration, all the joints are automatically positioned to a home position.

The clinician uses the Master interfaces to control the four degrees of freedoms of the endoscope: rotation, translation and bending of the two axes. The Master PC hosts the software that sends motion commands to the slave system which includes the endoscope and instruments. It also displays the images from the endoscope processor and from the OCT image console. To apply the motions to the endoscope a four-way navigation switch (North-South / West-East) is available in both Master controllers. One switch is programmed to control the bending of both axes and the other, the translation and rotation. This is shown in the picture of the master interface in Figure 4.5, where $T \rightarrow$ translation, $B \rightarrow$ bending, $R \rightarrow$ rotation, the

handle of the master interface incorporates the navigation switch, a trigger to actuate the closing/opening of the grasper instrument, and balancing weights. The figure also shows the L-shape bracket in which the handle is mounted, together with the support structure.

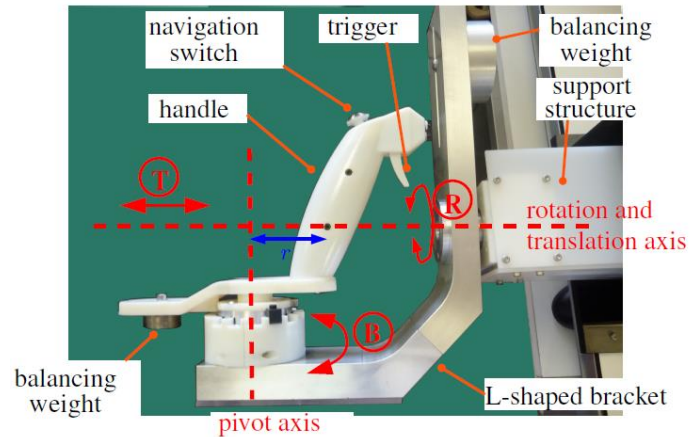


Figure 4.5 Close-up view of one of the master interfaces, © 2018, IEEE [98].

The OCT catheter is then teleoperated in the same manner as any other surgical instrument compatible with the robotized flexible endoscope; since the robot has two instrument channels, it is possible to use the second tool (such as the grasper) at the same time as the sample is imaged with the OCT catheter. Figure 4.6 describes the relation of the motions performed in the OCT catheter by the Master interface. The lateral rotation of the controller drives the bending of the tool as shown in the figure; the rotation and translation of the tool is performed by rotating-translating the L-shaped moving bracket; this makes 3 DoFs of motion for the steerable OCT catheter. The OCT catheter is rotated and translated due to the motion applied to the IM box in the cradle so that it is transmitted by the shaft to the distal end. The flexion is performed as explained before by the bending actuators enclosed into the IM.

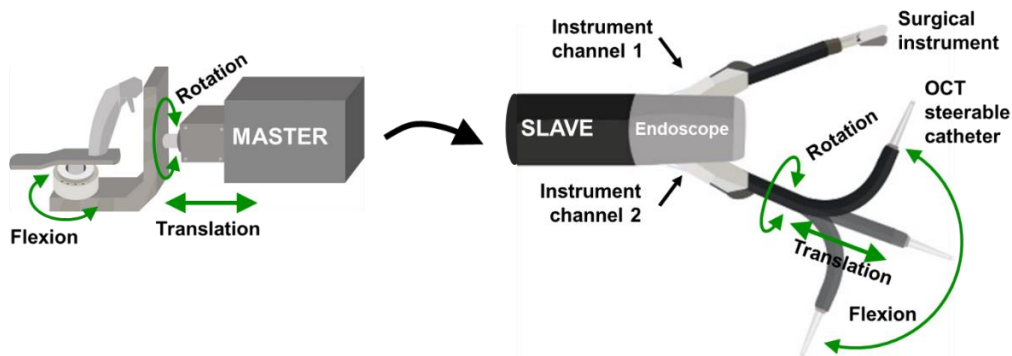


Figure 4.6 Relation of the degrees of freedom in the instrument and the master controller. The system works in Master-Slave configuration.

4.3 Characterization and optimization

Conventional OCT catheters are designed to be inserted in an endoscopic working channel. Their manipulation relies on performing manual motion to the endoscope and does not provide steerability or allow teleoperation. The scanning area of conventional OCT catheters performing rotational scanning is limited to the pullback/rotation motion covering a cylindrical area defined by the pullback length and the working distance of the catheter. This usually matches the outer diameter of the protecting sheath in the case of low-profile catheters, and the diameter of the balloon or capsule in the case of balloon and capsule catheters accordingly [309][185]. In the case of imaging the esophagus, commercially available endoscopic catheters such as the NvisionVLE® Imaging System of Ninepoint Medical, Inc. with imaging diameters from 2.33 mm for low-profile catheters, and 14 mm, 17 mm, 20 mm for balloon based probes [310]. With a pullback distance of 6 cm, the scanning area for such catheters is in the range of 9.87 to 37.7 cm². In the case of the tethered capsule, with a diameter of 12.8 mm and imaging distance length of up to 25 cm [185], it covers an area of about 100 cm².

The steerable OCT device described in this work, is an active catheter that can be teleoperated through the robotic system described in the previous section. This characteristic contributes to the extension of the scanning of a volumetric workspace in comparison with conventional passive catheters. From the definition of workspace in [311]: “*the workspace of a robotic manipulator is the total volume swept out by the end-effector as the manipulator executes all possible motions*”, and the end-effector being the lens of the OCT probe, this means that the reachable volumetric workspace for OCT scanning is defined by the 3 DoFs added for steerability and teleoperation. The geometrical model of the scanning workspace is analyzed and presented in the following paragraphs as well as the computation of the extended area and volume reachable by the steerable OCT device. Also, results from the validation of the workspace using an electromagnetic tracker are shown in this section. In addition, NURD characteristics for pullback scanning using translation of the inner optical probe is compared to the pullback of the whole OCT instrument provided by the robotic translation motion of the tool. Following integration of the OCT steerable catheter and the robotized flexible endoscope, a redundancy of these two degrees of freedom was noted.

4.3.1 Extended scanning workspace model

The steerable OCT device is an active catheter that can be teleoperated through the robotic system described in previous section. This characteristic contributes to the scanning of a volumetric workspace in comparison with conventional passive catheters. The geometrical model of the scanning workspace is analyzed and presented in the following paragraphs as well as computation of the extended area and volume reachable by the steerable OCT device. Also, results from the validation of the workspace using an electromagnetic tracker are shown in this section.

Workspace Model

The steerable OCT device is an active catheter of piecewise constant curvature; terminology well known in robotics referring to those mechanisms consisting of a finite set of curved links [312]. This is the case of the steerable OCT catheter. Figure 4.7(A) it is a detailed description of the simplified Figure 4.7(B).

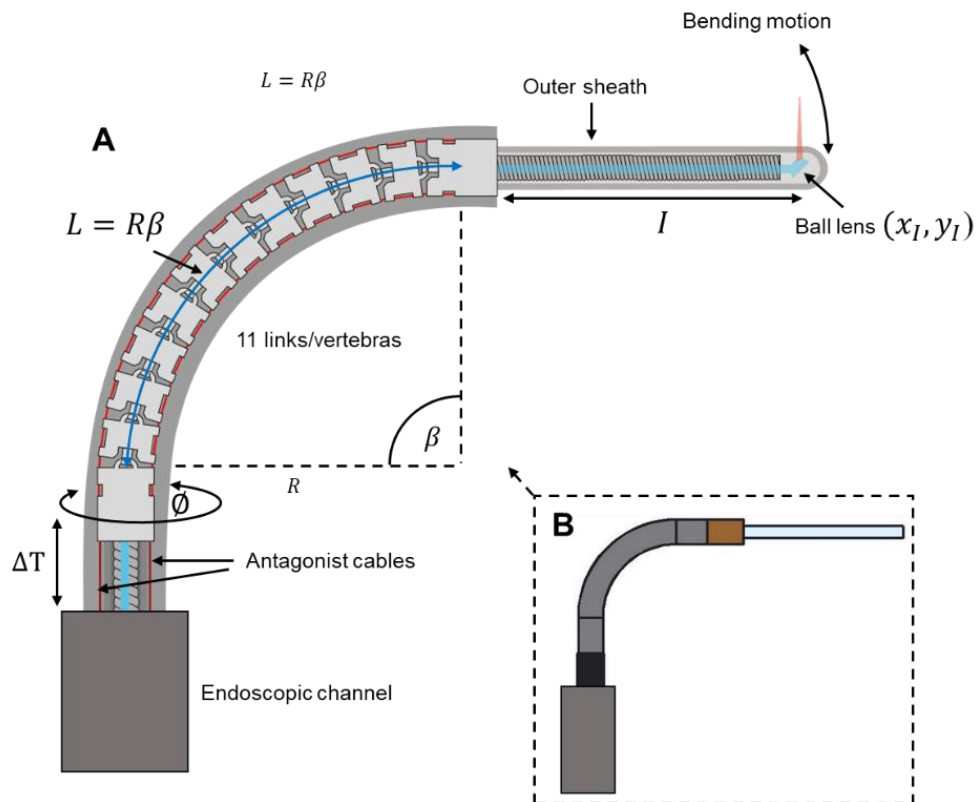


Figure 4.7 Active catheter of piecewise constant curvature, consisting of 11 vertebrae, L is the length of the vertebrae systems.

It shows the flexible section of the probe consisting of 11 links that are called vertebrae. The bending motion in both directions is driven by pulling the antagonist cables in red colors. The position of the tip depends on the varying parameters: bending angle β , the angle of rotation \emptyset , the translation of the tool ΔT and the fixed parameters: I_{max} for the maximum length of the rigid section and the length of the bending section L . In addition to this, it is possible to perform internal translation of the optics by pulling back the torque coil sheathing the optical fiber, so that the length of the rigid section I is variable.

For the catheter developed as a part of this doctoral project, the values measured for each parameter are mentioned below:

I_{max} → length of the fixed part from the flexible section to the tip = 29.25 mm.

I_{mp} → length of the fixed part from the flexible section to the tip for maximum OCT pullback = 9.67 mm.

L → length of the flexible section = 18.3 mm.

β → angle of flexion in $[-90^\circ, 90^\circ]$.

ΔT_{max} → tool translation = 28 mm.

\emptyset → Rotation in $[0, 360^\circ]$.

The equations expressing the position of the tip of the steerable catheter in Figure 4.7 are summarized below in Eq. 4.1 and Eq. 4.2. The pair (x_I, y_I) is expressed in parametric equations depending on β , and where L and I are constant values.

$$x_I = \frac{2L}{\beta} \left(\sin \left(\frac{\beta}{2} \right) \right)^2 + I \sin(\beta) \quad \text{Eq. 4.1}$$

$$y_I = \frac{L}{\beta} \sin(\beta) + I \cos(\beta) \quad \text{Eq. 4.2}$$

Equations Eq. 4.1 and Eq. 4.2 represents the position in the bending plane. The position is computed in the same way for any angle of rotation \emptyset . Further explanation of the deduction of these equations can be found in annex D. The workspace was computed using real dimensional values and is shown in Figure 4.8 as a three dimensional view, and in Figure 4.9 as a lateral view.

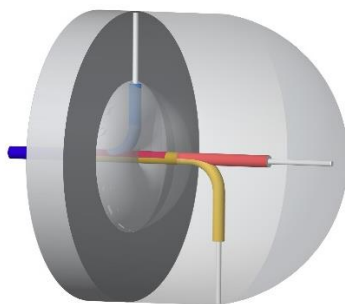


Figure 4.8 Three-dimensional illustration of the workspace in Figure 4.9.

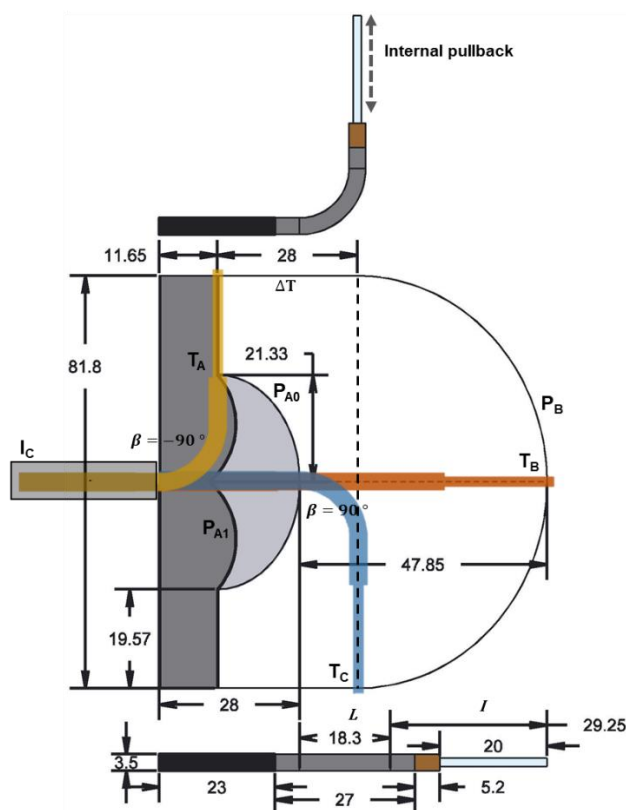


Figure 4.9 Lateral view of the scanning workspace.

The reachable workspace is covered by the white and light gray areas. The dark grey area represents the unreachable workspace of the system. This is the zone that is not reachable by the tip of the steerable tool without the motion of the main endoscope. The curved trajectory P_B is covered by bending the OCT device in the full range of -90° to 90° when it is fully extended with $\Delta T = 0$. Then, by adding rotational motion of the tool from 0° to 360° , it is possible to cover an area defined by the flexible section with maximum range of bending and having a fixed position in translation; P_B and the dotted line represents the borders of this area in the lateral view for the maximum range of the bending angle. If the OCT device is fixed at

its maximum bending angle in either direction, the next reachable area of the workspace is defined by performing translational motion in ΔT . This area can be modeled as the cylinder formed by adding rotational motion with the maximum bending angle and the translation range of $\Delta T = \Delta T_{max}$. The last area covered by the steerable instrument can be visualized in Figure 4.9 for the case when the tool is retracted by $\Delta T = \Delta T_{max}$ with maximum bending angle and performing internal pullback in T_A visualized in Figure 4.9. In this case the position of the ball lens is fully retracted following the trajectory P_{A0} by adding full range bending motion (or equivalently half full range in either bending direction). The full area covered by the tool when it is retracted is obtained by performing rotation to these trajectories. This describes areas represented by the white area in Figure 4.9. This area can be currently reached by either programmed routines in the robotic system in which there is no interaction with the user-controlled teleoperation. The light gray area is reachable by the steerable tool, but it is currently available only in the user-controlled teleoperation mode. To reach this area, the tool must be inserted beyond $\Delta T = \Delta T_{max}$ into the endoscopic channel T_C and at the same time the angle of flexion must be reduced. To model this case it is possible to use the same Eq. 4.1 and Eq. 4.2. In Figure 4.7(A) it can be observed that the length L consisting of 11 vertebrae is constant, so that R in Figure 4.7 must change according to the bending angle to keep L unchanged. In this case, as long as the tool is being inserted, L decreases and the bending motion depends on the number of vertebrae outside the channel. This causes the opposite effect: L decreases and R is kept constant according to the initial bending angle before starting the retraction motion beyond $\Delta T = \Delta T_{max}$. Implementation of programmed routine to reach the light gray area will be addressed in future work. The tip of the tool can be placed in any position inside the border area previously described and illustrated in Figure 4.9 covering a volume limited by this surface. Computation of the area and volume is described in the following paragraphs.

Area covered by the steerable OCT catheter for $\beta = [-90^\circ, 90^\circ]$ $\Delta T = 0$ and $\phi = [0^\circ, 360^\circ]$

The area of the flexible section can be computed by knowing the arc length formed by the trajectory P_B with respect to the beginning of the flexible section in which the first vertebra is considered as the origin of the base frame as in Figure 4.10. From Eq. 4.1 and Eq. 4.2 the equation of the arc length [313], [314] is defined in Eq. 4.3.

$$L_{arc} = \int_0^{\pi/2} \sqrt{\left(\frac{dx_I}{d\beta}\right)^2 + \left(\frac{dy_I}{d\beta}\right)^2} d\beta \quad \text{Eq. 4.3}$$

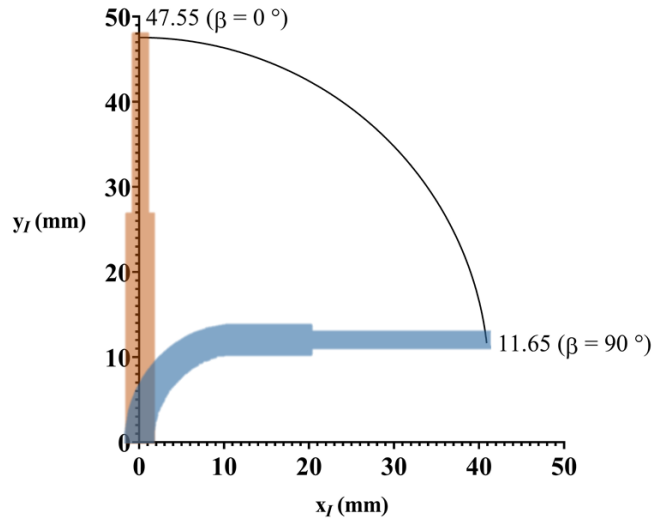


Figure 4.10 Trajectory of the distal end of the OCT catheter from 0° to 90° of bending with respect to beginning of the flexible section.

Using MATLAB to compute the integral in Eq. 4.3 for the range of $\beta = [0^\circ, 90^\circ]$, $L_{arc} = 59.52 \text{ mm}$, therefore $L_{arc_total} = 119.04 \text{ mm}$ for the full range of $\beta = [-90^\circ, 90^\circ]$. The area spanned when using the full rotation ϕ can be computed with the theorem of Pappus [315] for surfaces of revolution by solving the integral in Eq. D.45 included in annex D. The theorem of Pappus gives the area of a solid as from revolving the arc length about an axis. In this case the y-axis is used as the axis of revolution and solving for $\beta[0^\circ, 90^\circ]$:

$$A_{flex} = 2\pi \int_0^{\pi/2} y_I(\beta) \sqrt{\left(\frac{dx_I}{d\beta}\right)^2 + \left(\frac{dy_I}{d\beta}\right)^2} d\beta \quad \text{Eq. 4.4}$$

$$A_{flex} = 86.91$$

Area covered by the OCT probe for $\beta = 90^\circ$, $\Delta T = 28 \text{ mm}$, $\phi = [0^\circ, 360^\circ]$ and l_{max}

The area is composed of the cylinder formed by the full rotation of the tool with $\beta = 90^\circ$ and its translation over $\Delta T = 28 \text{ mm}$. From Figure 4.10 and Eq. 4.1 $r_{rig} = x_I(90^\circ)$, $x_I(90^\circ) = 40.90 \text{ mm}$.

$$A_{rig} = 2\pi r_{rig} \Delta T \quad \text{Eq. 4.5}$$

$$A_{rig} = 2\pi(4.09 \text{ cm})(2.80 \text{ cm})$$

$$A_{rig} = 72.19 \text{ cm}^2$$

Area covered by the OCT probe when the steerable OCT tool is retracted, $I = [Imp, Imax]$, $\beta = [-90^\circ, 90^\circ]$, $\Delta T \geq \Delta T_{max}$ and $\phi [0^\circ, 360^\circ]$

The region of interest is illustrated in Figure 4.11, where the back and lateral views are shown. The area consists of the white area due to the internal pullback translation of the optical probe $I = [Imp, Imax]$, plus the area composed of the bending section with $\beta [0^\circ, 90^\circ]$, translation of the tool in $\Delta T \geq \Delta T_{max}$, $I = Imp$ and rotation $\phi = [0^\circ, 360^\circ]$ represented by the gray area in Figure 4.11.

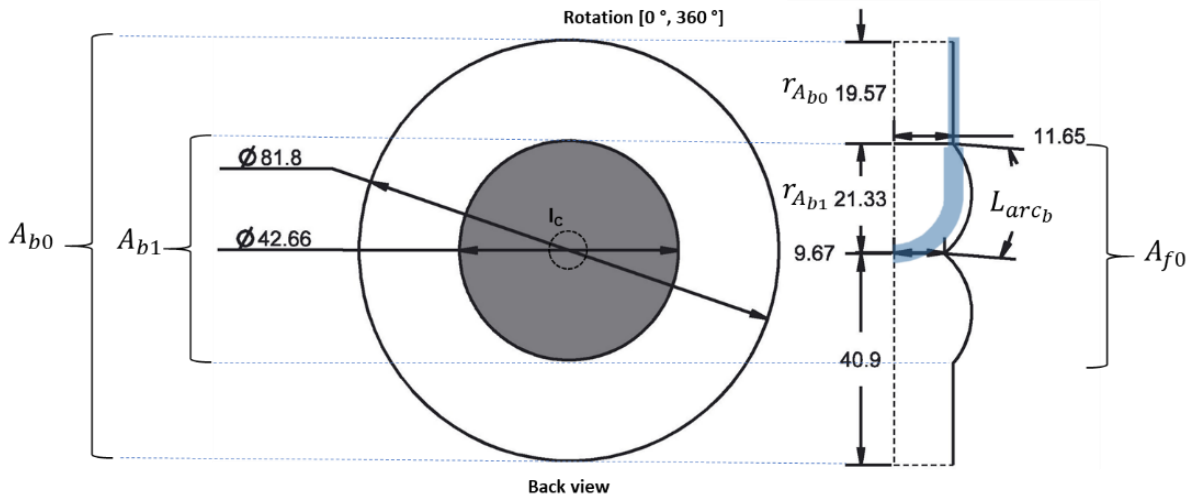


Figure 4.11 Back view of the workspace (A) and the lateral view of the back border of the workspace (B), all dimensions in mm.

The white region can be obtained by the subtraction of the regions $A_{b0} - A_{b1}$ in Figure 4.11 computed as the area of the circle and adding the area of the flexible section as A_{f0} . For the area of A_{f0} the Pappus theorem is used. Therefore, the total area A_b of the back view is:

$$A_b = A_{b0} - A_{b1} + A_{f0} \quad \text{Eq. 4.6}$$

$$A_{b0} = \pi(r_{Ab0} + r_{Ab1})^2 \rightarrow 52.55 \text{ cm}^2$$

$$A_{b1} = \pi(r_{Ab1})^2 \rightarrow 14.29 \text{ cm}^2$$

$$A_{f0} = 20.30 \text{ cm}^2 \text{ (see Eq. 4.4)}$$

The arc length was computed using Eq. 4.3 for $\beta = [0^\circ, 90^\circ]$ and $\Delta T \geq \Delta T_{max}$, Figure 4.12 shows the graph of the trajectory of the ball lens where $I = 9.67 \text{ mm}$ (Imp) and the end

of the flexible section in $I = 0 \text{ mm}$. The computed arc length is $L_{arc_b} = 23.79 \text{ mm}$. Therefore from Eq. 4.6 and using the theorem of Pappus, $A_b = 58.56 \text{ cm}^2$.

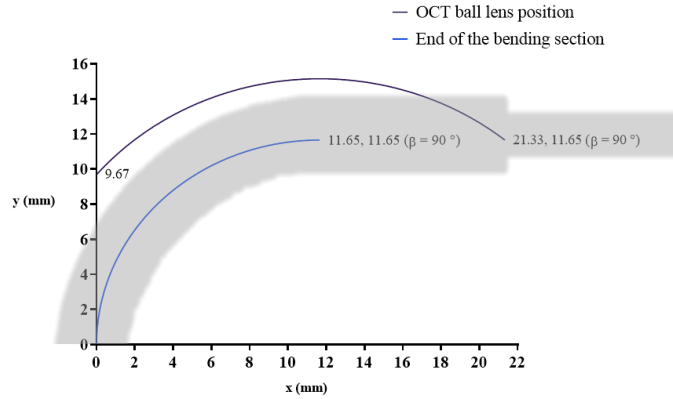


Figure 4.12 Trajectory of the OCT ball lens when the tool enters the channel in retraction maximum bending angle with respect to beginning of the flexible section, $I = 9.67 \text{ mm}$, $\beta [0^\circ, 90^\circ]$, $\Delta T \geq \Delta T_{max}$ and $\phi = 0^\circ$.

Total area of the envelope of the workspace

The total area of the workspace is defined as in Eq. 4.7:

$$A_T = A_{flex} + A_{rig} + A_b \quad \text{Eq. 4.7}$$

$$A_T = 217.66 \text{ cm}^2$$

Volume of the workspace

To compute the volume, it can be observed from Figure 4.13 that the volume is defined by Eq. 4.8, where V_{flex} is the volume determined by the bending section plus the V_{rig} being the volume cover by the cylinder formed by $\Delta T + y_{A_{f1}}$, where the last term $y_{A_{f1}}$ is related to the minimum distance between the tip of the tool and the entrance of the endoscopic channel in the unreachable workspace. The term V_u refers to the volume of the unreachable workspace.

Then the total volume is defined as:

$$V_T = V_{flex} + V_{rig} - V_u \quad \text{Eq. 4.8}$$

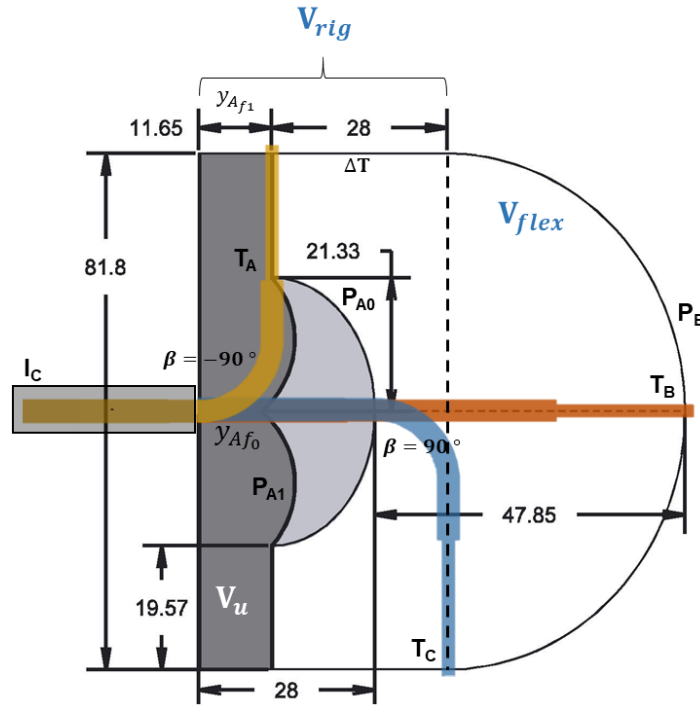


Figure 4.13 Lateral view of the volume of the workspace.

Volume of the flexible section

Since the arc length has already been computed as $L_{arc} = 59.52 \text{ mm}$, then maximum trajectory of the tip of the tool on each x-y component is given by $11.65 \text{ mm} \leq y_l \leq 47.55 \text{ mm}$, and $0 \text{ mm} \leq x_l \leq 40.9 \text{ mm}$ (see Figure 4.10), the transversal area formed by the trajectory P_B and the dotted line can be computed by integration of the parametric equations Eq. 4.1 -Eq. 4.2, then using the Pappus theorem to compute the volume of revolution about the y-axis. This is done by multiplying the transversal area and the distance travelled by the centroid \bar{x} of the region about the y-axis, the centroid is computed as in Eq. D.43 being $\bar{x} = 16.9 \text{ mm}$. The volume V_{flex} is computed as:

$$V_{flex} = 2\pi\bar{x} \int_0^{\pi/2} y_l(\beta)x_l'(\beta)d\beta \quad \text{Eq. 4.9}$$

$$V_{flex} = 119.28 \text{ cm}^3$$

Volume of the rigid section

The volume of the rigid section is defined as the cylinder with radius $r_{rig} = x_l(90^\circ)$ and height $h = \Delta T + y_{Af1}$. The volume is computed as:

$$V_{rig} = \pi r_{rig}^2 h \quad \text{Eq. 4.10}$$

$$V_{rig} = 208.37 \text{ cm}^3$$

Volume of the unreachable workspace

Computation of the unreachable workspace V_u is obtained by adding the volume defined by the outer section in white V_{ou} plus the volume of revolution defined by the hatched zone in Figure 4.14 under the bending trajectory V_{fu} . The volume of the non-hatched region V_{ou} is computed as the volume of a ring. The volume of the hatched section follows the same principle based on the theorem of Pappus.

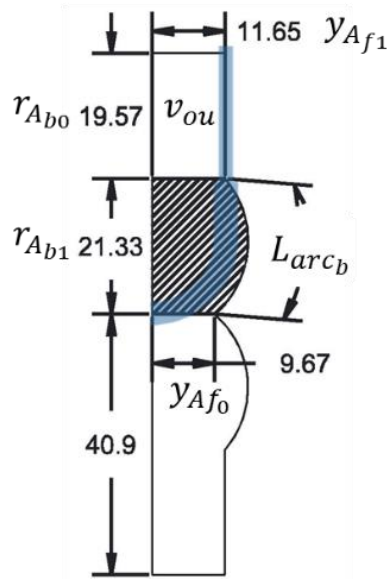


Figure 4.14 Lateral view of the volume of the unreachable workspace.

To compute V_{fu} equation Eq. 4.9 is used. For this case, $R = \frac{L}{\beta}$ is kept constant equal to $y_{Af1} = 11.65 \text{ mm}$ in Eq. 4.1-Eq. 4.2 to compute the desired trajectory for when the tool enters the channel in $\Delta T > 28 \text{ mm}$.

The centroid being $\bar{x} = 10.88 \text{ mm}$ (see Eq. D.43, Eq. D.47). Therefore:

$$V_{fu} = 20.03 \text{ cm}^3 \quad \text{Eq. 4.11}$$

Volume of the outer section of the unreachable workspace:

$$V_{ou} = y_{Af1} \pi \left((r_{Ab0} + r_{Ab1})^2 - r_{Ab1}^2 \right) \quad \text{Eq. 4.12}$$

$$V_{ou} = 44.57 \text{ cm}^3$$

Total volume of the unreachable workspace:

$$V_u = V_{fu} + V_{ou} \quad \text{Eq. 4.13}$$

$$V_u = 64.60 \text{ cm}^3$$

Total volume of the reachable workspace from Eq. 4.8:

$$V_T = 119.28 \text{ cm}^3 + 208.37 \text{ cm}^3 - 64.60 \text{ cm}^3$$

$$V_T = 263.05 \text{ cm}^3$$

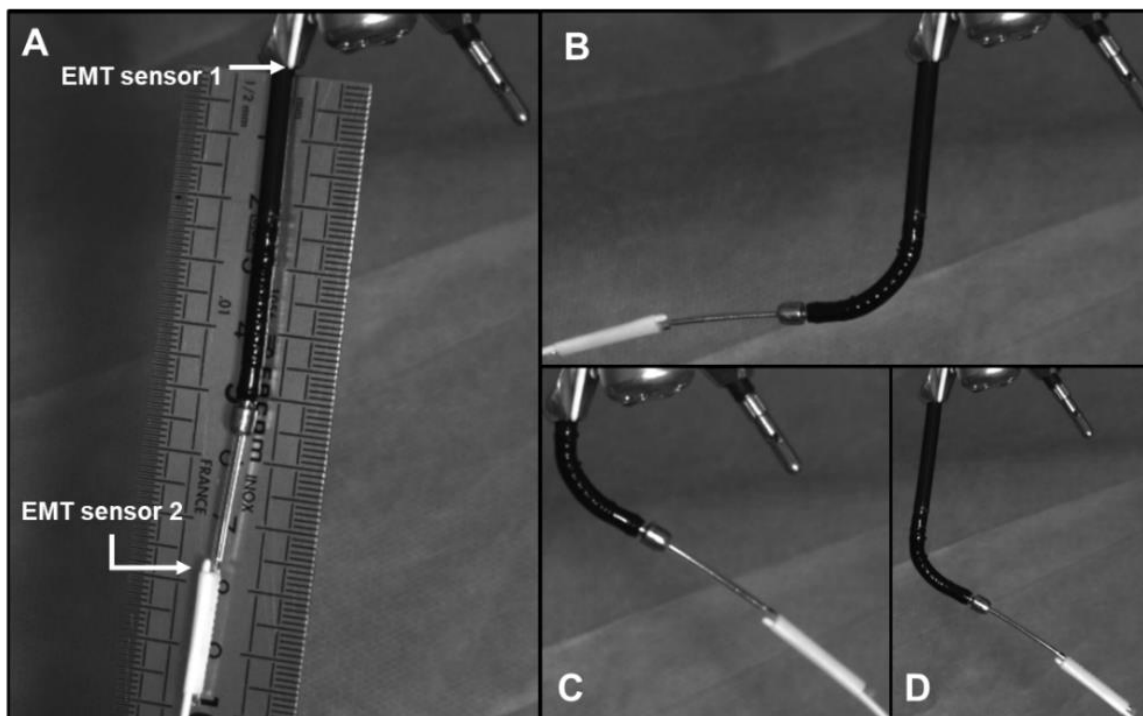


Figure 4.15 (A) Position of the two sensors of the electromagnetic tracker in the steerable OCT catheter. (B) Maximum bending to the right direction viewed from EMT sensor 1. (C) Maximum bending to the left direction viewed from EMT sensor 1 for $\Delta T = 28$, (D) Maximum bending to the left direction viewed from EMT sensor 1 for $\Delta T = 0$.

4.3.2 Experimental validation of the workspace

Validation of the workspace was performed using the Aurora electromagnetic tracker from NDI Digital, Inc. with two sensor coils 610060. Figure 4.15(A) shows the position of the sensors. The first sensor was placed at the output of the endoscopic channel and the second sensor as close as possible to the optical device. Figure 4.15(B) shows the maximum bending of the device in the right direction viewed from the sensor 1 with no retraction of the device.

Figure 4.15(C) represents maximum bending in the left direction viewed from the sensor 1 in retraction $\Delta T \approx 28 \text{ mm}$ for the reachable workspace. Figure 4.15(D) shows maximum bending to the left side viewed from the sensor 1 with no retraction. It can be observed that the bending is less than 90° because of the asymmetries previously explained in section 3.3.

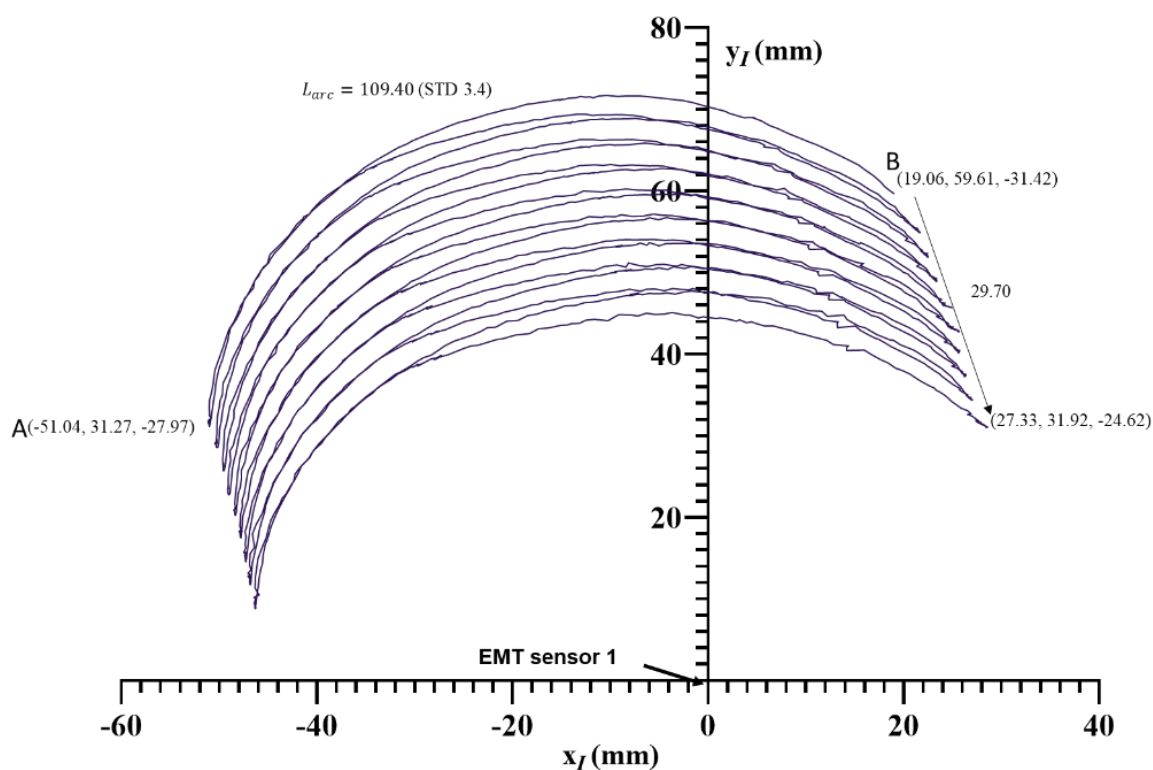


Figure 4.16 Position of the tip of the OCT catheter when performing repetitive trajectories over the range of -90° to 90° of bending angle and a translation of $\approx 30 \text{ mm}$ (XY view).

The experiment consisted in collecting 3D points representing the position of the tip of the tool with respect to the output of the endoscopic channel. In order to achieve this, various patterns of motion stimulating the flexion, rotation and translation of the tool were performed. For example, the sweep scanning pattern in the plane XY is shown in Figure 4.16 in the plane XY. The point (0,0) represents the position of the sensor 1. This pattern of a swing trajectory is achieved by engaging the maximum range of the bending of the tip from left to right with simultaneous translation motion of the catheter. The translation of 30 mm was performed in the experiment to test real limits. Translation of 29.70 mm was measured from the collected data, with an error of 6%. The distance from point A to point B in Figure 4.16 is 75.7 mm, the average for all the trajectories in Figure 4.16 is $76.7 \pm 0.2 \text{ mm}$, with an error of 6.2% with

respect to the expected value of 81.8 mm. The arc length measured was 109.4 (3.4) mm, with an error of 8%.

In addition to the motion in Figure 4.16, rotation of 360° was added obtaining the graph in Figure 4.17 in YX view. The same data plotted in ZX view is presented in Figure 4.18.

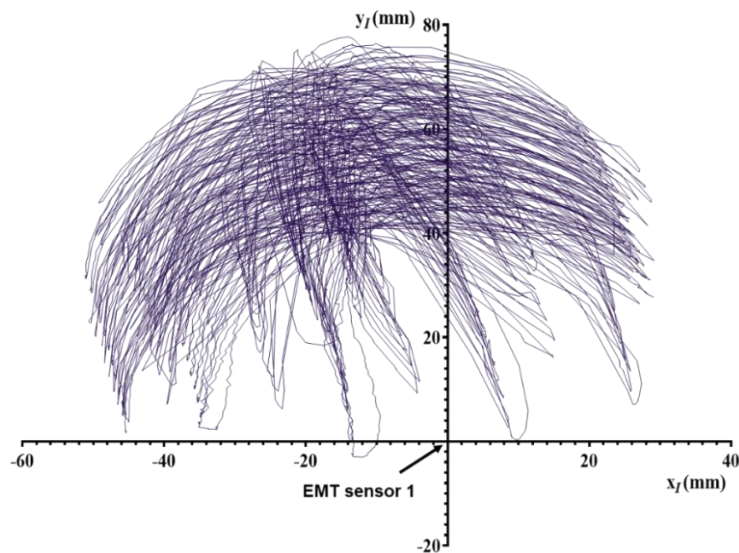


Figure 4.17 Position of the tip of the OCT catheter when performing repetitive trajectories over the range of -90° to 90° with a translation of ≈ 30 mm and a rotation range from 0 to 360° (YX view).

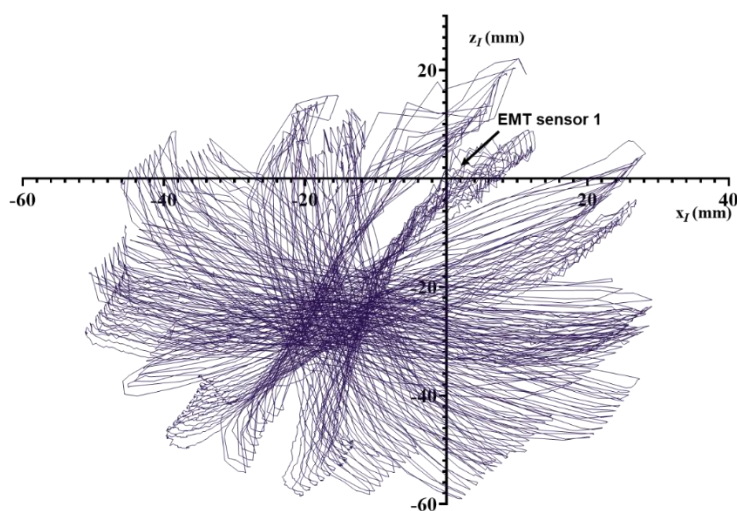


Figure 4.18 Position of the tip of the OCT catheter when performing repetitive trajectories over the range of -90° to 90° with a translation of ≈ 30 mm and a rotation range from 0 to 360° (XZ view).

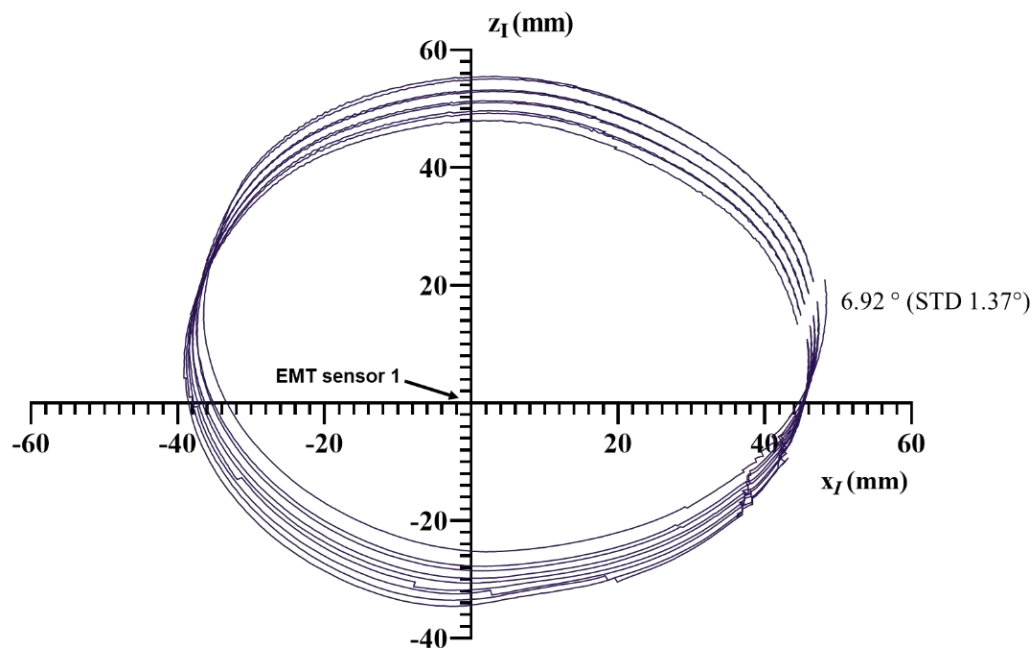


Figure 4.19 Position of the tip of the OCT catheter when performing repetitive rotational trajectories over the range of 0 to 360°.

Figure 4.19 shows the data collected for the experiment of repetitive rotational motions from 0° to 360°. The difference of 6.92° (1.37°) with respect to the expected 0° for full rotation can be observed. Although the rotation was performed in one direction, the tool can also be rotated in the other direction, which in practice would cover more than 360° of rotation. In this experiment the average diameter of the circular trajectory is 80.39 mm with a standard deviation of 4.77 mm and 1.7% of error with respect to 81.8 mm. In this case the diameter was closer to the expected value than that for the experimental results presented in Figure 4.17 because the fixed bending position of 90° was used from the bending direction in which the tool can reach this angle, while the rotation was performed.

Table 4.1 and Table 4.2 summarize the estimated and available validated values of areas and volumes based on the parameters measured from the collected data. It is important to note that the values with NA are those related to the unreachable workspace that were not validated by programmed routines in this work. An estimation of the total volume and area covered by the collected data was estimated using MeshLab software in Figure 4.20, and the values obtained are listed in Table 4.1 and Table 4.2.

Table 4.1 Summary of validated and estimated area.

Equation	Estimated (cm ²)	Validated (cm ²)
A_{flex}	86.91	93.99
A_{rig}	72.19	75.01
A_{b0}	52.55	50.76
A_{b1}	14.29	NA
A_{f0}	20.30	NA
$A_b = A_{b0} - A_{b1} + A_{f0}$	58.56	NA
$A_T = A_{flex} + A_{rig} + A_b$	217.66	209.69 (MeshLab)

In conclusion the validated area measured with MeshLab was 209.69 cm² with an error of 3.6% with respect to the 217.66 cm² of the estimated area. The volume measured by MeshLab was 255.29 cm³ in validation with an error of 3% with respect to 263.05 cm³ as estimated. It is important to clarify that the estimation with MeshLab was performed without considering the bending section at the full retraction of the tool, making it necessary to validate this section in the future for a more accurate estimation. The area covered by the steerable catheter is estimated to be about twice as large as the area covered by the tethered capsule. In addition, the steerable catheter provides a volumetric workspace which is not available in conventional endoscopic OCT catheters.

Table 4.2 Summary of validated and estimated volume.

Equation	Estimated (cm ³)	Validated (cm ³)
V_{flex}	119.28	203.90
V_{rig}	208.37	209.88
V_{fu}	20.03	NA
V_{ou}	44.57	NA
$V_u = V_{fu} + V_{ou}$	64.60	NA
$V_T = V_{flex} + V_{rig} - V_u$	263.05	255.29 (MeshLab)

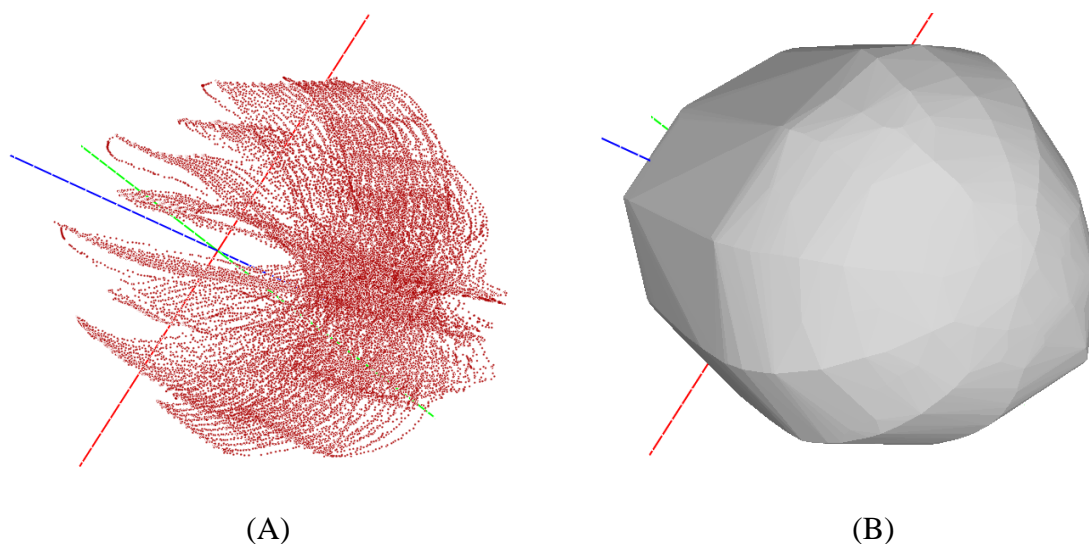


Figure 4.20 Point cloud rendered in MeshLab (A) resulting in an estimated area of 209.69 cm^2 and a volume of 255.29 cm^3 by using the convex hull filter (B). Axis x, y and z in red, green and blue colors respectively.

4.3.3 Three-dimensional artefacts in tool-based pullback scanning

Non-uniform rotational distortion has been analyzed in detail in section 3.4 according to the variation of the rotational speed for the regular catheter and the steerable catheter. In addition to the non-uniform rotational distortion, the precession of the OCT images between the frames acquired during the pullback scanning was also measured. The graph in Figure 3.30 shows this precession for the case of the regular pullback scanning of the inner optical probe in the steerable catheter. In this section, the effect on the rotational distortion and precession with the steerable catheter is analyzed when the pullback scanning is performed by the robotic instrument.

To perform the experiment, the pullback scanning was effectuated for the distance of about 20 mm to image the same target used for the previous NURD analysis. The actual scanning length was 20.9 mm and the speed of the pullback motion of the robotic instrument was 2.7 mm/s. The resulting NURD is plotted in Figure 4.21. The minimum distortion of $0.91 (0.64)^\circ$ was obtained at 1.06 mm and it reached its maximum of $6.03 (4.04)^\circ$ at 4.23 mm. There is a small improvement with respect to the maximum NURD of $7.03 (6.84)^\circ$ and $1.40 (0.96)^\circ$ with the regular pullback scanning. However, this difference is mainly due to the small variations of the velocity of the motor as shown in Figure 3.18 and Table 3.2, in which a standard deviation of 0.61 fps around the average speed of 127.43 fps is presented.

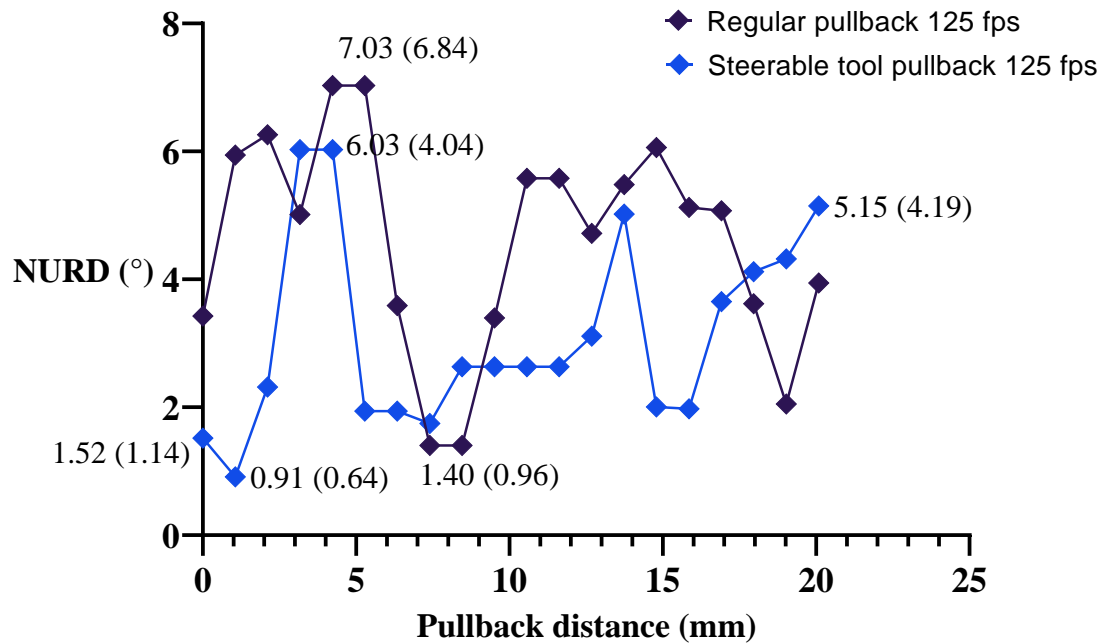


Figure 4.21 Rotational distortion versus pullback scanning distance for tool pullback with steerable catheter (mm).

On the other hand, there is an improvement in reducing the rotation of the image between frames (precession) when performing the scanning with the robotic pullback. This can be observed in the graph of Figure 4.22. The regular pullback scanning presents a rotation of -3.04° (4.05°) clockwise at 1.06 mm and a maximum rotation of 63.71° (6.45°) counterclockwise at 14 mm, ending in an angle of 28.55° (0.91°) at 20 mm. When performing the pullback with the robotic tool this rotation is reduced to a maximum of 6.03° (3.82°) counterclockwise at about 13 mm and the minimum angle of -5.83° (4.62°) at 18 mm and ending with the angle of -5.79° (4.91°). The improvement is of about 90% when using the robotic pullback scanning in terms of reducing the rotation between frames in comparison with the regular pullback scanning. Figure 4.23 shows the 3D reconstruction in both cases. The regular pullback scanning presents bigger deformation in Figure 4.23(A) due to the rotation of the image between frames, while it is reduced in the case of robotic pullback scanning in Figure 4.23(C). This difference can be observed in Figure 4.23(B) displaying the sum of the frames, in which the distortion due to the rotation is greater than that in Figure 4.23(D) corresponding to the robotic pullback scanning, in which the rectangular geometry is distinctive.

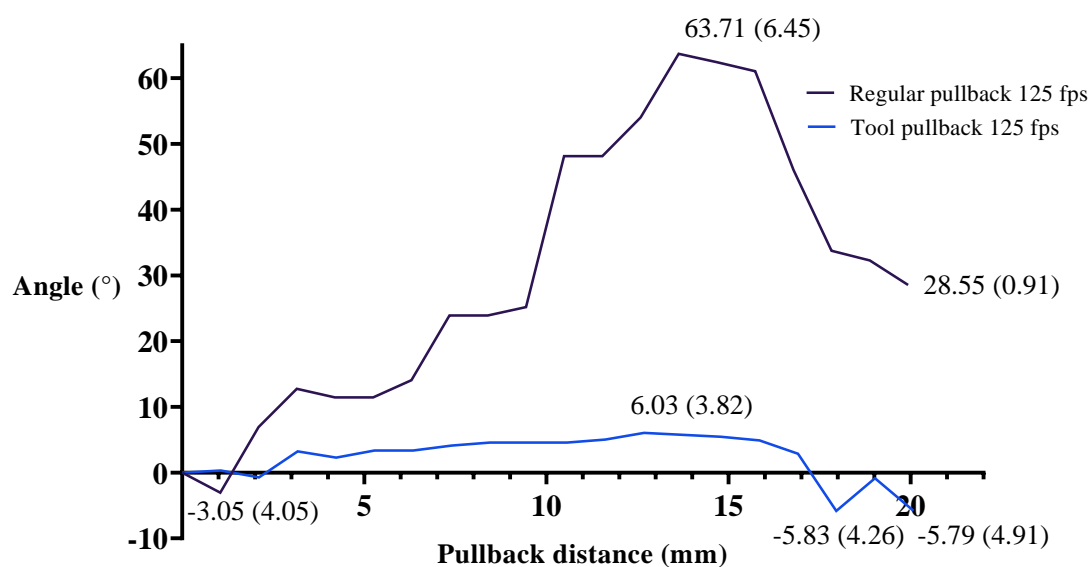


Figure 4.22 Angular rotation versus the pullback scanning distance (mm) for regular pullback and tool pullback with steerable catheter.

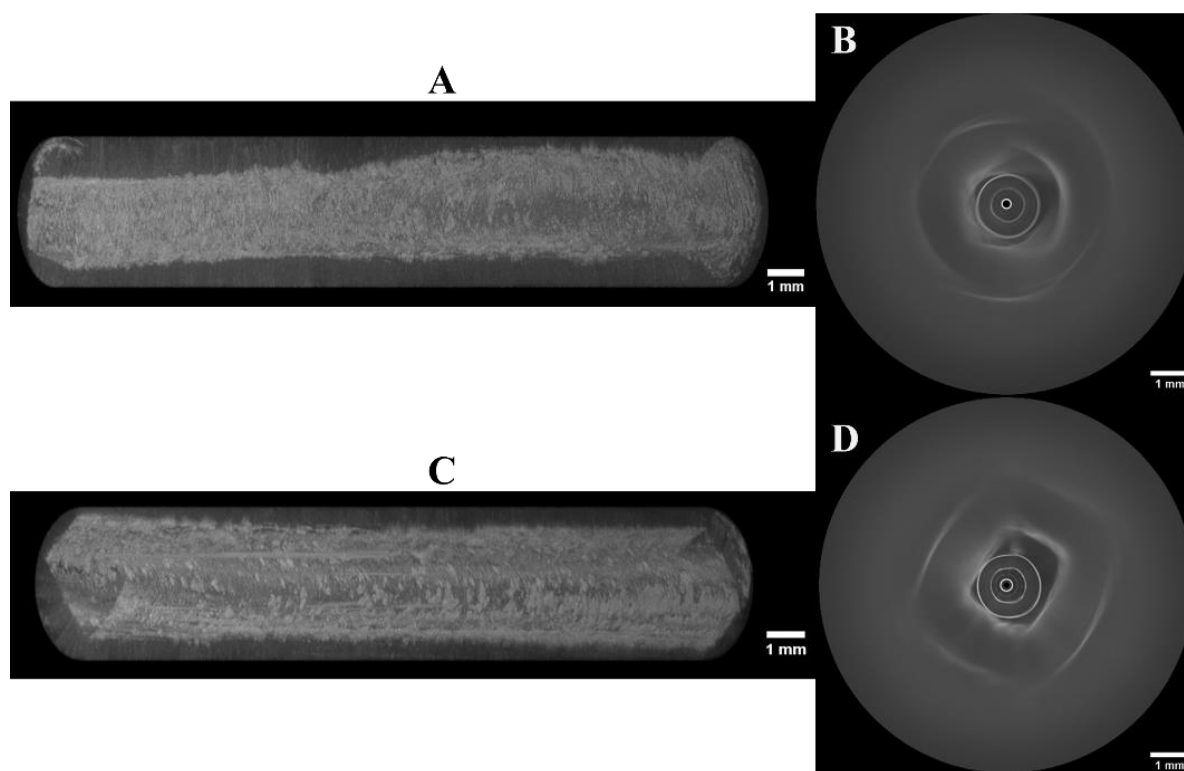


Figure 4.23 3D reconstruction of the rectangular tube by performing regular pullback scanning (a) at 125 fps, and robotic pullback scanning (c) at 125 fps, the sum of the frames corresponding to the regular pullback scanning (b) and the sum of the frames corresponding to the robotic pullback scanning (d).

The presented analysis has demonstrated the benefit of implementing the pullback scanning with the robotic tool instead of the conventional internal pullback, since this method reduces the precession of the OCT images by about 90% in comparison with the regular internal pullback. Regarding the variation of the speed of the motor, this is an issue that will be addressed by exploring the implementation of new control techniques in postdoctoral work.

4.4 Experimental validation

Figure 4.24 shows images of the experimental demonstration in a free space environment, in which mechanical motions of the instrument are operated by the user of the robot. In this case it was expected that the user could perform the flexion, rotation and translation motion of the OCT instrument.

The images in Figure 4.25 to Figure 4.27 show the motions performed by the user, from the initial position in image a) to image b) in which a translation motion in the forward direction was applied, followed by image c) demonstrating the flexion motion to the right direction, image d) representing the flexion motion to the left direction, in e) a rotation motion to the right direction together with flexion and finally d) showing the same rotation to the right applied in combination with flexion to the left direction. The last two images are shown in combination with the flexion motion to highlight that the rotation was performed, since the instrument does not have the capability of bending upward or downward. The only way to do this is by rotating the instrument and bending to the right or left directions. A full video was made demonstrating all the motions performed in this experiment from the endoscope view and the external view.

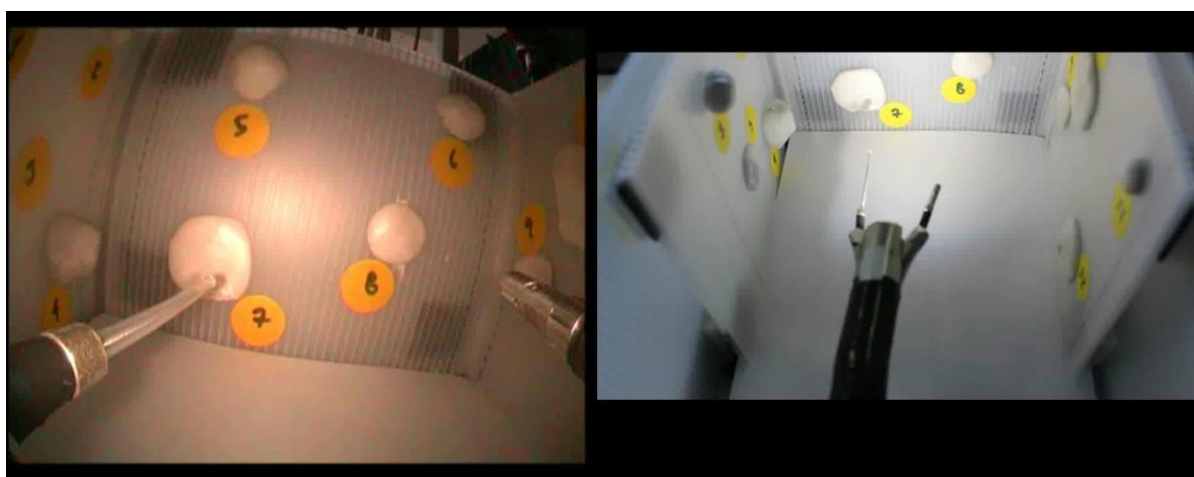
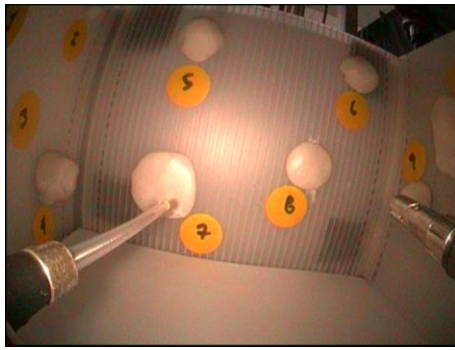


Figure 4.24 Free space test of the mechanical interaction of the system.

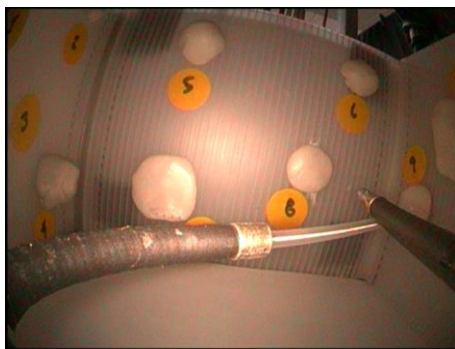


(A)



(B)

Figure 4.25 Free space test: (A) initial position, (B) forward translation.



(C)



(D)

Figure 4.26 Free space test: c) right side flexion, d) left side flexion, e) right side rotation and flexion, f) right side rotation and left side flexion.



(E)



(F)

Figure 4.27 Free space test: (E) right side rotation and flexion, (F) right side rotation and left side flexion.

4.5 Conclusions of the chapter

In Chapter 4, integration of the steerable OCT catheter with the robotic system has been described. Two degrees of freedom, translation and rotation of the tool have been added with

the incorporation of the catheter to the robot, such as well as teleoperation capabilities. Besides, the possibility of simultaneously manipulating the steerable OCT catheter and the second tool of the robot has been provided. The integration of the new OCT catheter to the robot has been done transparently due to the compatibility of the design.

The extended scanning workspace of the robotized OCT catheter area of the envelope of the volumetric scanning workspace and its volume have been estimated and experimentally confirmed with an electromagnetic tracker, measuring the actual values of arc length, translation, and workspace diameter. MeshLab was used for point cloud analysis and visualization. The difference of 6.92° (1.37°) with respect to the expected 0° was measured for full rotation in the rotational test. The average diameter of the circular trajectory obtained was 80.39 mm with standard deviation of 4.77 and 1.7% of error with respect to the expected 81.8 mm. The total validated area Measured with MeshLab was 209.69 cm^2 with an error of 3.6% with respect to the expected 217.66 cm^2 of the estimated area. The volume measured by MeshLab was 255.29 cm^3 in validation with an error of 3% with respect to 263.05 cm^3 as estimated. The area covered by the steerable catheter is estimated to be about twice as large as the area covered by the tethered capsule. In addition, the steerable catheter provided a volumetric scanning workspace which is not available in conventional endoscopic OCT catheters.

Non-uniform rotational distortion has been analyzed for the case of the steerable catheter. The comparison between performing regular pullback scanning and pullback scanning by using the translation of the robotic tool has been made; the outcome was a reduction of about 90% in terms of precession of the images. Demonstration of teleoperation of the tool was performed by stimulating the three degrees of freedom in a test box. Endoscopic images and a video of the demonstration have been registered.

4.6 French summary of the chapter

Le cathéter orientable décrit dans le chapitre précédent ne peut se fléchir que dans un plan. Dans cette partie, nous décrivons comment l'intégration du cathéter OCT orientable à l'endoscope robotisé permet d'ajouter 2 degrés de liberté supplémentaires (une translation et une rotation) au dispositif OCT.

Intégration mécatronique du système

STRAS est une plate-forme d'assistance robotique aux interventions chirurgicales par endoscopie flexible. Elle est basée sur la plate-forme manuelle Anubiscope™ développée par la société Karl Storz (Figure 4.1(A)). La robotisation de cette plate-forme se base sur la conception de systèmes modulaires télé-opérés assurant une installation facile tout en ajoutant un minimum de modifications à l'Anubiscope™ original. La motorisation de l'endoscope principal a été effectuée en remplaçant les molettes de la poignée de l'endoscope (figure 4.1(B)) par des motoréducteurs. Ils actionnent les 2 paires de câbles antagonistes assurant la flexion de l'endoscope dans deux plans perpendiculaires. La poignée de l'instrument dans la figure 4.1(B) a été remplacée par un module instrument (IM) incorporant le mécanisme d'actionnement. Ce dernier entraîne deux câbles antagonistes fléchissant l'instrument dans un plan. Le cathéter OCT orientable a été conçu pour être utilisé en combinaison avec l'endoscope flexible robotisé, ce qui implique qu'il n'est possible de le fléchir qu'à partir des commandes provenant de l'interface utilisateur du robot, et que la flexion manuelle n'est pas autorisée. De la même manière que tout autre instrument chirurgical, pour utiliser le cathéter OCT orientable il faut le coupler au système robotique en l'insérant dans le canal de l'endoscope, connecter l'IM au robot, et relier ses câbles de commande au panneau de commande principale du robot. En supplément, il est nécessaire de connecter la sonde optique au FORJ. Les fonctions d'imagerie OCT sont indépendantes du système robotique. Le clinicien dispose d'un retour visuel du contrôleur de l'endoscope et de la console d'imagerie OCT.

Compatibilité logicielle et contrôle du système

En ce qui concerne le logiciel de l'endoscope robotisé, aucune modification n'a été effectuée pour l'incorporation du nouveau cathéter OCT, la compatibilité de conception rendant l'intégration du cathéter OCT transparente pour le système.

Caractérisation et optimisation

La manipulation des cathéters OCT conventionnels consiste à exécuter un mouvement manuel vers l'endoscope. Il n'est pas possible de les diriger ou les télé-opérer. La zone de travail des cathéters OCT conventionnels effectuant un balayage rotatif se limite au mouvement de retrait/rotation. Elle couvre une zone cylindrique définie par la longueur de rétraction et la distance de travail du cathéter. Dans le cas de l'imagerie de l'œsophage, les cathéters

endoscopiques disponibles dans le commerce, tels que le système d'imagerie NvisionVLE® de Ninepoint Medical disposent de diamètres d'imagerie de 2,33 mm pour les cathéters à profil bas, et de 14 mm, 17 mm, 20 mm pour les sondes à base de ballonnet. Leur distance de retrait est de 6 cm. La zone de travail de ces cathéters est alors dans la gamme de 9,87 à 37,7 cm². Dans le cas d'une capsule intégrée, avec un diamètre de 12,8 mm et une longueur de distance d'imagerie allant jusqu'à 25 cm, il est possible de couvrir une surface d'environ 100 cm². Le dispositif d'OCT orientable décrit dans ce travail est un cathéter actif qui peut être télé-opéré grâce au système robotique décrit dans la partie précédente. Cette caractéristique permet d'augmenter le volume de l'espace de travail scanné par rapport aux cathéters passifs conventionnels.

La distorsion rotative non uniforme a été analysée en détail au chapitre 3, en fonction de la variation de la vitesse de rotation pour le cathéter régulier et le cathéter orientable. En plus de la distorsion rotative non uniforme, nous avons également caractérisé la précession des images OCT entre les trames acquises lors du balayage de retrait. Dans cette partie, nous analysons dans le cas du cathéter orientable, l'effet sur la distorsion rotative et la précession lorsque le balayage de retrait est effectué par l'instrument robotisé.

Validation expérimentale

La Figure 4.24 montre des images expérimentales en environnement libre, dans lequel les mouvements de l'instrument sont commandés par l'utilisateur du robot. Dans ce cas, l'utilisateur contrôlait les mouvements de flexion, de rotation et de translation de l'instrument OCT.

Les images des figures 4.25 à 4.27 montrent les mouvements effectués par l'utilisateur, à partir de la position initiale dans l'image a) à l'image b) pour laquelle une translation en avant a été appliquée, suivi par l'image c) montrant l'effet d'une flexion vers la droite, l'image d) représente une flexion vers la gauche, l'image e) montre une rotation vers droite combinée avec une flexion et enfin l'image f) montre la même rotation vers la droite combinée avec une flexion vers la gauche. Les deux dernières images sont présentées pour souligner qu'une rotation a été effectuée, puisque l'instrument n'a pas la possibilité de se fléchir selon la direction haut/bas. La seule façon d'y parvenir est de faire tourner l'instrument et de le fléchir selon la direction droite/gauche. Une vidéo complète a été réalisée pour présenter tous les mouvements effectués dans cette expérience depuis la vue de l'endoscope et la vue extérieure.

Conclusions du chapitre

Au chapitre 4, nous avons décrit l'intégration du cathéter OCT orientable avec le système robotique. Ceci a permis d'apporter deux degrés de liberté supplémentaires, la translation et la rotation de l'outil au cathéter OCT orientable ainsi que la possibilité de le téléopérer. Il est également possible de manipuler simultanément le cathéter OCT orientable et le deuxième outil du robot. L'intégration du nouveau cathéter OCT au robot s'est faite de manière transparente grâce à une conception optimale.

L'espace de travail étendu scanné par le cathéter OCT robotisé a été caractérisé en estimant son enveloppe et son volume. Ces données ont été validées expérimentalement avec un système de localisation électromagnétique ; en mesurant les valeurs réelles de la longueur d'arc, de la translation et du diamètre de l'espace de travail. MeshLab a été utilisé pour l'analyse et la visualisation des nuages de points. Sur l'essai en rotation, une différence de $6,92^\circ(1,37^\circ)$ par rapport au 0° prévu a été mesurée pour la rotation complète. Le diamètre moyen obtenu de la trajectoire circulaire est de 80,39 mm avec un écart-type de 4,77 soit 1,7% d'erreur par rapport aux 81,8 mm prévus. La surface expérimentale totale mesurée avec MeshLab est de 209,69 cm², soit une erreur de 3,6 % par rapport aux 217,66 cm² prévus de la surface estimée. Le volume expérimental mesuré par MeshLab est de 255,29 cm³, soit une erreur de 3 % par rapport à 263,05 cm³ estimé. La surface couverte par le cathéter orientable est estimée au double de la taille de la surface couverte par une capsule intégrée. De plus, le cathéter orientable est capable de scanner un espace de travail volumétrique, ce qui n'est pas le cas avec les cathéters OCT endoscopiques conventionnels.

La distorsion rotative non uniforme a été analysée dans le cas du cathéter orientable. La comparaison entre la réalisation d'un balayage régulier en retrait et le balayage en retrait en utilisant la translation de l'outil robotique a été faite ; le résultat a montré une réduction d'environ 90 % en termes de précession des images. La capacité de téléopérer l'outil a été testée en stimulant les trois degrés de liberté dans un environnement de test. Des images endoscopiques ainsi qu'une vidéo des tests ont été réalisées.

Chapter 5

Development of standardization model for pre-clinical validation

Content

5.1 Pre-clinical validation.....	140
5.2 The human colon model	140
5.3 Ex vivo swine intestine tissue imaging.....	143
5.4 Colorectal cancer phantom development.....	146
5.5 In vivo animal test.....	153
5.6 Conclusions of the chapter	156
5.7 French summary of the chapter	156

After the characterization of the robotized endoscopic OCT system developed, in this final chapter, the system is tested on phantoms, ex vivo swine tissue and finally on an in vivo swine colon.

5.1 Pre-clinical validation

Microscopic diagnosing of colorectal cancer requires development of novel catheter designs to allow for exploration of large areas of a colon that has complex geometry. However, there is limitation in the development, testing and in vivo validation of this novel optical approach of new imaging technologies such as the lack of a large animal (such as pigs) model for colon cancer. Also, clinical acceptance requires proof of reproducible and appropriate testing model for the system imaging performance. To solve this problem, tissue-mimicking optical phantoms are typically applied and provide the opportunity to evaluate the performance of the optical and spectroscopic instruments under controlled experimental conditions. A phantom is an artificial tissue with well-controlled optical properties, which can be specified according to the application. A variety of materials and methods for producing optical phantoms with known or verifiable properties has been already published [6-13].

The lack of a large animal model for colon cancer is a common limitation in the development and testing of new imaging technologies. Also, since clinical acceptance requires proof of reproducibility, an appropriate model for testing the system imaging performance is necessary. To solve this problem a new standardization model for benchtop validation was developed as a part of the doctoral project. This involved the development of optical phantoms that can mimic optical properties of normal and diseased polyps and can be inserted in the model of the human colon described in section 4.1. They were developed to mimic the thickness and near-infrared optical properties of each anatomical layer of a colon as well as the surface topography of colorectal polyps.

5.2 The human colon model

Figure 5.1(A) shows a picture of the ascending colon model LM107C [316] used to finalize the design of the OCT instrument and test the mechanical interaction and safety of the instrument integrated to the robotized flexible endoscope in a close-to-human environment.

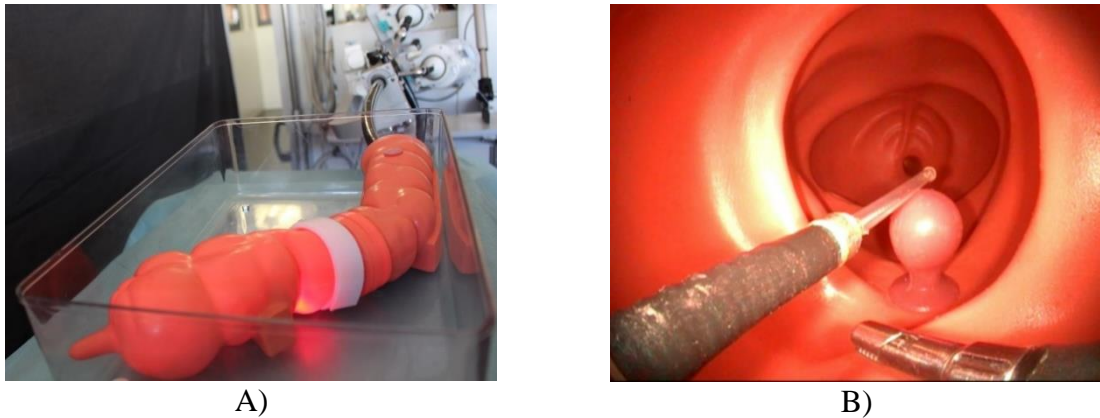


Figure 5.1 Ascending colon model LM107C used for test, (A) external view, (B) endoscope view and peduncular polyp.

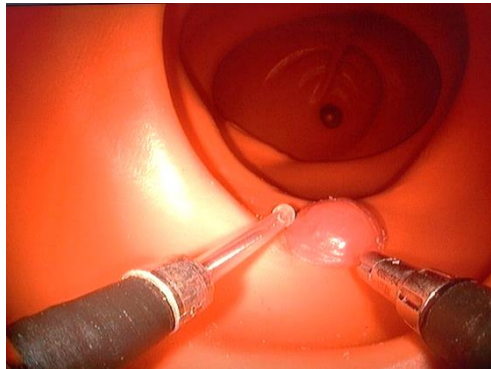


Figure 5.2 Ascending colon model LM107C used for testing, endoscope view and sessile polyp.

Figure 5.1(A) shows an external view of the ascending colon model and the robot, in which the light of the video endoscope can be noticed going through the wall of the phantom in red color. Figure 5.1(B) and Figure 5.2 are the views from the endoscope inserted inside the phantom. In these images it is possible to see the OCT instrument at the left side being steered to explore the phantom of a peduncular and sessile polyp that were also fabricated by the same company in [316]. In this experiment, based on subjective test of mechanical interaction of the new components integrated to the robot, the length of the OCT distal protective sheath was chosen. The system was tested by Dr. Bernard Dallemagne, an expert user of the robot. The objective was to obtain the first feedback from the point of view of the user perception and manipulation in a phantom that simulates the clinical case. In standard cardiovascular probes a pullback of 10 cm is available, such as 6 cm pullback in a balloon probe for the imaging of Barret's esophagus. During the test, the following lengths of the exposed transparent sheaths were used:

20 mm, 30 mm, and 40 mm. These lengths were tested to carry out a first evaluation of the ability of the user to explore the polyps as well as to navigate inside the phantom colon. The most important feedback from the perception of the user are listed below:

1. The longer the sheath of the probe the more difficult it is to place the tip of the probe in the desired position since it becomes less visible from the view of the endoscope camera.
2. The longer the sheath of the probe, the more difficult it is to interact with the second tool of the robot, since the differences in sizes add different perceptions related to each tool.
3. Placing the probe with the intention of imaging the front and rear sides of the peduncular polyp required the tool to be bent to 90°. This represents another difficulty, since the length from the base of the sheath to the point of flexion of the tool is about 21 mm, which allows a maximum of 39 mm for the length of the transparent sheath to perform 90° of flexion considering 60 mm for the diameter of descendant colon [317].
4. In the case of the sessile polyps, performing 90° of flexion for imaging is not a problem due to its shape, and for this case long sheath sizes can be used. However, a difficulty exists in the case of performing a parallel scanning from left to right or vice versa, the motion of which requires moving the endoscope itself while the probe remains stationary.
5. When exploring the peduncular polyp, the initial objective for the user is to scan the sample by moving the probe around the surface of the polyp while keeping the probe in contact with the tissue. This generates the problem of the probe being stuck when moving it near to the base of the polyp and changing direction to return back. This is not necessarily the only case in which this can happen, but it was the most common one during the experiment.
6. During manipulation it is difficult to estimate how much the probe is extended from the endoscope as the endoscope camera has no depth information. This is however a general limitation for the endoscope not only related to the OCT instrument but for all the tools.

The final length of 20 mm was chosen to ensure imaging of lesions ≤ 20 mm and keeping comfortable perception to the user. The clinical reason for choosing 20 mm of length is to ensure imaging lesions of at least 10 mm in diameter which present up to 38.5% of probability of dysplasia (precancerous lesions) [318]. It is important to highlight that the

previous list is a result of the very first trial to gain some initial feedback from an experienced user of robotized flexible endoscopes and to appreciate some of the limitations the user perceives in using the new robotic device. This feedback is important as a starting point for the design of more exhaustive experiments to optimize the system in the future.

5.3 Ex vivo swine intestine tissue imaging

The next step in validating the imaging performance of the OCT system developed consisted of imaging ex vivo swine small intestine in order to better understand the anatomy and optical properties of the tissue. A sample of swine intestine was collected in collaboration with IRCAD. The freshly excised tissue was frozen before imaging. For imaging, the tissue was then thawed and cut into smaller sections and cut lengthwise to open the intestine and give access to the lumen (Figure 5.3). The main objective of this study was to image the architecture of the intestine and to test the use of OCT for assistance in two steps typically performed during ESD procedures: margin marking with a cautery tool and submucosal injection of methylene blue injection. The tissue has been imaged using both benchtop and endoscopic sample arms (Figure 5.4). Following imaging, the tissue was submitted for histological processing (Figure 5.5).

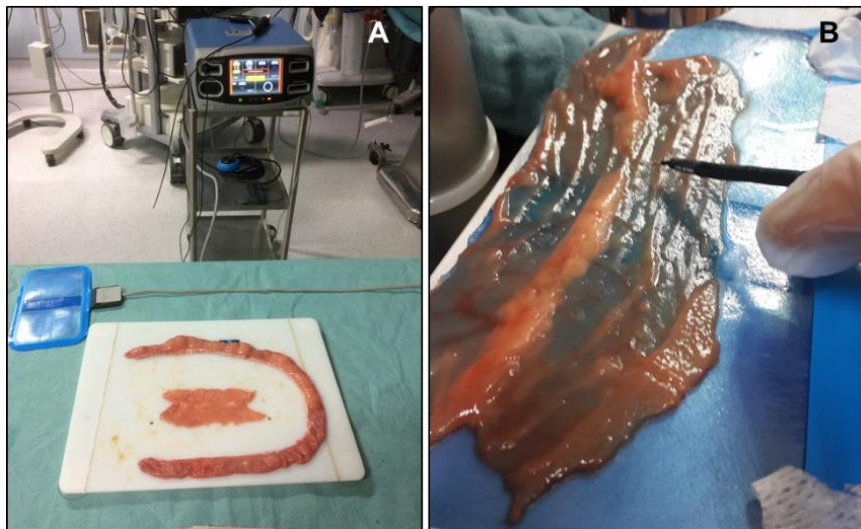


Figure 5.3 (A) Excised small swine intestine for ex vivo OCT imaging. (B) Closer view of the sample.

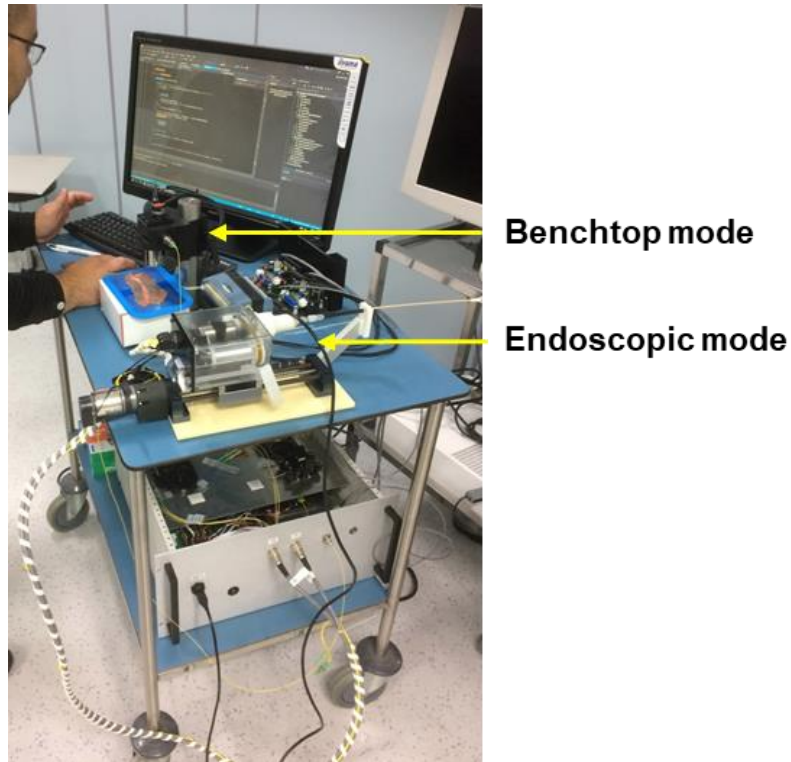


Figure 5.4 OCT imaging of the ex vivo sample using both, the benchtop and endoscopic modes.

Figure 5.5 shows the image of a sample of swine small intestine under OCT (A) in comparison to its histological image (B), in which is possible to distinguish three layers corresponding to the mucosa, submucosa and muscle layers. The axial resolution of the OCT image is $7 \mu\text{m}$ and the lateral resolution is $26 \mu\text{m}$.

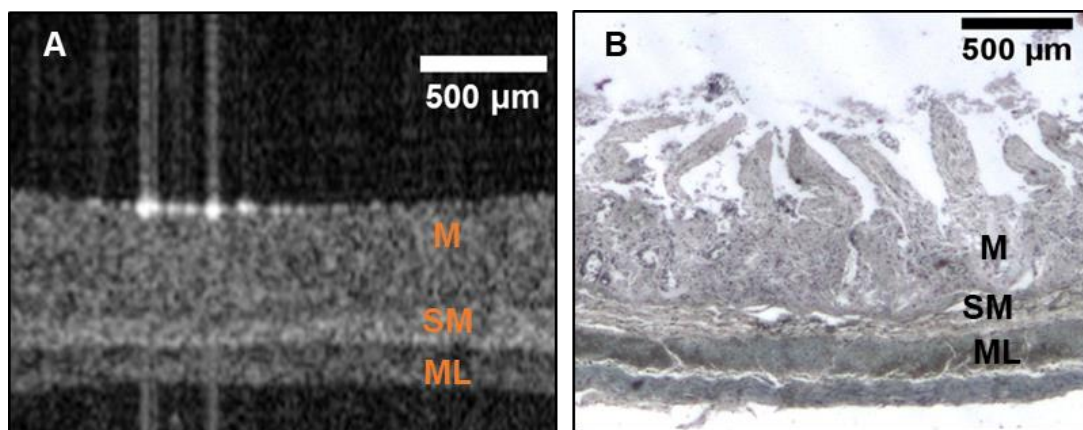


Figure 5.5 Ex vivo swine small intestine imaging, (A) OCT cross-section, (B) histology.

Cautery marking

The marking tissue test was performed by using a standard cautery tool used during endoscopic procedures. Figure 5.6(A) shows an excised ex vivo swine small intestine, in which tissue marking is done with the cautery tool with real-time monitoring with the OCT benchtop mode. Figure 5.6(B-D) shows the moment when the tool is placed before marking, during the marking so that the smoke caused by the cauterization is visualized in Figure 5.6(C). The mark is visualized under the OCT imaging system after cauterization in Figure 5.6(D).

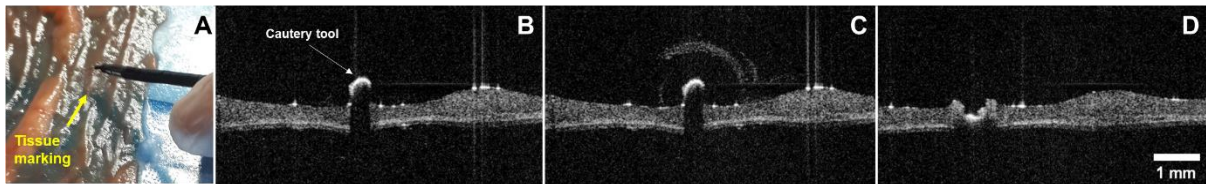


Figure 5.6 Tissue marking using a cautery tool under OCT imaging. (A) Excised ex vivo swine small intestine and cautery tool, (B) Tip of tool before cauterization, (C) during cauterization and (D) after cauterization.

Methylene blue injection

Methylene blue injection was also performed under the OCT benchtop real time image acquisition. The intention was to observe if it was possible to recognize the tip of the needle and to perform the injection of the liquid. This step is important since it is part of surgical procedure in endoscopic submucosal dissection. Figure 5.7 shows the tip being placed on the tissue before the injection was performed. In Figure 5.8 can be observed the needle and the drop of methylene blue after injection which appears transparent in the OCT image.

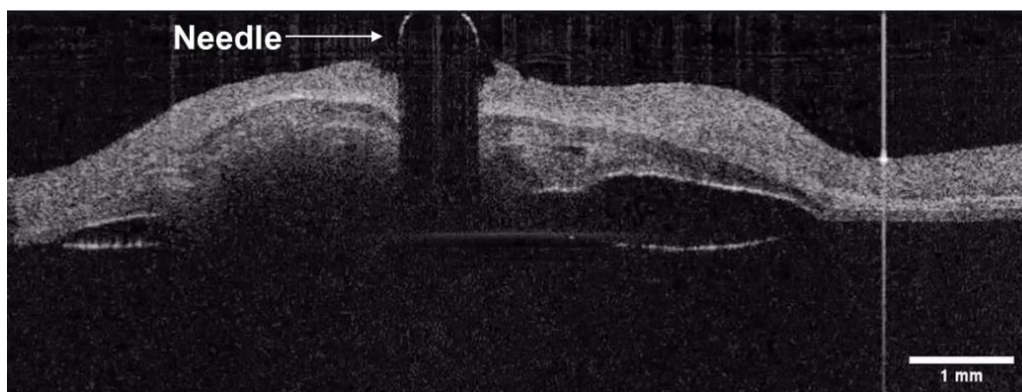


Figure 5.7 Methylene blue injection, needle placed in the ex vivo tissue before injection.

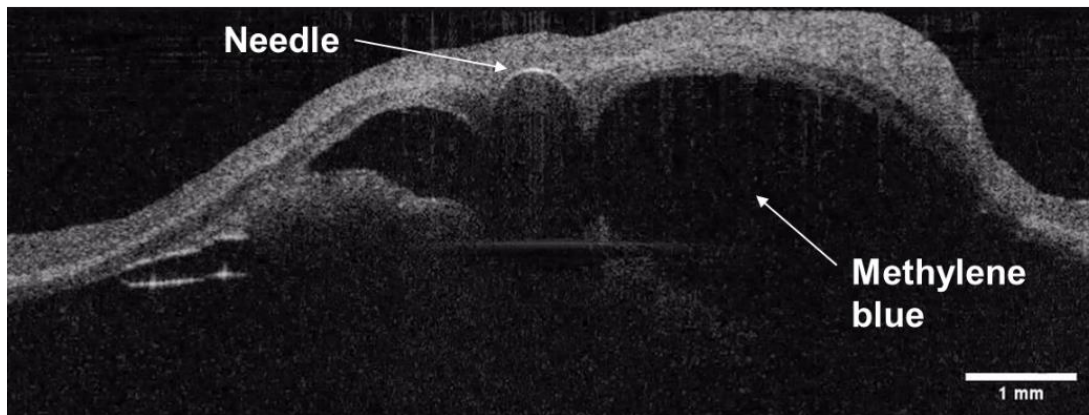


Figure 5.8 Methylene blue is visualized after injection.

5.4 Colorectal cancer phantom development

Based on a literature search and ex vivo imaging of the small intestine a protocol for manufacturing phantoms of colorectal normal and cancerous lesions was developed. A phantom is an artificial tissue with well-controlled optical properties, which can be specified according to the application. The optimal phantoms for gastro-endoscopic applications and minimally invasive treatment should have the following criteria:

- 1) The refractive index is close to approximating that of bio-tissue 1.43.
- 2) Controllable optical properties (scattering coefficient, absorption coefficient).
- 3) Controllable thickness and structure (layered, flat etc.).
- 4) High durability (stability over 6 months).
- 5) Color-matched for white light endoscopy.
- 6) Mounting system allowing placement in various locations of the bench-top colon model and removal using standard endoscopic tools.
- 7) Biocompatibility.

A variety of materials and methods for producing optical phantoms with known or verifiable properties have been already published [319]–[326]. Table 5.1 summarizes the properties of popular materials for phantom fabrication. Latex, commonly used for some tissue-mimicking phantoms, has sufficient elasticity, but it is highly absorbing, and its optical properties cannot be tuned to mimic the optical properties of tissue. Fibrin phantoms, while

compatible with biological materials, have limited shelf-life and limited ability to accommodate 3D-structure due to its high viscosity. PVA-C is highly elastic and optically tunable, but it has a complicated curing process that makes it difficult to create uniform layers or shapes [319]. Silicone (PDMS) is a convenient base material for phantoms fabrication, where elasticity is not required. It provides compatibility with a wide range of suitable scatters for adjustment of the optical properties. Another perspective material with unique optical and highly viscous properties is the silicone-based liquid polymer called Dragon Skin. It is often used for mold-castings, fabrication of full-face masks, and has recently been used for the fabrication of complex disease-mimicking optical phantoms [327]. It is sold commercially as a two-part polymer (part A and part B), is usually prepared by mixing parts A and B in a 1:1 ratio by weight and is available in a variety of curing times ranging from 30 minutes to 16 hours. Silicon-based forms such as PDMS or Dragon Skin are liquid and can be easily doped with any scatters (color pigments, nano- and microparticles).

All the aforementioned materials require a certain amount of specialized equipment, and complicated manufacturing protocol. Among the fabrication techniques, 3D printing is the most convenient method with a great number of available materials. One of them is a widely used acrylic based VeroWhite Resin. This material creates 3D printed objects from a base of photosensitive polymer liquid. This liquid is then solidified by UV light layer by layer to create a rigid and highly detailed 3D prints which are comparable to injection molded plastics.

Table 5.1 Materials for phantoms fabrication [319].

	Latex	Fibrin	PVA-C	PDMS	Dragon skin	VeroWhite
Cure time	Minutes	10 min	8 hours	90 min	30 min	ms
Curing process	Room temperature	Enzyme-induced proteolysis	Multiple freeze/thaw cycles	Heat 60-90°C	Room temp	3D printing/ Photocuring
Optically tunable	No	Yes	Yes	Yes	Yes	No
Shelf-life	Years	1 month	6 months	Years	Years	Years
Storage conditions	Air, room temperature	Saline, refrigerate	Water, room temp	Air, room temp	Air, room temp	Air, room temp

Layered phantom fabrication

The existing methodology for manufacturing PDMS based calibration phantoms for qualitative imaging of tissue properties with spatial frequency domain imaging [328] was modified to achieve layered phantom representing a healthy digestive wall. The first step was to calculate the right volume of PDMS silicon. The volume or mass of the solution which was poured into the mold determined the thickness of the layer. For example, if a square metallic mold has dimensions of 9x9 cm, in order to make a 600 μm layer representing mucosa, the following calculation needs to be followed: $V_{\text{mucosa}} = 9 \times 9 \times 0.06 = 4.9\text{ml}$ (or 5mg with taking into account PDMS density of 1.05 g/cm^3). Once the volume of the PDMS is known, different scattering properties are achieved by adding Titanium dioxide (TiO_2) particles (refractive index 2.49, anatase form, Sigma Aldrich, Saint Louis, Missouri) into the PDMS (refractive index 1.41, Sylgard® 184 Silicone Elastomer Dow Corning) [320]. Table 5.2 contains calculations of TiO_2 for each layer according to their thickness. The optical properties of the layers had to be modified to provide different scattering properties of each of them. The concentration of scatterer was changed to have a second layer with enough scattering contrast. The process was repeated three times in different molds by adjusting the mass of TiO_2 . At each step, the optical properties of the first and the second layer were compared, and the appropriate TiO_2 mass was used that allowed to have a high contrast between layers to mimic mucosa, submucosa, and muscle layer.

Table 5.2 Final composition of each layer and testing in the OCT system.

	Thickness	PDMS	PDMS in the mold	Curing agent	TiO_2
1 st : Mucosa	600 μm	10mL	5g	1mL	0,012g
2 nd : Submucosa	130 μm	10mL	1g	1mL	0,100g
3 rd : Muscle layer	700 μm	10mL	5g	1mL	0,022g

The desired absorption properties are obtained by adding nigrosine into the curing agent before mixing and curing both components of the phantom matrix. Since the phantoms are developed for the OCT that works in the near-infrared range the nigrosine is not used as it has a much smaller impact on the optical properties such as scattering. The fabrication procedure for manufacturing layer of a phantom for OCT imaging is summarized and represented in Figure E.3 in the annex E.

To mimic healthy mucosa three different layers were manufactured consecutively: mucosa = 600 μm , submucosa = 130 μm and muscle layer = 700 μm . The concentration of scatters was changed in each layer to provide different scattering properties. To confirm that the optical properties of the developed layered phantom are correct, the intensity profile of the averaged 50 A-lines was plotted using ImageJ and compared to the profile of previously published normal mouse colon tissue [329] (Figure 5.9).

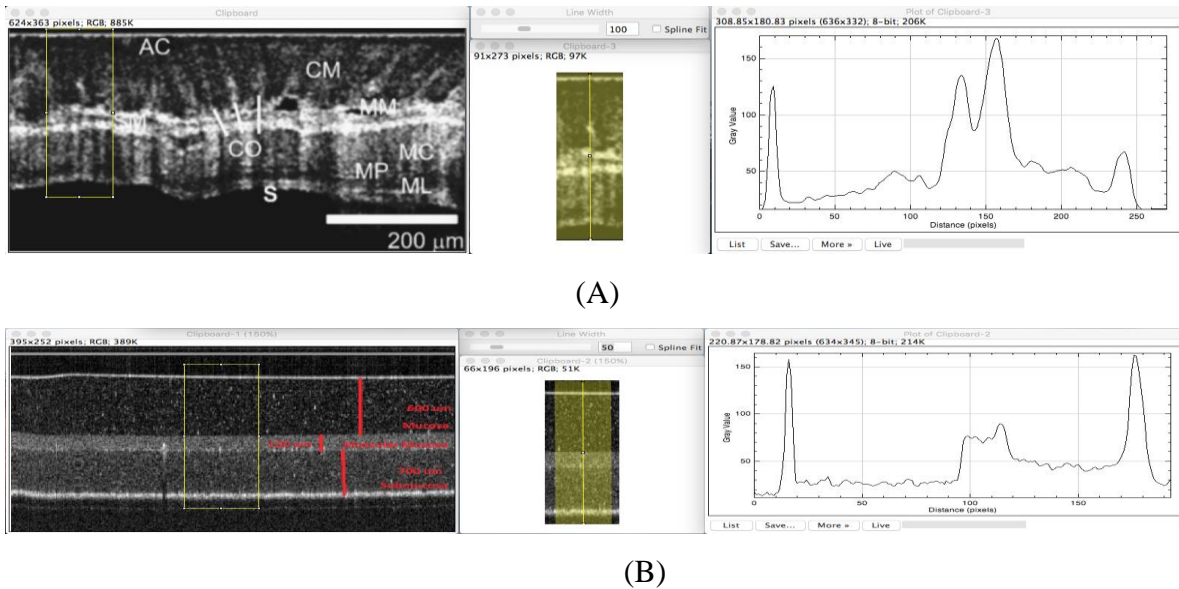


Figure 5.9 OCT B-scans and A-scans obtained with ImageJ of (A) normal mouse colon tissue [329] and (B) tissue-mimicking phantom.

Phantom design – form factor and mounting

Given the time and complexity of manufacturing and liquidity of the PDMS material, in order to achieve more complex structures of colorectal polyps, different manufacturing techniques were combined. A schematic representation of the major variants of type 0 neoplastic lesions of the digestive tract is shown in Figure 5.10 [330]. Phantoms corresponding to sessile, early stage pedunculated benign and malignant polyp types were developed using VeroWhite 3D-printing (Figure 5.11(A)). Following 3D printing the PDMS matrix with TiO_2 was inserted in the cancer inclusion. Once all the inclusions were cured, phantoms were covered with the Dragon skin layer mixed with a dye to mimic mucosa layer color (Figure 5.11(D)).



Figure 5.10 Superficial polyps schematic representation.

To enable placement of the developed phantoms in various locations of the bench-top colon model and their removal using standard endoscopic tools, small neodymium magnets were placed in the base of polyps. The polyps were then mounted by placing another neodymium magnet outside of the colon model (Figure 5.11(B-D)). Such a mounting system allows for testing the ability of OCT to assist during endoscopic removal of polyps.

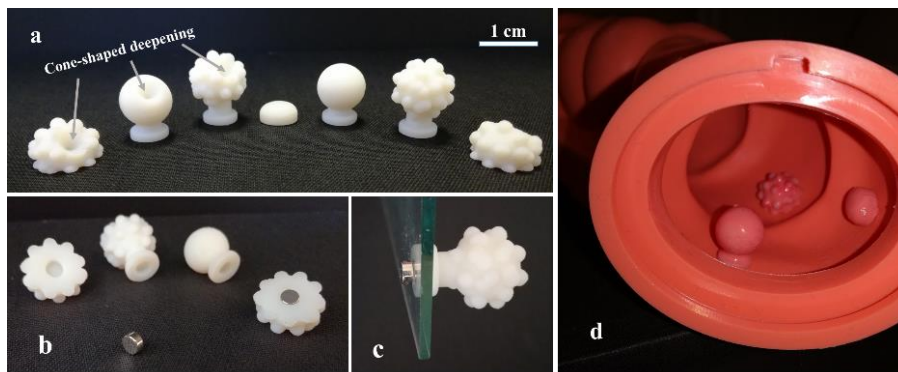


Figure 5.11 (A) Set of phantoms, (B-C) magnet mount, (D) positioning of phantoms in the artificial colon.

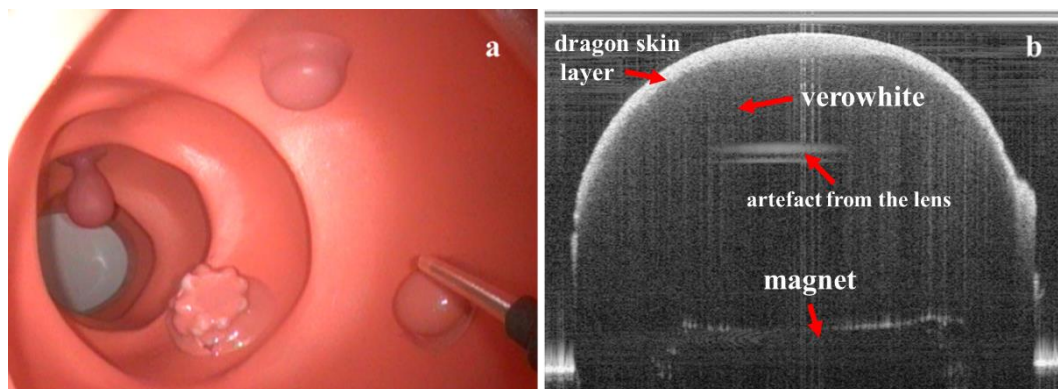


Figure 5.12 (A) White-light endoscopy image of artificial colon with phantoms, (B) bench-top OCT image of polyp phantom.

Color-matching was confirmed in endoscopic examination as shown in Figure 5.12(A). Three sessile and one pedunculated polyp mimicking phantoms are visible inside of the artificial colon together with the OCT catheter that was placed close to one of the phantoms.

The same sessile polyp phantom was imaged with the bench top OCT mode (Figure 5.12(B)). The surface layer of colored dragon skin can be observed as a highly scattering top layer followed by a low scattering VeroWhite. The neodymium magnet can also be seen inside the phantom.

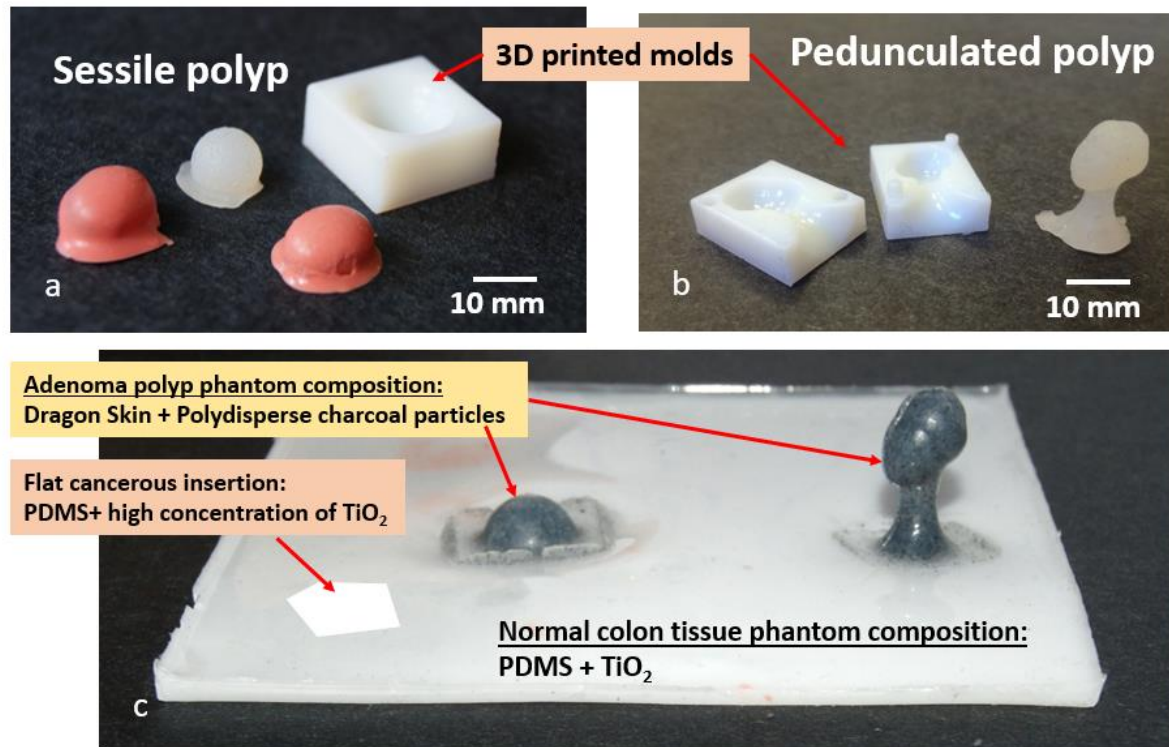


Figure 5.13 Sessile (A) and pedunculated (B) polyp phantoms with 3D-printed VeroWhite molds, (C) Polyp phantoms attached to normal colon tissue phantom with cancerous tissue insertion.

Multi-material phantom fabrication

VeroWhite 3D printing is a fast and convenient method to achieve various polyp shapes, however this manufacturing method has limitations in terms of the modification of the optical properties. Since it is a photocuring polymer, a change in the composition by insertion of scattering particles can lead to curing difficulties. Based on PDMS and 3D printing experience a multi-material manufacturing method was developed for straightforward and fast fabrication of phantoms. In this case 3D printing was used to create VeroWhite resin molds (Connex 350, Stratasys) to generate various phantom shapes with PDMS and Dragon Skin. The fabrication process involves first layer-by-layer formation of PDMS (Silicon elastomer 184, Sylgard Dow Corning) films doped with TiO₂ (Titanium (IV) oxide, 98+%, anatase powder, Acros Organic)

to mimic anatomical layers as in section 5.3. Polyp phantoms made of Dragon skin in 3D printed molds were then attached on layered PDMS structure and airbrush with colorant spray to modify the surface color and topology (Figure 5.13).

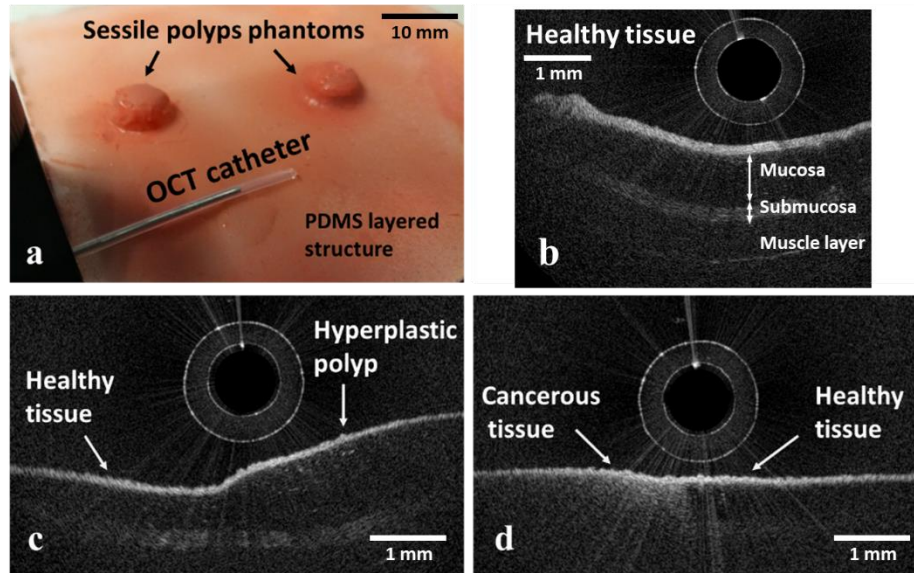


Figure 5.14 (A) image of tissue-mimicking phantom; OCT images of phantoms mimicking: (B) healthy tissue; (C) hyperplastic polyp, (D) cancer.

OCT tests of the PDMS/Dragon skin phantoms developed corresponded to hyperplastic sessile polyps, early stage sessile and pedunculated polyps and malignant flat polyp types as shown in Figure 5.13(B-D). The OCT catheter was placed close to the phantom surface to obtain the images. A healthy colon tissue phantom is presented in Figure 5.14(B), which shows a layered structure mimicking the mucosa, submucosa and muscle layer, with different scattering coefficients [331]. Hyperplastic polyps, which stay benign in most cases and might not be removed during biopsy or surgery, are anatomically represented by extension of mucosa and thus might be mimicked as a thickening of this tissue layer with the same optical properties (Figure 5.14(C)). This was obtained by using the same PDMS/TiO₂ mixture as for mucosa mimicking and applying it to the surface as a drop or with a sessile polyp VeroWhite mold. The flat malignant or most suspicious dysplastic polyp phantom is shown in Figure 5.14(D). The surface layer of such tissue has higher scattering which decreases in the bulk with no evidence of layered structure. Low scattering tissue is in good agreement with theoretical and experimental studies of malignant tissue optical properties and OCT imaging since it has less collagen than that present in normal tissue [332]. Higher scattering of cancerous tissue was

obtained by increased concentration of TiO_2 . Finally, the sessile polyps were covered by a thin layer of Dragon skin for color-matching.

Some first OCT phantoms with realistic optical properties and morphology have been obtained. These phantoms have served as a convenient tool to evaluate and standardize OCT image quality and measurement accuracy of the new system. Such performance standardization can lead to improved performance of measurements from clinical and research OCT devices, thus enhancing reliability of diagnostic decisions and facilitating the development of innovative diagnostic technologies.

5.5 In vivo animal test

The system mechanical and imaging performance have been verified in bench-top and ex vivo sample imaging, respectively. In the next step, the objective was to demonstrate the capability of acquiring real time images using the steerable and teleoperated OCT catheter being manipulated as a surgical instrument of the robotized endoscope in vivo in swine (Yorkshire, >20kg). The study protocol was approved by the Institutional Ethical Committee on Animal Experimentation, and animals were managed in accordance with French laws for animal use and care as well as European Community Council. The animal was anesthetized and before the procedure the bowel was cleaned using rinsing of the colon. The OCT steerable tool was inserted into the instrument channel of the endoscope and the driver was fixed in the proximal end of the endoscope. The cautery tool was inserted in the other channel of the endoscope. The robotized endoscopic system was turned on and all degrees of freedom were calibrated before the procedure. Following calibration, both instruments were retracted to their most proximal position and the distal side channels were folded. The endoscope light source and processor were turned on and the scope was manually inserted into the colon by a trained physician (Dr Bernard Dallemagne) using white light endoscopic images. Once in position, the OCT system and catheter scanning was started, and scope side channels were opened. Using master controllers and the white light endoscopy images, the physician navigated the main endoscope and placed the steerable OCT probe in contact with the tissue to obtain OCT cross-sectional images of the mucosa. OCT images were displayed in real-time on the second screen next to the endoscopic image. After the imaging procedure was finished, both instruments were again retracted to their most proximal positions and the channels were closed for removal of the endoscope. Following the procedure, the swine was euthanized. Figure 5.15(A) shows

preparation of the medical room at the Research Institute against Digestive Cancer (IRCAD). In Figure 5.15(B) the installation of the robot next to the surgical table is visualized.

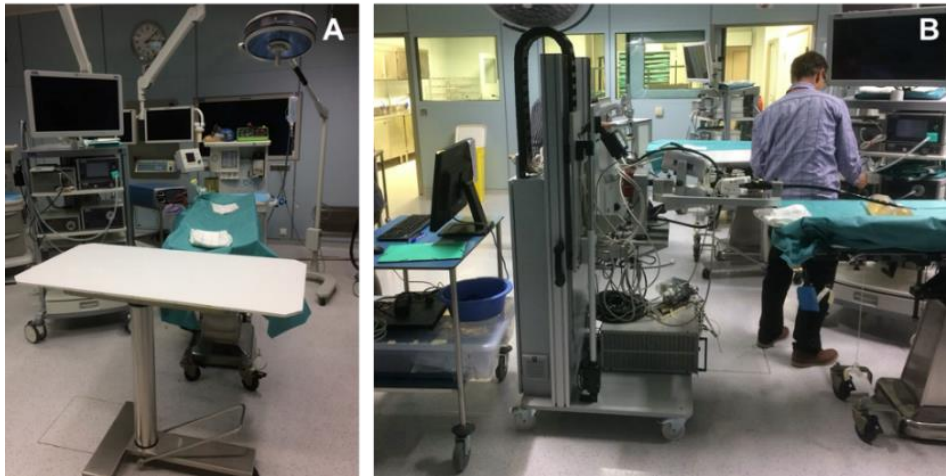


Figure 5.15 (A) Preparation of the medical room and (B) installation of the robotic system close to the surgical table.

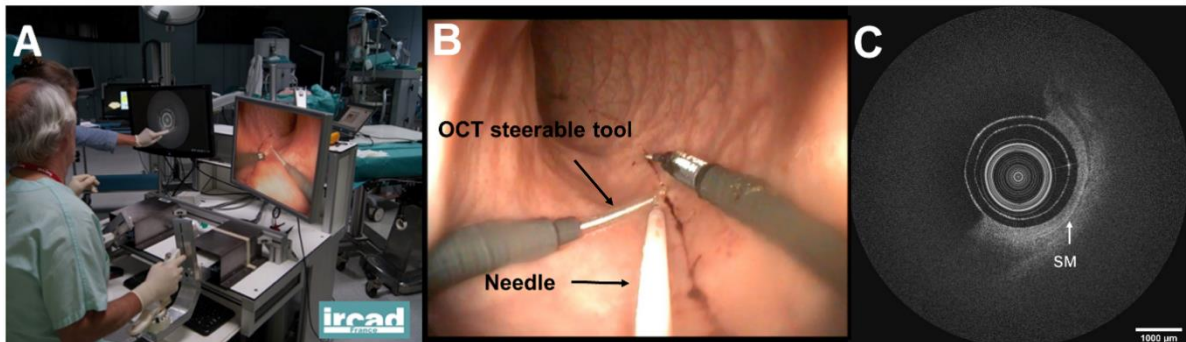


Figure 5.16 In vivo test: (A) The clinician manipulates the steerable OCT catheter by teleoperation. (B) Real time visualization of the colon wall in a living swine; Endoscopic view, (C) OCT view. The submucosa is shown as the brightest layer in the OCT image.

Figure 5.16(A) shows a picture of the physician teleoperating the OCT catheter from the master interface. Figure 5.16(B) shows the white light endoscopic view where the OCT device can be observed being placed on the tissue of the swine colon wall, the instrument at the right being a cautery tool. Figure 5.16(C) shows the real time acquisition of the OCT images, where the layering of the colon wall can be observed in which the submucosa is the most scattering layer indicated by the white arrow. The current design requires placing the

OCT probe in contact with the tissue to obtain optimal images since its focal length is about 1 mm from the sheath. The axial resolution is $7 \mu\text{m}$ and the spot size is $33 \mu\text{m}$.

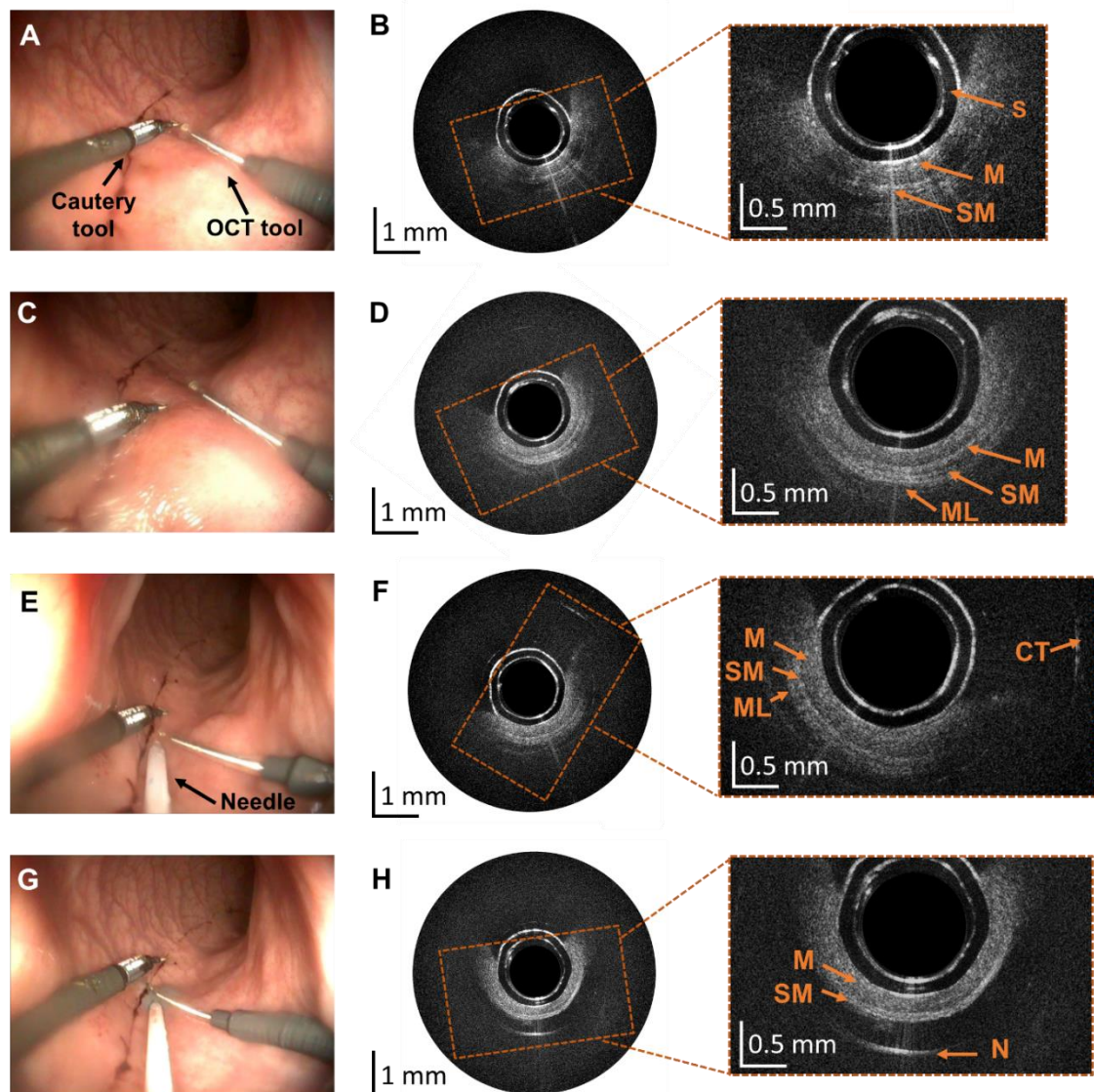


Figure 5.17 Results obtained during experiments in the swine bowel in vivo. (A, C) endoscopic views of the OCT and cauterization tool manipulation, (B, D) corresponding OCT images. (E, G) endoscopic views showing the needle injection, (F, H) corresponding OCT images.

Results obtained during experiments in the swine bowel in vivo are shown in Figure 5.17. Figure 5.17(A, C) displays screenshots from the white light endoscopic camera of the robotized endoscope showing a cauterization tool and the steerable OCT catheter in two positions. Figure 5.17(B, D) correspond to the OCT cross-sections with layered bowel architecture

comprising mucosa (M), submucosa (SM) and muscle (ML) visible in zoomed areas. Figure 5.17(E) shows screenshots from the white light endoscopic camera showing insertion of the needle using the endoscope's working channel. Figure 5.17(F) corresponds to OCT cross-section with visible reflection from the cautery tool (CT) that was just above the OCT catheter in Figure 5.17(E). Figure 5.17(G) shows needle injection of methylene blue to elevate submucosa. Figure 5.17(H) corresponds to OCT cross-section showing mucosa and submucosa layer, followed by the methylene blue clear to near-infrared radiation and strong reflection from the needle (N). In the center of all OCT-cross sections plastic transparent sheath is visible (S).

5.6 Conclusions of the chapter

Ex vivo swine small intestine tissue was imaged using the OCT benchtop system for comparison with histology. Based on this, phantoms mimicking the layering of the colonic wall were created. The development of these phantoms with specific optical properties was useful for testing the imaging system in preparation for pre-clinical trials. A detailed protocol to fabricate the phantom has been proposed.

In vivo swine experiment was performed to demonstrate that OCT images can be obtained in real time in a real scenario. Following insertion of the interventional endoscope in the colon, the OCT probe was advanced in the side instrument channel until visible in the white light endoscopic camera. The probe was navigated by a surgeon trained in operation of the robotized flexible endoscope. During navigation the steerable catheter was translated, rotated and bent without problems using one of the user controllers. Once positioned in contact with the tissue, mucosa and submucosa were visualized in real-time. No issues appeared with the operation of the probe and its maneuvering did not influence the quality of imaging. The OCT steerable catheter position was adjusted without the need for motion of the full endoscope, allowing maneuvering of the other interventional tool around the area of interest, as well as the insertion of a needle using a standard working channel and injection of methylene blue which is a standard step during ESD procedures.

5.7 French summary of the chapter

Suite à la caractérisation du système d'OCT endoscopique robotisé développé, dans ce dernier chapitre le système est testé sur des modèles de laboratoire, des tissus porcins ex vivo et enfin sur un colon porcine in vivo.

Le diagnostic microscopique des cancers colorectaux exige la mise au point de nouveaux modèles de cathéters pour permettre l'exploration de grandes zones du côlon, dont la géométrie peut être complexe. Toutefois, il y a des limites au développement, à l'essai et à la validation *in vivo* de cette nouvelle technologie optique d'imagerie, comme l'absence d'un modèle animal de grande taille (comme le porc) pour le cancer du côlon. De plus, l'acceptation clinique exige la preuve d'un modèle d'essai reproductible et approprié pour la performance du système d'imagerie. Pour résoudre ce problème, des modèles optiques imitant les tissus sont généralement utilisés et permettent d'évaluer la performance des instruments optiques et spectroscopiques dans des conditions expérimentales contrôlées. Le modèle est un tissu artificiel aux propriétés optiques bien contrôlées, qui peuvent être spécifiées en fonction de l'application. Une grande variété de matériaux et de méthodes pour produire des modèles optiques avec des propriétés connues ou vérifiables a déjà été publiée [6-13].

Validation préclinique

L'absence d'un modèle animal de grande taille pour le cancer du côlon est une limite courante dans le développement et l'essai de nouvelles technologies d'imagerie. De plus, comme l'acceptation clinique exige une preuve de reproductibilité, un modèle approprié pour tester la performance d'imagerie du système est nécessaire. Pour résoudre ce problème, un nouveau modèle de normalisation pour la validation en laboratoire a été élaboré dans le cadre du projet de doctorat. Cela a impliqué le développement de fantômes optiques qui peuvent imiter les propriétés optiques des polypes normaux et malades et qui peuvent être insérés dans le modèle du côlon humain décrit à la section 4.1. Ils ont été développés pour imiter l'épaisseur et les propriétés optiques dans le proche infrarouge de chaque couche anatomique d'un côlon ainsi que la topographie de surface des polypes colorectaux.

Le modèle du côlon humain

Le modèle de côlon ascendant LM107C a été utilisé pour finaliser la conception de l'instrument d'OCT pour tester l'interaction mécanique et de l'instrument intégré à l'endoscope flexible robotisé dans un environnement proche de l'homme.

Imagerie *ex vivo* des tissus de l'intestin du porc

L'étape suivante de la validation des performances d'imagerie du système OCT mis au point consistait en l'imagerie *ex vivo* de l'intestin grêle de porcs afin de mieux comprendre

l'anatomie et les propriétés optiques du tissu. Un échantillon d'intestin de porc a été prélevé en collaboration avec l'IRCAD. Le tissu fraîchement excisé a été congelé avant l'imagerie. Pour l'imagerie, le tissu a ensuite été décongelé et coupé en plus petites sections et coupé dans le sens de la longueur pour donner accès à la lumière du côlon (Figure 5.3). L'objectif principal de cette étude était d'imager l'architecture de l'intestin et de tester l'utilisation de l'OCT pour l'assistance à deux des étapes typiquement réalisées lors des procédures d'ESD : le marquage des marges avec un outil de cautérisation et l'injection sous-muqueuse de bleu de méthylène.

Développement d'un fantôme de cancer colorectal

Sur la base d'une recherche documentaire et de l'imagerie ex vivo de l'intestin grêle, un protocole de fabrication de fantômes de lésions colorectales normales et cancéreuses a été mis au point. Le fantôme est représenté par un tissu artificiel aux propriétés optiques bien contrôlées, qui peuvent être spécifiées en fonction de l'application.

Essai in vivo sur les animaux

L'objectif était de démontrer la capacité d'acquisition d'images en temps réel en utilisant le cathéter OCT orientable et téléopéré, manipulé comme un instrument chirurgical de l'endoscope robotisé, en environnement in vivo chez le porc (Yorkshire, >20kg). Le protocole de l'étude a été approuvé par le Comité d'éthique institutionnel sur l'expérimentation animale et les animaux ont été gérés conformément aux lois françaises sur l'utilisation et le soin des animaux ainsi qu'aux règles de la Communauté européenne. L'animal a été anesthésié et avant l'intervention, l'intestin a été nettoyé par rinçage du côlon.

Conclusions du chapitre

Les tissus de l'intestin grêle des porcs ont été imagés ex vivo à l'aide du système OCT de laboratoire pour comparaison avec l'histologie. Sur cette base, des fantômes imitant la stratification de la paroi du côlon ont été créés. Le développement de ces fantômes aux propriétés optiques spécifiques a été utile pour tester le système d'imagerie en préparation des essais précliniques. Un protocole détaillé pour la fabrication du fantôme a été proposé.

Une expérience in vivo sur des porcs a été réalisée pour démontrer qu'il est possible d'obtenir des images OCT en temps réel dans un scénario réaliste. Après l'insertion de l'endoscope interventionnel dans le côlon, la sonde OCT a été avancée dans le canal latéral de

l'instrument jusqu'à ce qu'elle soit visible dans l'image en lumière blanche de la caméra endoscopique. La sonde a été pilotée par un chirurgien formé à l'utilisation de l'endoscope flexible robotisé. Pendant la navigation, le cathéter orientable a été déplacé, tourné et béquillé sans problème à l'aide d'une des interfaces maître. Une fois positionné pour être en contact avec le tissu, la muqueuse et la sous-muqueuse ont été visualisées en temps réel. Aucun problème n'est apparu dans le fonctionnement de la sonde et son déplacement n'a pas dégradé la qualité de l'imagerie. La position du cathéter orientable OCT a été réglée sans qu'il soit nécessaire de déplacer l'endoscope complet, ce qui permet de manœuvrer l'autre outil d'intervention autour de la zone d'intérêt, ainsi que d'insérer une aiguille en utilisant un canal de travail standard et d'injecter du bleu de méthylène (étape standard lors des procédures ESD).

Conclusions and future work

Content

Main conclusions	162
Future Work	162
French summary.....	165

Minimally invasive treatment and diagnostic of diseases in the lower gastrointestinal tract, such as colorectal cancer has been addressed in the literature with different solutions and a review of the available technologies has been described. Even though a large number of advanced imaging techniques has been introduced, the standard and high definition white light endoscopy (WLE) remains the standard of care for detection of polyps and inflammatory bowel diseases. Digital chromoendoscopy techniques such as NBI, FICE and I-SCAN have been reported in the literature to provide significance improvement in polyps characterization with respect to WLE. Confocal laser endomicroscopy (CLE) is comparable with histology for polyps and inflammatory bowel diseases characterization due to the high resolution, but because of the small depth penetration and small field of view it does not provide improvement in polyps detection with respect to WLE. In the case of Autofluorescence imaging (AFI), its clinical effectiveness remains unclear in comparison with WLE. Optical coherence tomography has been reported as a promising solution for malignant tissue characterization, providing a balance between high resolution and depth penetration for early detection of cancer.

Challenges of minimally invasive treatment in the gastrointestinal tract has been described as requiring high level of technical skills in the case of endoscopic submucosa dissection, which is time consuming and presents risks such as bleeding due to perforation. The complex task in terms of treatments has led to the development of a new field of robotic endoscopy. Several robotics platforms have been reported aiming to enhance dexterity of the clinician by adding teleoperation for better control of the tool, 3D visualization and automatic positioning of the endoscope. The STRAS robotic system developed at the ICube Laboratory and university of Strasbourg, which enables single user operation and enhances the ability of non-trained clinicians to perform ESD procedures while reducing the time of completion of the tasks was chosen in this work.

The objective of the doctoral project was to develop a new technology that brings together the benefits of Optical Coherence Tomography as a promising advanced imaging technique for tissue characterization and early colorectal cancer diagnosis, with the advantages provided by the robotized flexible interventional endoscope of the STRAS platform, such as enhancing the skills of the clinician to perform interventional procedures. This combination has resulted in a solution that has the potential of providing in situ diagnosis for colorectal diseases, enhanced maneuverability of the endoscopic OCT device, and improvement of the

procedure performance with active OCT assistance during treatment in robotized flexible endoscopy.

Main conclusions

The outcomes from every stage of the development of the doctoral project were described in detail in chapters 2 to 5 and are summarized as follows:

In Chapter 2 the OCT imaging console (OCT-IC) for acquisition and processing of the OCT data has been developed to support two imaging modes. Chapter 3 has described the low-cost endoscopic OCT catheter construction, such as the implementation of the custom 3D scanner actuators to perform helical scanning. Bending capabilities has been added to the design to introduce the novel steerable OCT catheter compatible with the robotized interventional endoscope. A new methodology for the analysis of the variation of NURD according to the speed of rotation has been introduced, as well as its variation according to the angle of bending in the case of the steerable catheter. In Chapter 4 the integration of the steerable OCT catheter with the robotic system has been presented by which two degrees of freedom, translation and rotation have been added to the OCT catheter and providing teleoperation capabilities. The extended scanning workspace has been estimated and described. NURD analysis has been done when performing pullback scanning by translation of the robotic tool using a pre-programmed routine, obtaining 90% of reduction of the precession in the OCT images. Chapter 5 has described the fabrication of phantoms mimicking the layering of the colonic wall based on ex vivo OCT imaging of an animal colon. The protocol for fabrication of the phantoms has been proposed. Finally, an in vivo experiment has been performed to demonstrate real time OCT and teleoperation capabilities with the steerable OCT catheter integrated to the STRAS robotic platform.

Future Work

Having developed the robotized endoscopic OCT system, during this work it became clear what the next steps would be to improve it. These details are given below.

OCT-IC compact size

While the current OCT-IC is portable and can be carried on a medical cart, its size could be reduced to make it more compact and lighter, which would be desirable for portability and

easy installation in the medical room. This could be achieved by taking the small PC out of the OCT-IC box and fixing it up on the rear side of the monitor, using translation stages with embedded controllers for both the 3D scanner actuators and the stage of the reference arm and employing a smaller power supply that would free part of the space and lighten the OCT-IC.

Longer optical working distance for non-contact OCT probe

A new design of focusing micro-optics with a longer working distance, so that non tissue contact is required for optimal OCT imaging will be important to implement in the future in procedures in which there is interaction with a secondary tool, i.e., when performing needle injection or tissue marking with a cautery tool.

OCT catheter diameter for standard flexible endoscopy

The current development of the steerable OCT catheter is based a specialized surgical instrument with a diameter of 3.5 mm, which is different from conventional diameter sizes of less than 3 mm. In order to meet compatibility with conventional endoscopes it will be necessary to explore new methodologies of flexible mechanisms with smaller diameter sizes.

Frame rate stabilization to reduce image artefacts during visualization and 3D pullback scanning

The steerable OCT catheter suffers from image artefacts produced by NURD and non-constant speed of the motor driving the rotation of the probe, resulting in an unstable image and distorted image in real time visualization and 3D reconstruction. It is necessary to implement a better control of the motor speed to stabilize the image and to reduce the distortion for 3D image reconstruction.

Complete validation of the scanning workspace

The validation of the workspace was partially carried out in this project. But, due to the complexity of implementing special programmed routines to collect data when the tool is being fully retracted inside the cannal, implementing this new routine will allow completion of the validation of the workspace.

Automatic scanning routines taking advantage of the extended workspace of the steerable-teleoperated OCT catheter

Performing OCT scanning with pre-programmed routines by taking advantage of the extended scanning workspace will be useful for OCT scanning of longer sections of the colon; thus, eliminating non-precise motions induced by the teleoperator. The use of these routines would also extend the OCT imaging capabilities of the catheter even for small sheath length of the exposed optical device at the distal end.

Robotization of a conventional flexible endoscope for larger sections imaging of the colon

Since the length of the main currently robotized endoscope is of 535 mm and the length of the colon is about 1600 mm, the system is limited to procedures up to the sigmoid colon. Robotization of a standard flexible endoscope will provide capability of imaging the full organ with the same steerability and teleoperation features.

Automatic positioning capabilities for real time guidance of therapeutic procedures like needle injection and laser marking

The use of the OCT images for automatic guidance to position the OCT catheter will be important for accurate tissue marking, motion compensation and needle injection. If needle injection was performed by automatic control, the risk of bleeding due to perforation could be reduced and in addition, procedure training would require a lower learning curve and experience.

Image processing techniques to differentiate healthy from disease tissue

Automatic differentiation between healthy from disease tissue will assist clinicians to provide faster diagnosis in situ. The introduction of these methodologies could then lead OCT from just being used in tissue characterization to the detection of polyp types in the case of cancer screening.

French summary

Conclusions et travaux futurs

Le traitement et le diagnostic minimalement invasifs des maladies du tractus gastro-intestinal inférieur, comme le cancer colorectal, ont été abordés dans la littérature avec différentes solutions, avec un descriptif des technologies disponibles à cet effet. Même si un grand nombre de techniques d'imagerie avancées ont été proposées, l'endoscopie à lumière blanche (WLE), standard et haute définition, reste la référence thérapeutique pour la détection des polypes et des maladies inflammatoires de l'intestin. Les techniques de chromo-endoscopie numérique telles que NBI, FICE et I-SCAN apparaissent également dans la littérature : elles fournissent une amélioration significative de la caractérisation des polypes comparé à la technique de WLE. L'endo-microscopie confocale au laser (CLE) est comparable à l'histologie pour la caractérisation des polypes et des maladies inflammatoires de l'intestin grâce à sa haute résolution, mais en raison de sa faible pénétration en profondeur et de son champ de vision limité, elle ne permet pas d'améliorer la détection des polypes par rapport au WLE. Toujours par comparaison avec le WLE, l'imagerie par auto-fluorescence (AFI) n'a pas encore une efficacité clinique certaine. La tomographie par cohérence optique est signalée comme une solution prometteuse pour la caractérisation des tissus malins, car elle rend possible l'équilibre entre une haute résolution et une bonne pénétration en profondeur pour la détection précoce du cancer.

Les défis du traitement mini-invasif dans le tractus gastro-intestinal nécessitant un haut niveau de compétences techniques dans le cas de la dissection endoscopique de la sous-muqueuse, qui prend du temps et présente des risques tels que les saignements dus à la perforation. La complexité des traitements a conduit au développement d'un nouveau domaine de l'endoscopie robotisée. Plusieurs plateformes robotiques visent à améliorer la dextérité du clinicien en ajoutant la télé-opération pour un meilleur contrôle de l'outil, la visualisation 3D et le positionnement automatique de l'endoscope. Le système robotique STRAS développé au laboratoire ICube et à l'Université de Strasbourg, qui nécessite un seul utilisateur et améliore la capacité des cliniciens non formés à effectuer des procédures ESD tout en réduisant le temps de réalisation des tâches, a été choisi pour ce travail.

L'objectif du projet de doctorat était de développer une nouvelle technologie qui combine les avantages de la tomographie par cohérence optique comme technique d'imagerie

avancée prometteuse pour la caractérisation des tissus et le diagnostic précoce du cancer colorectal, avec les avantages fournis par l'endoscope interventionnel flexible robotisé de la plateforme STRAS, tels que l'amélioration des compétences du clinicien pour effectuer des procédures interventionnelles. Cette combinaison a donné lieu à une solution qui a le potentiel de fournir un diagnostic in situ pour les maladies colorectales, une meilleure maniabilité de l'appareil d'OCT endoscopique et une amélioration de la performance de la procédure avec une assistance active de l'OCT pendant le traitement dans l'endoscopie flexible robotisée.

Principales conclusions

Les résultats de chaque étape de l'élaboration du projet de doctorat ont été décrits en détail aux chapitres 2 à 5 et sont résumés comme suit :

Au chapitre 2, la console d'imagerie OCT (OCT-IC) pour l'acquisition et le traitement des données OCT a été développée pour prendre en charge deux modes d'imagerie. Le Chapitre 3 a décrit la construction de cathéters d'OCT endoscopiques à faible coût, ainsi que la mise en œuvre des actionneurs de scanner 3D personnalisés pour effectuer un balayage hélicoïdal. Des capacités de pliage ont été ajoutées à la conception pour introduire le nouveau cathéter OCT orientable compatible avec l'endoscope interventionnel robotisé. Une nouvelle méthodologie pour l'analyse de la variation de la NURD en fonction de la vitesse de rotation a été présentée, ainsi que sa variation en fonction de l'angle de flexion dans le cas du cathéter orientable. Au l'intégration du cathéter OCT orientable avec le système robotique a été présentée. Deux degrés de liberté, de translation et de rotation, ont été ajoutés au cathéter OCT rendant possible la télé-opération du système. L'espace de travail étendu pour la numérisation a été estimé et décrit. L'analyse NURD a été effectuée lors du balayage de retrait par translation de l'outil robotique au moyen d'une routine préprogrammée, ce qui a permis d'obtenir une réduction de 90 % de la précession dans les images OCT. Le chapitre 5 a décrit la fabrication de fantômes imitant la stratification de la paroi colique sur la base de l'imagerie OCT ex vivo d'un côlon animal. Le protocole de fabrication des fantômes a été présenté. Enfin, une expérience in vivo a été réalisée pour démontrer les capacités de l'OCT et de la télé-opération en temps réel avec le cathéter OCT orientable intégré à la plateforme robotique STRAS.

Travaux futurs

Après avoir développé le système robotisé d'OCT endoscopique, il est apparu clairement au cours de ces travaux quelles seraient les prochaines étapes pour l'améliorer. Ces détails sont donnés ci-dessous.

OCT-IC taille compacte

Bien que l'OCT-IC actuel soit portable et puisse être transporté sur un chariot médical, sa taille pourrait être réduite pour le rendre plus compact et plus léger, ce qui serait souhaitable pour la portabilité et la facilité d'installation dans la salle médicale. Cela pourrait être réalisé en sortant l'ordinateur du boîtier de l'OCT-IC et en le fixant sur la face arrière d'écran, en utilisant les translations avec des contrôleurs intégrés pour les actionneurs du scanner 3D et l'étage du bras de référence et en utilisant une alimentation électrique plus compacte qui libérerait une partie de l'espace et allégerait l'OCT-IC.

Distance de travail optique plus longue pour une sonde OCT sans contact

Il sera important à l'avenir de mettre en œuvre une nouvelle conception de micro-optique de focalisation avec une distance de travail plus longue, de sorte qu'un contact non tissulaire soit nécessaire pour une imagerie TCO optimale, dans les procédures où il y a interaction avec un outil secondaire, c'est-à-dire lorsqu'on effectue une injection d'aiguille ou un marquage tissulaire avec un outil de cautérisation.

Diamètre de cathéter OCT pour l'endoscopie flexible standard

Le développement actuel du cathéter OCT orientable est basé sur un instrument chirurgical spécialisé d'un diamètre de 3,5 mm, qui se distingue des tailles conventionnelles de moins de 3 mm. Pour assurer la compatibilité avec les endoscopes conventionnels, il sera nécessaire d'explorer de nouvelles méthodologies de mécanismes flexibles avec des diamètres plus réduits.

Stabilisation de la fréquence d'images pour réduire les artefacts d'image pendant la visualisation et la numérisation 3D en retrait

La sonde OCT orientable est impactée par des artefacts d'image produits par le NURD et par la vitesse non constante du moteur entraînant la rotation de la sonde, ce qui se traduit par une image instable et une image déformée en visualisation en temps réel et en reconstruction

3D. Il est nécessaire de mettre en place un meilleur contrôle de la vitesse du moteur pour stabiliser l'image et réduire la distorsion pour la reconstruction de l'image 3D.

Validation complète de l'espace de travail de numérisation

La validation de l'espace de travail a été partiellement réalisée dans le cadre de ce projet. Mais, en raison de la complexité de la mise en œuvre de routines programmées spéciales pour collecter des données lorsque l'outil est entièrement rétracté à l'intérieur du canal endoscopique, la mise en œuvre de cette nouvelle routine permettra d'achever la validation de l'espace de travail.

Routines de numérisation automatique tirant profit de l'espace de travail étendu du cathéter OCT à commande téléopérée et orientable

L'exécution d'un balayage OCT avec des routines pré-programmées profitant de l'espace de travail de numérisation étendu sera utile pour la numérisation OCT de sections plus longues du côlon. Ainsi, l'imprécision induite par les mouvements du téléopérateur serait éliminée. L'utilisation de ces routines permettrait également d'étendre les capacités d'imagerie OCT du cathéter, même pour une petite longueur de gaine du dispositif optique exposée à l'extrémité distale.

Robotisation d'un endoscope flexible conventionnel pour l'imagerie de grandes sections du côlon

Comme la longueur de l'endoscope robotisé principal est de 535 mm et que la longueur du côlon est d'environ 1600 mm, le système est limité aux interventions jusqu'au côlon sigmoïde. La robotisation d'un endoscope flexible standard permettra d'obtenir des images de l'organe entier avec les mêmes caractéristiques d'orientation et de télé-opération.

Capacités de positionnement automatique pour le guidage en temps réel de procédures thérapeutiques telles que l'injection d'aiguilles et le marquage au laser

L'utilisation des images OCT pour le guidage automatique du positionnement du cathéter OCT sera importante pour le marquage précis des tissus, la compensation des mouvements et l'injection d'aiguilles. Si l'injection par aiguille était effectuée par commande automatique, le

risque de saignement dû à la perforation pourrait être réduit et, de plus, la formation à la procédure exigerait un temps d'apprentissage et une expérience plus faible.

Techniques de traitement d'images pour différencier les tissus sains des tissus malades

La différenciation automatique entre les tissus sains et les tissus malades aidera les cliniciens à établir un diagnostic plus rapide in situ. L'introduction de ces méthodologies pourrait alors faire passer l'OCT du simple usage dans la caractérisation des tissus à la détection des types de polypes dans le cas du dépistage du cancer.

Annexes

Content

A. AJCC TNM System.....	171
B. Optics.....	173
C. Actuation controllers.....	177
D. Geometrical model of the flexible instrument	178
E. Phantom fabrication.....	183
F. Datasheets	184

A. AJCC TNM System

The following tables summarize the TNM systems, this information has been taken from the AJCC TNM system manual 8th edition [333].

Table A.1 Definition of Primary Tumor.

T Category	T Criteria
TX	Primary tumor cannot be assessed
T0	No evidence of primary tumor
Tis	Carcinoma in situ, intramucosal carcinoma (involvement of lamina propria with no extension through muscularis mucosae)
T1	Tumor invades the submucosa (through the muscularis mucosa but not into the muscularis propria)
T2	Tumor invades the muscularis propria
T3	Tumor invades through the muscularis propria into-pericorectal tissues
T4	Tumor invades* the visceral peritoneum or invades or adheres** to adjacent organ or structure
T4a	Tumor invades* through the visceral peritoneum (including gross perforation of the bowel through tumor and continuous invasion of tumor through areas of inflammation to the surface of the visceral peritoneum)
T4b	Tumor directly invades* or adheres** to adjacent organs or structures

Table A.2 Definition of Regional Lymph Node (N).

N Category	N Criteria
NX	Regional lymph nodes cannot be assessed
N0	No regional lymph node metastasis
N1	One to three regional lymph nodes are positive (tumor in lymph nodes measuring ≥ 0.2 mm), or any number of tumor deposits are present and all identifiable lymph nodes are negative
N1a	One regional lymph node is positive
N1b	Two or three regional lymph nodes are positive
N1c	No regional lymph nodes are positive, but there are tumor deposits in the: <ul style="list-style-type: none"> • subserosa • mesentery • or non-peritonealized pericolic, or perirectal/mesorectal tissues.
N2	Four or more regional nodes are positive
N2a	Four to six regional lymph nodes are positive
N2b	Seven or more regional lymph nodes are positive

Table A.3 Definition of distant Metastasis.

M Category	M Criteria
M0	No distant metastasis by imaging, etc. no evidence of tumor in distant sites or organs (This category is not assigned by pathologists.)
M1	Metastasis to one or more distant sites or organs or peritoneal metastasis is identified
M1a	Metastasis to one site or organ is identified without peritoneal metastasis
M1b	Metastasis to two or more sites or organs is identified without peritoneal metastasis
M1c	Metastasis to the peritoneal surface is identified alone or with other site or organ metastases

Table A.4 AJCC prognostic stage groups.

When T is...	When N is...	When M is...	Then the stage group is...
Tis	N0	M0	0
T1, T2	N0	M0	I
T3	N0	M0	IIA
T4a	N0	M0	IIB
T4b	N0	M0	IIC
T1–T2	N1/N1c	M0	IIIA
T1	N2a	M0	IIIA
T3–T4a	N1/N1c	M0	IIIB
T2–T3	N2a	M0	IIIB
T1–T2	N2b	M0	IIIB
T4a	N2a	M0	IIC
T3–T4a	N2b	M0	IIC
T4b	N1–N2	M0	IIC
Any T	Any N	M1a	IVA
Any T	Any N	M1b	IVB
Any T	Any N	M1c	IVC

Table A.5 Categorization by cancer registries [334].

In situ	0
Localized	I-II
Regional	III
Distant	IV
Unknown	Not enough information to determine the stage

B. Optics

OCT parameters

Numerical Aperture [335]

$$NA \equiv n \cdot |\sin U| \approx n \cdot |U| \quad \text{Eq. B.1}$$

n is refraction index of the medium between the sample and the lens.

U is the real marginal ray angle.

Relative aperture [335] $f/\#$

$$f/\# = \frac{f_E}{D_{EP}} \approx \frac{1}{2NA} \quad \text{Eq. B.2}$$

f_E Effective focal length.

D_{EP} diameter of the entrance pupil.

Spot size [336]

$$d = \frac{4}{\pi} \lambda \approx \frac{1.27\lambda}{NA} \quad \text{Eq. B.3}$$

Transverse resolution at FWHM [336]

$$\Delta x_{FWHM} = \frac{0.59 \times \frac{2}{\pi} \lambda}{NA} \rightarrow \frac{0.59 \times d}{2} \quad \text{Eq. B.4}$$

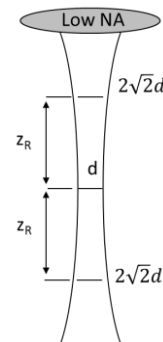
$$\Delta x_{FWHM} = \frac{0.59 \times d}{2} \quad \text{Eq. B.5}$$

Depth of field [117]

$$\text{DOF} = \frac{\pi \Delta x^2}{2\lambda} = n \frac{8\lambda}{\pi} \left(\frac{1}{NA^2} \right) \rightarrow 2z_R \quad \text{Eq. B.6}$$

Axial resolution [117]

$$\Delta z = \frac{2 \ln 2}{n \cdot \pi} \left(\frac{\lambda^2}{\Delta \lambda} \right) \quad \text{Eq. B.7}$$



Lateral and axial resolution computation

The Benchtop mode uses the GVSM002/M - 2D Galvo System from Thorlabs, the scan lens for laser scanning microscopy LSM04 mounted in the GCM102/M - Mounting Adapter and the C1511/M - Ø1.5" Post Mounting Clamp, P200/M - Ø1.5" Mounting Post plus the Pedestal Base Adapter PB4/M, the Clamping Fork PF175 and the collimator F220APC-1310 to collimate the received light from the optical fiber of the sample arm (Figure 2.8).

The optical parameters of the system are the depth of field, the lateral and axial resolution. The corresponding equations for computation of these parameters are summarized in annex B.

The parameters require to estimate optical properties are as follows:

LSM04 Effective Focal Length: 54 mm (EFL),

Collimator F220APC-1310 output beam diameter: 2 mm (entrance pupil EP),

$$\text{Focal ratio: } f/\# = \frac{EFL}{EP} \rightarrow 27$$

$$\text{Numerical aperture: } NA = \frac{1}{2f/\#} = 0.018,$$

Wavelength: $\lambda = 1300 \text{ nm}$

Optical properties of the system are spot size, depth of field, lateral and axial resolution and field of view:

$$\text{Spot size: } d = \frac{1.27\lambda}{NA} = 89.24 \mu\text{m},$$

$$\text{Lateral OCT Resolution: } \Delta x_{FWHM} = \frac{0.59 \times d}{2} = 26.32 \mu\text{m},$$

Another combination of scan lens and collimator has been acquired to increase lateral resolution:

LSM03 Effective Focal Length: 36 mm (EFL).

Collimator F280APC-C output beam diameter: 3.4 mm (entrance pupil EP).

$$\text{Focal ratio: } f/\# = \frac{EFL}{EP} \rightarrow 10.59$$

$$\text{Numerical aperture: } NA = \frac{1}{2f/\#} = 0.047$$

Wavelength: $\lambda = 1300 \text{ nm}$,

$$\text{Spot size: } d = \frac{1.27\lambda}{NA} = 35.13 \mu m$$

$$\text{Lateral OCT Resolution: } \Delta x_{FWHM} = \frac{0.59 \times d}{2} = 10.36 \mu m$$

The axial resolution is independent of the optics; it only depends on the laser bandwidth and central wavelength, considering free space medium with refractive index $n = 1$:

$$\Delta z = \frac{2 \ln 2}{n \cdot \pi} \left(\frac{\lambda^2}{\Delta \lambda} \right) \rightarrow \frac{2 \ln 2}{\pi} \left(\frac{(1300 \text{ nm})^2}{133 \text{ nm}} \right) = 5.6 \mu m$$

Depth of field (DOF) refers to the zone in which the target is in acceptable focus, and it corresponds to twice the Rayleigh range z_R : $DOF = \frac{\pi d^2}{2\lambda} \rightarrow \frac{\pi(89.24 \mu m)^2}{2 \times 1300 \text{ nm}} = 9.6 \text{ mm}$, and 1.5 mm accordingly to each configuration of the scanning lens and collimator. The field of view when using the LSM04 is $14.1 \times 14.1 \text{ mm}^2$ and $9.3 \times 9.3 \text{ mm}^2$ for the LSM03.

All computations above are considering refractive index in air $n = 1$, however in human tissue it is typically $n = 1.35$, thus $\Delta z = 5.6 \mu m \times 1.35 \rightarrow 7.56 \mu m$.

Loops computation

Table B.6 Loops sample arm for endoscopic mode.

SAMPLE ARM	Intermediate paths	Length (mm)			Length (mm)	
RJ	Fiber RJ output	2000.00	SMF-28	1.4677	2935.40	
	RJ fiber to ferrule	131.20	SMF-29	1.4677	192.56	
Catheter	Ferrule to driveshaft	53.00	SMF-30	1.4677	77.78	
	Driveshaft	2500.00	SMF-31	1.4677	3669.25	
	Ball lens	0.254	SMF-32	1.4677	0.37	
WD	WD	1.00	Air	1.00	1.00	
A1					Total Length (Air)	6876.37 mm
					Fiber length	4685.13 mm

Table B.7 Loops reference arm for dual mode.

REFERENCE ARM	Intermediate paths	Length (mm)			Length (mm)	
F22APC-1310	Ferrule to lens	8.05	Air	1.00	8.05	
	Lens	5.03	DZK3M	1.57	7.91	
Path	To mirror	88.00	Air	1.00	88.00	
A2					Total Length	104.00 mm
A1-A2					Difference in Air	6772.40 mm
A1-A2					Fiber loop length	4614.30 mm

Table B.8 Loops sample arm for the benchtop mode.

GALVO SAMPLE ARM	Intermediate paths	Length (mm)			Length (mm)	
F280APC-C-1310	Ferrule to lens	16.85	Air	1.00	16.85	
	Lens	2.17	DZK3M	1.57	3.41	
Galvo	To galvo	32.48	Air	1.00	32.48	
	Galvo to LSM04	7.09	Air	1.00	7.09	
LSM03	In air	12.20	Air	1.00	12.20	
	N-BAK1 glass	17.80	N-BAK1	1.59	28.30	
WD	WD	25.10	Air	1.00	25.10	
A3					Total Length	125.45 mm
A1-A3					Difference in Air	6750.92 mm
A1-A3					Fiber loop length	4599.66 mm

C. Actuation controllers

Speed controller

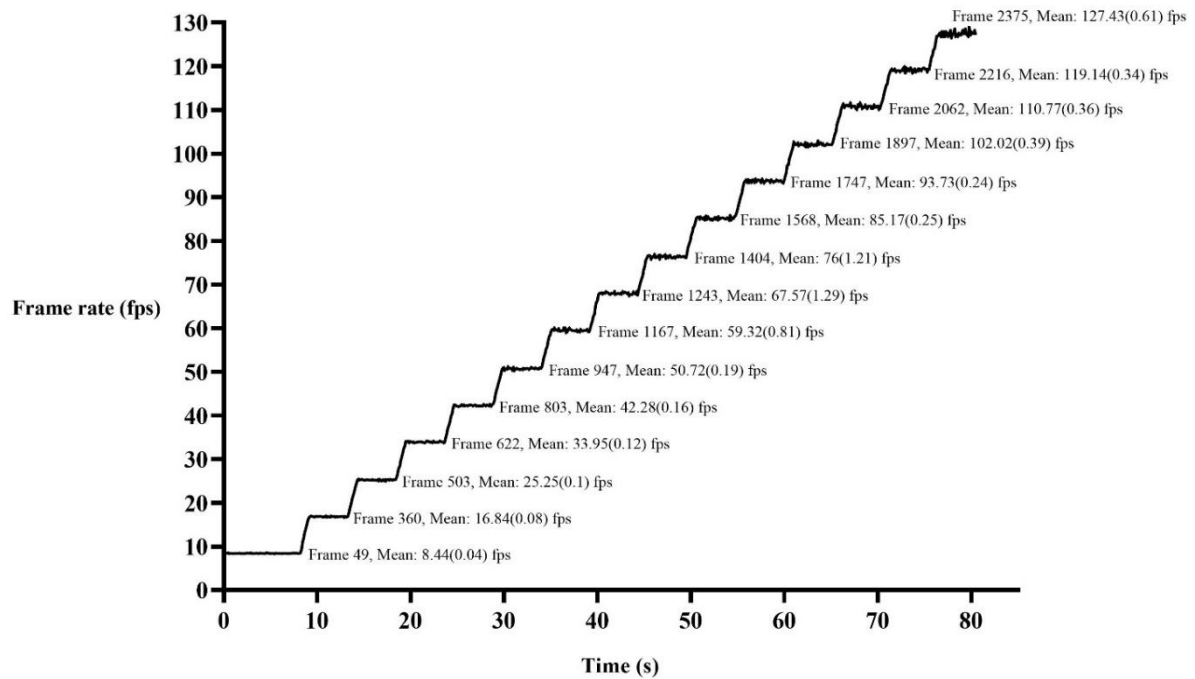


Figure C.1 Speed controller, performing a swept of set speed values from 5000 rpms (8.33 fps) to 7500 rpm (125 fps) with the regular catheter. Frame rate (fps) versus time (s). The graph also shows the chosen frame for image NURD analysis, the mean and standard deviation of the mean.

D. Geometrical model of the flexible instrument

Geometrical model of the flexible section, see reference [337].

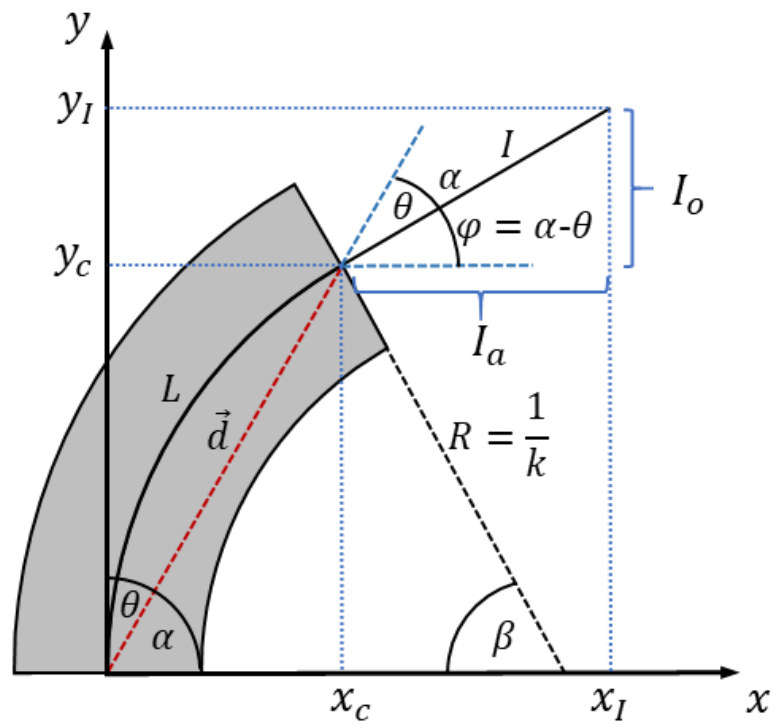


Figure D.2 Geometrical model of the flexible section.

Direct geometrical model

The position of the end-effector i.e. tip of the instrument can be computed as:

$$x_I = x_c + I_a \quad \text{Eq. D.8}$$

$$y_I = y_c + I_o \quad \text{Eq. D.9}$$

where (x_I, y_I) represents the coordinates of the tip of the flexible part in the base frame.

The following relations can be determined:

- $I \rightarrow$ length of the fixed part.
- $k \rightarrow$ curvature of the radius.
- $\vec{d} \rightarrow$ vector norm of (x_c, y_c) .
- $L \rightarrow$ length of the flexible part.

x_c and y_c components

- The curvature radius can be computed as:

$$R = \frac{1}{k} \quad \text{Eq. D.10}$$

$$R = \frac{L}{\beta} \quad \text{Eq. D.11}$$

- $\beta \rightarrow$ angle of the arc formed by bending the flexible part,

$$\beta = kL \quad \text{Eq. D.12}$$

$$k = \frac{\beta}{L}$$

- $\theta \rightarrow$ angle of the vector (x_c, y_c) with respect to the y – axis,

Flexion angle:

$$\alpha + \frac{\beta}{2} = \frac{\pi}{2} \quad \text{Eq. D.13}$$

$$\theta = \frac{\pi}{2} - \alpha \quad \text{Eq. D.14}$$

- Substituting Eq. D.12 in Eq. D.13 then in Eq. D.14 then in,

$$\theta = \frac{kL}{2} \quad \text{Eq. D.15}$$

$$\theta = \frac{\beta}{2} \quad \text{Eq. D.16}$$

- components (x_c, y_c) ,

$$\frac{d}{2} = R \cos(\alpha) \quad \text{Eq. D.17}$$

$$\frac{d}{2} = \frac{1}{k} \cos\left(\frac{\pi}{2} - \frac{\beta}{2}\right) \quad \text{Eq. D.18}$$

$$\frac{d}{2} = \frac{1}{k} \sin\left(\frac{\beta}{2}\right) \quad \text{Eq. D.19}$$

$$d = \frac{2}{k} \sin\left(\frac{\beta}{2}\right) \quad \text{Eq. D.20}$$

- components (x_c, y_c) in terms of θ ,

$$x_c = d \sin(\theta) \quad \text{Eq. D.21}$$

$$y_c = d \cos(\theta) \quad \text{Eq. D.22}$$

- based on Eq. D.16,

$$x_c = d \sin\left(\frac{\beta}{2}\right), y_c = d \cos\left(\frac{\beta}{2}\right) \quad \text{Eq. D.23}$$

$$x_c = \frac{2L}{\beta} \sin\left(\frac{\beta}{2}\right) \sin\left(\frac{\beta}{2}\right) \quad \text{Eq. D.24}$$

$$y_c = \frac{2L}{\beta} \sin\left(\frac{\beta}{2}\right) \cos\left(\frac{\beta}{2}\right) \quad \text{Eq. D.25}$$

Components (x_I, y_I)

$$I_a = I \cos \varphi \quad \text{Eq. D.26}$$

$$I_o = I \sin \varphi \quad \text{Eq. D.27}$$

- $\varphi \rightarrow$ angle formed by the fixed part with respect to axis x ,

$$\varphi = \alpha - \theta \quad \text{Eq. D.28}$$

$$\varphi = \left(\frac{\pi}{2} - \frac{\beta}{2}\right) - \frac{\beta}{2} \quad \text{Eq. D.29}$$

$$\varphi = \frac{\pi}{2} - \beta \quad \text{Eq. D.30}$$

$$\varphi = -\left(\beta - \frac{\pi}{2}\right) \quad \text{Eq. D.31}$$

- $I_a \rightarrow$ adjacent side of the triangle formed by the fixed part,

$$I_a = I \cos\left(\beta - \frac{\pi}{2}\right) \quad \text{Eq. D.32}$$

$$I_a = I \sin(\beta) \quad \text{Eq. D.33}$$

- $I_o \rightarrow$ opposite side of the triangle formed by the fixed part

$$I_o = I \sin\left(\frac{\pi}{2} - \beta\right) \quad \text{Eq. D.34}$$

$$I_o = I \cos(-\beta) \quad \text{Eq. D.35}$$

$$I_o = I \cos(\beta) \quad \text{Eq. D.36}$$

- components (x_I, y_I) ,

$$x_I = x_c + I \sin(\beta) \quad \text{Eq. D.37}$$

$$y_I = y_c + I \cos(\beta) \quad \text{Eq. D.38}$$

$$x_I = \frac{2L}{\beta} \left(\sin\left(\frac{\beta}{2}\right)\right)^2 + I \sin(\beta) \quad \text{Eq. D.39}$$

$$y_I = \frac{2L}{\beta} \sin\left(\frac{\beta}{2}\right) \cos\left(\frac{\beta}{2}\right) + I \cos(\beta) \quad \text{Eq. D.40}$$

- $I_o \rightarrow$ using the relation $\sin(2\sigma) = 2 \sin \sigma \cos \sigma$ in Eq. D.40.

$$y_I = \frac{L}{\beta} \sin(\beta) + I \cos(\beta) \quad \text{Eq. D.41}$$

Pappus's Centroid Theorem, arc length and centroid

See reference [315].

Arc Length

$$L = \int_a^b \sqrt{\left(\frac{dx_I}{d\beta}\right)^2 + \left(\frac{dy_I}{d\beta}\right)^2} d\beta \quad \text{Eq. D.42}$$

Centroid (\bar{x}, \bar{y}) of a region R

$$\bar{x} = \frac{\int_a^b xf(x) dx}{\int_a^b f(x) dx} \quad \text{Eq. D.43}$$

$$\bar{y} = \frac{\int_a^b \frac{1}{2}(f(x))^2 dx}{\int_a^b f(x) dx} \quad \text{Eq. D.44}$$

Surface of revolution about the x-axis (S_x) and y-axis (S_y)

$$S_x = 2\pi \int_a^b y_I(\beta) \sqrt{\left(\frac{dx_I}{d\beta}\right)^2 + \left(\frac{dy_I}{d\beta}\right)^2} d\beta \quad \text{Eq. D.45}$$

$$S_y = 2\pi \int_a^b x_I(\beta) \sqrt{\left(\frac{dx_I}{d\beta}\right)^2 + \left(\frac{dy_I}{d\beta}\right)^2} d\beta \quad \text{Eq. D.46}$$

Volume of revolution about y-axis

$$\text{Volume} = (\text{Area of the Region})(\text{distance traveled by the centroid}) \quad \text{Eq. D.47}$$

E. Phantom fabrication

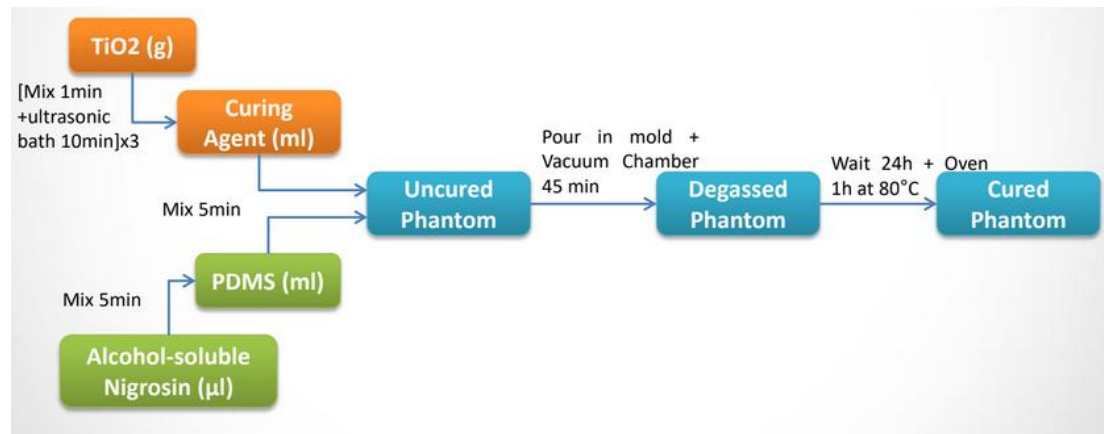


Figure E.3 Fabrication procedure

- 1) Calculate the volume of the PDMS based on the capacity of the mold and desired thickness of the phantom.
- 2) Use the syringe, take the curing agent (1/10 relative to the amount PDMS) and pour into the 15 mL graduated tube.
- 3) Weigh the desired quantity of TiO₂, using the precision balance.
- 4) Add the TiO₂ to the curing agent in the graduated tube (or scaled plastic tube) and stir for 30 seconds, using the spatula.
- 5) Close the graduated tube and place it in the ultrasonic bath for 15 min at 40°C.
- 6) While waiting for the end of the ultrasonic bath, pour the desired quantity of PDMS in a 50 mL beaker.
- 7) Add the graduated tube content in the PDMS beaker through a filter paper and stir it 1 min with the spatula.
- 8) Pour and spread uniformly the obtained mixture into the mold using the spatula. Be careful, this is the key step to get a great thickness homogeneity.
- 9) Place the mold in the vacuum chamber and repeat vacuuming and filing cycles until all bubbles are eliminated.
- 10) Place the mold with the phantom in an oven for 60 minutes at 80° C. This step is not necessary. The silicon drying process should take approximatively 72 hours without an oven.

11) One fully dry repeat step 1-10 to achieve an additional layer on top.

F. Datasheets

Lenses data sheet

Technical drawing of an OCT Scan Lens (LSM04) showing dimensions and a 3D perspective view. The drawing includes the following dimensions:

- Overall diameter: $\varnothing 34.0\text{mm}$ [1.34in]
- External thread: M25x0.75
- Top section height: 4.5mm [0.18in]
- Main body height: 38.5mm [1.52in]
- Total height: 42.3mm [1.67in]

3D perspective view of the lens showing the green lens element and the THORLABS logo.

DRAWING PROJECTION		THORLABS www.thorlabs.com	
NAME	DATE	OCT SCAN LENS	
DRAWN	CJ	21/JAN/15	
APPROVAL	CS	21/JAN/15	
MATERIAL		N/A	REV B
COPYRIGHT © 2015 BY THORLABS		ITEM #	APPROX WEIGHT
VALUES IN PARENTHESES ARE CALCULATED AND MAY CONTAIN ROUND-OFF ERRORS.		LSM04	0.17 kg

FOR INFORMATION ONLY
NOT FOR MANUFACTURING PURPOSES

ITEM	MATERIAL
① HOUSING	303 STAINLESS STEEL
② FC/APC PLUG ADAPTER	303 STAINLESS STEEL
③ $\varnothing 7.2\text{mm}$, $f=1.26\text{mm}$ LENS	MOLDED ASPHERE

SPECIFICATIONS

DESIGN WAVELENGTH	1310nm
DESIGN MFD	9.2 μm
OUTPUT $1/e^2$ BEAM DIAMETER	2.04 mm
FULL ANGLE BEAM DIVERGENCE	0.047°
AR COATING	Ravg<0.5% FROM 1050-1620nm

Technical drawing of an F220APC-1310 collimation package showing dimensions and a cross-section view. The drawing includes the following dimensions:

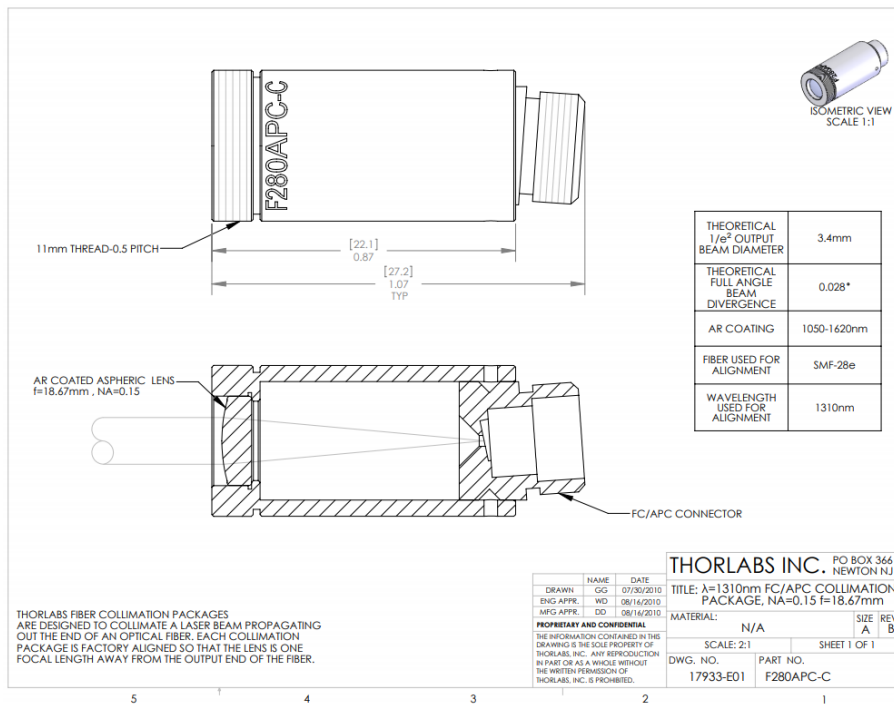
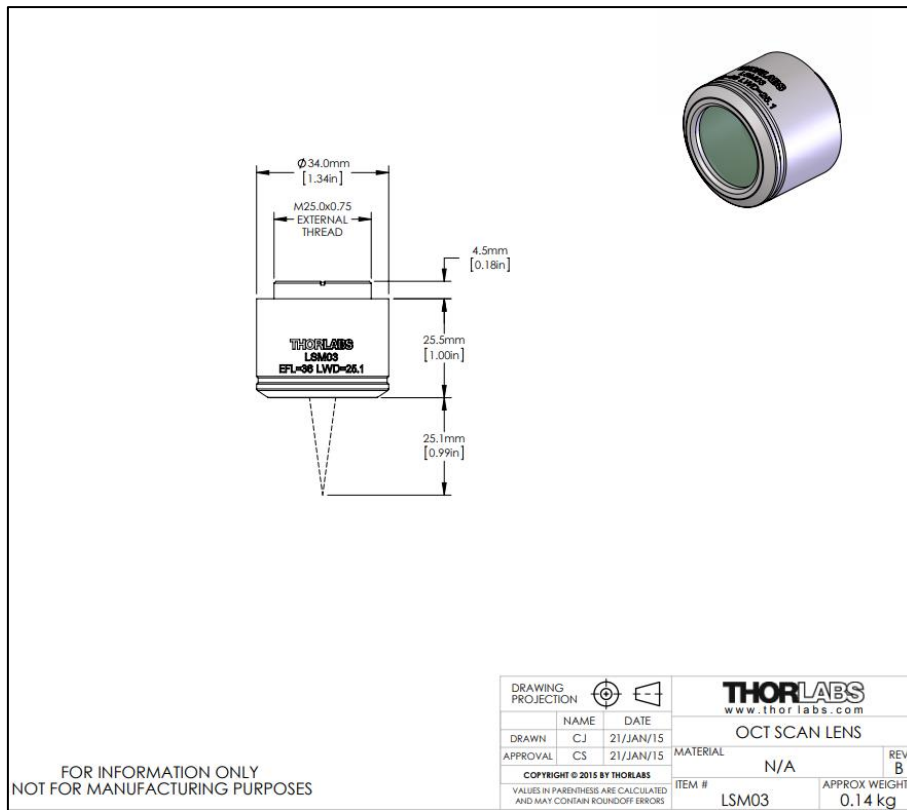
- Overall length: 0.63in [15.6mm]
- Length with plug: 0.81in [20.6mm] TYP
- Thread: M11X0.5
- Inner diameter: $\varnothing 0.43\text{in}$ [11.0mm]

Cross-section view (SECTION A-A) showing the housing (1), FC/APC plug adapter (2), and lens (3).

THORLABS FIBER COLLIMATION PACKAGES ARE DESIGNED TO COLLIMATE A LASER BEAM PROPAGATING OUT THE END OF AN OPTICAL FIBER. EACH COLLIMATION PACKAGE IS FACTORY ALIGNED SO THAT THE BEST POSSIBLE DIVERGENCE IS ACHIEVED.

FOR INFORMATION ONLY
NOT FOR MANUFACTURING PURPOSES

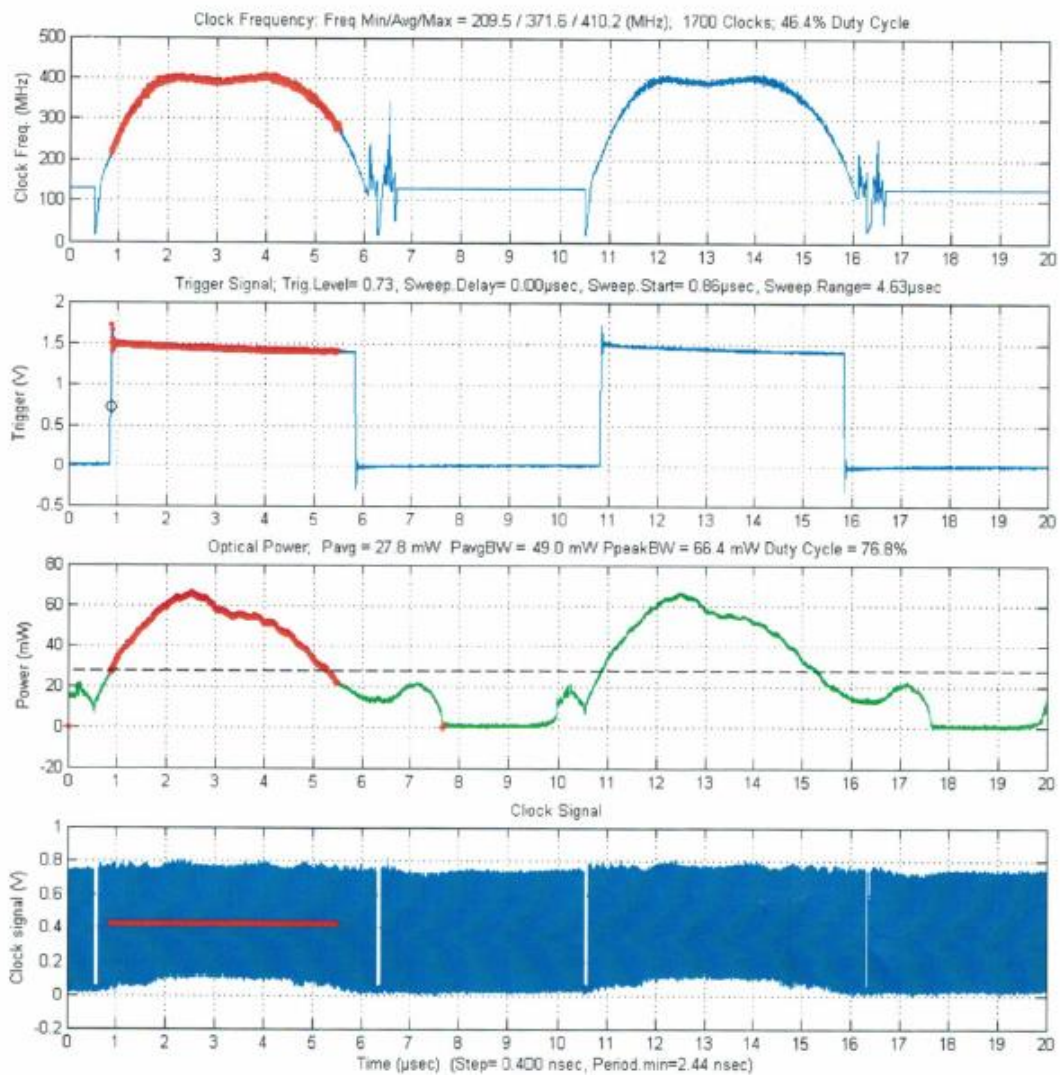
DRAWING PROJECTION		THORLABS www.thorlabs.com	
NAME	DATE	$\lambda=1310\text{nm}$ FC/APC COLLIMATION PACKAGE, NA=0.25 $f=1.26\text{mm}$	
DRAWN	ST	18/MAY/15	
APPROVAL	BW	20/MAY/15	
MATERIAL		SEE TABLE	REV A
COPYRIGHT © 2015 BY THORLABS		ITEM #	APPROX WEIGHT
VALUES IN PARENTHESES ARE CALCULATED AND MAY CONTAIN ROUND-OFF ERRORS.		F220APC-1310	7.4 g



1310nm SS-OCT Laser Engine Final Test Report

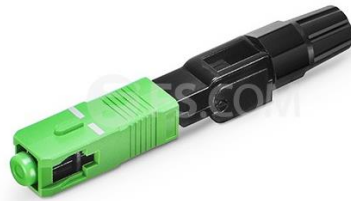
Test information

Serial number: A16005955
Part Number: AXP50124-17
Test date: 12-08-2016 20:15:28
Report date: 2016 December 08
Test operator: skhu
Firmware version: Axsun OCT Firmware V1.13.1



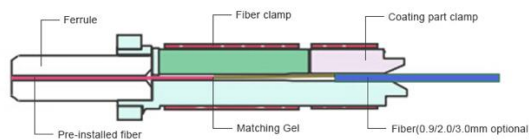
SC/APC connector

SC/APC Type A Singlemode 0.9/2.0/3.0mm Pre-polished Ferrule Field Assembly Connector Fast/Quick Connector, images taken from fs.com [287].



FS P/N: FS-FAOC-SCA-SM-P

Structure Example



Installation Procedure

Always make sure the fast connectors and optic fiber are clean and clear of any debris.

<p>1 Arrange for a FAOC to assemble</p>	<p>2 Insert screw cap into optical cable</p>	<p>3 Strip the coating of optic cable over 45mm</p>	<p>4 Cut off the fiber at the length of 12mm using cleaver</p>
<p>5 Insert optic cable into the fiber guide on the boot until you see a slight bend in the cable</p>	<p>6 Keep the cable bending with right hand, push the connecting holder forward to the end to fix the fiber</p>	<p>7 Take the boot cover down, connect the screw cap with boot by turning it</p>	<p>8 Turn the protrusion of housing toward the bottom and unite it to the body</p>

Reassembling

<p>+</p> <p>Pull out the housing and then separate them by turning the screw cap.</p>	<p>+</p> <p>Pull the fiber connecting holder in reverse with procedure 8. And then, pull out the cable and reassemble.</p>
---	--

Epoxy

EPO-TEK 730, information taken from [338].



EPO-TEK® 730

Technical Data Sheet
For Reference Only
General Purpose Epoxy

Date: September 2017
Rev: V
No. of Components: Two
Mix Ratio by Weight: 1 : 1
Specific Gravity: Part A: 1.12 Part B: 0.94
Pot Life: 1 Hour
Shelf Life- Bulk: One year at room temperature

Recommended Cure: 80°C / 2 Hours

Minimum Alternative Cure(s):
May not achieve performance properties listed below
 100°C / 30 Minutes
 23°C / 24 Hours

NOTES:

- Container(s) should be kept closed when not in use.
- Filled systems should be stirred thoroughly before mixing and prior to use.
- Performance properties (rheology, conductivity, others) of the product may vary from those stated on the data sheet when bi-pak/syringe packaging or post-processing of any kind is performed. Epoxy's warranties shall not apply to any products that have been reprocessed or repackaged from Epoxy's delivered status/container into any other containers of any kind, including but not limited to syringes, bi-paks, cartridges, pouches, tubes, capsules, films or other packages.
- Syringe packaging will impact initial viscosity and effective pot life, potentially beyond stated parameters.

Product Description: EPO-TEK® 730 is a two component, thixotropic, room temperature-curing epoxy adhesive.

Typical Properties: Cure condition: 80°C / 2 Hours Different batches, conditions & applications yield differing results.
 Data below is not guaranteed. To be used as a guide only, not as a specification. * denotes test on lot acceptance basis

PHYSICAL PROPERTIES:		
* Color (before cure):	Part A: Tan	Part B: Tan
* Consistency:	Smooth paste	
* Viscosity (23°C) @ 2.5 rpm:	80,000-120,000	cPs
Thixotropic Index:	2.1	
* Glass Transition Temp:	≥ 55 °C (Dynamic Cure: 20-200°C/ISO 25 Min; Ramp -10-200°C @20°C/Min)	
Coefficient of Thermal Expansion (CTE):		
Below Tg:	66	x 10 ⁻⁶ in/in°C
Above Tg:	248	x 10 ⁻⁶ in/in°C
Shore D Hardness:	64	
Lap Shear @ 23°C:	> 2,000	psi
Die Shear @ 23°C:	≥ 10	Kg 3,556 psi
Degradation Temp:	364 °C	
Weight Loss:		
	@ 200°C:	1.41 %
	@ 250°C:	2.22 %
	@ 300°C:	4.16 %
Suggested Operating Temperature:	< 250 °C (Intermittent)	
Storage Modulus:	123,527	psi
* Particle Size:	≤ 20 microns	
ELECTRICAL AND THERMAL PROPERTIES:		
Thermal Conductivity:	N/A	
Volume Resistivity @ 23°C:	≥ 3 x 10 ¹³	Ohm-cm
Dielectric Constant (1KHz):	3.17	
Dissipation Factor (1KHz):	0.021	

Epoxy and Adhesives for Demanding Applications™

This information is based on data and tests believed to be accurate. Epoxy Technology, Inc. makes no warranties (expressed or implied) as to its accuracy and assumes no liability in connection with any use of this product.

EPOXY TECHNOLOGY, INC.
 14 FORTUNE DRIVE, BILLERICA, MA 01821 (978) 667-3805, FAX (978) 663-9782
www.epotek.com

EPO-TEK 353ND-T, information taken from [339].



EPO-TEK® 353ND-T

Technical Data Sheet

For Reference Only

High Temperature Thixotropic Epoxy

Date: July 2019
Rev: VIII
No. of Components: Two
Mix Ratio by Weight: 10 : 1
Specific Gravity: Part A: 1.12 Part B: 1.02
Pot Life: 3 Hours
Shelf Life- Bulk: One year at room temperature
Shelf Life- Syringe: Six months at -40°C

Recommended Cure: 150°C / 1 Hour

Minimum Alternative Cure(s):

May not achieve performance properties listed below

150°C / 1 Minute
 120°C / 5 Minutes
 100°C / 10 Minutes
 80°C / 30 Minutes

NOTES:

- Container(s) should be kept closed when not in use.
- Filled systems should be stirred thoroughly before mixing and prior to use.
- Performance properties (rheology, conductivity, others) of the product may vary from those stated on the data sheet when bi-pak/syringe packaging or post-processing of any kind is performed. Epoxy's warranties shall not apply to any products that have been reprocessed or repackaged from Epoxy's delivered status/container into any other containers of any kind, including but not limited to syringes, bi-paks, cartridges, pouches, tubes, capsules, films or other packages.
- Syringe packaging will impact initial viscosity and effective pot life, potentially beyond stated parameters.
- **TOTAL MASS SHOULD NOT EXCEED 25 GRAMS**

Product Description: EPO-TEK® 353ND-T is a two component, highly thixotropic epoxy with non-flowing properties and high temperature resistance.

Typical Properties: Cure condition: 150°C / 1 Hour Different batches, conditions & applications yield differing results.
 Data below is not guaranteed. To be used as a guide only, not as a specification. * denotes test on lot acceptance basis

PHYSICAL PROPERTIES:			
* Color (before cure):	Part A: Tan	Part B: Amber	
* Consistency:	Smooth thixotropic paste		
* Viscosity (23°C) @ 20 rpm:	9,000 - 15,000	cPs	
Thixotropic Index:	3.8		
* Glass Transition Temp:	≥ 90	°C (Dynamic Cure: 20-200°C/ISO 25 Min; Ramp -10-200°C @20°C/Min)	
Coefficient of Thermal Expansion (CTE):			
	Below Tg:	43	x 10 ⁻⁶ in/in°C
	Above Tg:	231	x 10 ⁻⁶ in/in°C
Shore D Hardness:	80		
Lap Shear @ 23°C:	1,953	psi	
Die Shear @ 23°C:	≥ 15	Kg	5,334 psi
Degradation Temp:	409	°C	
Weight Loss:			
	@ 200°C:	0.53	%
	@ 250°C:	1.22	%
	@ 300°C:	2.37	%
Suggested Operating Temperature:	< 325	°C (Intermittent)	
Storage Modulus:	559,120	psi	
Ion Content:	Cl ⁻ :	471 ppm	Na ⁺ : 143 ppm
	NH ₄ ⁺ :	400 ppm	K ⁺ : 15 ppm
* Particle Size:	99% ≤ 20	microns	
ELECTRICAL AND THERMAL PROPERTIES:			
Thermal Conductivity:	N/A		
Volume Resistivity @ 23°C:	≥ 4 x 10 ¹²	Ohm-cm	
Dielectric Constant (1KHz):	3.21		
Dissipation Factor (1KHz):	0.003		

Epoxyes and Adhesives for Demanding Applications™

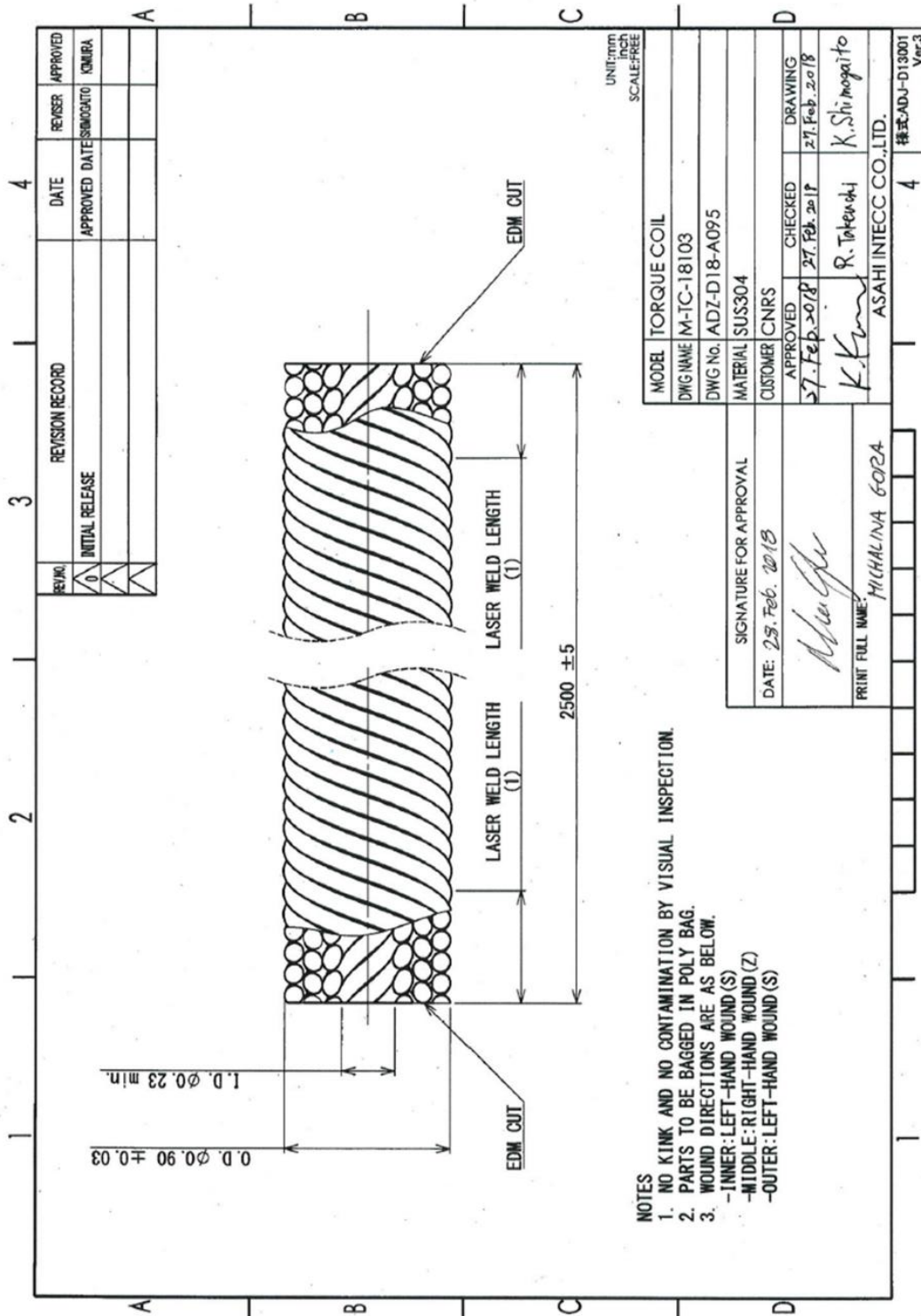
This information is based on data and tests believed to be accurate. Epoxy Technology, Inc. makes no warranties (expressed or implied) as to its accuracy and assumes no liability in connection with any use of this product.

EPOXY TECHNOLOGY, INC.

14 FORTUNE DRIVE, BILLERICA, MA 01821 (978) 667-3805, FAX (978) 663-9782

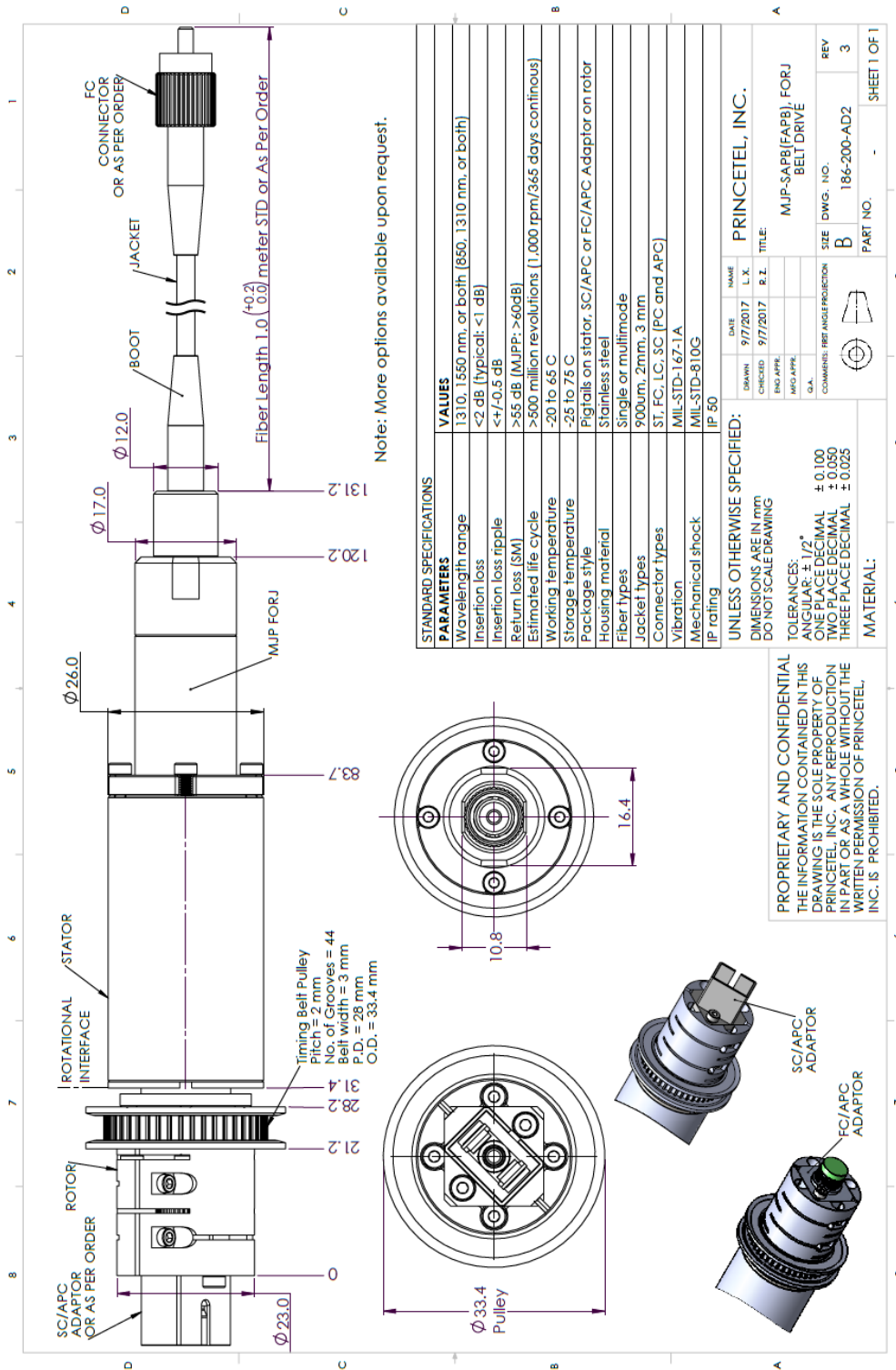
www.epotek.com

Torque coil



- NOTES
1. NO KINK AND NO CONTAMINATION BY VISUAL INSPECTION.
 2. PARTS TO BE BAGGED IN POLY BAG.
 3. WOUND DIRECTIONS ARE AS BELOW.
 - INNER: LEFT-HAND WOUND(S)
 - MIDDLE: RIGHT-HAND WOUND(Z)
 - OUTER: LEFT-HAND WOUND(S)

Fiber optic rotary joint (FOR)



Optical sensor (photointerrupter)

Extracted form the data sheet

SHARP

GP1A52LRJ00F

GP1A52LRJ00F

Gap : 3mm, Slit : 0.5mm

*OPIC Output

Case package Transmissive
Photointerrupter**■ Description**

GP1A52LRJ00F is a standard, OPIC output, transmissive photointerrupter with opposing emitter and detector in a case, providing non-contact sensing. For this family of devices, the emitter and detector are inserted in a case, resulting in a through-hole design.

■ Features

1. Transmissive with OPIC output
2. Highlights :
 - Vertical Slit for alternate motion detection
 - Output High Level at intercepting optical path
3. Key Parameters :
 - Gap Width : 3mm
 - Slit Width (detector side) : 0.5mm
 - Package : 12.2x10x5mm
4. RoHS directive compliant

■ Agency approvals/Compliance

1. Compliant with RoHS directive

■ Applications

1. General purpose detection of object presence or motion.
2. Example : Printer, FAX, Optical storage unit

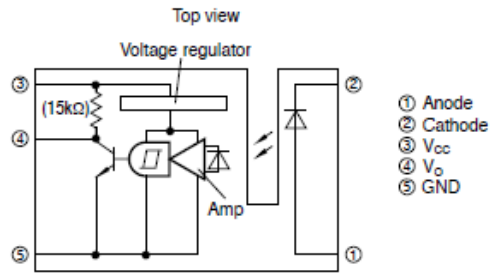
* "OPIC"(Optical IC) is a trademark of the SHARP Corporation. An OPIC consists of a light-detecting element and a signal-processing

Notice The content of data sheet is subject to change without prior notice.
In the absence of confirmation by device specification sheets, SHARP takes no responsibility for any defects that may occur in equipment using any SHARP devices shown in catalogs, data books, etc. Contact SHARP in order to obtain the latest device specification sheets before using any SHARP device.



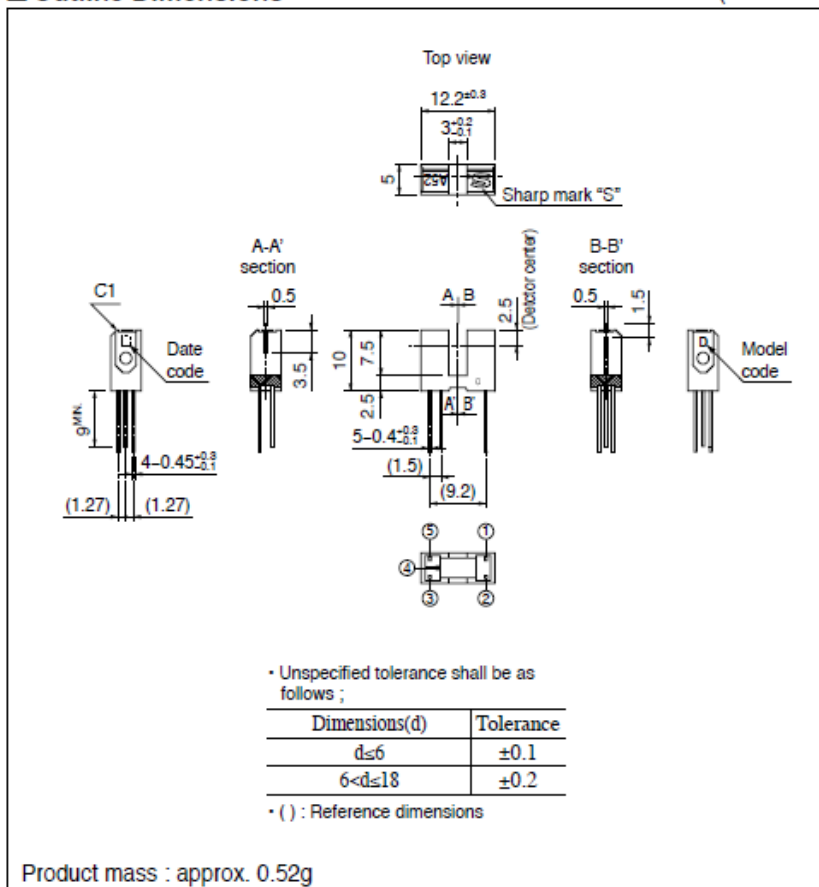
GP1A52LRJ00F

Internal Connection Diagram



Outline Dimensions

(Unit : mm)



Dip soldering material : Sn-3Ag-0.5Cu

SHARP

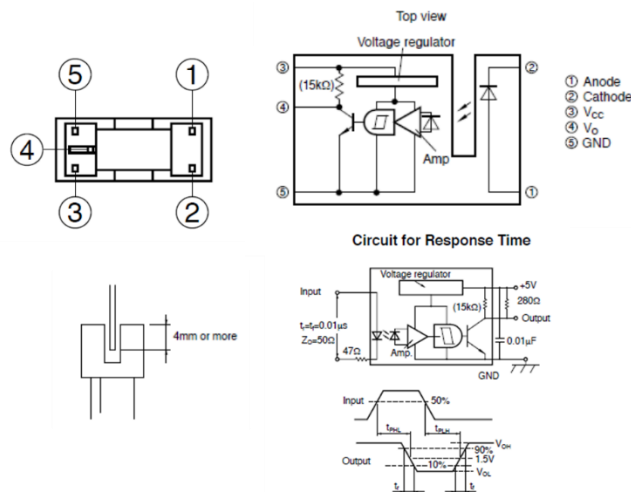
GP1A52LRJ00F

Absolute Maximum Ratings $(T_c=25^\circ\text{C})$

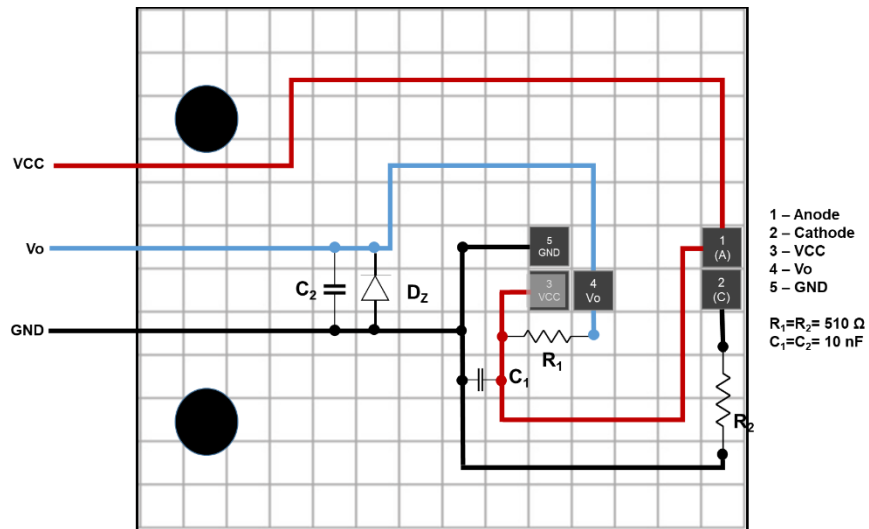
Parameter	Symbol	Rating	Unit
Input	^{*1} Forward current	I_F	50 mA
	^{*1,2} Peak forward current	I_{FM}	1 A
	Reverse voltage	V_R	6 V
	Power dissipation	P	75 mW
Output	Supply voltage	V_{CC}	-0.5 to +17 V
	Output current	I_O	50 mA
	Power dissipation	P_O	250 mW
Operating temperature	T_{opr}	-25 to +85	$^\circ\text{C}$
Storage temperature	T_{stg}	-40 to +100	$^\circ\text{C}$
^{*3} Soldering temperature	T_{sld}	260	$^\circ\text{C}$

^{*1} Refer to Fig. 1, 2, 3^{*2} Pulse width $\leq 100\mu\text{s}$, Duty ratio=0.01^{*3} For 5s or less**Electro-optical Characteristics** $(T_c=25^\circ\text{C})$

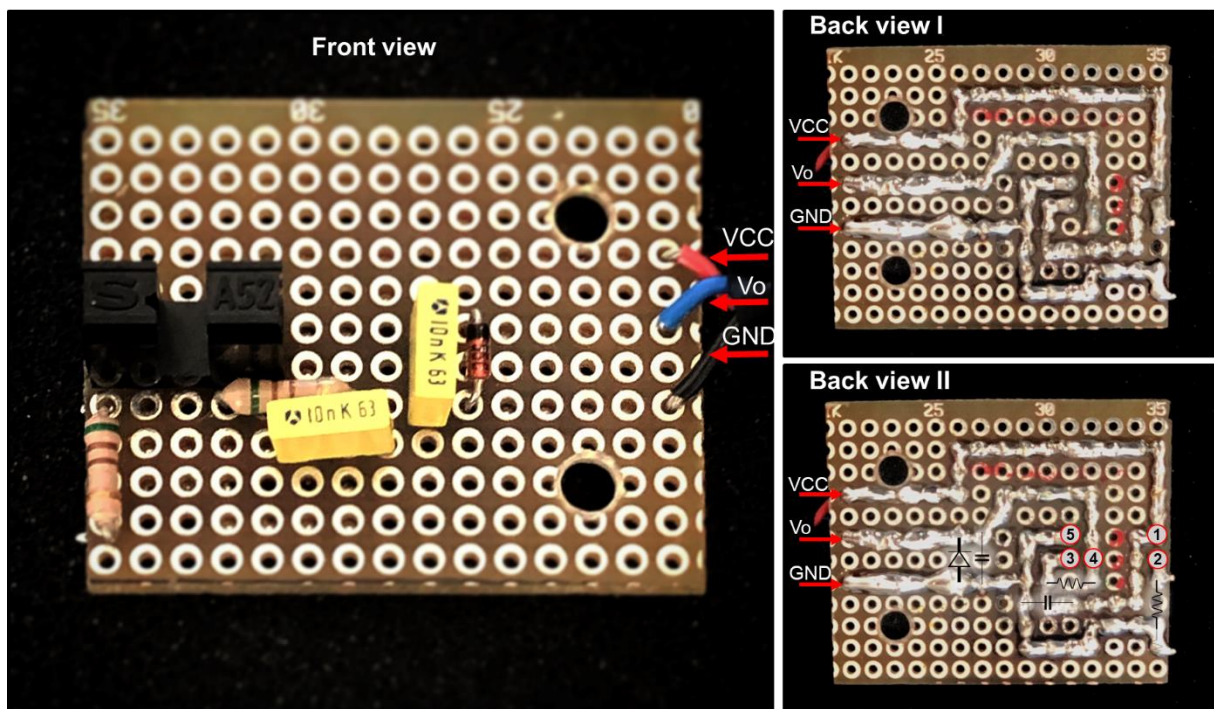
Parameter	Symbol	Condition	MIN.	TYP.	MAX.	Unit		
Input	Forward voltage	V_F	$I_F=5\text{mA}$	-	1.1	1.4	V	
	Reverse current	I_R	$V_R=3\text{V}$	-	-	10	μA	
Output	Operating supply voltage	V_{CC}	-	4.5	-	17	V	
	Low level output voltage	V_{OL}	$V_{CC}=5\text{V}, I_{OL}=16\text{mA}, I_F=5\text{mA}$	-	0.15	0.4	V	
	High level output voltage	V_{OH}	$V_{CC}=5\text{V}, I_F=0$	4.9	-	-	V	
	Low level supply current	I_{CCL}	$V_{CC}=5\text{V}, I_F=5\text{mA}$	-	1.7	3.8	mA	
	High level supply current	I_{CCH}	$V_{CC}=5\text{V}, I_F=0$	-	0.7	2.2	mA	
Transfer characteristics	^{*3} "Low→High" threshold input current	I_{FHL}	$V_{CC}=5\text{V}$	-	1	5	mA	
	^{*4} Hysteresis	I_{PLH}/I_{PHL}	$V_{CC}=5\text{V}$	0.55	0.75	0.95	-	
	Response time ^{*6}	"High→Low" Propagation delay time	t_{PHL}	$V_{CC}=5\text{V}, I_F=5\text{mA}, R_L=280\Omega$	-	3	9	μs
		"Low→High" Propagation delay time	t_{PLH}		-	5	15	
		Rise time	t_r		-	0.1	0.5	
		Fall time	t_f		-	0.05	0.5	

^{*4} I_{PHL} represents forward current when output goes from "High" to "Low".^{*5} I_{PLH} represents forward current when output goes from "Low" to "High".^{*6} Test circuit for response time is shown in Fig. 12.**Recommended operating conditions**

Parameter	Symbol	MIN.	TYP.	MAX.	Unit
Output current	I_O	-	-	16	mA
Forward current	I_F	10	-	20	mA
Operating temperature	T_{opr}	0	-	70	$^\circ\text{C}$



(A)




(B)

Figure F.4 (A) Matrix board wiring of the synchronization sensor of the helical scanner. (B) Back view schematic drawing. (B) Pictures of the wired circuit, front and back views.

Pulley

High Torque Timing Pulleys - 1.5GT, 2GT

For 2GT High Torque Timing Belts, see **P1459** and for 2GT Idlers with Teeth, see **P1453**. For 1.5GT High Torque Timing Belts, see the VONA Site.

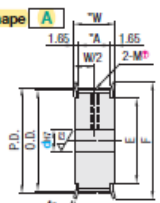
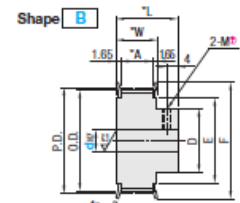


RoHS

Type	Belt Width				Material		Surface Treatment	Accessory Set Screws
	4mm	6mm	8mm	9mm	Pulley	Flange		
GPA	GT15040	GT2040	GT2060	GT2090	A200 Series Aluminum Alloy	Aluminum Alloy	Clear Anodize	EN 1.4301 Equiv.

* The above material and accessory might be changed to the ones equivalent to the originals.
 † Flange is installed, and set screws are included with Shaft Bore P and N.

• Pulley Shape

Shape A  **Shape B** 

Standard Tooth Profile
 Tooth groove dimensions slightly vary according to the number of teeth.
 Top (Pitch: 1.5mm)
 Bottom (Pitch: 2.0mm)
 † Shaft Bore Specs. H (Round Hole) do not have tapped holes.

Number of Teeth, Dimension: 1.5GT

mm	Number of Teeth			
P.D.	16	20	24	36
O.D.	8.19	9.55	11.46	14.32
D	8.13	9.09	11.00	13.96
F	13	14	16	18
E	6	7	8	10

Number of Teeth, Dimension: 2GT

mm	Number of Teeth																				
P.D.	14	15	16	18	20	21	22	24	25	26	28	30	32	34	36	38	40	44	48	50	60
O.D.	8.91	9.55	10.19	11.46	12.73	13.37	14.01	15.28	15.92	16.55	17.83	19.10	20.37	21.65	22.92	24.19	25.46	28.01	30.56	31.83	38.21
D	8.40	9.04	9.68	10.95	12.22	12.86	13.50	14.77	15.41	16.04	17.32	18.59	19.86	21.14	22.41	23.68	24.95	27.50	30.05	31.32	37.69
F	13	14	14	16	17	18	18	20	20	21	23	24	25	27	27	29	30	32	36	36	42
E	6	7	7	8	9	10	10	12	12	12	14	15	17	18	18	20	21	23	26	27	33

Belt Nominal Width / Dimension


mm	Nominal			
A	5.0	5.0	7.0	10.0
W	8.3	8.3	10.3	13.3
L	16.0	16.0	18.0	21.0

Tapped Hole Dimensions (Shaft Bore Specs: P, N)

d _{HT}	M (Coarse)	Accessory Set Screws
5	M3	M3x3
6-22	M4	M4x3

• Shaft Bore Specs. † Surface treatment may not be applied to shaft bores.

H Round Hole **P** Round Hole + Tap **N** New JIS Keywayed Bore + Tap



† No tapped holes or set screws.
 † For A-Shape pulley, the screw holes are set at around 120° to keep away from peaks.
 † For Keyway Dimension Details, see P1377. When selecting the shaft bore dia. 10 and the keyway width 4.0mm (height 1.8mm), specify NK10.

1.5GT

Type	Number of Teeth	Type Nominal Width	Pulley Shape	Pulley Shape					
				A			B		
				H Round Hole	P Round Hole + Tap	N Keyway + Tap	H Round Hole	P Round Hole + Tap	N Keyway + Tap
Aluminum GPA	16	GT15040	A	3, 4	-	-	-	-	-
	20	GT15040	A	4, 4.5, 5	-	-	-	-	-
	24	GT15040	A	4, 4.5, 5, 6	-	-	-	-	-
	30	GT15040	A	5, 6	-	-	4	5, 6	-
	36	GT15040	B	5, 6, 6.35, 7, 8	5, 6, 6.35, 7, 8	B	5, 6, 6.35, 7, 8	5, 6, 6.35, 7, 8	8

2GT

Type	Number of Teeth	Type Nominal Width	Pulley Shape	Pulley Shape					
				A			B		
				H Round Hole	P Round Hole + Tap	N Keyway + Tap	H Round Hole	P Round Hole + Tap	N Keyway + Tap
Aluminum GPA	14	GT2040	A	3	-	-	-	-	-
	15			3, 4	-	-	-	-	
	16			3, 4	-	-	-	-	
	18			4, 4.5, 5	-	-	-	-	
	20			4, 4.5, 5, 6	-	-	-	-	
	21			4-6	-	-	-	-	
	22			4-6	-	-	4	-	
	24			5, 6, 6.35, 7	-	-	5	-	
	25			5, 6, 6.35, 7	-	-	5, 6, 6.35, 7	-	
	26			5, 6, 6.35, 7, 8	-	-	5, 6, 6.35, 7, 8	-	
	28			5, 6, 6.35, 7, 8	-	-	5, 6, 6.35, 7, 8	-	
	30			5, 6, 6.35, 7, 8	-	-	5, 6, 6.35, 7, 8	-	
	32			5, 6, 6.35, 7-10	5, 6, 6.35, 7-10	-	5, 6, 6.35, 7, 8	5, 6	
	34			6, 6.35, 7-10	6, 6.35, 7-10	-	6, 6.35, 7-10	6, 6.35, 7, 8	
	36			6, 6.35, 7-10	6, 6.35, 7-10	-	6, 6.35, 7-10	6, 6.35, 7, 8	
	38			6, 6.35, 7-10	6, 6.35, 7-10	-	6, 6.35, 7-10	6, 6.35, 7, 8	
40	6, 6.35, 7-12	6, 6.35, 7-12	B	6, 6.35, 7-10	6, 6.35, 7, 8				
44	6, 6.35, 7-15	6, 6.35, 7-15	B, 10, NK10	6, 6.35, 7-15	6, 6.35, 7-10				
48	8-17	8-15	8, 10, NK10, 11-13	8-16	8				
50	8-17	8-16	8, 10, NK10, 11-14	8-16	8-12				
60	8-24	8-22	8, 10, NK10, 11-16	8-24	8				

Ordering Example: Part Number - Pulley Shape - Shaft Bore Spec. I.D.
 GPA32GT2060 - A - H8



Number of Teeth	Body Price								Shaft Bore Machining Charge (Body Price +)			
	2000 Series Aluminum Alloy (Clear Anodize)								1.5GT		2GT	
	GT15040		GT2040		GT2090		GT2090		P Hole	N Hole	P Hole	N Hole
	Shape A	Shape B	Shape A	Shape B	Shape A	Shape B	Shape A	Shape B				
14												
15												
16												
18												
20												
21												
22												
24												
25												
26												
28												
30												
32												
34												
36												
38												
40												
44												
48												
50												
60												

Alterations Part Number - Pulley Size - Shaft Bore Specs. (D) - (KC90-etc.)
 GPA32GT2090 - A - H9 - NFC

Alterations	Set Screw Angle	No Flange	Single Flange	Flange Cut	Hub Shortening
Code	KC90	NFC	RFC, LFC	FC	BC
Spec.	Changes an angle of set screw to 90°. For A-Shape pulley, the screw holes are set at around 90° to keep away from peaks.	(Flange 2 pcs. Included) (Flange 2 pcs. Excluded) NFC	(Flange 1 pc. Included) (Flange 1 pc. Excluded) RFC	Cut the flange O.D. in 0.5mm increment. (Flange 1 pc. Excluded) FC17 Application Note: FC$(D.D.)+1$ FC$F-2$ No surface treatment is applied on flange circumference.	Cut the hub length in 0.5mm increment. (Flange 2 pcs. Excluded) BC5 Application Note: Shaft Bore Specs. H: 3\timesBC$L-W$ Shaft Bore Specs. P, N: M+3\timesBC$L-W$ Not available for Shape A.

Alterations	Side Through Hole / Side Tapped Hole, 3 places	Side Through Hole / Side Tapped Hole, 4 places	Side Through Hole / Side Tapped Hole, 6 places
Code	KTC, QTC	KFC, QFC	KSC, QSC
Spec.	Machine Through Hole / Tapped Hole on the side surface of hub side (Through Hole / Tapped Hole) KTC20-K5.0 (Through Hole / Tapped Hole) QTC28-M4 (Through Hole / Tapped Hole / Side) K4.0-K8.0 (0.5mm Increment) (Through Hole / Tapped Hole / Side) M3, M4, M5, M6, M8 Application Note: When KTC/QTC is selected for Shaft Bore Specs. P and N, KC90 is not available. Not available for 1.5GT.	Machine Through Hole / Tapped Hole on the side surface of hub side (Through Hole / Tapped Hole) KFC20-K5.0 (Through Hole / Tapped Hole) QFC28-M4 (Through Hole / Tapped Hole / Side) K4.0-K8.0 (0.5mm Increment) (Through Hole / Tapped Hole / Side) M3, M4, M5, M6, M8 Application Note: Specify KC90 when selecting KFC/QFC for Shaft Bore Specs. P, N and C. Side holes and both side tapped holes might interfere with each other. For details, see the relevant CAD data. Not available for 1.5GT.	Machine Through Hole / Tapped Hole on the side surface of hub side (Through Hole / Tapped Hole) KSC20-K5.0 (Through Hole / Tapped Hole) QSC28-M4 (Through Hole / Tapped Hole / Side) K4.0-K8.0 (0.5mm Increment) (Through Hole / Tapped Hole / Side) M3, M4, M5, M6, M8 Application Note: KSC/QSC is not applicable to the Shaft Bore Specs. P and N. Not available for 1.5GT.

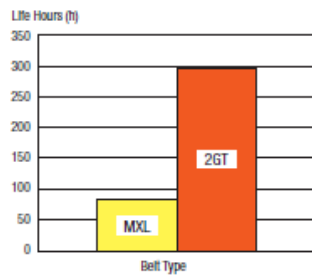
For details, see the "Timing Pulley Alterations - Overview" section (pg. P.137a).

Performance Comparison between MXL and 2GT Belts

Reference ①: Durability

<Performance Conditions>
 Number of belt teeth: 126
 Belt Width: 9.5mm
 Number of Pulley Teeth: 12 (2GT)
 : 14 (MXL)
 Speed: 7,900rpm
 Load Torque: 24.2N·m

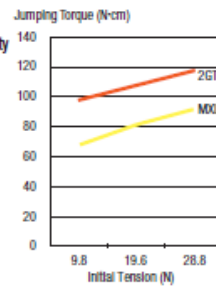
* For technical data of backlash, see pg. P.137f.



Reference ②: Jumping Torque Capability

<Performance Conditions>
 Number of belt teeth: 126
 Belt Width: 4.8mm
 Number of Pulley Teeth: 20 (2GT)
 : 20 (MXL)
 Speed: 1,120rpm
 Tooth Height
 MXL: 0.51mm
 2GT: 0.75mm

* Jumping Torque represents the max. torque when a jumping occurs.



Bibliography

- [1] MedlinePlus, “Digestive diseases: MedlinePlus Medical Encyclopedia.” [Online]. Available: <https://medlineplus.gov/ency/article/007447.htm>. [Accessed: 03-Jun-2019].
- [2] Terese Winslow LLC., “Terese Winslow LLC, Medical and Scientific Illustration.” [Online]. Available: <https://www.teresewinslow.com/#/digestion/>. [Accessed: 01-Dec-2019].
- [3] M. E. (Neurologist) Smith and D. G. Morton, *The digestive system : basic science and clinical condition*. Churchill Livingstone, 2010.
- [4] A. Rehfeld, M. Nylander, K. Karnov, A. Rehfeld, M. Nylander, and K. Karnov, “The Digestive System I: The Alimentary Canal,” in *Compendium of Histology*, Springer International Publishing, 2017, pp. 433–473.
- [5] K. S. Saladin, *Human Anatomy*, 5th ed. 2017.
- [6] “Definition of squamous cell carcinoma - NCI Dictionary of Cancer Terms - National Cancer Institute.” [Online]. Available: <https://www.cancer.gov/publications/dictionaries/cancer-terms/def/squamous-cell-carcinoma>. [Accessed: 22-Oct-2019].
- [7] PDQ Adult Treatment Editorial Board, *Esophageal Cancer Treatment (PDQ®): Patient Version*. 2002.
- [8] PDQ Adult Treatment Editorial Board, *Gastric Cancer Treatment (PDQ®): Patient Version*. 2002.
- [9] “What Is Colorectal Cancer?” [Online]. Available: <https://www.cancer.org/cancer/colon-rectal-cancer/about/what-is-colorectal-cancer.html>. [Accessed: 09-Jun-2018].
- [10] “Fact Sheets by Population.” [Online]. Available: http://globocan.iarc.fr/Pages/fact_sheets_population.aspx.
- [11] “What Are the Survival Rates for Colorectal Cancer, by Stage?” [Online]. Available: <https://www.cancer.org/cancer/colon-rectal-cancer/detection-diagnosis-staging/survival-rates.html>. [Accessed: 09-Jan-2018].
- [12] Cancer Today-IARC, “Cancer Today.” [Online]. Available: http://gco.iarc.fr/today/online-analysis-pie?v=2018&mode=cancer&mode_population=continents&population=900&populations=900&key=total&sex=0&cancer=39&type=0&statistic=5&prevalence=0&population_group=0&ages_group%5B%5D=0&ages_group%5B%5D=17&nb_items=7&group_. [Accessed: 22-Oct-2019].

-
- [13] M. Fleming, S. Ravula, S. F. Tatishchev, and H. L. Wang, “Colorectal carcinoma: Pathologic aspects,” *Journal of Gastrointestinal Oncology*, vol. 3, no. 3. Pioneer Bioscience Publishing, pp. 153–173, 2012.
- [14] The American Cancer Society medical and editorial content team, “Colorectal Cancer Risk Factors.” [Online]. Available: <https://www.cancer.org/cancer/colon-rectal-cancer/causes-risks-prevention/risk-factors.html>. [Accessed: 04-Jun-2019].
- [15] J. G. Williams *et al.*, “Management of the malignant colorectal polyp: ACPGBI position statement,” *Color. Dis.*, vol. 15, pp. 1–38, Aug. 2013.
- [16] “Colo-Rectal Cancer: ESMO Clinical Practice Guidelines | ESMO.” [Online]. Available: <http://www.esmo.org/Guidelines/Gastrointestinal-Cancers/Rectal-Cancer>. [Accessed: 09-Jun-2018].
- [17] “ESMO Consensus Guidelines: Management of Patients with Colon and Rectal Cancer. A personalized approach to clinical decision making | ESMO.” [Online]. Available: <http://www.esmo.org/Guidelines/Gastrointestinal-Cancers/Management-of-patients-with-colon-and-rectal-cancer.-A-personalized-approach-to-clinical-decision-making>. [Accessed: 09-Jun-2018].
- [18] “Colorectal cancer. The diagnosis and management of colorectal cancer. | National Guideline Clearinghouse.” [Online]. Available: <https://www.guideline.gov/summaries/summary/48931/colorectal-cancer-the-diagnosis-and-management-of-colorectal-cancer>. [Accessed: 09-Jun-2018].
- [19] Johns Hopkins Gastroenterology and Hepatology, “Sporadic (Nonhereditary) Colorectal Cancer: Therapy.” [Online]. Available: https://www.halstedurgery.org/GDL_Disease.aspx?CurrentUDV=31&GDL_Cat_ID=551CDCA7-A3C1-49E5-B6A0-C19DE1F94871&GDL_Disease_ID=FB4F2BE3-FC13-44E4-BB69-2CCE936A6CD5. [Accessed: 01-Jun-2018].
- [20] “Colorectal Cancer Screening Tests.” [Online]. Available: <https://www.cancer.org/cancer/colon-rectal-cancer/detection-diagnosis-staging/screening-tests-used.html>. [Accessed: 09-Jun-2018].
- [21] P. Guidelines, “Polyp Guideline: Diagnosis, Treatment, and Surveillance for Patients With Colorectal Polyps*,” *Science (80-.)*, vol. 95, no. 11, p. 9270, 2000.
- [22] A. J. C. O. CANCER, “AJCC - American Joint Committee on Cancer.” [Online]. Available: <https://cancerstaging.org/Pages/default.aspx>. [Accessed: 27-May-2019].
- [23] “How Cancer Is Diagnosed - National Cancer Institute.” [Online]. Available: <https://www.cancer.gov/about-cancer/diagnosis-staging/diagnosis>. [Accessed: 04-Jun-2019].
- [24] F. P. & J. Waschke, *Sobotta Atlas of Human Anatomy, Vol. 2*, 15th ed. Elsevier, 2011.
- [25] O. Corporation, “OLYMPUS CV-290 Specifications.”

- [26] “SEER*Explorer Application.” [Online]. Available: https://seer.cancer.gov/explorer/application.php?site=20&data_type=4&graph_type=6&compareBy=stage&chk_sex_1=1&chk_race_1=1&chk_age_range_1=1&chk_stage_101=101&chk_stage_104=104&chk_stage_105=105&chk_stage_106=106&adopt_precision=1&showDataFor=sex_1_and_r. [Accessed: 01-Jun-2019].
- [27] S. Hattori *et al.*, “Narrow-band imaging observation of colorectal lesions using NICE classification to avoid discarding significant lesions.,” *World J. Gastrointest. Endosc.*, vol. 6, no. 12, pp. 600–5, Dec. 2014.
- [28] V. Subramanian and K. Rangunath, “Advanced endoscopic imaging: A review of commercially available technologies,” *Clin. Gastroenterol. Hepatol.*, vol. 12, no. 3, pp. 368–76.e1, Mar. 2014.
- [29] J. East *et al.*, “Advanced endoscopic imaging: European Society of Gastrointestinal Endoscopy (ESGE) Technology Review,” *Endoscopy*, vol. 48, no. 11, pp. 1029–1045, Oct. 2016.
- [30] H. Aihara, S. Saito, and H. Tajiri, “Rationale for and clinical benefits of colonoscopy with narrow band imaging: pathological prediction and colorectal screening.,” *Int. J. Colorectal Dis.*, vol. 28, no. 1, pp. 1–7, Jan. 2013.
- [31] H. Aihara, S. Saito, and H. Tajiri, “Rationale for and clinical benefits of colonoscopy with narrow band imaging: Pathological prediction and colorectal screening,” *International Journal of Colorectal Disease*, vol. 28, no. 1. pp. 1–7, Jan-2013.
- [32] “FICE Dual Mode | Fujifilm Europe.” [Online]. Available: <https://www.fujifilm.eu/eu/products/medical-systems/endoscopy/technology/fice-dual-mode>. [Accessed: 09-Jun-2019].
- [33] S. N. Ket, E. Bird-Lieberman, and J. E. East, “Electronic Imaging to Enhance Lesion Detection at Colonoscopy,” *Gastrointest. Endosc. Clin. N. Am.*, vol. 25, no. 2, pp. 227–242, Apr. 2015.
- [34] L. K. Wanders, J. E. East, S. E. Uitentuis, M. M. G. Leeflang, and E. Dekker, “Diagnostic performance of narrowed spectrum endoscopy, autofluorescence imaging, and confocal laser endomicroscopy for optical diagnosis of colonic polyps: a meta-analysis,” *Lancet Oncol.*, vol. 14, no. 13, pp. 1337–1347, Dec. 2013.
- [35] H. Aihara, H. Tajiri, and T. Suzuki, “Application of autofluorescence endoscopy for colorectal cancer screening: rationale and an update.,” *Gastroenterol. Res. Pract.*, vol. 2012, p. 971383, 2012.
- [36] “OLYMPUS | News Release: World’s First(*note) Gastrointestinal Videoscopes with Auto Fluorescence Imaging Capability.” [Online]. Available: <https://www.olympus-global.com/en/news/2007a/nr070117evis.html>. [Accessed: 09-Jun-2019].
- [37] Z. Nabi and D. N. Reddy, “Optical biopsy in gastroenterology: Focus on confocal laser endomicroscopy,” *Indian J. Gastroenterol.*, Oct. 2019.

-
- [38] M. Wallace *et al.*, “Miami classification for probe-based confocal laser endomicroscopy,” *Endoscopy*, vol. 43, no. 10, pp. 882–91, Oct. 2011.
- [39] S. Beg, A. Wilson, and K. Raganath, “The use of optical imaging techniques in the gastrointestinal tract,” *Frontline Gastroenterol.*, vol. 7, no. 3, pp. 207–215, Jul. 2016.
- [40] M. J. Suter *et al.*, “Image-guided biopsy in the esophagus through comprehensive optical frequency domain imaging and laser marking: a study in living swine,” *Gastrointest. Endosc.*, vol. 71, no. 2, pp. 346–353, 2010.
- [41] NinePoint Medical, “NvisionVLE® Imaging System - NinePoint Medical.” [Online]. Available: <http://www.ninepointmedical.com/nvisionvle-imaging-system/>. [Accessed: 11-Jun-2019].
- [42] P. R. Pfau *et al.*, “Criteria for the diagnosis of dysplasia by endoscopic optical coherence tomography,” *Gastrointest. Endosc.*, vol. 58, no. 2, pp. 196–202, Aug. 2003.
- [43] B. Shen *et al.*, “In vivo colonoscopic optical coherence tomography for transmural inflammation in inflammatory bowel disease,” *Clinical Gastroenterology and Hepatology*, vol. 2, no. 12, pp. 1080–1087, 2004.
- [44] X. Qi, Y. Pan, M. V Sivak, J. E. Willis, G. Isenberg, and A. M. Rollins, “Image analysis for classification of dysplasia in Barrett’s esophagus using endoscopic optical coherence tomography,” *Biomed. Opt. Express*, vol. 1, no. 3, pp. 825–847, 2010.
- [45] J. A. Evans and N. S. Nishioka, “The use of optical coherence tomography in screening and surveillance of Barrett’s esophagus,” *Clin. Gastroenterol. Hepatol.*, vol. 3, no. 7 Suppl 1, pp. S8-11, 2005.
- [46] null E. C. R. Group, “Update on the Paris Classification of Superficial Neoplastic Lesions in the Digestive Tract,” *Endoscopy*, vol. 37, no. 6, pp. 570–578, Jun. 2005.
- [47] T. Kaltenbach and R. Soetikno, “Endoscopic Resection of Large Colon Polyps,” *Gastrointest. Endosc. Clin. N. Am.*, vol. 23, no. 1, pp. 137–152, Jan. 2013.
- [48] “Endoscopic mucosal resection for management of large colorectal polyps - Mayo Clinic.” [Online]. Available: <https://www.mayoclinic.org/medical-professionals/digestive-diseases/news/endoscopic-mucosal-resection-for-management-of-large-colorectal-polyps/mac-20442005>. [Accessed: 12-Jun-2019].
- [49] M. Kato, “Endoscopic Mucosal Resection (EMR),” in *Advanced Colonoscopy*, New York, NY: Springer New York, 2014, pp. 31–38.
- [50] M. Ferlitsch *et al.*, “Colorectal polypectomy and endoscopic mucosal resection (EMR): European Society of Gastrointestinal Endoscopy (ESGE) Clinical Guideline,” *Endoscopy*, vol. 49, no. 03, pp. 270–297, Feb. 2017.
- [51] K. Niimi, M. Fujishiro, and K. Koike, “Endoscopic Submucosal Dissection (ESD),” in *Advanced Colonoscopy*, New York, NY: Springer New York, 2014, pp. 39–51.

-
- [52] K. Niimi, M. Fujishiro, and K. Koike, "Endoscopic submucosal dissection (ESD)," in *Advanced Colonoscopy: Principles and Techniques Beyond Simple Polypectomy*, Springer New York, 2014, pp. 39–51.
- [53] C. Huang, R.-X. Huang, and Z.-J. Qiu, "Natural orifice transluminal endoscopic surgery: New minimally invasive surgery come of age," *World J. Gastroenterol.*, vol. 17, no. 39, p. 4382, 2011.
- [54] F. Tendick, S. S. Sastry, R. S. Fearing, and M. Cohn, "Applications of micromechatronics in minimally invasive surgery," *IEEE/ASME Trans. Mechatronics*, vol. 3, no. 1, pp. 34–42, Mar. 1998.
- [55] "Minimally Invasive and Robotic Surgery: Johns Hopkins Medicine in Baltimore, MD." [Online]. Available: https://www.hopkinsmedicine.org/minimally_invasive_robotic_surgery/. [Accessed: 08-Jun-2018].
- [56] J. Troccaz, G. Dagnino, and G.-Z. Yang, "Frontiers of Medical Robotics: From Concept to Systems to Clinical Translation," *Annu. Rev. Biomed. Eng.*, vol. 21, no. 1, pp. 193–218, Jun. 2019.
- [57] V. Vitiello, S. L. Lee, T. P. Cundy, and G. Z. Yang, "Emerging robotic platforms for minimally invasive surgery," *IEEE Rev. Biomed. Eng.*, vol. 6, pp. 111–126, 2013.
- [58] Y. S. Kwoh, J. Hou, E. A. Jonckheere, and S. Hayati, "A Robot with Improved Absolute Positioning Accuracy for CT Guided Stereotactic Brain Surgery," *IEEE Trans. Biomed. Eng.*, vol. 35, no. 2, pp. 153–160, 1988.
- [59] A. L. Benabid, P. Cinquin, S. Lavalley, J. F. Le Bas, J. Demongeot, and J. de Rougemont, "Computer-Driven Robot for Stereotactic Surgery Connected to CT Scan and Magnetic Resonance Imaging," *Stereotact. Funct. Neurosurg.*, vol. 50, no. 1–6, pp. 153–154, 1987.
- [60] S. Lavalley, J. Troccaz, L. Gaborit, P. Cinquin, A. L. Benabid, and D. Hoffmann, "Image guided operating robot: A clinical application in stereotactic neurosurgery," in *Proceedings - IEEE International Conference on Robotics and Automation*, 1992, vol. 1, pp. 618–624.
- [61] H. A. Paul *et al.*, "A surgical robot for total hip replacement surgery," in *Proceedings - IEEE International Conference on Robotics and Automation*, 1992, vol. 1, pp. 606–611.
- [62] W. L. Bargar, A. Bauer, and M. Börner, "Primary and revision total hip replacement using the ROBODOC® system," in *Clinical Orthopaedics and Related Research*, 1998, no. 354, pp. 82–91.
- [63] "Robotic Surgery." [Online]. Available: <https://spinoff.nasa.gov/spinoff2000/hm1.htm>. [Accessed: 22-Nov-2019].
- [64] J. M. Sackier and Y. Wang, "Robotically assisted laparoscopic surgery - From concept

- to development,” *Surg. Endosc.*, vol. 8, no. 1, pp. 63–66, Jan. 1994.
- [65] S. E. Butner and M. Ghodoussi, “Transforming a Surgical Robot for Human Telesurgery,” *IEEE Trans. Robot. Autom.*, vol. 19, no. 5, pp. 818–824, Oct. 2003.
- [66] J. Marescaux *et al.*, “Transatlantic robot-assisted telesurgery,” *Nature*, vol. 413, no. 6854, pp. 379–380, Sep. 2001.
- [67] A. Schweikard, H. Shiomi, and J. Adler, “Respiration tracking in radiosurgery,” *Med. Phys.*, vol. 31, no. 10, pp. 2738–2741, Sep. 2004.
- [68] M. Jakopc, F. Rodriguez y Baena, S. J. Harris, P. Gomes, J. Cobb, and B. L. Davies, “The Hands-On Orthopaedic Robot ‘Acrobot’: Early Clinical Trials of Total Knee Replacement Surgery,” *IEEE Trans. Robot. Autom.*, vol. 19, no. 5, pp. 902–911, Oct. 2003.
- [69] E. I. George, T. C. Brand, A. LaPorta, J. Marescaux, and R. M. Satava, “Origins of Robotic Surgery: From Skepticism to Standard of Care,” *JSLs J. Soc. Laparoendosc. Surg.*, vol. 22, no. 4, Oct. 2018.
- [70] S. Voros, G. P. Haber, J. F. Menudet, J. A. Long, and P. Cinquin, “ViKY robotic scope holder: Initial clinical experience and preliminary results using instrument tracking,” *IEEE/ASME Trans. Mechatronics*, vol. 15, no. 6, pp. 879–886, Dec. 2010.
- [71] Y. Feng *et al.*, “An efficient cardiac mapping strategy for radiofrequency catheter ablation with active learning,” *Int. J. Comput. Assist. Radiol. Surg.*, pp. 1–9, May 2017.
- [72] L. DI BIASE *et al.*, “Ablation of Atrial Fibrillation Utilizing Robotic Catheter Navigation in Comparison to Manual Navigation and Ablation: Single-Center Experience,” *J. Cardiovasc. Electrophysiol.*, vol. 20, no. 12, pp. 1328–1335, Dec. 2009.
- [73] C. V. Riga, C. D. Bicknell, A. Rolls, N. J. Cheshire, and M. S. Hamady, “Robot-assisted fenestrated endovascular aneurysm repair (FEVAR) using the magellan system,” *J. Vasc. Interv. Radiol.*, vol. 24, no. 2, pp. 191–196, Feb. 2013.
- [74] R. J. Webster, J. P. Swensen, J. M. Romano, and N. J. Cowan, “Closed-Form Differential Kinematics for Concentric-Tube Continuum Robots with Application to Visual Servoing,” in *Springer Tracts in Advanced Robotics*, 2009, vol. 54, pp. 485–494.
- [75] P. Sears and P. Dupont, “A steerable needle technology using curved concentric tubes,” in *IEEE International Conference on Intelligent Robots and Systems*, 2006, pp. 2850–2856.
- [76] I. H. Lieberman *et al.*, “Bone-mounted Miniature Robotic Guidance for Pedicle Screw and Translaminar Facet Screw Placement,” *Neurosurgery*, vol. 59, no. 3, pp. 641–650, Sep. 2006.

-
- [77] Y. Herry, C. Batailler, T. Lording, E. Servien, P. Neyret, and S. Lustig, “Improved joint-line restitution in unicompartmental knee arthroplasty using a robotic-assisted surgical technique,” *Int. Orthop.*, vol. 41, no. 11, pp. 2265–2271, Nov. 2017.
- [78] J. E. Lang *et al.*, “Robotic systems in orthopaedic surgery,” *Journal of Bone and Joint Surgery - Series B*, vol. 93 B, no. 10, pp. 1296–1299, Oct-2011.
- [79] S. Lang *et al.*, “A european multicenter study evaluating the flex robotic system in transoral robotic surgery,” *Laryngoscope*, vol. 127, no. 2, pp. 391–395, Feb. 2017.
- [80] “Intuitive Surgical Announces Innovative Single Port Platform — the da Vinci SP® Surgical System | Intuitive Surgical.” [Online]. Available: <https://isrg.intuitive.com/news-releases/news-release-details/intuitive-surgical-announces-innovative-single-port-platform-da>. [Accessed: 23-Nov-2019].
- [81] “Auris Health Unveils the FDA-Cleared Monarch Platform, Ushering in a New Era of Medical Intervention - Auris Health.” [Online]. Available: <https://www.aurishealth.com/about/press-releases/monarch-bronchoscopy-auris-health-fda-clearance>. [Accessed: 23-Nov-2019].
- [82] “Types of Minimally Invasive Surgery (Robotic, Endoscopic, Laparoscopic): Johns Hopkins Medicine in Baltimore, MD.” [Online]. Available: https://www.hopkinsmedicine.org/minimally_invasive_robotic_surgery/types.html#no-n-robotic. [Accessed: 08-Jun-2018].
- [83] B. M. Kraft, C. Jäger, K. Kraft, B. J. Leibl, and R. Bittner, “The AESOP robot system in laparoscopic surgery: Increased risk or advantage for surgeon and patient?,” *Surg. Endosc. Other Interv. Tech.*, vol. 18, no. 8, pp. 1216–1223, Aug. 2004.
- [84] M. O. Schurr *et al.*, “Trocar and instrument positioning system TISKA: An assist device for endoscopic solo surgery,” *Surg. Endosc.*, vol. 13, no. 5, pp. 528–531, May 1999.
- [85] G. F. Buess *et al.*, “A new remote-controlled endoscope positioning system for endoscopic solo surgery: The FIPS endoarm,” *Surg. Endosc.*, vol. 14, no. 4, pp. 395–399, Apr. 2000.
- [86] D. LaRose *et al.*, “A Telerobotic Assistant for Laparoscopic Surgery,” *IEEE Eng. Med. Biol. Mag.*, vol. 14, no. 3, pp. 279–288, 1995.
- [87] P. B. Nebot, Y. Jain, K. Haylett, R. Stone, and R. McCloy, “Comparison of task performance of the camera-holder robots EndoAssist and Aesop,” *Surg. Laparosc. Endosc. Percutan. Tech.*, vol. 13, no. 5, pp. 334–8, Oct. 2003.
- [88] “Endocontrol Medical – for easier endoscopic surgery for the benefit of the patient.” [Online]. Available: <http://www.endocontrol-medical.com/en/home/>. [Accessed: 08-Jun-2018].
- [89] S. Pandalai, D. O. Kavanagh, and P. Neary, “Robotic assisted laparoscopic colectomy,” *Ir. Med. J.*, vol. 103, no. 6, pp. 181–2, Jun. 2010.

-
- [90] J. Jarry, A. Moreau Gaudry, J. A. Long, E. Chipon, P. Cinquin, and J. L. Faucheron, "Miniaturized Robotic Laparoscope-Holder for Rectopexy: First Results of a Prospective Study," *J. Laparoendosc. Adv. Surg. Tech.*, vol. 23, no. 4, pp. 351–355, Apr. 2013.
- [91] A. G. Timoney, B. L. Davies, and R. D. Hibberd, "Robotic Surgery," *IEEE Eng. Med. Biol. Mag.*, vol. 12, no. 1, pp. 120–125, 1993.
- [92] "Intuitive | da Vinci | Robotic Surgical Systems." [Online]. Available: <https://www.intuitive.com/en-us/products-and-services/da-vinci>. [Accessed: 24-Nov-2019].
- [93] "Colonoscopy Solution: Safe and Easy-to-Use Colonoscopy - GI-View." [Online]. Available: <http://www.giview.com/>. [Accessed: 08-Jun-2018].
- [94] "HIT - Endotics." [Online]. Available: <http://www.endotics.com/8-hit.html>. [Accessed: 08-Jun-2018].
- [95] E. Tumino, R. Sacco, M. Bertini, M. Bertoni, G. Parisi, and A. Capria, "Endotics system vs colonoscopy for the detection of polyps.," *World J. Gastroenterol.*, vol. 16, no. 43, pp. 5452–6, Nov. 2010.
- [96] "Flex® Robotic System: Expanding the reach of surgery® | Medrobotics." [Online]. Available: <https://medrobotics.com/gateway/flex-robotic-system/?c=US>. [Accessed: 08-Jun-2018].
- [97] A. De Donno, L. Zorn, P. Zanne, F. Nageotte, and M. de Mathelin, "Introducing STRAS: A new flexible robotic system for minimally invasive surgery," *Proc. - IEEE Int. Conf. Robot. Autom.*, pp. 1213–1220, May 2013.
- [98] L. Zorn *et al.*, "A Novel Telemanipulated Robotic Assistant for Surgical Endoscopy: Preclinical Application to ESD," *IEEE Trans. Biomed. Eng.*, vol. 65, no. 4, pp. 797–808, Apr. 2018.
- [99] B. P. M. Yeung and P. W. Y. Chiu, "Application of robotics in gastrointestinal endoscopy: A review.," *World J. Gastroenterol.*, vol. 22, no. 5, pp. 1811–25, Feb. 2016.
- [100] H. Pullens *et al.*, "Colonoscopy with robotic steering and automated lumen centralization: a feasibility study in a colon model," *Endoscopy*, vol. 48, no. 03, pp. 286–290, Jun. 2015.
- [101] K. Kume, T. Kuroki, M. Shingai, and M. Harada, "Endoscopic submucosal dissection using the endoscopic operation robot," *Endoscopy*, vol. 44, no. S 02, pp. E399–E400, Nov. 2012.
- [102] T. Rösch *et al.*, "A motor-driven single-use colonoscope controlled with a hand-held device: a feasibility study in volunteers," *Gastrointest. Endosc.*, vol. 67, no. 7, pp. 1139–1146, Jun. 2008.

-
- [103] A. Eickhoff *et al.*, “Computer-assisted colonoscopy (the NeoGuide Endoscopy System): Results of the first human clinical trial (‘PACE Study’),” *Am. J. Gastroenterol.*, vol. 102, no. 2, pp. 261–266, Feb. 2007.
- [104] J. Pfeffer *et al.*, “The Aer-O-Scope: Proof of the Concept of a Pneumatic, Skill-Independent, Self-Propelling, Self-Navigating Colonoscope in a Pig Model,” *Endoscopy*, vol. 38, no. 2, pp. 144–148, Feb. 2006.
- [105] “Colonoscopy Solution: Safe and Easy-to-Use Colonoscopy - GI-View.” [Online]. Available: <http://www.giview.com/>. [Accessed: 14-Dec-2019].
- [106] “Painless and Safer Colonoscope - Endotics.” [Online]. Available: <http://www.endotics.com/>. [Accessed: 14-Dec-2019].
- [107] F. Cosentino, E. Tumino, G. R. Passoni, E. Morandi, and A. Capria, “Functional evaluation of the Endotics System, a new disposable self-propelled robotic colonoscope: In vitro tests and clinical trial,” *Int. J. Artif. Organs*, vol. 32, no. 8, pp. 517–527, 2009.
- [108] C. C. Y. Poon, B. Leung, C. K. W. Chan, J. Y. W. Lau, and P. W. Y. Chiu, “Design of wormlike automated robotic endoscope: dynamic interaction between endoscopic balloon and surrounding tissues,” *Surg. Endosc.*, vol. 30, no. 2, pp. 772–778, Feb. 2016.
- [109] K. Y. Ho *et al.*, “Endoscopic submucosal dissection of gastric lesions by using a Master and Slave Transluminal Endoscopic Robot (MASTER),” *Gastrointest. Endosc.*, vol. 72, no. 3, pp. 593–599, Sep. 2010.
- [110] N. Cauche *et al.*, “Sa1435 Endomina : the Endoluminal Universal Robotized Triangulation System: Description and Preliminary Results in Isolated Pig Stomach,” *Gastrointest. Endosc.*, vol. 77, no. 5, pp. AB204–AB205, May 2013.
- [111] N. Suzuki *et al.*, “Scorpion shaped endoscopic surgical robot for NOTES and SPS with augmented reality functions,” in *Lecture Notes in Computer Science (including subseries Lecture Notes in Artificial Intelligence and Lecture Notes in Bioinformatics)*, 2010, vol. 6326 LNCS, pp. 541–550.
- [112] D. J. Abbott, C. Becke, R. I. Rothstein, and W. J. Peine, “Design of an endoluminal NOTES robotic system,” in *IEEE International Conference on Intelligent Robots and Systems*, 2007, pp. 410–416.
- [113] C. C. Y. Poon *et al.*, “A bioinspired flexible robot with hybrid actuation mechanisms for endoscopic surgery,” *Hamlyn Symp. Med. Robot.*, p. 81, 2014.
- [114] C. A. Seneci, J. Shang, and G. Z. Yang, “Design of a bimanual end-effector for an endoscopic surgical robot,” *Hamlyn Symp. Med. Robot.*, pp. 83–84, 2014.
- [115] B. Dallemagne and J. Marescaux, “The ANUBIS™ project,” *Minim. Invasive Ther. Allied Technol.*, vol. 19, no. 5, pp. 257–261, Oct. 2010.

-
- [116] D. Huang *et al.*, “Optical coherence tomography,” *Science* (80-.), vol. 254, no. 5035, pp. 1178–81, Nov. 1991.
- [117] Wolfgang Drexler and J. G. Fujimoto, *Optical Coherence Tomography*. 2010.
- [118] M. A. Duguay and A. T. Mattick, “Ultrahigh Speed Photography of Picosecond Light Pulses and Echoes,” *Appl. Opt.*, vol. 10, no. 9, p. 2162, Sep. 1971.
- [119] J. Fujimoto and E. Swanson, “The development, commercialization, and impact of optical coherence tomography,” *Investigative Ophthalmology and Visual Science*, vol. 57, no. 9. Association for Research in Vision and Ophthalmology Inc., pp. OCT1–OCT13, 2016.
- [120] J. G. Fujimoto, S. De Silvestri, E. P. Ippen, C. A. Puliafito, R. Margolis, and A. R. Oseroff, “FEMTOSECOND OPTICAL RANGING IN BIOLOGICAL SYSTEMS.,” 1985, p. 104.
- [121] K. Takada, I. Yokohama, K. Chida, and J. Noda, “New measurement system for fault location in optical waveguide devices based on an interferometric technique,” *Appl. Opt.*, vol. 26, no. 9, p. 1603, May 1987.
- [122] A. F. Fercher, K. Mengedoht, and W. Werner, “Eye-length measurement by interferometry with partially coherent light,” *Opt. Lett.*, vol. 13, no. 3, p. 186, Mar. 1988.
- [123] T. Yoshizawa, *Handbook of Optical Metrology Principles and Applications, Second Edition*. Taylor & Francis Group, 2015.
- [124] P. C. Montgomery and J.-P. Fillard, “Peak fringe scanning microscopy: submicron 3D measurement of semiconductor components,” 1993, pp. 12–23.
- [125] M. Davidson, K. Kaufman, I. Mazor, and F. Cohen, “An Application Of Interference Microscopy To Integrated Circuit Inspection And Metrology,” in *Integrated Circuit Metrology, Inspection, & Process Control*, 1987, vol. 0775, p. 233.
- [126] P. J. Caber, “Interferometric profiler for rough surfaces,” *Appl. Opt.*, vol. 32, no. 19, p. 3438, Jul. 1993.
- [127] P. J. de Groot, “Interference microscopy for surface structure analysis,” in *Handbook of Optical Metrology: Principles and Applications, Second Edition*, CRC Press, 2015, pp. 791–828.
- [128] P. C. Montgomery, F. Anstötz, D. Montaner, and F. Salzenstein, “Chapter 11 Real-Time and High-Quality Online 4D FF-OCT Using Continuous Fringe Scanning with a High-Speed Camera and FPGA Image Processing,” in *Handbook of Full-Field Optical Coherence Microscopy*, Pan Stanford Publishing Pte. Ltd., 2016, pp. 393–428.
- [129] A. Dubois, K. Grieve, G. Moneron, R. Lecaque, L. Vabre, and C. Boccara, “Ultrahigh-resolution full-field optical coherence tomography,” *Appl. Opt.*, vol. 43, no. 14, pp. 2874–2883, May 2004.

-
- [130] A. F. Fercher, C. K. Hitzenberger, G. Kamp, and S. Y. El-Zaiat, "Measurement of intraocular distances by backscattering spectral interferometry," *Opt. Commun.*, vol. 117, no. 1–2, pp. 43–48, 1995.
- [131] S. R. Chinn, E. A. Swanson, and J. G. Fujimoto, "Optical coherence tomography using a frequency-tunable optical source," *Opt. Lett.*, vol. 22, no. 5, p. 340, 1997.
- [132] B. Golubovic, B. E. Bouma, G. J. Tearney, and J. G. Fujimoto, "Optical frequency-domain reflectometry using rapid wavelength tuning of a Cr⁴⁺:forsterite laser," *Opt. Lett.*, vol. 22, no. 22, p. 1704, 1997.
- [133] M. Choma, M. Sarunic, C. Yang, and J. Izatt, "Sensitivity advantage of swept source and Fourier domain optical coherence tomography," *Opt. Express*, vol. 11, no. 18, p. 2183, 2003.
- [134] J. F. de Boer, B. Cense, B. H. Park, M. C. Pierce, G. J. Tearney, and B. E. Bouma, "Improved signal-to-noise ratio in spectral-domain compared with time-domain optical coherence tomography," *Opt. Lett.*, vol. 28, no. 21, p. 2067, 2003.
- [135] R. Leitgeb, C. Hitzenberger, and A. Fercher, "Performance of fourier domain vs time domain optical coherence tomography," *Opt. Express*, vol. 11, no. 8, p. 889, 2003.
- [136] M. Wojtkowski, T. Bajraszewski, P. Targowski, and A. Kowalczyk, "Real-time in vivo imaging by high-speed spectral optical coherence tomography," *Opt. Lett.*, vol. 28, no. 19, p. 1745, 2003.
- [137] S. Yun, G. Tearney, B. Bouma, B. Park, and J. de Boer, "High-speed spectral-domain optical coherence tomography at 13 μm wavelength," *Opt. Express*, vol. 11, no. 26, p. 3598, 2003.
- [138] S. Yun, G. Tearney, J. de Boer, N. Iftimia, and B. Bouma, "High-speed optical frequency-domain imaging," *Opt. Express*, vol. 11, no. 22, p. 2953, 2003.
- [139] R. Huber, M. Wojtkowski, K. Taira, J. G. Fujimoto, and K. Hsu, "Amplified, frequency swept lasers for frequency domain reflectometry and OCT imaging: design and scaling principles," *Opt. Express*, vol. 13, no. 9, p. 3513, 2005.
- [140] R. Huber, M. Wojtkowski, and J. G. Fujimoto, "Fourier Domain Mode Locking (FDML): A new laser operating regime and applications for optical coherence tomography," *Opt. Express*, vol. 14, no. 8, p. 3225, 2006.
- [141] M. Wojtkowski, R. Leitgeb, A. Kowalczyk, T. Bajraszewski, and A. F. Fercher, "In vivo human retinal imaging by Fourier domain optical coherence tomography," *J. Biomed. Opt.*, vol. 7, no. 3, p. 457, 2002.
- [142] M. R. Hee *et al.*, "Topography of diabetic macular edema with optical coherence tomography," *Ophthalmology*, vol. 105, no. 2, pp. 360–370, 1998.
- [143] J. S. Schuman *et al.*, "Optical coherence tomography: A new tool for glaucoma diagnosis," *Curr. Opin. Ophthalmol.*, vol. 6, no. 2, pp. 89–95, 1995.

- [144] M. R. Hee *et al.*, “Optical Coherence Tomography of the Human Retina,” *Arch. Ophthalmol.*, vol. 113, no. 3, pp. 325–332, 1995.
- [145] M. R. Hee, “Optical coherence tomography of the eye,” Massachusetts Institute of Technology, 1997.
- [146] V. Pierre-Kahn, R. Tadayoni, B. Haouchine, P. Massin, and A. Gaudric, “Comparison of optical coherence tomography models OCT1 and Stratus OCT for macular retinal thickness measurement,” *Br. J. Ophthalmol.*, vol. 89, no. 12, pp. 1581–1585, Dec. 2005.
- [147] L. Vignali, E. Solinas, and E. Emanuele, “Research and Clinical Applications of Optical Coherence Tomography in Invasive Cardiology: A Review,” *Curr. Cardiol. Rev.*, vol. 10, no. 4, pp. 369–376, Jul. 2014.
- [148] G. J. Tearney *et al.*, “Consensus standards for acquisition, measurement, and reporting of intravascular optical coherence tomography studies: A report from the International Working Group for Intravascular Optical Coherence Tomography Standardization and Validation,” *J. Am. Coll. Cardiol.*, vol. 59, no. 12, pp. 1058–1072, Mar. 2012.
- [149] A. Pagnoni *et al.*, “Optical coherence tomography in dermatology,” *Ski. Res. Technol.*, vol. 5, no. 2, pp. 83–87, May 1999.
- [150] C.-P. Liang *et al.*, “Optical coherence tomography-guided laser marking with tethered capsule endomicroscopy in unsedated patients,” *Biomed. Opt. Express*, vol. 10, no. 3, pp. 1207–1222, Feb. 2019.
- [151] M. J. Gora *et al.*, “Tethered capsule endomicroscopy for microscopic imaging of the esophagus, stomach, and duodenum without sedation in humans (with video),” *Gastrointest. Endosc.*, vol. 88, no. 5, pp. 830-840.e3, Nov. 2018.
- [152] M. J. Gora, M. J. Suter, G. J. Tearney, and X. Li, “Endoscopic optical coherence tomography: technologies and clinical applications [Invited],” *Biomed. Opt. Express*, vol. 8, no. 5, pp. 2405–2444, Apr. 2017.
- [153] M. J. Gora *et al.*, “Tethered capsule endomicroscopy: from bench to bedside at a primary care practice,” *J. Biomed. Opt.*, vol. 21, no. 10, p. 104001, Oct. 2016.
- [154] M. V Sivak Jr *et al.*, “High-resolution endoscopic imaging of the GI tract using optical coherence tomography,” *Gastrointest. Endosc.*, vol. 51, no. 4 Pt 1, pp. 474–479, Apr. 2000.
- [155] S. Jäckle *et al.*, “In vivo endoscopic optical coherence tomography of the human gastrointestinal tract--toward optical biopsy,” *Endoscopy*, vol. 32, no. 10, pp. 743–749, Oct. 2000.
- [156] S.-W. Huang, A. D. Aguirre, R. A. Huber, D. C. Adler, and J. G. Fujimoto, “Swept source optical coherence microscopy using a Fourier domain mode-locked laser,” *Opt. Express*, vol. 15, no. 10, pp. 6210–6217, May 2007.

-
- [157] J. H. Cheon and W. H. Kim, "Recent advances of endoscopy in inflammatory bowel diseases," *Gut Liver*, vol. 1, no. 2, pp. 118–125, Dec. 2007.
- [158] K. Liang *et al.*, "Endoscopic forward-viewing optical coherence tomography and angiography with MHz swept source," *Opt. Lett.*, vol. 42, no. 16, pp. 3193–3196, Aug. 2017.
- [159] Y. Luo *et al.*, "Endomicroscopic optical coherence tomography for cellular resolution imaging of gastrointestinal tracts," *J. Biophotonics*, vol. 11, no. 4, pp. e201700141–e201700141, Apr. 2018.
- [160] S. Brand, J. M. Ponerós, B. E. Bouma, G. J. Tearney, C. C. Compton, and N. S. Nishioka, "Optical Coherence Tomography in the Gastrointestinal Tract," *Endoscopy*, vol. 32, no. 10, pp. 796–803, Oct. 2000.
- [161] C. Pitris, C. Jesser, S. A. Boppart, D. Stamper, M. E. Brezinski, and J. G. Fujimoto, "Feasibility of optical coherence tomography for high-resolution imaging of human gastrointestinal tract malignancies," *J. Gastroenterol.*, vol. 35, no. 2, pp. 87–92, 2000.
- [162] G. J. Tearney, M. E. Brezinski, J. F. Southern, B. E. Bouma, S. A. Boppart, and J. G. Fujimoto, "Optical biopsy in human pancreatobiliary tissue using optical coherence tomography," *Dig. Dis. Sci.*, vol. 43, no. 6, pp. 1193–1199, Jun. 1998.
- [163] J. H. Hwang, M. J. Cobb, M. B. Kimmey, and X. Li, "Optical coherence tomography imaging of the pancreas: a needle-based approach," *Clin. Gastroenterol. Hepatol.*, vol. 3, no. 7 Suppl 1, pp. S49–S52, Jul. 2005.
- [164] P. A. Testoni *et al.*, "Optical coherence tomography compared with histology of the main pancreatic duct structure in normal and pathological conditions: an 'ex vivo' study," *Dig. Liver Dis.*, vol. 38, no. 9, pp. 688–695, Sep. 2006.
- [165] P. A. Testoni, A. Mariani, B. Mangiavillano, P. G. Arcidiacono, S. Di Pietro, and E. Masci, "Intraductal optical coherence tomography for investigating main pancreatic duct strictures," *Am. J. Gastroenterol.*, vol. 102, no. 2, pp. 269–274, Feb. 2007.
- [166] P. A. Testoni and B. Mangiavillano, "Optical coherence tomography for bile and pancreatic duct imaging," *Gastrointest. Endosc. Clin. N. Am.*, vol. 19, no. 4, pp. 637–653, Oct. 2009.
- [167] L. van Manen *et al.*, "Validation of full-field optical coherence tomography in distinguishing malignant and benign tissue in resected pancreatic cancer specimens," *PLoS One*, vol. 12, no. 4, pp. e0175862–e0175862, Apr. 2017.
- [168] A. Tyberg, M.-M. Xu, M. Gaidhane, and M. Kahaleh, "Second generation optical coherence tomography: Preliminary experience in pancreatic and biliary strictures," *Dig. Liver Dis.*, vol. 50, no. 11, pp. 1214–1217, Nov. 2018.
- [169] B. Bouma *et al.*, "Optical Coherence Tomography for Optical Biopsy Properties and Demonstration of Vascular Pathology," *Opt. Lett.*, vol. 20, no. 13, pp. 1486–8, Jul. 1995.

-
- [170] E. V. Zagaynova *et al.*, “Optical coherence tomography in guided surgery of GI cancer,” 2005, p. 367.
- [171] B. B. E. Bouma, G. G. J. Tearney, C. C. Compton, and N. S. Nishioka, “High-resolution imaging of the human esophagus and stomach in vivo using optical coherence tomography,” *Gastrointest. Endosc.*, vol. 51, no. 4, pp. 467–474, 2000.
- [172] J. G. Fujimoto, C. Pitris, S. A. Boppart, and M. E. Brezinski, “Optical coherence tomography: an emerging technology for biomedical imaging and optical biopsy,” *Neoplasia*, vol. 2, no. 1–2, pp. 9–25, 2000.
- [173] J. G. Fujimoto, “Optical coherence tomography for ultrahigh resolution in vivo imaging,” *Nat Biotechnol*, vol. 21, no. 11, pp. 1361–1367, 2003.
- [174] B. Bouma and G. Tearney, “High-resolution imaging of the human esophagus and stomach in vivo using optical coherence tomography,” *Gastrointest. Endosc.*, vol. 51, no. 4, pp. 467–474, 2000.
- [175] N. Iftimia, M. Mujat, and A. Hicks, “Image-guided breast biopsy with optical coherence tomography,” *Lasers and Electro-Optics (CLEO), 2011 Conference on*, 2011. [Online]. Available: <http://ezproxy.itcr.ac.cr:2127/document/5950841/>.
- [176] G. J. Tearney *et al.*, “In vivo endoscopic optical biopsy with optical coherence tomography,” *Science*, vol. 276, no. 5321, pp. 2037–9, 1997.
- [177] G. J. Tearney *et al.*, “High speed catheter/endoscopic optical coherence tomography for the optical biopsy of in vivo tissues,” p. 850, 1997.
- [178] I. Grulkowski *et al.*, “Anterior segment imaging with Spectral OCT system using a high-speed CMOS camera,” *Opt. Express*, vol. 17, no. 6, p. 4842, 2009.
- [179] M. Gora *et al.*, “Ultra high-speed swept source OCT imaging of the anterior segment of human eye at 200 kHz with adjustable imaging range,” *Opt. Express*, vol. 17, no. 17, p. 14880, 2009.
- [180] P. B. Garcia-Allende, I. Amygdalos, H. Dhanapala, R. D. Goldin, G. B. Hanna, and D. S. Elson, “Morphological analysis of optical coherence tomography images for automated classification of gastrointestinal tissues,” *Biomed. Opt. Express*, vol. 2, no. 10, p. 2821, Oct. 2011.
- [181] H. Yu, J.-H. Shen, R. J. Shah, N. Simaan, and K. M. Joos, “Evaluation of microsurgical tasks with OCT-guided and/or robot-assisted ophthalmic forceps,” *Biomed. Opt. Express*, vol. 6, no. 2, pp. 457–72, Feb. 2015.
- [182] “2016 - In vivo endoscopic Doppler optical coherence tomography imaging of mouse colon.pdf.” .
- [183] V. X. D. Yang *et al.*, “Endoscopic Doppler optical coherence tomography in the human GI tract: Initial experience,” *Gastrointest. Endosc.*, vol. 61, no. 7, pp. 879–890, 2005.

-
- [184] R. A. Leitgeb, R. M. Werkmeister, C. Blatter, and L. Schmetterer, "Doppler Optical Coherence Tomography," *Prog. Retin. Eye Res.*, vol. 41, pp. 26–43, Jul. 2014.
- [185] M. J. Gora *et al.*, "Tethered capsule endomicroscopy enables less invasive imaging of gastrointestinal tract microstructure.," *Nat. Med.*, vol. 19, no. 2, pp. 238–40, 2013.
- [186] E. Zagaynova, N. Gladkova, N. Shakhova, G. Gelikonov, and V. Gelikonov, "Endoscopic OCT with forward-looking probe: Clinical studies in urology and gastroenterology," *J. Biophotonics*, vol. 1, no. 2, pp. 114–128, 2008.
- [187] T. Xie, H. Xie, G. K. Fedder, and Y. Pan, "Endoscopic optical coherence tomography with a modified microelectromechanical systems mirror for detection of bladder cancers.," *Appl. Opt.*, vol. 42, no. 31, pp. 6422–6, 2003.
- [188] G. Isenberg *et al.*, "Accuracy of endoscopic optical coherence tomography in the detection of dysplasia in Barrett's esophagus: A prospective, double-blinded study," *Gastrointest. Endosc.*, vol. 62, no. 6, pp. 825–831, 2005.
- [189] A. M. Rollins *et al.*, "Real-time in vivo imaging of human gastrointestinal ultrastructure by use of endoscopic optical coherence tomography with a novel efficient interferometer design.," *Opt. Lett.*, vol. 24, no. 19, pp. 1358–1360, Oct. 1999.
- [190] V. Westphal, A. M. Rollins, J. Willis, M. V. Sivak, and J. A. Izatt, "Correlation of endoscopic optical coherence tomography with histology in the lower-GI tract," *Gastrointest. Endosc.*, vol. 61, no. 4, pp. 537–546, 2005.
- [191] P. C. Montgomery, J.-M. Lussert, P. Vabre, and D. Benhaddou, "Super-resolution 3D optical imaging of semiconductors using coherence microscopy," 1995, pp. 88–94.
- [192] P. C. Montgomery, A. Benatmane, E. Fogarassy, and J. P. Ponpon, "Large area, high resolution analysis of surface roughness of semiconductors using interference microscopy," in *Materials Science and Engineering B: Solid-State Materials for Advanced Technology*, 2002, vol. 91–92, pp. 79–82.
- [193] P. Montgomery, F. Anstötz, G. Johnson, and R. Kiefer, "Real time surface morphology analysis of semiconductor materials and devices using 4D interference microscopy," *J. Mater. Sci. Mater. Electron.*, vol. 19, no. SUPPL. 1, 2008.
- [194] P. Targowski, B. Rouba, M. Góra, L. Tyimińska-Widmer, J. Marczak, and A. Kowalczyk, "Optical coherence tomography in art diagnostics and restoration," *Appl. Phys. A Mater. Sci. Process.*, vol. 92, no. 1, pp. 1–9, Jul. 2008.
- [195] P. Lambelet, "Parallel Optical Coherence Tomography (POCT) for industrial 3D inspection," in *Proceedings of SPIE - The International Society for Optical Engineering*, 2011, vol. 8082.
- [196] B. Fischer, C. Wolf, and T. Härtling, "Large field optical tomography system," *Smart Sens. Phenomena, Technol. Networks, Syst. Integr.* 2013, vol. 8693, no. April 2013, p. 86930P, 2013.

-
- [197] W. Drexler, U. Morgner, R. K. Ghanta, F. X. Kärtner, J. S. Schuman, and J. G. Fujimoto, "Ultra-high-resolution ophthalmic optical coherence tomography," *Nat. Med.*, vol. 7, no. 4, pp. 502–507, Apr. 2001.
- [198] Y. Hori *et al.*, "Automatic characterization and segmentation of human skin using three-dimensional optical coherence tomography," *Opt. Express*, vol. 14, no. 5, p. 1862, Mar. 2006.
- [199] D. C. Adler *et al.*, "Three-dimensional endomicroscopy of the human colon using optical coherence tomography," *Opt. Express*, vol. 17, no. 2, pp. 784–796, 2009.
- [200] "NinePoint Medical - See more deeply." [Online]. Available: <http://www.ninepointmedical.com/>. [Accessed: 10-Jun-2018].
- [201] "Ocelot | Avinger." [Online]. Available: <http://avinger.com/devices/ocelot/>. [Accessed: 10-Jun-2018].
- [202] M. E. Brezinski *et al.*, "Optical coherence tomography for optical biopsy: Properties and demonstration of vascular pathology," *Circulation*, vol. 93, no. 6, pp. 1206–1213, Mar. 1996.
- [203] Melissa J. Suter, Brett E. Bouma, and Guillermo J. Tearney, "Optical Coherence Tomography in Cardiology, Gastroenterology, and Pulmonary Applications - Access Engineering from McGraw-Hill," *Chapter (McGraw-Hill Professional, 2011)*, 2011. [Online]. Available: <https://ezproxy.itcr.ac.cr:2470/browse/in-vivo-clinical-imaging-and-diagnosis/c9780071626835ch04?s.num=4#>. [Accessed: 10-Oct-2016].
- [204] M. J. Gora, M. J. Suter, G. J. Tearney, and X. Li, "Endoscopic optical coherence tomography: technologies and clinical applications [Invited]," *Biomed. Opt. Express*, vol. 8, no. 5, p. 2405, May 2017.
- [205] M. S. Shishkov, G. J. Tearney, and B. E. Bouma, "Sculptured optical fiber tips for narrow diameter optical catheters," in *Biomedical Topical Meeting*, 2004, p. SE5.
- [206] P. R. Herz *et al.*, "Micromotor endoscope catheter for in vivo, ultrahigh-resolution optical coherence tomography," *Opt. Lett.*, vol. 29, no. 19, pp. 2261–2263, Oct. 2004.
- [207] W. Liang, K. Murari, Y. Zhang, Y. Chen, M.-J. Li, and X. Li, "Increased illumination uniformity and reduced photodamage offered by the Lissajous scanning in fiber-optic two-photon endomicroscopy," *J. Biomed. Opt.*, vol. 17, no. 2, p. 021108, Feb. 2012.
- [208] J. Wu, M. Conry, C. Gu, F. Wang, Z. Yaqoob, and C. Yang, "Paired-angle-rotation scanning optical coherence tomography forward-imaging probe," *Opt. Lett.*, vol. 31, no. 9, p. 1265, May 2006.
- [209] G. J. Tearney *et al.*, "Single-mode fiber-optic catheter/endoscope for optical coherence tomography," *Conf. Proc. - Lasers Electro-Optics Soc. Annu. Meet.*, pp. 57–58, 1996.
- [210] G. J. Tearney *et al.*, "Catheter-based optical imaging of a human coronary artery," *Circulation*, vol. 94, no. 11, p. 3013, 1996.

-
- [211] I. K. Jang, G. Tearney, and B. Bouma, "Visualization of tissue prolapse between coronary stent struts by optical coherence tomography: Comparison with intravascular Ultrasound," *Circulation*, vol. 104, no. 22, p. 2754, Nov. 2001.
- [212] G. J. Tearney, "In Vivo Endoscopic Optical Biopsy with Optical Coherence Tomography," *Science (80-.)*, vol. 276, no. 5321, pp. 2037–2039, Jun. 1997.
- [213] A. Sergeev *et al.*, "In vivo endoscopic OCT imaging of precancer and cancer states of human mucosa," *Opt. Express*, vol. 1, no. 13, p. 432, Dec. 1997.
- [214] F. Feldchtein *et al.*, "Endoscopic applications of optical coherence tomography," *Opt. Express*, vol. 3, no. 6, p. 257, Sep. 1998.
- [215] M.-M. Xu, S. M. Lagana, and A. Sethi, "Mo1551 Use of Optical Coherence Tomography (OCT) in the Evaluation of Gastric Lesions," *Gastrointest. Endosc.*, vol. 81, no. 5, pp. AB462–AB463, May 2015.
- [216] E. Masci, B. Mangiavillano, L. Albarello, A. Mariani, C. Doglioni, and P. A. Testoni, "Pilot study on the correlation of optical coherence tomography with histology in celiac disease and normal subjects," *J. Gastroenterol. Hepatol.*, vol. 22, no. 12, pp. 2256–2260, Dec. 2007.
- [217] B. J. Vakoc *et al.*, "Comprehensive esophageal microscopy by using optical frequency-domain imaging (with video){A figure is presented}," *Gastrointest. Endosc.*, vol. 65, no. 6, pp. 898–905, May 2007.
- [218] T.-H. Tsai *et al.*, "Structural markers observed with endoscopic 3-dimensional optical coherence tomography correlating with Barrett's esophagus radiofrequency ablation treatment response (with videos)," *Gastrointest. Endosc.*, vol. 76, no. 6, pp. 1104–1112, Dec. 2012.
- [219] H.-C. Lee *et al.*, "Assessment of the radiofrequency ablation dynamics of esophageal tissue with optical coherence tomography," *J. Biomed. Opt.*, vol. 22, no. 7, p. 076001, Jul. 2017.
- [220] C. Zhou *et al.*, "Characterization of buried glands before and after radiofrequency ablation by using 3-dimensional optical coherence tomography (with videos)," *Gastrointest. Endosc.*, vol. 76, no. 1, pp. 32–40, Jul. 2012.
- [221] W. C. Y. Lo *et al.*, "Balloon catheter-based radiofrequency ablation monitoring in porcine esophagus using optical coherence tomography," *Biomed. Opt. Express*, vol. 10, no. 4, p. 2067, 2019.
- [222] F. CP, Q. KJ, and R. AM., "Toward guidance of epicardial cardiac radiofrequency ablation therapy using optical coherence tomography," *J {Biomed} {Opt} 2010;15(4)041510. doi*, vol. 10.
- [223] X. Zhao *et al.*, "Integrated RFA/PSOCT catheter for real-time guidance of cardiac radio-frequency ablation," *Biomed. Opt. Express*, vol. 9, no. 12, p. 6400, 2018.

-
- [224] M. T. El-Haddad and Y. K. Tao, “Advances in intraoperative optical coherence tomography for surgical guidance,” *Curr. Opin. Biomed. Eng.*, vol. 3, pp. 37–48, 2017.
- [225] S. Chitchian, T. P. Weldon, and N. M. Fried, “Segmentation of optical coherence tomography images for differentiation of the cavernous nerves from the prostate gland,” *J. Biomed. Opt.*, vol. 14, no. 4, 2009.
- [226] M. Aron *et al.*, “Preliminary experience with the NirisTM optical coherence tomography system during laparoscopic and robotic prostatectomy,” *J. Endourol.*, vol. 21, no. 8, pp. 814–818, 2007.
- [227] K. Mizumoto, M. Gosho, M. Iwaki, and M. Zako, “Ocular parameters before and after steep trendelenburg positioning for robotic-assisted laparoscopic radical prostatectomy,” *Clin. Ophthalmol.*, vol. 11, pp. 1643–1650, 2017.
- [228] S. Chitchian, T. P. Weldon, M. A. Fiddy, and N. M. Fried, “Combined image-processing algorithms for improved optical coherence tomography of prostate nerves,” *J. Biomed. Opt.*, vol. 15, no. 4, 2010.
- [229] K. Hirooka *et al.*, “The Effect of Steep Trendelenburg Positioning on Retinal Structure and Function during Robotic-Assisted Laparoscopic Procedures,” *J. Ophthalmol.*, vol. 2018, 2018.
- [230] D. W. Skarecky *et al.*, “Zero positive surgical margins after radical prostatectomy: is the end in sight,” *Expert Rev. Med. Devices*, vol. 5, no. 6, pp. 709–717, Nov. 2008.
- [231] Y. Taketani *et al.*, “Transient but significant visual field defects after robot-assisted laparoscopic radical prostatectomy in deep trendelenburg position,” *PLoS One*, vol. 10, no. 4, 2015.
- [232] P. P. Dangle, K. K. Shah, B. Kaffenberger, and V. R. Patel, “The use of high resolution optical coherence tomography to evaluate robotic radical prostatectomy specimens,” *Int. Braz. J. Urol.*, vol. 35, no. 3, pp. 344–353, 2009.
- [233] R. K. Goel and J. H. Kaouk, “Optical coherence tomography: the past, present and future,” *J. Robot. Surg.*, vol. 1, no. 3, pp. 179–184, 2007.
- [234] M. Finke *et al.*, “Automatic scanning of large tissue areas in neurosurgery using optical coherence tomography,” *Int. J. Med. Robot. Comput. Assist. Surg.*, vol. 8, no. 3, pp. 327–336, Sep. 2012.
- [235] S. R. Kantelhardt, M. Finke, A. Schweikard, and A. Giese, “Evaluation of a completely robotized neurosurgical operating microscope,” *Neurosurgery*, vol. 72 Suppl 1, pp. 19–26, Jan. 2013.
- [236] I. K. Kim *et al.*, “Concurrent multi-scale imaging: Optical coherence tomography under MRI guidance for neurosurgery,” in *Proceedings of the IEEE Annual Northeast Bioengineering Conference, NEBEC*, 2013, pp. 307–308.
- [237] J. D. Díaz, D. Kundrat, K.-F. Goh, O. Majdani, and T. Ortmaier, *Towards intra-*

- operative OCT guidance for automatic head surgery: First experimental results*, vol. 8151 LNCS, no. PART 3. 2013.
- [238] J. Díaz Díaz, M. H. Riva, O. Majdani, and T. Ortmaier, “Accuracy of optical navigation systems for automatic head surgery: Optical tracking versus optical coherence tomography,” in *Photonic Therapeutics and Diagnostics X*, 2014, vol. 8926.
- [239] S. S. Gurbani *et al.*, “Robot-assisted three-dimensional registration for cochlear implant surgery using a common-path swept-source optical coherence tomography probe,” *J. Biomed. Opt.*, vol. 19, no. 5, 2014.
- [240] M. Zhao *et al.*, “Sensing and three-dimensional imaging of cochlea and surrounding temporal bone using swept source high-speed optical coherence tomography,” in *Progress in Biomedical Optics and Imaging - Proceedings of SPIE*, 2013, vol. 8571.
- [241] Y. Huang, C. Song, X. Liu, and J. U. Kang, “Motion-compensated hand-held common-path Fourier-domain optical coherence tomography probe for image-guided intervention,” in *Progress in Biomedical Optics and Imaging - Proceedings of SPIE*, 2013, vol. 8571, p. 85711N.
- [242] C. Song, P. L. Gehlbach, and J. U. Kang, “CP-OCT sensor guided SMART micro-forceps,” in *Progress in Biomedical Optics and Imaging - Proceedings of SPIE*, 2014, vol. 8938.
- [243] C. Yeo, H.-C. Park, S. Jang, P. L. Gehlbach, and C. Song, “Dual optical coherence tomography sensor guided, two-motor, horizontal SMART micro-scissors,” *Opt. Lett.*, vol. 41, no. 20, pp. 4723–4726, 2016.
- [244] D. Koo, H.-C. Park, P. L. Gehlbach, and C. Song, “Development and preliminary results of bimanual smart micro-surgical system using a ball-lens coupled OCT distance sensor,” *Biomed. Opt. Express*, vol. 7, no. 11, pp. 4816–4826, Oct. 2016.
- [245] I. Park, M. J. Kim, and W. K. Chung, “The development of system for measurement of needle insertion force into eye,” in *13th International Conference on Ubiquitous Robots and Ambient Intelligence, URAI 2016*, 2016, pp. 899–900.
- [246] J. H. Cho, H. G. Shin, Y. Yoon, K. H. Kim, M. J. Kim, and W. K. Chung, “Ophthalmic microsurgical motion and suture shape evaluation using Optical Coherence Tomography,” in *2016 13th International Conference on Ubiquitous Robots and Ambient Intelligence, URAI 2016*, 2016, pp. 124–127.
- [247] M. Draelos, B. Keller, C. Toth, A. Kuo, K. Hauser, and J. Izatt, “Teleoperating robots from arbitrary viewpoints in surgical contexts,” in *2017 IEEE/RSJ International Conference on Intelligent Robots and Systems, IROS 2017*, 2017, vol. 2017-Sept, pp. 2549–2555.
- [248] C.-W. Chen *et al.*, “Semiautomated optical coherence tomography-guided robotic surgery for porcine lens removal,” *J. Cataract Refract. Surg.*, vol. 45, no. 11, pp. 1665–1669, 2019.

-
- [249] J. T. Wilson *et al.*, “Intraocular robotic interventional surgical system (IRISS): Mechanical design, evaluation, and master–slave manipulation,” *Int. J. Med. Robot. Comput. Assist. Surg.*, vol. 14, no. 1, 2018.
- [250] M. Draelos, B. Keller, G. Tang, A. Kuo, K. Hauser, and J. Izatt, “Real-Time Image-Guided Cooperative Robotic Assist Device for Deep Anterior Lamellar Keratoplasty,” in *2018 IEEE International Conference on Robotics and Automation, ICRA 2018*, 2018, pp. 4013–4018.
- [251] M. Zhou *et al.*, “6DOF Needle Pose Estimation for Robot-Assisted Vitreoretinal Surgery,” *IEEE Access*, vol. 7, pp. 63113–63122, 2019.
- [252] M. Ourak, B. Tamadazte, and N. Andreff, “Partitioned camera-OCT based 6 DOF visual servoing for automatic repetitive optical biopsies,” in *IEEE International Conference on Intelligent Robots and Systems*, 2016, vol. 2016-Novem, pp. 2337–2342.
- [253] M. Ourak, A. De Simone, B. Tamadazte, G. J. Laurent, A. Menciassi, and N. Andreff, “Automated in-plane OCT-probe positioning towards repetitive optical biopsies,” in *2016 IEEE International Conference on Robotics and Automation (ICRA)*, 2016, pp. 4186–4191.
- [254] L.-A. Duflot, R. Reisenhofer, B. Tamadazte, N. Andreff, and A. Krupa, “Wavelet and shearlet-based image representations for visual servoing,” *Int. J. Rob. Res.*, vol. 38, no. 4, pp. 422–450, 2019.
- [255] L.-A. Duflot, B. Tamadazte, N. Andreff, and A. Krupa, “Wavelet-Based Visual Servoing Using OCT Images,” in *Proceedings of the IEEE RAS and EMBS International Conference on Biomedical Robotics and Biomechatronics*, 2018, vol. 2018-Augus, pp. 621–626.
- [256] E. Ayvali, C.-P. Liang, M. Ho, Y. Chen, and J. P. Desai, “Towards a discretely actuated steerable cannula for diagnostic and therapeutic procedures,” *Int. J. Rob. Res.*, vol. 31, no. 5, pp. 588–603, 2012.
- [257] E. Ayvali, M. Ho, and J. P. Desai, “A novel discretely actuated steerable probe for percutaneous procedures,” in *Springer Tracts in Advanced Robotics*, 2014, vol. 79, pp. 115–123.
- [258] G. Del Giudice, L. Wang, J.-H. Shen, K. Joos, and N. Simaan, “Continuum robots for multi-scale motion: Micro-scale motion through equilibrium modulation,” in *2017 IEEE/RSJ International Conference on Intelligent Robots and Systems, IROS 2017*, 2017, vol. 2017-Sept, pp. 2537–2542.
- [259] Y. Baran, K. Rabenorosoa, G. J. Laurent, P. Rougeot, N. Andreff, and B. Tamadazte, “Preliminary results on OCT-based position control of a concentric tube robot,” in *2017 IEEE/RSJ International Conference on Intelligent Robots and Systems (IROS)*, 2017, pp. 3000–3005.
- [260] C. Song, D. Y. Park, P. L. Gehlbach, S. J. Park, and J. U. Kang, “Fiber-optic OCT

- sensor guided ‘SMART’ micro-forceps for microsurgery,” *Biomed. Opt. Express*, vol. 4, no. 7, pp. 1045–1050, Jun. 2013.
- [261] C.-W. Chen *et al.*, “Intraocular robotic interventional surgical system (IRISS): Semi-automated OCT-guided cataract removal,” *Int. J. Med. Robot. Comput. Assist. Surg.*, vol. 14, no. 6, 2018.
- [262] “Automatic Optical Coherence Tomography Imaging of Stationary and Moving Eyes with a Robotically-Aligned Scanner - IEEE Conference Publication,” 2019. [Online]. Available: <https://ieeexplore.ieee.org/document/8793524>. [Accessed: 06-Nov-2019].
- [263] H. Yu, J. H. Shen, K. M. Joos, and N. Simaan, “Design, calibration and preliminary testing of a robotic telemanipulator for OCT guided retinal surgery,” in *Proceedings - IEEE International Conference on Robotics and Automation*, 2013, pp. 225–231.
- [264] N. Gessert, M. Schlüter, and A. Schlaefel, “A deep learning approach for pose estimation from volumetric OCT data,” *Med. Image Anal.*, vol. 46, pp. 162–179, May 2018.
- [265] M. Zhou *et al.*, “Needle localization for robot-assisted subretinal injection based on deep learning,” in *2019 International Conference on Robotics and Automation, ICRA 2019*, 2019, vol. 2019-May, pp. 8727–8732.
- [266] A. Mendizabal, R. Sznitman, and S. Cotin, “Force classification during robotic interventions through simulation-trained neural networks,” *Int. J. Comput. Assist. Radiol. Surg.*, vol. 14, no. 9, pp. 1601–1610, 2019.
- [267] A. Mendizabal, T. Fountoukidou, J. Hermann, R. Sznitman, and S. Cotin, “A Combined Simulation and Machine Learning Approach for Image-Based Force Classification During Robotized Intravitreal Injections,” *21st International Conference on Medical Image Computing and Computer Assisted Intervention, MICCAI 2018*, vol. 11073 LNCS. Springer Verlag, Inria, Strasbourg, France, pp. 12–20, 2018.
- [268] N. Gessert, M. Gromniak, M. Schlüter, and A. Schlaefel, “Two-path 3D CNNs for calibration of system parameters for OCT-based motion compensation,” in *Medical Imaging 2019: Image-Guided Procedures, Robotic Interventions, and Modeling*, 2019, vol. 10951.
- [269] A. Mendizabal, R. Sznitman, and S. Cotin, “Force classification during robotic interventions through simulation-trained neural networks,” *Int. J. Comput. Assist. Radiol. Surg.*, vol. 14, no. 9, pp. 1601–1610, 2019.
- [270] R. C. Newton *et al.*, “Robot-assisted transvaginal peritoneoscopy using confocal endomicroscopy: A feasibility study in a porcine model,” *Surg. Endosc.*, vol. 26, no. 9, pp. 2532–2540, 2012.
- [271] B. Rosa, M. S. Erden, T. Vercauteren, B. Herman, J. Szewczyk, and G. Morel, “Building large mosaics of confocal edomicroscopic images using visual servoing,” *IEEE Trans. Biomed. Eng.*, vol. 60, no. 4, pp. 1041–1049, 2013.

- [272] A. Technologies, “Swept Lasers for OCT 1060 & 1310 nm Swept Lasers for OCT.”
- [273] A. Technologies, “1310 nm SS-OCT Laser Engine Final test Report,” 2016.
- [274] A. Technologies, *Axsun Swept-Source OCT Ethernet / PCIe Data Acquisition Board, Installation Guide and Operator’s Manual*. 2018.
- [275] A. M. D. Lee, H. Pahlevaninezhad, V. X. D. Yang, S. Lam, C. MacAulay, and P. Lane, “Fiber-optic polarization diversity detection for rotary probe optical coherence tomography,” *Opt. Lett.*, vol. 39, no. 12, pp. 3638–41, Jun. 2014.
- [276] D. Liao, A. E. Pivonka, B. R. Haberle, D. C. Petersen, B. M. Hoeling, and R. C. Haskell, “Limits to performance improvement provided by balanced interferometers and balanced detection in OCT/OCM instruments,” in *Coherence Domain Optical Methods and Optical Coherence Tomography in Biomedicine VIII*, 2004, vol. 5316, p. 467.
- [277] A. G. Podoleanu, “Unbalanced versus balanced operation in an optical coherence tomography system,” *Appl. Opt.*, vol. 39, no. 1, p. 173, Jan. 2000.
- [278] A. D. Kersey, M. J. Marrone, and A. Dandridge, “Polarization diversity detection for fiber interferometers using active feedback control of output polarization-mode selection,” *Opt. Lett.*, vol. 15, no. 22, p. 1315, Nov. 1990.
- [279] S. H. Yun and S. J. J. Kwok, “Light in diagnosis, therapy and surgery,” *Nature Biomedical Engineering*, vol. 1, no. 1. Nature Publishing Group, 10-Jan-2017.
- [280] A. M. Rollins and J. A. Izatt, “Optimal interferometer designs for optical coherence tomography,” *Opt. Lett.*, vol. 24, no. 21, p. 1484, Nov. 1999.
- [281] Wolfgang Drexler, J. G. Fujimoto, and N. Graf, *Optical Coherence Tomography*, 2nd ed. 2010.
- [282] A. F. Fercher, W. Drexler, C. K. Hitzenberger, and T. Lasser, “Optical coherence tomography - Principles and applications,” *Reports Prog. Phys.*, vol. 66, no. 2, pp. 239–303, Feb. 2003.
- [283] X. Zhu, Y. Liang, Y. Mao, Y. Jia, Y. Liu, and G. Mu, “Analyses and calculations of noise in optical coherence tomography systems,” *Front. Optoelectron. China*, vol. 1, no. 3–4, pp. 247–257, 2008.
- [284] M. A. Choma, M. V. Sarunic, C. Yang, and J. Izatt, “Sensitivity advantage of swept source and Fourier domain optical coherence tomography,” *Opt. Express*, vol. 11, no. 18, pp. 2183–2189, 2003.
- [285] A. Agrawal, T. J. Pfefer, P. D. Woolliams, P. H. Tomlins, and G. Nehmetallah, “Methods to assess sensitivity of optical coherence tomography systems,” *Biomed. Opt. Express*, vol. 8, no. 2, p. 902, 2017.
- [286] IDIL Fibres Optiques, “End Fiber Shaping - IDIL Fibres Optiques.” [Online].

- Available: <https://www.idil-fibres-optiques.com/product/end-fiber-shaping/>. [Accessed: 31-May-2018].
- [287] fs.com, “SC/APC Type A Singlemode 0.9/2.0/3.0mm Pre-polished Ferrule Field Assembly Connector Fast/Quick Connector | FS Fiberstore.” [Online]. Available: <https://www.fs.com/products/48517.html>. [Accessed: 30-Oct-2019].
- [288] B. P. M. Yeung and T. Gourlay, “A technical review of flexible endoscopic multitasking platforms,” *International Journal of Surgery*, vol. 10, no. 7, pp. 345–354, 2012.
- [289] N. Medical, “NvisionVLE® Imaging System - NinePoint Medical.” [Online]. Available: <http://www.ninepointmedical.com/nvisionvle-imaging-system/#advanced-system>. [Accessed: 12-Sep-2018].
- [290] M. J. Gora *et al.*, “Tethered capsule endomicroscopy for microscopic imaging of the esophagus, stomach, and duodenum without sedation in humans (with video),” *Gastrointest. Endosc.*, vol. 88, no. 5, pp. 830–840.e3, Nov. 2018.
- [291] N. Medical, “Bile Duct | NinePoint Medical.” [Online]. Available: <https://www.ninepointmedical.com/bile-duct>. [Accessed: 31-Oct-2019].
- [292] M. Gschwantler *et al.*, “High-grade dysplasia and invasive carcinoma in colorectal adenomas: a multivariate analysis of the impact of adenoma and patient characteristics,” *Eur. J. Gastroenterol. Hepatol.*, vol. 14, no. 2, pp. 183–8, Feb. 2002.
- [293] G. van Soest, J. G. Bosch, and A. F. W. van der Steen, “Alignment of intravascular optical coherence tomography movies affected by non-uniform rotation distortion,” in *Coherence Domain Optical Methods and Optical Coherence Tomography in Biomedicine XII*, 2008, vol. 6847, p. 684721.
- [294] M. L. Dufour *et al.*, “Tools for experimental characterization of the non-uniform rotational distortion in intravascular OCT probes,” 2011, vol. 7883, p. 788339.
- [295] G. van Soest, J. G. Bosch, and A. F. W. van der Steen, “Azimuthal registration of image sequences affected by nonuniform rotation distortion,” *IEEE Trans. Inf. Technol. Biomed.*, vol. 12, no. 3, pp. 348–355, May 2008.
- [296] A. M. D. Lee *et al.*, “*In vivo* lung microvasculature visualized in three dimensions using fiber-optic color Doppler optical coherence tomography,” *J. Biomed. Opt.*, vol. 18, no. 5, p. 050501, Apr. 2013.
- [297] J. Izatt *et al.*, “Optical coherence tomography for gastrointestinal endoscopy: clinical update,” in *Biomedical Optical Spectroscopy and Diagnostics*, 2000, p. SuC7.
- [298] A. M. Sergeev *et al.*, “*In vivo* endoscopic OCT imaging of precancer and cancer states of human mucosa,” *Opt. Express*, vol. 1, no. 13, pp. 432–440, Dec. 1997.
- [299] B. J. F. Wong *et al.*, “*In vivo* optical coherence tomography of the human larynx: normative and benign pathology in 82 patients,” *Laryngoscope*, vol. 115, no. 11, pp.

- 1904–11, Nov. 2005.
- [300] W. Kang *et al.*, “Motion artifacts associated with in vivo endoscopic OCT images of the esophagus,” *Opt. Express*, vol. 19, no. 21, pp. 20722–35, 2011.
- [301] O. O. Ahsen *et al.*, “Correction of rotational distortion for catheter-based en face OCT and OCT angiography,” *Opt. Lett.*, vol. 39, no. 20, p. 5973, 2014.
- [302] C. Sun *et al.*, “In vivo feasibility of endovascular Doppler optical coherence tomography,” *Biomed. Opt. Express*, vol. 3, no. 10, p. 2600, Oct. 2012.
- [303] N. Uribe-Patarroyo and B. E. Bouma, “Rotational distortion correction in endoscopic optical coherence tomography based on speckle decorrelation,” *Opt. Lett.*, vol. 40, no. 23, p. 5518, Dec. 2015.
- [304] Y. Kawase *et al.*, “Comparison of nonuniform rotational distortion between mechanical IVUS and OCT using a phantom model,” *Ultrasound Med. Biol.*, vol. 33, no. 1, pp. 67–73, Jan. 2007.
- [305] “Multi-matériaux pour impression 3D Polyjet | Initial.” [Online]. Available: <https://www.initial.fr/materiaux/matieres-plastiques/multimateriaux/>. [Accessed: 03-Oct-2019].
- [306] “Connex3 Objet500 and Objet350 Multi-Material 3D Printers | Stratasys.” [Online]. Available: <https://www.stratasys.com/3d-printers/objet-350-500-connex3>. [Accessed: 03-Oct-2019].
- [307] C. J. Willmott and K. Matsuura, “Advantages of the mean absolute error (MAE) over the root mean square error (RMSE) in assessing average model performance,” *Clim. Res.*, vol. 30, no. 1, pp. 79–82, Dec. 2005.
- [308] “Our Journey – History from 1945 | KARL STORZ Endoskope | France.” [Online]. Available: <https://www.karlstorz.com/fr/en/history.htm>. [Accessed: 27-Dec-2019].
- [309] W. Kang *et al.*, “Endoscopically guided spectral-domain OCT with double-balloon catheters,” *Opt. Express*, vol. 18, no. 16, pp. 17364–17372, 2010.
- [310] NinePoint Medical, “NvisionVLE® Imaging System - NinePoint Medical.” [Online]. Available: <https://www.ninepointmedical.com/nvisionvle-imaging-system>. [Accessed: 24-Oct-2019].
- [311] K. Waldron and J. Schmiedeler, “Kinematics,” in *Springer Handbook of Robotics*, Berlin, Heidelberg: Springer Berlin Heidelberg, 2008, pp. 9–33.
- [312] B. A. Jones and I. D. Walker, “Kinematics for multisection continuum robots,” *IEEE Trans. Robot.*, vol. 22, no. 1, pp. 43–55, Feb. 2006.
- [313] E. W. Weisstein, “ArcLength,” *MathWorld*. [Online]. Available: <http://mathworld.wolfram.com/ArcLength.html>.
- [314] T. Banchoff and S. Lovett, *Differential Geometry of Curves and Surfaces*. CRC Press,

- 2010.
- [315] H. Anton, I. C. Bivens, and S. Davis, *Calculus, 10th Edition*. 2012.
- [316] K. C. LTD, “Colonoscopy (Lower GI Endoscopy) Simulator Type II LM-107 : KOKEN CO.,LTD.” [Online]. Available: http://www.kokenmpc.co.jp/english/products/life_simulation_models/medical_education/lm-107/index.html. [Accessed: 01-Jun-2018].
- [317] K. M. Horton, F. M. Corl, and E. K. Fishman, “CT evaluation of the colon: Inflammatory disease,” *Radiographics*, vol. 20, no. 2. Radiological Society of North America Inc., pp. 399–418, 2000.
- [318] L. B. F. de Pierola, J. Cubiella, F. Mugica, L. Hijona, and C. J. Cobian Malaver, “Malignant Colorectal Polyps: Diagnosis, Treatment and Prognosis,” in *Colonoscopy and Colorectal Cancer Screening - Future Directions*, InTech, 2013.
- [319] G. T. Smith, K. L. Lurie, D. V Zlatev, J. C. Liao, and A. K. Ellerbee Bowden, “Multimodal 3D cancer-mimicking optical phantom,” *Biomed. Opt. Express*, vol. 7, no. 2, p. 648, 2016.
- [320] D. M. de Bruin *et al.*, “Optical phantoms of varying geometry based on thin building blocks with controlled optical properties,” *J. Biomed. Opt.*, vol. 15, no. 2, p. 25001, 2010.
- [321] R. B. Saager, C. Kondru, K. Au, K. Sry, F. Ayers, and A. J. Durkin, “Multilayer silicone phantoms for the evaluation of quantitative optical techniques in skin imaging,” *Design and Performance Validation of Phantoms Used in Conjunction with Optical Measurement of Tissue II*. SPIE, 2010.
- [322] G. Lamouche *et al.*, “Review of tissue simulating phantoms with controllable optical, mechanical and structural properties for use in optical coherence tomography,” *Biomed. Opt. Express*, vol. 3, no. 6, p. 1381, 2012.
- [323] M. R. N. Avanaki, A. G. Podoleanu, M. C. Price, S. A. Corr, and S. A. Hojjatoleslami, “Two applications of solid phantoms in performance assessment of optical coherence tomography systems,” *Appl. Opt.*, vol. 52, no. 29, p. 7054, 2013.
- [324] C. Yang, V. Hou, L. Y. Nelson, and E. J. Seibel, “Color-matched and fluorescence-labeled esophagus phantom and its applications,” *J. Biomed. Opt.*, vol. 18, no. 2, p. 26020, 2013.
- [325] K. L. Lurie, G. T. Smith, S. A. Khan, J. C. Liao, and A. K. Ellerbee, “Three-dimensional, distendable bladder phantom for optical coherence tomography and white light cystoscopy,” *J. Biomed. Opt.*, vol. 19, no. 3, p. 36009, 2014.
- [326] P. Diep *et al.*, “Three-dimensional printed optical phantoms with customized absorption and scattering properties,” *Biomed. Opt. Express*, vol. 6, no. 11, p. 4212, 2015.

-
- [327] G. T. Smith, K. L. Lurie, D. V. Zlatev, J. C. Liao, and A. K. Ellerbee Bowden, "Multimodal 3D cancer-mimicking optical phantom," *Biomed. Opt. Express*, vol. 7, no. 2, p. 648, Feb. 2016.
- [328] F. Ayers, A. Grant, D. Kuo, D. J. Cuccia, and A. J. Durkin, "Fabrication and characterization of silicone-based tissue phantoms with tunable optical properties in the visible and near infrared domain," 2008, p. 687007.
- [329] A. R. Tumlinson *et al.*, "In vivo ultrahigh-resolution optical coherence tomography of mouse colon with an achromatized endoscope," *J. Biomed. Opt.*, vol. 11, no. 6, p. 064003, 2006.
- [330] P. in the P. Workshop, "The Paris endoscopic classification of superficial neoplastic lesions: esophagus, stomach, and colon," *Gastrointest. Endosc.*, vol. 58, no. 6, pp. S3–S43, 2003.
- [331] A. N. Bashkatov, E. A. Genina, V. I. Kochubey, V. S. Rubtsov, E. A. Kolesnikova, and V. V. Tuchin, "Optical properties of human colon tissues in the 350 – 2500 nm spectral range," *Quantum Electron.*, vol. 44, no. 8, pp. 779–784, 2014.
- [332] E. Zagaynova, N. Gladkova, N. Shakhova, G. Gelikonov, and V. Gelikonov, "Endoscopic OCT with forward-looking probe: clinical studies in urology and gastroenterology," *J. Biophotonics*, vol. 1, no. 2, pp. 114–128, 2008.
- [333] "AJCC - American Joint Committee on Cancer." [Online]. Available: <https://cancerstaging.org/Pages/default.aspx>. [Accessed: 05-Jun-2019].
- [334] "Cancer Staging - National Cancer Institute." [Online]. Available: <https://www.cancer.gov/about-cancer/diagnosis-staging/staging>. [Accessed: 04-Jun-2019].
- [335] J. E. Greivenkamp, *Field Guide to Geometrical Optics*. 1000 20th Street, Bellingham, WA 98227-0010 USA: SPIE, 2004.
- [336] T. S. Tkaczyk, *Field Guide to Microscopy*. 1000 20th Street, Bellingham, WA 98227-0010 USA: SPIE, 2010.
- [337] R. J. Webster and B. A. Jones, "Design and Kinematic Modeling of Constant Curvature Continuum Robots: A Review," *Int. J. Rob. Res.*, vol. 29, no. 13, pp. 1661–1683, Jun. 2010.
- [338] Epotek, "EPO-TEK ® 730," 2017. [Online]. Available: www.epotek.com. [Accessed: 30-Oct-2019].
- [339] Epotek, "EPO-TEK ® 353ND-T Technical Data Sheet For Reference Only High Temperature Thixotropic Epoxy," 2019. [Online]. Available: www.epotek.com. [Accessed: 30-Oct-2019].